January 2014

Investigating The Heterogeneous Chemistry Of Polycyclic Aromatic Hydrocarbons And Other Organic Species In Atmospheric Aerosols

Richard Cochran

INVESTIGATING THE HETEROGENEOUS CHEMISTRY OF POLYCYCLIC AROMATIC HYDROCARBONS AND OTHER ORGANIC SPECIES IN ATMOSPHERIC AEROSOLS

by

Richard Eugene Cochran
Bachelor of Science, University of North Dakota, 2010

A Dissertation

Submitted to the Graduate Faculty

of the

University of North Dakota

in partial fulfillment of the requirements

for the degree of

Doctor of Philosophy

Grand Forks, North Dakota
December
2014

This dissertation, submitted by Richard Cochran in partial fulfillment of the requirements for the Degree of Doctor of Philosophy from the University of North Dakota, has been read by the Faculty Advisory Committee under whom the work has been done and is hereby approved.

Dr. Alena Kubátová, Chair

Dr. Evguenii Kozliak

Dr. David Pierce

Dr. Julia Zhao

Dr. Frank Bowman

This dissertation is being submitted by the appointed advisory committee as having met all of the requirements of the School of Graduate Studies at the University of North Dakota and is hereby approved.

Wayne Swisher
Dean of the School of Graduate Studies

November 26, 2014
Date

PERMISSION

Title	Investigating the Heterogeneous Chemistry of Polycyclic Aromatic Hydrocarbons and Other Organic Species in Atmospheric Aerosols
Department	Chemistry
Degree	Doctor of Philosophy

In presenting this dissertation in partial fulfillment of the requirements for a graduate degree from the University of North Dakota, I agree that the library of this University shall make it freely available for inspection. I further agree that permission for extensive copying for scholarly purposes may be granted by the professor who supervised my dissertation work or, in her absence, by the Chairperson of the department or the dean of the School of Graduate Studies. It is understood that any copying or publication or other use of this dissertation or part thereof for financial gain shall not be allowed without my written permission. It is also understood that due recognition shall be given to me and to the University of North Dakota in any scholarly use which may be made of any material in my thesis or dissertation.

Richard E. Cochran
September 29, 2014

TABLE OF CONTENTS

LIST OF FIGURES

LIST OF TABLES

LIST OF SCHEMES

Scheme Page

ABBREVIATIONS

Abbreviation	Full Meaning
APCI	Atmospheric Pressure Chemical Ionization
BSTFA	*N,O*-Bis(trimethylsilyl)trifluoroacetamide
CCN	Cloud Condensation Nuclei
CPC	Condensation Particle Counter
DCM	Dichloromethane
DE	Diesel exhaust
DEP	Diesel engine particles
DI	Direct Infusion
DMA	Differential Mobility Analyzer
EC	Elemental Carbon
EI	Electron Ionization
ESI	Electrospray Ionization
FIA	Flow Injection Analysis
GC	Gas Chromatography
HMW	High Molecular Weight
HPLC	High Performance Liquid Chromatography
HRMS	High Resolution Mass Spectrometry
LC	Liquid Chromatography
LMW	Low Molecular Weight
LOD	Limit of Detection
LOQ	Limit of Quantitation
LRMS	Low Resolution Mass Spectrometry
MeOH	Methanol
MS	Mass Spectrometry
NICI	Negative-Ion Chemical Ionization
NIST	National Institute of Standard & Technology
OA	Organic Aerosol
OC	Organic Carbon
PAH	Polycyclic Aromatic Hydrocarbon
PFE	Pressurized Fluid Extraction
POA	Primary Organic Aerosol
POM	Polycyclic Organic Matter
Py	Pyrolysis
Q-MS	Quadrupole Mass Spectrometer
SIM	Selected Ion Monitoring
SITI	Selected Ion-Total Ion
SMPS	Scanning Mobility Particle Sizer

SOA	Secondary Organic Aerosol
SPE	Solid Phase Extraction
SRM	Standard Reference Material
TIC	Total Ion Current
TD	Thermal Desorption
TOF	Time of Flight
US EPA	United States Environmental Protection Agency
WS PM	Wood Smoke Particulate Matter

SYMBOLS

Symbol	Symbol Representation
ΔH_{vap}	Vaporization Enthalpy Measured for Neat Standard
ΔH_{vap}^{eff}	Vaporization Enthalpy Measured for Adsorbed Species
${}^{\alpha}\Delta H_{vap}^{eff}$	Vaporization Enthalpy Measured for Adsorbed Species (Trace)
${}^{\beta}\Delta H_{vap}^{eff}$	Vaporization Enthalpy Measured for Adsorbed Species (Bulk)
E_a^{vap}	Activation Energy of Vaporization Measured for Neat Standard
$E_a^{vap,eff}$	Activation Energy of Vaporization Measured for Adsorbed Species
${}^{\alpha}E_a^{vap,eff}$ (Trace)	Activation Energy of Vaporization Measured for Adsorbed Species
${}^{\beta}E_a^{vap,eff}$ (Bulk)	Activation Energy of Vaporization Measured for Adsorbed Species
T_{low}	Onset Temperature of Vaporization
T_{high}	Ending Temperature of Vaporization
T_{avg}	Temperature at Maximum Rate of Mass Loss

ACKNOWLEDGMENTS

I sincerely thank my advisors Dr. Alena Kubátová and Dr. Evguenii Kozliak for their guidance, mentorship, help, support, advice and encouragement during my graduate tenure at the University of North Dakota. I would also like to extend my appreciation to Dr. David Pierce, Dr. Frank Bowman, Dr. Sean Hightower, and Dr. Julia Zhao, all who served on my graduate advisory committee throughout my tenure.

I would like to thank all of my colleagues and friends within Dr. Kubatova's research group, who were always willing to help. Special thanks to Haewoo Jeong for being an integral part in many of these projects, especially with designing and constructing the large-scale aerosol chamber system. Great thanks to the many undergraduate students, Zach Hoggarth, Sandra Minchala, Luke Van Els, Honza Bílek, Laura Elsbernd, and Allie Smith. Additional thanks to Dr. Josef Beranek and Dr. Nagaraju Dongari.

I am very grateful for the financial support from the National Science Foundation, North Dakota EPSCoR, SUNRISE Education and Research Program, Department of Chemistry at the University of North Dakota, the Office of Academic Affairs and Provost, the Graduate School at the University of North Dakota, and the Chemistry Graduate Student Association at the University of North Dakota.

Finally I would like to thank my wife Michelle and my two children, Micah and Hayley, for their endless support, love and patience during my graduate career. Without them none of this would be possible.

ABSTRACT

Organic aerosols (OA; organic compounds present on the surface or within aerosols) in the atmosphere may play a significant role in various atmospheric processes as well as have an impact on human health. While many primary (direct) sources of OA (POA) are known, a significant portion of OA is formed through the oxidation of primary precursors, creating secondary organic aerosols (SOA) through processes that are still unclear. This dissertation, therefore, focuses on the development of analytical methods for characterizing SOA as well as investigating the mechanism behind their formation and aerosol chemistry.

In the first phase of this work, methods were developed to identify and quantify the large number of products formed during the oxidation of PAHs, utilizing analysis techniques such as chromatography (gas and liquid) and mass spectrometry (low and high resolution). In addition, extraction and sample preparation methods were evaluated with the focus on increasing the sensitivity in detecting PAH oxidation products.

The mechanisms behind the heterogeneous oxidation of 3-4 ring PAHs were investigated by simulating reactions of PAHs in the presence of various gas-phase oxidants under atmospheric conditions. Both a small and large-scale aerosol simulation chamber were designed and constructed to study the oxidation of PAHs adsorbed to the surfaces of diesel exhaust aerosols.

To aid in modeling, the interactions of SOA with aerosol surfaces experiments were performed using thermogravimetry-differential scanning calorimetry (TGA-DSC) to

define the changes in vaporization enthalpies (ΔH_{vap}) of common OA species when adsorbed to different aerosol surface types. Differences observed between values calculated for neat analyte solutions and those when spiked to the model particles provided the extent of adsorption (i.e., the enthalpy of adsorption, or ΔH_{ads}).

CHAPTER 1

1. INTRODUCTION

1.1. Atmospheric Aerosols and Particulate Matter

Particles in the atmosphere can arise from various natural (e.g., windborne dust, seaspray and volcanic eruptions) or anthropogenic activities (e.g., combustion of fossil fuels). While the technical definition of the term "aerosol" is a suspension of solid or liquid particles in a gas, common usage refers to aerosols as the particulate component only (e.g., all substances except pure water).[1] Typical atmospheric concentration of aerosols in the troposphere range between 10^2–10^5 cm^{-3} and 1–100 μg m^{-3}.[2]

1.2. Sources and Chemical Composition of Atmospheric Aerosols

Atmospheric aerosols occur in sizes ranging from a few nanometers to several hundred micrometers.[1] Aerosol sizes are divided into two main groups: those less than 2.5 μm in diameter (referred to as "fine") and those greater than 2.5 μm in diameter (termed as "coarse"). For the most part, fine and coarse are subjected to different origination, transformation and removal mechanisms. Fine aerosols are typically formed through the condensation of gas-phase to produce small nanoparticles which act as a substrate for additional gas-phase species to condense and form larger aerosols up to a few microns in diameter.[3] Coarse aerosols are generally formed through mechanical processes such as windblown dust and sea spray

A predominant portion of tropospheric aerosols is anthropogenic in origin.[4] The larger fraction of the aerosol weight contains sulfate, ammonium, nitrate, sodium,

chloride, tracemetals, carbonaceous material, crustal elements and water.[5] Carbonaceous aerosol components are commonly the largest fraction of aerosol mass and consist of two major components—graphitic or black carbon (also referred to as "elemental" or "free carbon") and organic material. While the latter can be directly emitted or produced from atmospheric reactions of gas-phase organic precursors, elemental carbon can only be produced through combustion processes, generally those occurring at extreme temperatures (e.g., diesel fuel combustion).

1.3. Aging and Fate of Aerosols in the Atmosphere

Tropospheric aerosols undergo a variety of transformation processes during their lifetime and have many different sinks. Fine particles are mainly subject to condensation of gas-phase organics and coagulation between aerosols. These pathways lead to larger micron-sized particles that are either washed out by rain or, if able to, grow up to many microns in diameter where they undergo sedimentation due to their relatively higher mass. Due to their longer lifetimes, fine aerosols undergo many chemical processes, thereby increasing their chemical complexity. Due to the ambiguous composition of fine aerosols, much research is currently devoted to characterizing its organic fraction, especially that which may lead to negative health effects to humans.

1.4. Polycyclic Aromatic Hydrocarbons in Atmospheric Aerosols

1.4.1. Sources and Distribution

Polycyclic aromatic hydrocarbons (PAHs) are members of a unique class of atmospheric pollutants known to have significant impacts on human health. Major sources of PAHs include incomplete combustion during the burning or pyrolysis of organic matter under oxygen-deficient conditions, occurring through both anthropogenic and natural activities.[6] These have been commonly termed as "primary sources". During

such, PAHs are emitted as part of a highly complex mixture of polycyclic organic matter (POM), which according to the U.S. Clean Air Act Amendments of 1990, is defined as "organic matter with more than one benzene ring, and which have a boiling point greater than or equal to 212 °F (100 °C).".[7] While the exact nature of POM is still the subject of many studies, known to include more than 100 PAH species, the remainder of this text will refer to specific PAH species found within the POM fraction.

Atmospheric PAHs are exhibited in the gas phase (e.g., highly volatile 2-ring species, such as naphthalene), solid phase (adsorbed/absorbed to the surfaces of aerosols; e.g., 5+-ring species such as benzo[*a*]pyrene), and semivolatile species that partition between the gas and aerosol phases (e.g., 3- and 4-ring compounds such as phenanthrene and pyrene, respectively). In general, there are five major PAH emission sources including domestic, mobile, industrial, agricultural and natural processes. While natural sources such as forest fires and volcanic eruptions also produce PAHs, anthropogenic activities are the predominant source.[1]

1.4.2. Significance of PAHs

Since the 1930's PAHs have been known to contribute to indirect toxicological and carcinogenic effects through their promutagenic properties.[3] While a variety of data sources exist supporting the carcinogenicity of PAHs, one key source is a list of "Priority Pollutants" devised by the U.S EPA, which is a compilation of species regularly monitored in the atmosphere. PAHs are toxic through their ability to be inhaled and transferred into the human body through the alveolar cells of the lung.[8–10] This occurs for PAHs in the gas and aerosol phases, with the latter being limited to aerosols that are small enough to become embedded in the alveolar cells (i.e., aerosols with diameters ≤ 2.5 μm).[8]

1.4.3. Analysis of Polycyclic Aromatic Hydrocarbons

For the analysis of atmospheric PAHs, gas chromatography (GC) has been commonly used, mainly due to its greater selectivity, resolution and sensitivity compared to other analytical systems (e.g., liquid chromatography).[11] Generally GC is coupled to mass spectrometry (MS) to yield better sensitivity and lower limits of detection than other detection methods (e.g., flame-ionization and electron capture detectors). However, GC-MS detection of PAH species with relatively high molecular weight (e.g., species with 5+ rings) is limited due to their volatility, and thus a combination of GC and LC techniques have been used.[12]

1.5. Oxidation Products of Polycyclic Aromatic Hydrocarbons in Atmospheric Aerosols

1.5.1. Sources and Distribution

As previously mentioned, PAHs are emitted through a variety of primary sources and occur in the atmosphere either in the gas or aerosol phases, in some cases partitioning between both. PAH derivatives, which typically incorporate a polar functional group onto the main PAH structure, are also emitted through primary sources. However, the majority of these derivatives are formed through "secondary" oxidation reactions between PAHs and gas-phase oxidants (e.g., ozone, nitrate and hydroxy radicals) as well as photolysis. The resulting nitrated and oxygenated products are characterized by their higher molecular weight and decreased vapor pressure compared to their parent PAH precursors, increasing their partitioning into the aerosol phase.

The secondary oxidation reactions for PAHs with gas-phase oxidants can occur with the PAH species either in the gas (homogeneous reaction) or aerosol phase (heterogeneous reaction). While the mechanisms behind the homogeneous oxidation of

PAHs have been extensively reported,[13,14] the process by which the heterogeneous oxidation of PAHs is still unclear.

Oxidation products of PAHs can be divided into two main groups: nitrated and oxygenated species. Nitrated species occur as derivatives with an attached nitro group (name nitro-PAHs), while oxygenated products are broken down to three classes: species with a carbonyl group (oxy-PAHs), hydroxyl group (hydroxy-PAHs) or carboxylic acid group (carboxy-PAHs).

1.5.2. Significance of PAH Oxidation Products

Oxidation products of PAHs have been found to exhibit similar toxicological and carcinogenic behavior as their PAH precursors. However, some nitrated and oxygenated species have been found to be even more toxic through their directly mutagenic activity.[13,15–17] While species of nitro-PAHs are emitted through primary sources (e.g., incomplete combustion of diesel fuel), most nitrated and oxygenated species are formed through secondary processes, some of which have been found to be even more toxic than those formed through primary sources. An example of this is the formation pathways of the 1- and 2- isomers of nitropyrene. While 1-nitropyrene is the most abundant nitro-PAH found in diesel exhaust emissions, 2-nitropyrene has been shown to be formed through •OH and •NO_3 radical initiated reactions.[18–21]

1.5.3. Analytical Methods for Detecting Oxidation Products of PAHs

In order to obtain reliable concentration measurements of individual PAH derivatives (concentrations sometimes as low as a few ng/g of total aerosol mass), versatile and robust analytical methods enabling their effective separation and identification are required. As with PAHs, most nitro-PAHs analyses are performed using GC-MS.[22] While electron ionization (EI) was the more commonly used ionization

technique for the detection of nitro-PAHs in earlier work, negative-ion chemical ionization (NICI) has become the preferred method.[23,24] In comparison to EI, NICI has yielded significantly improved sensitivity for nitro-PAHs.[25] This is mainly due to the excellent ability of the nitro group to resonance capture thermal electrons created during the ionization of reagent gas in NICI, creating a high degree of selectivity with ionization and therefore improved sensitivity. Alternatively to GC methods, HPLC has been commonly deployed for the analysis of nitro-PAHs, being used in tandem with a fluorescence detector (FD), electrochemical detector (ED), and a chemiluminescnce detector (CD).[22,26,27] In addition low resolution MS techniques have also been used for detecting nitro-PAHs with HPLC separation.[28,29] In some cases HPLC separation has been found to be advantageous over GC methods for thermally labile nitro-PAHs species.[22]

For oxygenated PAHs, GC-MS is also the method of choice.[17] While typically more thermally stable than nitro-PAHs, some oxygenated PAHs are not suitable for GC-MS analysis due to the potential formation of sampling artifacts. For example, 9,10-phenanthrenedione has been observed to undergo decarbonylation during injection to give 9-fluorenone, resulting in an overestimation of 9-fluorenone and underestimation of 9,10-phenanthrenedione.[30] For the most part, EI is generally preferred during MS detection of oxygenated compounds, however, recent work has shown the ability to detect some species with NICI.[31]

While GC methods are the most widely reported for the detection of oxygenated PAHs, LC methods are also commonly utilized. LC becomes advantageous for thermally labile and higher molecular weight compounds that are not easily detected with GC

methods. In terms of ionization sources, atmospheric pressure chemical ionization (APCI) has been used more than other methods such as atmospheric pressure photo-ionization (APPI) and electrospray ionization (ESI). Delhomme *et al.* compared APCI and ESI for the detection of oxy-PAHs (both ketone and diketone species) and found that APCI provided enhanced sensitivity.[32] In addition, Grosse and Letzel investigated both APCI and ESI for 30 different species of oxy-PAHs, hydroxy-PAHs and carboxy-PAHs, and found that APCI yielded greater response for compounds compared to ESI.[33]

1.5.4. Identification of PAH Oxidation Products

For the most part, previously reported studies utilizing GC or LC separation methods with various detection techniques have done so through the use of individual high purity standards. However, the number of products formed through various PAH oxidation pathways has been suggested to be in the hundreds of compounds, much more than the 20–40 currently reported in analytical methods. Most of these currently do not have high purity standards readily available. Therefore, detection techniques that include the ability to provide information in the identity of the unknown product are greatly needed.

Of the detection techniques used for nitrated and oxygenated PAH products, MS methods offer more potential information. This is ever more true for techniques such as EI (for GC) and ESI and APCI (for LC) methods, each having the ability to provide insight into the molecular structure through the fragmentation induced by ionizing the intact molecule. By determining trends in fragmentation and ionization patterns between compounds with different functional groups, many oxidation products of PAHs that were previously unknown can be more readily identified.

1.6. Partitioning of Organic Aerosol Species in the Atmosphere

1.6.1. Theory of Gas-Particle Partitioning

PAHs and their oxidation products are only minor components of the fraction of organic material observed in atmospheric aerosols. In the lower troposphere, organic compounds can account for between 20–90% of the total aerosol mass.[34] These organic compounds are commonly referred to as "organic aerosol" (OA), which is produced from primary sources (primary OA; POA) or through secondary transformation processes once emitted into the atmosphere (secondary OA; SOA). While POA has been well characterized, the evolution of SOA in the troposphere is mostly uncertain.

SOA is formed through the oxidation of semivolatile compounds, resulting in products with lower volatility that more readily condense into the aerosol phase. The transformation processes behind the production of SOA are only partially characterized (20–50% of compounds identified).[35] Consequentially, information on the specific role of organics in the atmosphere is limited and cannot be well represented in current climate models or health assessment studies. In order to effectively model the behavior of OA in the atmosphere and under laboratory conditions, a correct implementation of the gas-particle phase partitioning of OA species is essential. In this respect, the volatility of organics is a key property as it determines the phase partitioning of individual species and provides insights into the contribution of secondary processes to the organic content of aerosols. While the volatility of OA was studied previously, matrix-analyte interactions were not accounted for thus leading to incorrect estimates and poor modeling. The understanding of OA partitioning is also essential for obtaining a comprehensive chemical characterization of OA, which has been problematic due to its complexity, covering a wide range of volatilities.

1.6.2. Influence of the Aerosol Surface on Gas-Particle Partitioning

Current models aimed at addressing the behavior of SOA in the atmosphere are based on the volatility and hygroscopicity of individual SOA compounds.[34,36–39] Nevertheless, previous work has shown that the volatility of standard compounds (i.e., under ideal conditions) is not an accurate tool to determine the desorption of analytes from the aerosol matrix.[40] The incorporation of SOA and oxidized POA into the aerosol matrix can exert a significant effect on the resulting volatility of all species present within the total OA fraction. This, in turn, exhibits a direct influence on the gas-particle phase partitioning of OA in the atmosphere. These induced matrix-analyte interactions have yet to be accounted for to ensure high accuracy of the models describing the role of OA in atmospheric processes.

1.6.3. Analytical Methods for Defining Matrix-Analyte Interactions

A comprehensive characterization of OA can be problematic due to the interactions of semi-volatile and non-volatile organic species. For the analysis of OA samples, gas chromatography with mass spectrometry detection (GC-MS) is the most commonly employed technique. However, as previously mentioned, current GC-MS methods are not suitable for the analysis of less-volatile and non-volatile high molecular weight species. Other MS techniques have been deployed using various ionization methods with limitations in detailed identification of low volatility species due to complex MS spectra and ionization suppression from background species.[41–43] Analytical thermal desorption (TD) and pyrolysis (Py) coupled to GC-MS was used for qualitative OA characterization.[40] However the quantification, and in turn the gas-particle phase partitioning, of semi-volatile and non-volatile species has not been addressed.[44–46] TD-Py/GC-MS was recently shown to be a valuable tool in establishing matrix-analyte

interactions and induced volatilities of OA species in aerosols.[40] With TD-Py/GC-MS, low volatility species that are not detected with GC-MS are either thermally desorbed (at 300–400°C) from the aerosol matrix or pyrolyzed (>400°C) and transferred to the GC-MS system. Pyrolysis involves the thermal decomposition of organic molecules, thus at pyrolysis temperatures only decomposition products are observed. Thus parent molecules can be identified through the detection of signature molecular fragments.

Additionally, thermogravimetry coupled to differential scanning calorimetry (TGA-DSC) can be a powerful tool in providing direct estimations of activation energies (E_a) and vaporization enthalpies (ΔH_{vap}). By estimating the vaporization characteristics of an individual standard as both a neat standard and adsorbed to a particle substrate surface (e.g., silica, graphite, or graphene particles), the influences of the particle surface can be calculated based on the differences between them.

CHAPTER 2

2. SUMMARY AND OBJECTIVES

With the heterogeneous oxidation of polycyclic aromatic hydrocarbons producing a complex array of products, analytical methods capable of detecting, identifying and quantifying the wide range of derivatives are needed. This is even more important for derivatives that, for the most part, are present in aerosols in minor amounts, down to the order of ng/g. While current methods exist that would allow for the detection of individual oxidation products, identification of the detected compound is problematic due to a lack of available standards. Additionally, current analytical techniques are limited in their ability to detect analytes at sub-ppm (on the order of ng/g) levels (e.g., nitro-PAHs) due to the large amount of background organic matter in atmospheric aerosols. Therefore this work first focused on developing more sensitive methods to simultaneously detect, identify and quantitate the wide range of PAH oxidation products. These classes of PAH derivatives included nitro-PAHs (containing a nitro group), oxy-PAHs (carbonyl containing species), hydroxy-PAHs (containing a hydroxyl group) and carboxy-PAHs (containing a carboxylic acid group). Method development was focused on extraction and sample preparations, optimizing analysis conditions and identifying the targeted groups of PAH derivatives.

In the second major body of this work, the developed methods were applied to detecting and identifying products formed during the heterogeneous oxidation of PAH in

both a small-scale flow reactor and then a large-scale atmospheric simulation chamber with real-world diesel exhaust particles.

During this work the following research projects were accomplished: **(1)The development and optimization of a sample preparation procedure to simultaneously detect and quantify trace concentrations of PAH derivatives in atmospheric aerosols.** Utilizing a combination of Soxhlet extraction and solid phase extraction (SPE), PAHs and PAH derivatives were extracted from atmospheric aerosols and fractionated to improve sensitivity in their detection and quantification. With gas-chromatography separation, classes of derivatives were detected by quadrupole mass spectrometry (Q-MS) using electron ionization (EI) for oxy-, hydroxy-, and carboxy-PAHs and negative-ion chemical ionization (NICI) for nitro-PAHs. Due to the limited capability of GC-MS analysis to detect hydroxy- and carboxy-PAHs, these species were derivativized prior to their analysis. In order to enhance the GC-Q-MS method, MS data acquisition was performed in selected ion-total ion (SITI) mode, which combines the advantage of comprehensive spectral data given by total ion current (TIC) mode and the sensitivity of selected ion monitoring (SIM) mode. Sensitivities between the SITI and SIM modes were compared for 62 different PAH derivatives. The results from this project are presented and discussed in Chapter 3, Simultaneous Analysis of Polycyclic Aromatic Hydrocarbons and Their Various Oxidation Products.

(2) Optimizing PFE to efficiently extract polar PAH derivatives from atmospheric aerosols. PFE was optimized by investigating the impact of extraction temperature, pressure, time, volume and solvent selection. Initial optimization was performed using a mixture of standards of representative species. The optimized method

was then applied to wood smoke PM (WS PM) (a relatively polar aerosol matrix) and diesel exhaust PM (SRM 2975). The amounts extracted were compared to those obtained with Soxhlet extraction (a standard and exhaustive extraction method). For SRM 2975, the mass fractions obtained in this work were compared to previously reported data as well as certified values. The results of this work are presented and discussed in Chapter 4, Extraction of Polycyclic Aromatic Hydrocarbons and Their Oxidation Products Using Pressurized Fluid Extraction.

(3) Evaluating the ionization and fragmentation patterns exhibited by nitrated and oxygenated derivatives of PAHs during their analysis by APCI-HRMS to develop a tool in identifying unknown polar derivatives of PAHs. Fragmentation and ionization patterns of PAH derivative compounds with APCI were investigated first by direct infusion of individual standards of polar PAH derivatives, including nitro-, oxy-, hydroxy- and carboxy-PAHs. The compounds tested were specifically chosen as to represent a wide range of functional groups and also stereoisomers. Focus was given to observing trends in fragmentation patterns between similar species. Using high resolution MS data, the mechanisms behind fragmentation were proposed. Observations from the APCI-HRMS analysis of standards were then applied to identifying unknown products formed during the heterogeneous ozonation of pyrene in a small-scale flow reactor. Using the neutral loss and fragmentation patterns observed, multiple products were identified. The full results are presented and discussed in Chapter 5, Determination of Nitrated and Oxygenated Derivatives of Polycyclic Aromatic Hydrocarbons Using Atmospheric Pressure Chemical Ionization with High Resolution Mass Spectrometry (APCI-HRMS).

(4) Investigating products formed during the heterogeneous oxidation of 3- and 4-ring PAHs in a small-scale flow reactor. Atmospheric reactions involving the heterogeneous oxidation of 3- and 4-ring PAHs were simulated in a small-scale flow reactor. Reactions between PAHs adsorbed to quartz filters (aerosol surrogate) and various gas phase oxidations (i.e., NO_2, O_3 and NO_3/N_2O_5) were performed at reaction lengths between 5–300 min. Specific focus was given to detecting and identifying a comprehensive range of products. Data and results are presented in Chapter 6, Heterogeneous Nitration and Ozonation of 3- and 4-ring Polycyclic Aromatic Hydrocarbons.

(5) Atmospheric reactions of diesel exhaust particle and gas emissions with gas-phase oxidants in a large-scale aerosol reaction chamber to evaluate the mechanism behind the formation/loss of PAHs and nitro-PAH derivatives. A large-scale aerosol reaction chamber (LAC) was designed and constructed to simulate the processing of diesel exhaust aerosols in the atmosphere. The performance of the LAC system was evaluated by determining wall loss rates for both gas- and particle phase species. The chemical processing of diesel engine exhaust (both aerosols and gas-phase material) was then evaluated by connecting a diesel engine to the LAC system and injecting diesel engine exhaust into the reactor. Experiments were performed with different oxidants (i.e., NO_2 and UV exposure). Products observed during the small-scale flow reactor project were targeted during the analysis of samples collected from the LAC reactor during diesel engine experiments. The results from this work and pertinent discussion are presented in Chapter 7, Formation and Decay of Aerosol-Associated Nitrated PAHs in Diesel Engine Exhaust Exposed to Atmospheric Oxidants.

(6) Investigating the influence of the aerosol matrix on the gas-particle partitioning of PAHs and polar PAH derivatives in atmospheric aerosols by calculating vaporization enthalpies and activation energies while adsorbed to different surrogate aerosol surfaces. Using TGA-DSC and TD-Py/GC-MS, the thermodynamic and kinetic behavior of PAHs were evaluated while adsorbed to various types of surrogate aerosol surfaces. Initial experiments were performed to optimize various experimental conditions to accurately determine values of ΔH_{vap} and E_a from the DSC and TGA data, respectively. Values of ΔH_{vap} and E_a were first determined for individual species in the form of solid neat chemicals using different calculation approaches to establish the most accurate and precise method. Anthracene was then adsorbed to various surrogate aerosol surfaces (i.e., silica, graphite, activated carbon and graphene particles). Effective ΔH_{vap}^{eff} and E_a^{eff} values were then calculated and compared to those obtained for the neat standard, providing direct insight to the influence of the particle surface on the portioning of the PAH compound. Results are provided in Chapter 8, Investigating the Influence of Particle Surfaces on the Gas-Particle Partitioning of Organic Aerosol Species in Atmospheric Aerosols.

CHAPTER 3

3. SIMULTANEOUS ANALYSIS OF POLYCYCLIC AROMATIC HYDROCARBONS AND THEIR VARIOUS OXIDATION PRODUCTS.

3.1. Experimental

3.1.1. Materials and Reagents

Method development was performed using two different types of particulate matter: (1) Standard reference material (SRM) 2975, industrial forklift diesel exhaust particulate matter, purchased from NIST (Gaithersburg, MD, USA), and (2) WS PM generated previously from softwood and hardwood combustion.[47] All reagents were of analytical-reagent grade with a purity of ≥98% unless stated otherwise. GC-grade dichloromethane (DCM) and LC-MS optima grade methanol (MeOH) were obtained from Fisher Scientific (Chicago, IL, USA) and *n*-hexane (HPLC grade, 95%) was obtained from Sigma-Aldrich (St. Louis, MO, USA). The individual standards, recovery standards (R.S.s) and internal standard (I.S.), along with their manufacturers, are listed in Table 1. Standards of PAHs were obtained as a mixture called QTM PAH mix (15 PAHs) from Sigma-Aldrich. Hydroxy-PAHs were derivatized using 99% N,O-*bis*(trimethylsilyl)trifluoroacetamide (BSTFA) with 1% of trimethylchlorosilane (TMCS) obtained from Sigma-Aldrich.

Table 1. Analytes investigated in the development of the SPE procedure, including information on their purpose, source, retention data and ion used for quantitative GC-MS analysis.

Analyte[a]	Molecular formula	MW (g/mol)	t_R/t_{RIS}[b]	MS Ions (*m/z*) Quant.	Confirm.	Purpose	Manufacturer
PAHs							
Naphthalene	$C_{10}H_8$	128	0.45	128	102, 64	Analyte	Supelco
Acenaphthylene	$C_{12}H_8$	152	0.61	152	126, 76	Analyte	Supelco
Acenaphthene	$C_{12}H_{10}$	154	0.64	154	126, 76	Analyte	Supelco
Fluorene	$C_{13}H_{10}$	166	0.73	166	139, 82	Analyte	Supelco
Phenanthrene	$C_{14}H_{10}$	178	0.83	178	152, 89	Analyte	Supelco
Anthracene	$C_{14}H_{10}$	178	0.84	178	152, 89	Analyte	Supelco
Phen/Anth-C_1 A T[c]	$C_{15}H_{12}$	192	0.90	192	191, 165	Analyte	NA[a]
Phen/Anth-C_1 B T[c]	$C_{15}H_{12}$	192	0.91	192	191, 165	Analyte	NA
Phen/Anth-C_1 C T[c]	$C_{15}H_{12}$	192	0.92	192	191, 165	Analyte	NA
Phen/Anth-C_1 D T[c]	$C_{15}H_{12}$	192	0.92	192	191, 165	Analyte	NA
Fluoranthene	$C_{16}H_{10}$	202	1.00	202	106, 92	Analyte	Supelco
Pyrene	$C_{16}H_{10}$	202	1.03	202	174, 101	Analyte	Supelco
Cyclopenta[cd]pyrene[f]	$C_{18}H_{10}$	226	1.18	226	113	Analyte	NA
Flu/Pyr-C_1 A T[c]	$C_{17}H_{12}$	216	1.07	216	215, 189	Analyte	NA
Flu/Pyr-C_1 B T[c]	$C_{17}H_{12}$	216	1.08	216	215, 190	Analyte	NA
Flu/Pyr-C_1 C T[c]	$C_{17}H_{12}$	216	1.09	216	215, 191	Analyte	NA
Flu/Pyr-C_1 D T[c]	$C_{17}H_{12}$	216	1.10	216	215, 192	Analyte	NA
Flu/Pyr-C_1 E T[c]	$C_{17}H_{12}$	216	1.10	216	215, 193	Analyte	NA
Flu/Pyr-C_1 A T[c]	$C_{17}H_{12}$	216	1.11	216	215, 194	Analyte	NA
Flu/Pyr-C_1 B T[c]	$C_{17}H_{12}$	216	1.12	216	215, 195	Analyte	NA
Benzo[*ghi*]fluoranthene T[d]	$C_{18}H_{10}$	226	1.18	216	224, 112	Analyte	NA
Benzo[*a*]anthracene	$C_{18}H_{12}$	228	1.21	228	114, 101	Analyte	Supelco
Triphenylene T[d]	$C_{18}H_{12}$	228	1.21	228	114, 101	Analyte	NA
Chrysene	$C_{18}H_{12}$	228	1.22	228	114,101	Analyte	Supelco
Benzo[*b*]fluoranthene	$C_{20}H_{12}$	252	1.36	252	126, 113	Analyte	Supelco
Benzo[*a*]pyrene	$C_{20}H_{12}$	252	1.40	252	126, 113	Analyte	Supelco
Indeno[1,2,3-*cd*]pyrene T[d]	$C_{22}H_{12}$	276	1.54	276	138, 124	Analyte	Supelco
Dibenzo[*a*,*h*]anthracene	$C_{22}H_{14}$	278	1.80	278	139, 124	Analyte	Supelco
Benzo[*ghi*]perylene	$C_{22}H_{12}$	276	1.58	276	138, 124	Analyte	Supelco
Nitro-PAHs							
2-Methyl-1-nitronaphthalene	$C_{11}H_9NO_2$	187	0.75	187	171	Analyte	Sigma-Aldrich
2-Nitrobiphenyl	$C_{12}H_9NO_2$	199	0.79	199	183, 156	Analyte	Accustandard
5-Nitroquinoline	$C_9H_6N_2O_2$	174	0.73	174	158, 144	Analyte	Sigma-Aldrich
3-Nitrobiphenyl	$C_{12}H_9NO_2$	199	0.86	199	183, 156	Analyte	Sigma-Aldrich
5-Nitroacenaphthene	$C_{12}H_9NO_2$	199	0.97	199	183, 154	Analyte	Sigma-Aldrich
2-Nitrofluorene	$C_{13}H_9NO_2$	211	1.02	211	204, 195	Analyte	Sigma-Aldrich
1-Nitronaphthalene	$C_{10}H_7NO_2$	173	0.74	173	157, 141	Analyte	Sigma-Aldrich
2-Nitronaphthalene	$C_{10}H_7NO_2$	173	0.77	173	157, 141	Analyte	Sigma-Aldrich
9-Nitroanthracene	$C_{14}H_9NO_2$	223	1.04	223	207, 216	Analyte	Sigma-Aldrich
2-Nitro-9-fluorenone	$C_{13}H_7NO_3$	225	1.07	225	209, 195	Analyte	Sigma-Aldrich
9-Nitrophenanthrene	$C_{14}H_9NO_2$	223	1.07	223	207, 195	Analyte	Accustandard
3-Nitrophenanthrene	$C_{14}H_9NO_2$	223	1.10	223	207, 191	Analyte	Accustandard
3-Nitrofluoranthene	$C_{16}H_9NO_2$	247	1.23	247	231, 215	Analyte	Sigma-Aldrich
1-Nitropyrene	$C_{16}H_9NO_2$	247	1.23	247	231, 215	Analyte	Sigma-Aldrich
7-Nitrobenzo[*a*]anthracene[e]	$C_{18}H_{11}NO_2$	273	1.35	273	257, 241	Analyte	NA
6-Nitrochrysene	$C_{18}H_{11}NO_2$	273	1.40	273	257, 241	Analyte	Sigma-Aldrich
1,3-Dinitropyrene	$C_{16}H_8N_2O_4$	292	1.45	292	262, 246	Analyte	Sigma-Aldrich
1,6-Dinitropyrene	$C_{16}H_8N_2O_4$	292	1.50	292	276, 262	Analyte	Sigma-Aldrich
1,8-Dinitropyrene	$C_{16}H_8N_2O_4$	292	1.52	292	262, 246	Analyte	Sigma-Aldrich
1-Nitrobenzo[*e*]pyrene[h]	$C_{20}H_{11}NO_2$	297	1.64	297	281, 267	Analyte	NA
6-Nitrobenzo[*a*]pyrene	$C_{20}H_{11}NO_2$	297	1.66	297	281, 267	Analyte	Sigma-Aldrich
3-Nitrobenzo[*e*]pyrene[h]	$C_{20}H_{11}NO_2$	297	1.79	297	281, 267	Analyte	NA

Table 1. cont.

Analyte[a]	Molecular formula	MW (g/mol)	t_R/t_{RIS}[b]	MS Ions (*m/z*) Quant.	MS Ions (*m/z*) Confirm.	Purpose	Manufacturer
Oxy-PAHs							
1,3-Indanedione	$C_9H_6O_2$	146.14	0.55	146	104, 76	Analyte	Sigma-Aldrich
1,4-Naphthoquinone	$C_{10}H_6O_2$	158.15	0.59	158	130, 104	Analyte	Sigma-Aldrich
1-Naphthaldehyde	$C_{11}H_8O$	156.18	0.65	156	127, 101	Analyte	Sigma-Aldrich
9-Fluorenone	$C_{13}H_8O$	180.2	0.80	180	152, 126	Analyte	Sigma-Aldrich
Xanthone	$C_{13}H_8O_2$	196.2	0.88	196	168, 139	Analyte	Sigma-Aldrich
Anthrone	$C_{14}H_{10}O$	194.23	0.93	194	165, 139	Analyte	Sigma-Aldrich
Anthrone A T[e]	$C_{14}H_{10}O$	194.23	0.86	194	165, 139	Analyte	NA
Anthrone B T[e]	$C_{14}H_{10}O$	194.23	0.88	194	165, 139	Analyte	NA
Anthrone C T[e]	$C_{14}H_{10}O$	194.23	0.89	194	165, 139	Analyte	NA
Anthrone D T[e]	$C_{14}H_{10}O$	194.23	0.89	194	165, 139	Analyte	NA
9,10-Anthraquinone	$C_{14}H_8O_2$	208.21	0.95	208	180, 165	Analyte	Sigma-Aldrich
9,10-Phenanthroquinone	$C_{14}H_8O_2$	208.21	1.06	180	208, 152	Analyte	Sigma-Aldrich
Benzanthracenone A T[f]	$C_{17}H_{10}O$	230	1.16	202	230, 101	Analyte	NA
Benzanthracenone B T[f]	$C_{17}H_{10}O$	230	1.18	202	230, 101	Analyte	NA
Benzanthracenone C T[f]	$C_{17}H_{10}O$	230	1.19	202	230, 101	Analyte	NA
Benzanthracenone D T[f]	$C_{17}H_{10}O$	230	1.24	202	230, 101	Analyte	NA
Benzanthracenedione A T[f]	$C_{18}H_{10}O_2$	258	1.28	202	230, 101	Analyte	NA
Benzanthracenedione B T[f]	$C_{18}H_{10}O_2$	258	1.29	202	230, 258	Analyte	NA
6,13-Pentacenequinone	$C_{22}H_{12}O_2$	308	1.72	308	280, 252	Analyte	Sigma-Aldrich
Bianthrone	$C_{28}H_{16}O_2$	384	1.86	355	384, 162	Analyte	Sigma-Aldrich
Hydroxy- & Carboxy-PAH[g]							
2-Hydroxybiphenyl	$C_{12}H_{10}O$	242.39	0.76	242	227, 242	Analyte	Alfa Aesar
4-Hydroxybiphenyl	$C_{12}H_{10}O$	242.39	0.85	242	227, 211	Analyte	Alfa Aesar
4-Hydroxyindole	C_8H_7NO	205.33	0.79	205	190, 163	Analyte	Sigma-Aldrich
5-Hydroxyindole	C_8H_7NO	205.33	0.80	205	190, 163	Analyte	Sigma-Aldrich
2-Hydroxy-9-fluorenone	$C_{13}H_8O_2$	268.38	1.01	268	268, 195	Analyte	Sigma-Aldrich
4-Phenanthrenemethanol	$C_{15}H_{12}O$	282.45	1.03	280	280, 265	Analyte	Sigma-Aldrich
9-Anthracenemethanol	$C_{15}H1_2O$	282.45	1.03	280	280, 265	Analyte	Sigma-Aldrich
9-Phenanthrenecarboxylic acid	$C_{15}H_{10}O_2$	296.44	1.10	294	205, 294	Analyte	Sigma-Aldrich
9-Phenanthrol	$C_{14}H_{10}O$	268.43	1.01	266	251, 235	Analyte	Sigma-Aldrich
1-Hydroxypyrene	$C_{16}H_{10}O$	292.45	1.16	290	275, 250	Analyte	Sigma-Aldrich
1,8-Dihydroxyanthraquinone	$C_{14}H_8O_4$	384.11	1.17	369	370, 177	Analyte	Sigma-Aldrich
Recovery Standards							
Naphthalene-d_8	$C_{10}D_8$	136.22	0.45	136	108, 68	R.S.	Sigma-Aldrich
Phenanthrene-d_{10}	$C_{14}D_{10}$	188.23	0.83	188	160, 94	R.S.	Supelco
Anthracene-d_{10}	$C_{14}D_{10}$	188.23	0.84	188	160, 94	R.S.	Supelco
Pyrene-d_{10}	$C_{16}D_{10}$	212.31	1.03	212	106, 92	R.S.	Isotec
1-Nitronaphthalene-d_7	$C_{10}D_7NO_2$	180.21	0.74	180	164, 144	R.S.	CDN isotopes
2-Nitrofluorene-d_9	$C_{13}D_9NO_2$	220.27	1.02	220	188, 168	R.S.	CDN isotopes
9-Nitroanthracene-d_9	$C_{14}D_9NO_2$	232.29	1.03	232	220, 193	R.S.	CDN isotopes
1-Nitropyrene-d_9	$C_{16}D_9NO_2$	256.31	1.26	256	240, 226	R.S.	CDN isotopes
6-Nitrochrysene-d_{11}	$C_{18}D_{11}NO_2$	284.36	1.40	284	268, 238	R.S.	CDN isotopes
2-Chloroanthraquinone	$C_{14}H_7ClO_2$	242.66	1.04	242	214, 212	R.S.	Sigma-Aldrich
1-Hydroxypyrene-d_9	$C_{16}HD_9O$	301.18	1.15	299	284, 267	R.S.	CDN isotopes
2'-Chloro-2-hydroxy-4-methylbenzophenone	$C_{14}H_{11}ClO_2$	318.87	1.00	303	73, 91	R.S.	Sigma-Aldrich
Internal Standards							
Fluoranthene-d10	$C_{16}D_{10}$	212.31	1.00	212	174, 101	I.S.	Supelco

[a] "T" denominates tentative idetification based on mass spectra match with NIST library; standards were not available (NA).
[b] The relative retention time was calculated using I.S. Fluoranthene-d_{10}
[c] Quantified using the standard of the non-methylated PAH
[d] Quantified using benz[*a*]anthracene
[e] Quantified using the 9-fluorenone standard
[f] Quantified using the pyrene standard
[g] For hydroxy-PAHs the data listed pertain to their trimethylsilyl derivatives.

3.1.2. Extraction

Extractions were performed in triplicate using either ~50 mg of diesel exhaust SRM-2975 material or ~10 mg of WS PM. The bulk PM was spiked with a R.S. mixture (standards listed in Table 1) prior to extraction. The amount of the recovery standards spiked to SRM 2975 and WS PM was ~0.2 µg with respect to the majority of the analytes with the exception of hydroxy-PAH, which was at ~2 µg.

Glass thimbles were used for all Soxhlet extractions to avoid the contamination observed for cellulose thimbles in preliminary experiments. The Soxhlet extractions were carried out sequentially with 90 mL of DCM and 90 mL of MeOH each for 18 h. After the extraction, the DCM and MeOH fractions were cooled to room temperature and evaporated under a stream of nitrogen gas. DCM fractions were evaporated to 100 µL while the MeOH extracts were completely dried and re-dissolved in 100 µL of DCM. Both extracts were then diluted to 1.0 mL with *n*-hexane and submitted to SPE fractionation.

3.1.3. SPE Fractionation and Preparation for GC analysis

The SPE protocol previously employed for the purification of nitro-PAHs by Bamford et al. was further developed in the present study to allow for the fractionation of PAHs, oxy-PAHs, nitro-PAHs, and hydroxy-PAHs.[23] An aminopropyl SPE cartridge with 500 mg of sorbent, 55 – 105 µm particle size, and a 125 Å pore size was used (Sep-Pak, Waters, Milford, MA). Prior to fractionation, the SPE sorbent was conditioned sequentially with DCM and *n*-hexane (6 mL each). Initial tests revealed that conditioning with MeOH prior to DCM resulted in the early elution of hydroxy-PAHs in 20 % DCM in *n*-hexane; therefore, methanol was not used as a conditioning solvent in this study.

Optimization of SPE eluting conditions was performed using a mixture of standards representative for each class of compounds. Originally, the elution solvents

were employed sequentially using 6.0 mL (2 × 3 mL) solutions of 0, 20, 50, 100 % (v/v) of DCM in *n*-hexane followed by 50 % (v/v) DCM in methanol and 100 % methanol. However, while applying the SPE protocol to PM extracts, the 100 % DCM and 50 % DCM in MeOH fractions did not exhibit significant recoveries of the evaluated species. Therefore these fractionation steps were removed from the final SPE protocol. The collected SPE fractions were concentrated to 200 µL under a gentle nitrogen stream, and then divided into two 100 µL aliquots. One aliquot was used to determine PAHs, oxy-PAHs and nitro-PAHs and the other was evaporated and derivatized with 100 µL of BSTFA+TMCS at 70 °C for 6 h (as recommended by the manufacturer) for GC-MS analysis of hydroxy-PAHs. Reaction times necessary to achieve complete trimethylsilylation were evaluated, with 6 h assuring complete derivatization. For hydroxyindoles, both mono-TMS and di-TMS derivatives can be observed; however, only di-TMS derivatives were observed with a 6 h reaction time. Fluoranthene-d_{10} (10 µL of 10 ng μL^{-1}) was used as the internal standard for all analyses.

3.1.4. GC-MS Analysis

Determination of PAHs, oxy-, hydroxy- and nitro-PAHs was performed using an Agilent 6890N GC coupled to a 5975C MS with interchangeable EI and NICI ion sources. The analyses were accomplished on a 30 m long DB-5MS column with 0.25 mm I.D., and 0.25 µm film thickness (J&W Scientific, Inc., Folsom, CA). Ultra pure helium (99.999 %) was used as the carrier gas with a constant flow rate of 1.0 mL min^{-1}. A split/splitless liner with deactivated glass wool was used (Restek, Bellefonte, PA). The injection volume was 1.0 µL. The temperatures of split/splitless injector and transfer line temperatures were set at 250 °C and 280 °C, respectively.

For the analysis of PAHs, oxy-, and hydroxy-PAHs, the impact of splitless time (0.5 – 2 min) and pressure pulse was evaluated. The final conditions were 1 min splitless time with a pressure pulse of 25 psi for 0.95 min. The GC oven temperature program started at 40 °C for 1 min, increased at a rate of 20 °C min^{-1} to 140 °C, followed by a gradient of 10 °C min^{-1} to 290 °C, and an increase at the rate of 15 °C min^{-1} to 310 °C, and was held at the final temperature for 12 min with the overall runtime of 34.3 min. The ion source temperature was set at 230 °C.

For the GC-NICI-MS determination of nitro-PAHs, the optimized injection splitless time was 1.5 min with a pressure pulse of 25 psi for 1.45 min. The temperature program started at 35 °C and held for 1 min, then increased at the rate of 30 °C min^{-1} to 150 °C, followed by an increase at the rate of 15 °C min^{-1} to 300 °C, and held at the final temperature for 10 min. The NICI source temperatures were optimized for nitro-PAHs in a range of 150–300 °C, and themethane gas flow rate was optimized within a range of 1.0–2.5 mL min^{-1}. The final NICI conditions used for the analysis of PM samples were a source temperature of 300 °C and a methane flow rate of 2.5 mL min^{-1}. For GC-NICI-MS analysis of oxy-PAH, the same temperature program was used as in EI analysis using the NICI conditions optimized for nitro-PAHs.

The GC-MS data were acquired either in selected-ion monitoring (SIM) mode or a combination of the total ion current (TIC) and SIM modes, i.e., selected-ion-total-ion (SITI). SITI combines the advantages of improved sensitivity, resulting from the use of SIM monitoring single ions, and compound identification ability using TIC. A dwell time of 25 ms was used for all ions listed in Table 3 for both SIM and TIC modes and a range of 50–500 m/z was used for TIC. For the PM sample analysis SITI mode was employed.

3.1.5. Data Processing

The LODs were determined based on the signal of the target ions with the highest signal-to-noise ratios (Table 1). Instrumental LODs were calculated from the calibration curves using the equation LOD = $3.3*s_y/k$, where k was a slope of the calibration curve and s_y was the standard error of the predicted y-value for each x-value obtained by a least square linear regression. From the acquired calibration profiles, only the points within one order of magnitude of the LOD were used for the LOD calculations.

For quantification, an internal standard method was used employing fluoranthene-d_{10} as the internal standard. A single I.S. used was correcting for final volume changes of sample injected. To determine the extraction efficiencies during the sample preparation, an R.S. mixture was added (Table 1) to each sample. The R.S. mixture consisted of representative species for each class of compounds studied and its recoveries were determined using least square calibration curves. Using R.S. yields, two quantification approaches were employed: 1) based on the total response across all SPE fractions, and 2) based on the response of a single SPE fraction that exhibited the greatest response for the particular compound class (i.e., hexane fraction for PAHs, 20 % DCM for oxy- and nitro-PAHs, and 100 % MeOH for hydroxy-PAHs). Recovery standards were used to correct for analyte losses during the extraction and fractionation procedures, using the total recovery percentage (R.S. %) for quantification of combined SPE fractions and a single fraction R.S. % for quantification based on the single fraction.

3.2. Results and Discussion

3.2.1. GC-MS Conditions

The GC-MS methods targeting analysis of selected PAHs or their oxidation products were previously reported,[24,31,48–54] thus only selected parameters were evaluated to achieve higher sensitivity while reducing contribution from the matrix.

Nitro-PAHs are known to decompose at high temperatures; thus, a cool on-column injection is typically preferred for their analysis by GC-MS.[24] However, on-column injection is not favored when other interfering contaminating species may be present, decreasing the sensitivity of nitro-PAH analysis. Thus we have employed a split/splitless injection port. For nitro-PAHs, the use of pressure pulse was investigated (Figure 1), giving a slight increase in response. The injection splitless time (0.5–2 min) was then evaluated while employing pulsed injection (Figure 2). As expected, an increase in the splitless time from 0.5 min to 1 min resulted in a significantly higher response, without a significant impact on peak shape. A further increase in splitless time was not significant for PAHs, oxy-, and hydroxy-PAHs and thus 1 min splitless time was used for all GC-EI-MS analyses. For nitro-PAHs, the sensitivity of analysis was improved by extending the splitless time to 1.5 min, without a negative impact on peak shape.

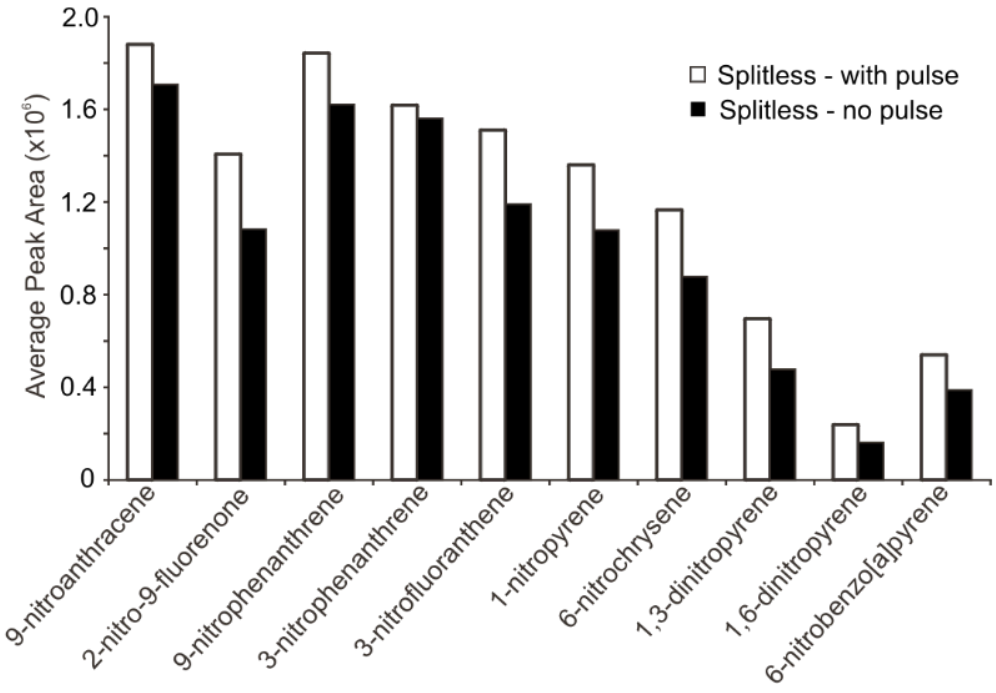

Fig. 1. Evaluation of the pressure pulse effect on response of nitro-PAHs using GC-NICI-MS. A splitless time of 1.5 min was used. Determination of the response was based on the peak area of quantification ions (see Table 3) using TIC data.

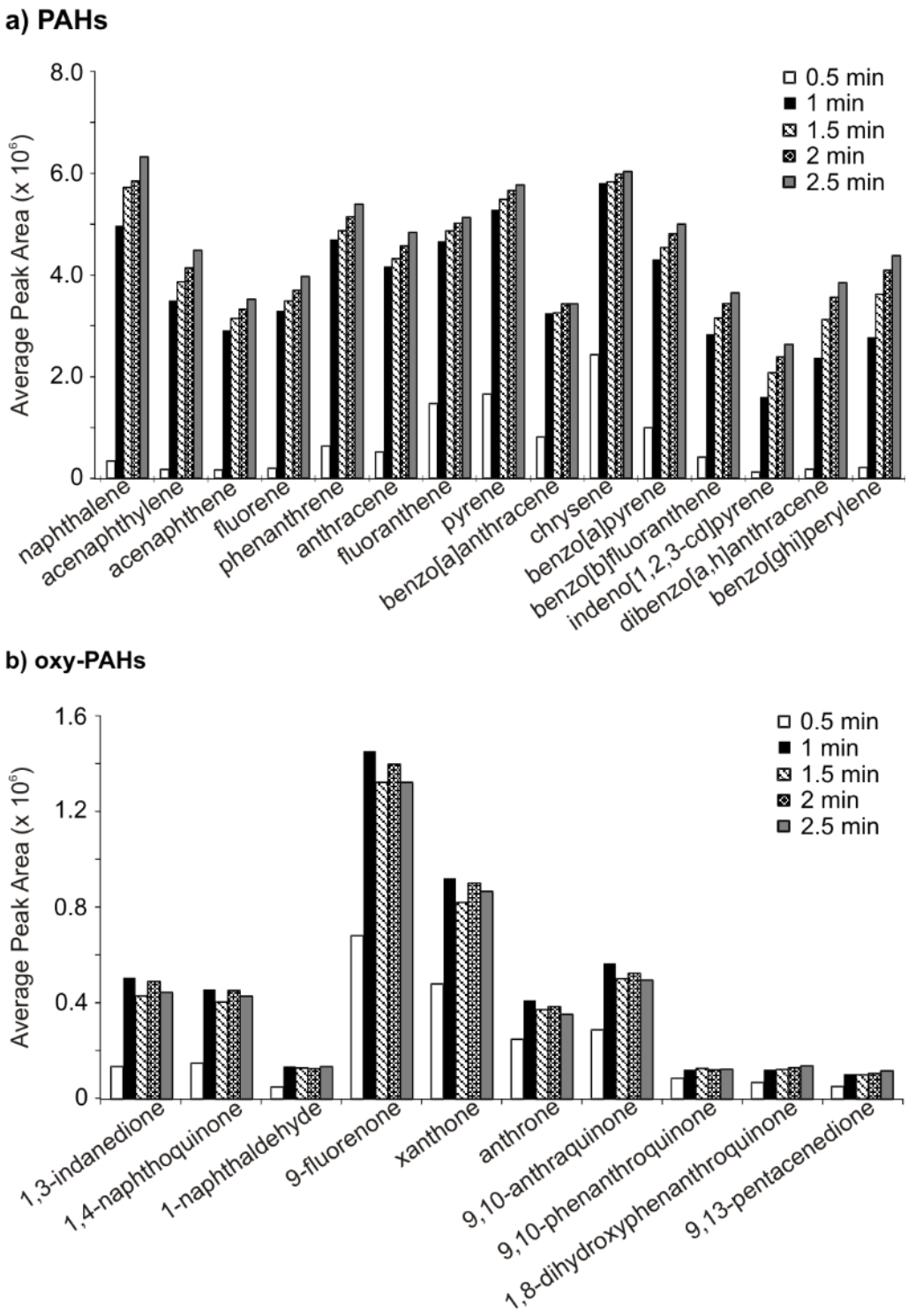

Fig. 2. Impact of splitless time on (a) PAH and (b) oxy-PAH response. All analyses were performed with a 1.45 min pressure pulse at 25 psi. Determination of the response was based on the peak area of the quantification ions (see Table 1) using TIC data.

In this study, GC-MS with EI was utilized for quantitative determination of PAHs, oxy- and hydroxy-PAHs. For nitro-PAHs and oxy-PAHs, a NICI source was previously employed.[24,31] To further enhance the detectability of these species in trace concentrations, we have evaluated the impact of the source temperature and methane gas flow rate (demonstrated for select species and conditions in Figure 3). Increasing the ion source temperature did not significantly impact the response at lower temperatures (<250 °C). However, increasing the temperature to 300 °C provided a notably higher response (Figure 3a), possibly due to removal of interferences from the background. The effect of methane flow rate was more pronounced, giving the highest response at 2.5 mL min^{-1}(Figure 3b). This may be explained by an increase in the number of thermal electrons that can effectively enhance ionization.[55] The optimal conditions used in all further experiments were an ion source temperature of 300 °C and a flow rate of 2.5 mL min^{-1}.

3.2.2. Limits of Detection and Calibration Parameters

The limits of detection were evaluated for the GC-EI-MS and GC-NICI-MS methods using the SIM and SITI-SIM modes for PAHs and their oxidation products (Table 2). Although SIM (as expected) exhibited slightly lower LODs for the majority of species, most likely due to the decreased number of data points across the peak for SITI-SIM compared to SIM, the results obtained for the two acquisition modes were similar (Table 2). For PAHs, LODs were in a range of 4–30 pg, with the higher molecular weight species comprising the upper part of the range. Oxy-PAHs gave LODs within 5–136 pg and hydroxy-PAHs (as TMS derivatives) in a range of 0.8–21 ng. Analysis of nitro-PAHs in NICI mode yielded LODs of 10 pg or less. The SITI method was employed for trace analysis of PAHs and polar PAH derivatives in PM since it is not only suitable for the

determination of trace concentrations of the analytes, but also enables the identification of possible unknowns in TIC mode.

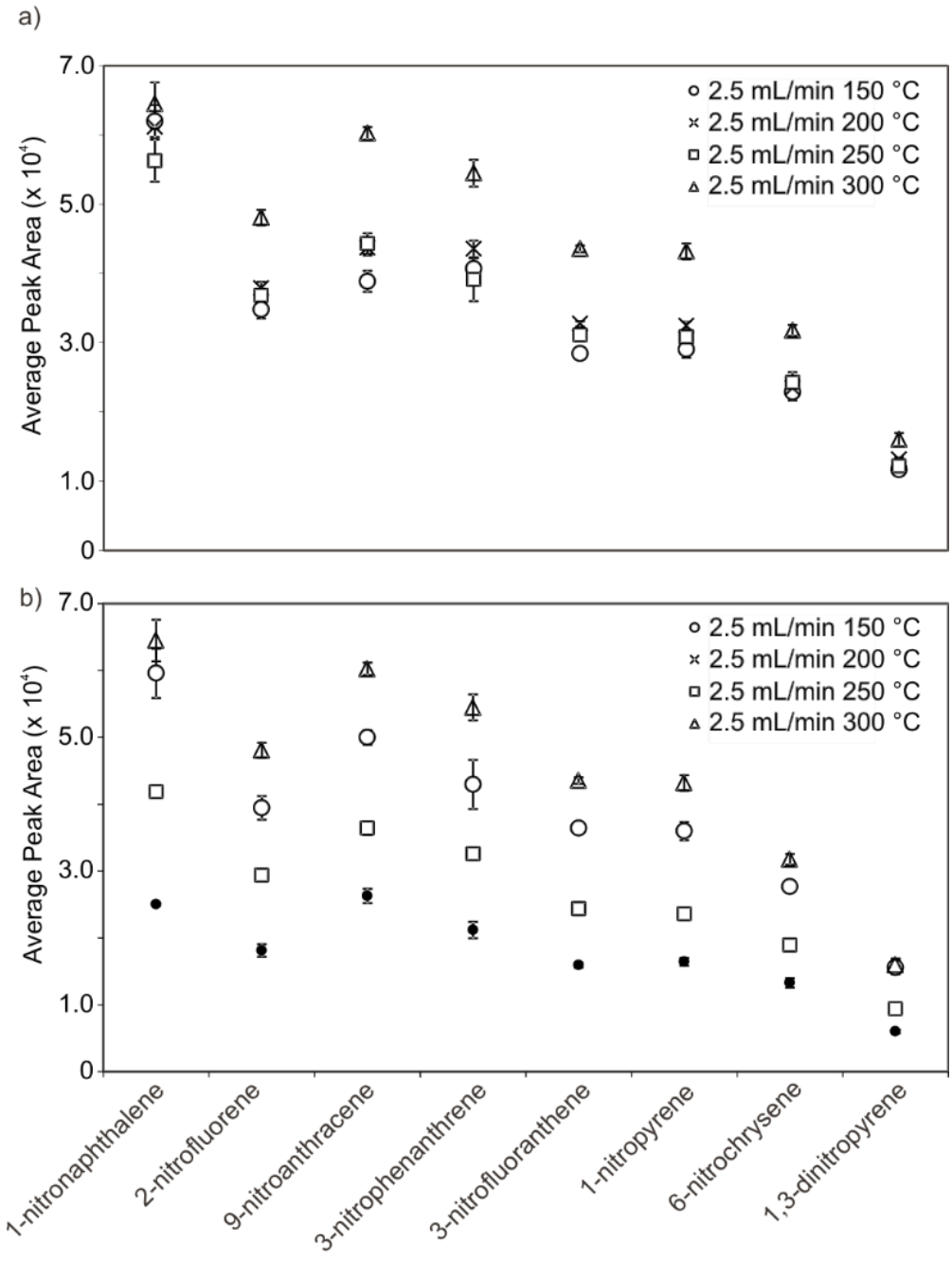

Fig. 3. The impact of (a) NICI temperature at 300 °C (at a methane flow rate of 2.5 mL min^{-1}) and (b) methane flow rate (at an ion source temperature of 300 °C), on the response of representative nitro-PAHs.Analyses were randomly performed in triplicate; the data are presented as mean ± one standard deviation.

Oxy-PAHs are typically quantified using GC-EI-MS.[51,56] Their analysis in NICI mode has also been reported as the carbonyl group within oxy-PAHs is able to stabilize the excess negative charge associated with the capture of thermal electrons within the NICI process.[31,55] However, to the best of our knowledge, the LODs of the NICI method were not evaluated. Our evaluation of LODs of oxy-PAHs analyzed in the NICI mode showed significantly higher values in comparison to those obtained in the EI mode (Table 2). Nevertheless, the acquisition in NICI mode may be a valuable tool for the identity confirmation of tentatively identified oxy-PAHs (using MS library) when no standards are available. For example, benzanthrone (or possibly benzo[*n*]fluorenone) isomers that were tentatively identified in extracts of both PM matrices were confirmed upon analysis in the NICI mode (Figure 4).

Table 2 reports also other calibration parameter including slopes and correlation coefficients. For some compounds lower slopes usually along with lower correlation coefficient (of 0.97 and 0.98) were observed. This was observed for large molecular weight PAHs and nitro-PAHs suggesting interferences from stationary phase for later eluting species. Lower correlation coefficients for selected polar species such as 5-nitroquinoline and some quionones were attributed to interactions with the stationary phase.

Table 2. Least linear regression data LODs for PAHs and polar PAH derivatives in both SITI-SIM and SIM

Compound	Regression data obtained in SITI-SIM mode				LOD (ng)	
	Slope	Intercept	S_y	R^2	SITI-SIM	SIM
PAHs (GC-EI-MS)						
Naphthalene	0.901	-0.131	0.098	0.9960	0.011	0.010
Acenaphthylene	0.597	-0.030	0.025	0.9994	0.011	0.012
Acenaphthene	0.687	-0.056	0.037	0.9990	0.013	0.013
Fluorene	1.003	-0.005	0.030	0.9997	0.008	0.008
Phenanthrene	0.992	-0.020	0.025	0.9998	0.004	0.008
Anthracene	1.074	-0.037	0.034	0.9997	0.008	0.007
Fluoranthene	1.080	-0.086	0.055	0.9991	0.010	0.012
Pyrene	0.834	-0.178	0.147	0.9896	0.032	0.030
Benzo[*a*]anthracene	1.183	-0.103	0.081	0.9984	0.029	0.024
Chrysene	1.019	-0.187	0.146	0.9931	0.022	0.017
Benzo[*b*]fluoranthene	0.798	-0.198	0.171	0.9849	0.021	0.016
Benzo[*a*]pyrene	0.501	-0.149	0.142	0.9740	0.032	0.022
Indeno[1,2,3-*cd*]pyrene	0.560	-0.141	0.122	0.9843	0.034	0.018
Dibenzo[*a*,*h*]anthracene	0.703	-0.159	0.128	0.9891	0.021	0.014
Benzo[*ghi*]perylene	0.000	0.000	0.000	0.0000	0.000	0.000
Nitro-PAHs (GC-NICI-MS)						
2-Methyl-1-nitronaphthalene	0.460	0.032	0.080	0.9976	0.005	0.006
2-Nitrobiphenyl	1.307	0.137	0.306	0.9842	0.005	0.005
5-Nitroquinoline	0.685	0.158	0.231	0.9912	0.002	0.006
1-Nitronaphthalene	0.628	0.040	0.144	0.9957	0.008	0.043
2-Nitronaphthalene	0.554	0.028	0.114	0.9967	0.002	0.003
3-Nitrobiphenyl	0.445	-0.074	0.071	0.9979	0.007	0.006
5-Nitroacenaphthene	1.206	0.118	0.417	0.9906	0.003	0.002
2-Nitrofluorene	0.945	0.127	0.300	0.9917	0.003	0.005
9-Nitroanthracene	1.685	-0.221	0.225	0.9948	0.008	0.004
2-Nitro-9-fluorenone	0.833	0.080	0.306	0.9891	0.004	0.003
9-Nitrophenanthrene	0.746	0.000	0.190	0.9948	0.010	0.004
3-Nitrophenanthrene	1.169	-0.0065	0.267	0.9958	0.005	0.004
3-Nitrofluoranthene	1.139	0.023	0.258	0.9959	0.001	0.002
1-Nitropyrene	1.557	-0.327	0.355	0.9959	0.002	0.002
6-Nitrochrysene	1.774	-0.269	0.334	0.9899	0.004	0.004
1,3-Dinitropyrene	2.518	0.271	0.363	0.9893	0.009	0.006
1,6-Dinitropyrene	0.821	-0.249	0.319	0.9881	0.007	0.006
6-Nitrobenzo[*a*]pyrene	0.000	0.000	0.000	0.0000	0.000	0.000
Oxy-PAHs (GC-EI-MS)						
1,3-Indanedione	0.478	-0.144	0.123	0.9940	0.009	0.010
1,4-Naphthoquinone	0.081	-0.020	0.020	0.9946	0.027	0.012
1-Naphthaldehyde	1.251	-0.219	0.209	0.9975	0.008	0.006
9-Fluorenone	1.136	-0.310	0.253	0.9956	0.005	0.006
Xanthone	0.855	-0.333	0.333	0.9865	0.011	0.017
Anthrone	0.749	-0.217	0.172	0.9953	0.010	0.010
9,10-Anthraquinone	0.389	-0.257	0.297	0.9533	0.050	0.039
9,10-Phenanthraquinone	0.330	-0.165	0.180	0.9740	0.049	0.018
1,8-Dihydroxyphenanthraquinone	0.298	-0.214	0.270	0.9359	0.016	0.010
6,13-Pentacenedione	0.019	-0.003	0.004	0.9898	0.136	0.105
Bianthrone	0.000	0.000	0.000	0.0000	0.000	0.000
Oxy-PAHs (GC-NICI-MS)						
1,3-Indanedione	0.021	0.015	0.066	0.9778	0.084	0.061
1,4-Naphthoquinone	0.004	-0.008	0.012	0.9848	0.036	0.017
1-Naphthaldehyde	0.029	0.026	0.094	0.9774	0.065	0.012
9-Fluorenone	0.004	-0.008	0.011	0.9899	0.108	0.086
Xanthone	0.007	-0.005	0.009	0.9991	0.035	0.010
9,10-Anthraquinone	0.007	-0.018	0.004	0.9997	0.816	0.442
6,13-Pentacenedione	0.010	-0.009	0.013	0.9318	0.058	0.024
Anthrone	0.000	0.000	0.000	0.0000	0.000	0.000

Table 2. cont.

Compound	Regression data obtained in SITI-SIM mode				LOD (ng)	
	Slope	Intercept	S_y	R^2	SITI-SIM	SIM
Hydroxy-PAHs (GC-EI-MS)[a]						
2-Hydroxybiphenyl	0.099	-0.021	0.0957	0.9988	0.0008	0.0001
4-Hydroxybiphenyl	0.018	0.007	0.0419	0.9936	0.009	0.002
4-Hydroxyindole	0.068	-0.035	0.1217	0.9961	0.011	0.013
5-Hydroxyindole	0.062	-0.043	0.0728	0.9983	0.012	0.007
9-Phenanthrol	0.047	-0.084	0.0587	0.9981	0.009	0.003
2-Hydroxy-9-fluorenone	0.501	-0.171	0.7110	0.9912	0.016	0.013
4-Phenanthrenemethanol	0.018	-0.017	0.0490	0.9908	0.001	0.001
9-Phenanthrenecarboxylic acid	0.141	-0.165	0.1475	0.9987	0.021	0.016
1-Hydroxypyrene	0.173	-0.444	0.2941	0.9965	0.001	0.002
1,8-Dihydroxyanthraquinone	0.000	0.000	0.0000	0.0000	0.006	0.003

[a] Hydroxy-PAHs detected as trimethylsilyl derivatives; both 4- and 5-hydroxyindole detected as di-trimethylsilyl derivatives
*S_y: Standard error of the y estimates
R^2: Correlation coefficient

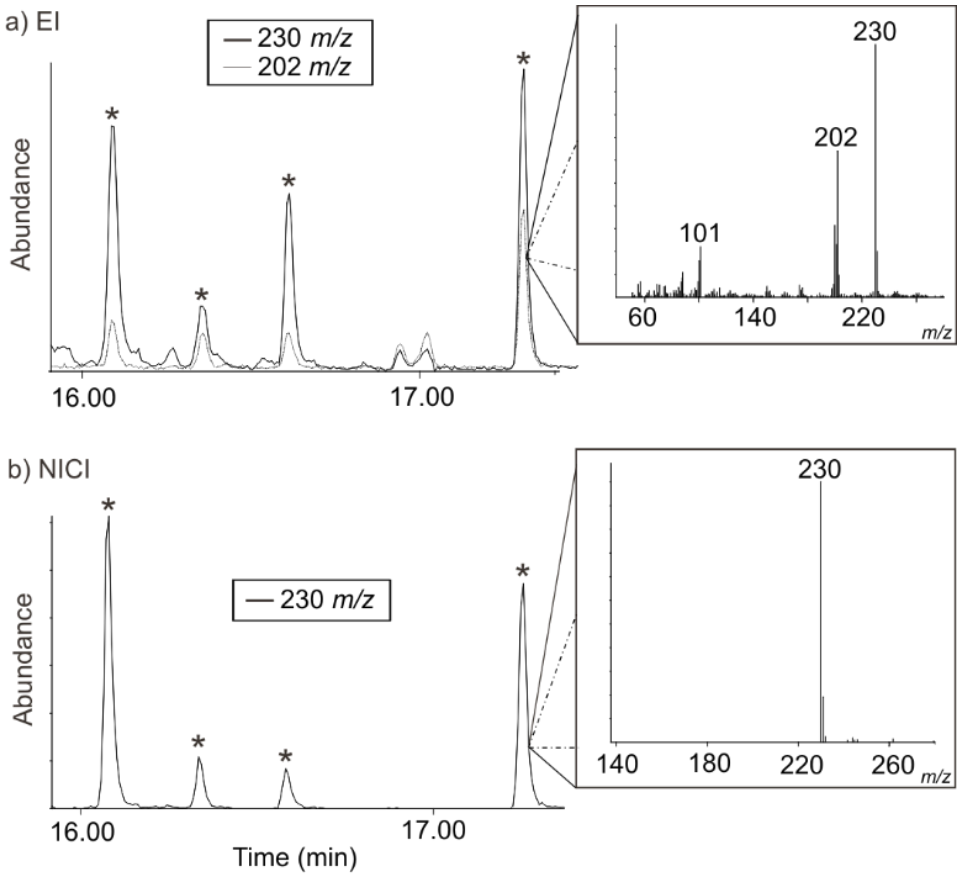

Fig. 4. GC-MS extracted ion chromatograms (TIC) of benzanthrone and its isomers in 20% DCM in hexane SPE fractions of wood smoke PM extracts, analyzed with EI and NICI. Both chromatograms were obtained in SITI mode.

3.2.3. SPE Fractionation

The SPE method, previously developed for purification of nitro-PAHs,[23,24] was optimized to fractionate and purify PAHs and their oxidation products, using an aminopropyl phase SPE cartridge with a solvent elution gradient (i.e., eluting the analytes of different polarity by using solvents of different polarity). In the initial evaluation of the method, it was taken into consideration that nitro-PAHs were effectively eluted previously with 20 % DCM in hexane.[23,24] This was confirmed in the initial fractionation of representative compounds for PAHs, hydroxy-, oxy- and nitro-PAHs (Figure 5). PAHs then eluted in the 100 % hexane fraction; oxy-PAHs and nitro-PAHs in 20 and 50 % methylene chloride (in hexane) fractions and hydroxy-PAHs in the 100 % DCM fraction (Figure 5). As of note, lower molecular weight species (in this case nitroquinoline and hydroxybiphenyl) eluted later compared to higher molecular weight species (i.e., structures with three or more aromatic rings), perhaps due to a decreased steric hindrance and thus greater affinity for the sorbent phase.

Based on the results reported above, *n*-hexane, 20 % DCM, 50 % DCM and 100 % MeOH were used in the protocol applied to PM. Although hydroxy-PAHs eluted within the 100 % DCM fraction in the preliminary experiments, the 100 % MeOH fraction was used to ensure the elution of all highly polar species that may be present in PM. Even though the step with 50 % DCM in hexane was not essential for the target analyte elution, it was used in the final protocol to ensure elimination of compounds that may interfere with the hydroxy-PAH analysis in PM extracts.

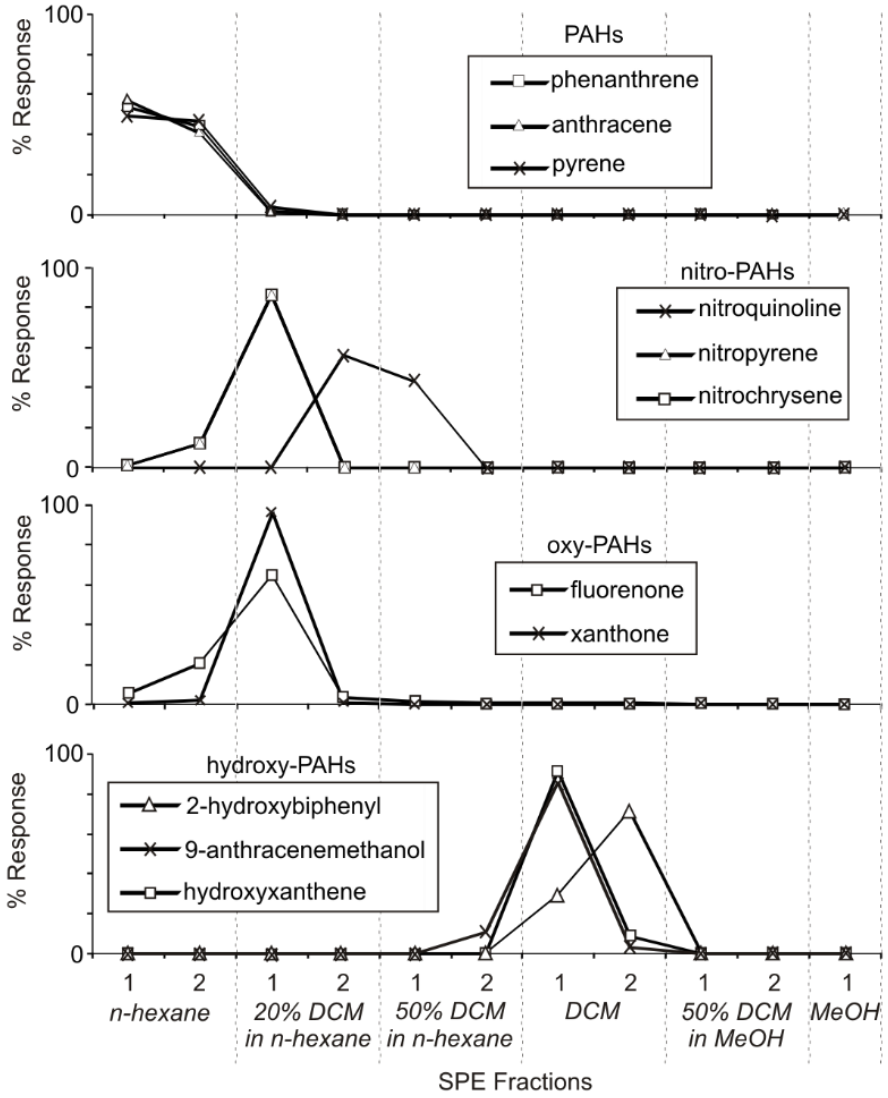

Fig. 5. SPE fractionation of standards of PAHs and polar PAH derivatives using an amino-propyl cartridge. Data are shown as average values. All standard deviations were within 5% RSD.

3.2.4. Characterization of PM

Two PM matrices, diesel exhaust (SRM 2975) and WS PM, were characterized using the method developed in this study. To ensure high efficiency, sequential Soxhlet extraction with DCM and methanol was employed. The majority of all PAHs and polar PAH derivatives were exhaustively extracted from SRM 2975 using DCM. This was

confirmed by subsequent Soxhlet extraction of remaining residue particles using MeOH. For WS PM, only residual concentrations (<10 %) were found in such methanol extracts. The analytes of interest were not detected in the methanol extracts of SRM 2975, probably due to their significantly lower concentrations in this matrix. Using the developed SPE procedure, the Soxhlet extracts were fractionated. Elution distribution profiles (see Appendices I & II) were consistent with those observed in standard mixtures, with PAHs mainly eluting in hexane, oxy- and nitro-PAHs being recovered mostly in the fraction eluted by 20 % DCM in hexane, and hydroxy-PAHs being completely isolated within the 100 % MeOH fraction. The only exceptions were 9-fluorenone and 9,10-phenanthroquinone which yielded significant recoveries in 20 % DCM in hexane.

From a practical standpoint, it is easier to quantify selected species by analyzing a single SPE fraction, which contains the highest abundance of the analytes. To evaluate the accuracy of this quantification approach, the recoveries of individual species in the SPE fraction with the highest abundance were compared to the recoveries of these species from all SPE fractions combined (Table 3). As mentioned in the experimental section, the accuracy of recoveries was ensured by the use of appropriate recovery standards. The determined recoveries for diesel exhaust PM SRM 2975 were also compared to those published by NIST and previous studies.[23,24,57]

Despite the significant differences in concentrations in diesel exhaust and WS PM, similar SPE fractionation trends were observed for most compounds using both quantification methods. It should be noted that the recoveries obtained for the recovery standards (R.S.) using the two quantification methods were significantly different, i.e.,

the R.S. % obtained for total SPE quantification was higher than that obtained from a single fraction R.S. %. This difference may be due to fractions containing target analytes below the LOD and R.S. of significant abundance (e.g., 5–20 %), leading to an underestimation of analytes when quantified by the sum of all fractions.

Table 3. Mass concentration of PAHs and their polar derivatives in both diesel exhaust PM (SRM 2975) and WS PM.

Analytes	SRM 2975 NIST data[c] µg g^{-1}	Diesel exhaust SRM 2975 SPE-total fractions[a] µg g^{-1}	Diesel exhaust SRM 2975 SPE-fraction[b] µg g^{-1}	Wood smoke PM SPE-total fractions[a] µg g^{-1}	Wood smoke PM SPE-fraction[b] µg g^{-1}
PAHs			**100% hexane**		**100% hexane**
Phenanthrene	17 ± 2.80	13.84 ± 0.24	14.03 ± 0.21	198.8 ± 5.7	210.2 ± 6.4
Anthracene	0.038 ± 0.008	0.51 ± 0.08	0.55 ± 0.08	25.99 ± 0.82	27.82 ± 0.67
Phen/Anth-C_1 A T	0 ± 0.00	0.86 ± 0.04	0.91 ± 0.04	19.34 ± 0.95	20.44 ± 0.98
Phen/Anth-C_1 B T		1.75 ± 0.07	1.85 ± 0.06	24.27 ± 1.15	25.65 ± 1.19
Phen/Anth-C_1 C T		0.53 ± 0.01	0.55 ± 0.02	6.38 ± 0.07	6.74 ± 0.08
Phen/Anth-C_1 D T		0.88 ± 0.02	0.93 ± 0.02	17.27 ± 0.68	18.26 ± 0.75
Phen/Anth-C_1 E T		ND	ND	20.33 ± 0.38	21.49 ± 0.43
Fluoranthene	26.6 ± 5.1	18.61 ± 0.34	18.86 ± 0.51	169.9 ± 6.0	171.9 ± 6.0
Pyrene	0.9 ± 0.24	0.61 ± 0.04	0.64 ± 0.05	174.1 ± 6.8	177.1 ± 6.9
Benzo[*a*]anthracene	0.317 ± 0.066	0.42 ± 0.02	0.44 ± 0.02	67.0 ± 2.5	61.1 ± 2.2
Triphenylene T	5.22 ± 0.20	4.63 ± 0.78	4.32 ± 0.72	ND	ND
Chrysene	4.56 ± 0.16	4.34 ± 0.44	4.00 ± 0.35	76.7 ± 3.6	71.9 ± 3.3
Benzo[*b*]fluoranthene	11.5 ± 3.6	10.85 ± 0.36	8.75 ± 0.06	62.9 ± 2.6	48.9 ± 3.0
Benzo[*a*]pyrene	0.0522 ± 0.0053	1.85 ± 0.29	1.57 ± 0.20	49.8 ± 2.1	38.4 ± 1.8
Indeno[1,2,3-*cd*]pyrene	1.4 ± 0.2	0.83 ± 0.46	0.64 ± 0.12	32.7 ± 1.5	19.42 ± 1.04
Dibenzo[*a*,*h*]anthracene	0.37 ± 0.07	0.32 ± 0.05	0.14 ± 0.02	ND	ND
Total PAHs		**60.8 ± 1.2**	**58.2 ± 1.0**	**945.5 ± 12.3**	**919.3 ± 12.5**
Oxy-PAHs			**20% DCM in hexane**		**20% DCM in hexane**
9-Fluorenone	NA	4.42 ± 0.47	3.53 ± 0.06	52.51 ± 0.53	44.45 ± 0.58
Xanthone	NA	ND	ND	21.26 ± 0.29	21.26 ± 0.29
Anthrone B T	NA	4.78 ± 0.31	2.34 ± 0.13	18.80 ± 0.51	19.35 ± 0.51
Anthrone D T	NA	2.71 ± 0.31	2.71 ± 0.28	35.48 ± 0.95	14.44 ± 0.64
Anthrone E T	NA	2.56 ± 0.31	2.56 ± 0.17	34.59 ± 0.65	14.35 ± 0.34
9,10-Anthraquinone	NA	8.71 ± 0.33	7.70 ± 0.34	ND	ND
Benzanthrone A T	NA	0.71 ± 0.07	0.71 ± 0.07	3.55 ± 0.09	3.65 ± 0.09
Benzanthrone B T	NA	0.64 ± 0.07	0.64 ± 0.07	5.88 ± 0.18	3.57 ± 0.12
Benzanthrone C T	NA	0.75 ± 0.10	0.65 ± 0.07	3.57 ± 0.05	3.60 ± 0.05
Benzanthrone D T	NA	2.39 ± 0.28	2.17 ± 0.24	7.95 ± 0.28	8.26 ± 0.28
Benzanthracenedione A T	NA	2.10 ± 0.28	2.10 ± 0.28	2.58 ± 0.10	2.69 ± 0.10
Benzanthracenedione B T	NA	0.24 ± 0.02	0.24 ± 0.02	2.37 ± 0.12	2.51 ± 0.12
Total oxy-PAHs		**20.2 ± 3.4**	**15.5 ± 2.8**	**188.5 ± 1.5**	**138.1 ± 1.1**

Table 3. continued.

Analytes	SRM 2975 NIST data[c] µg g^{-1}	Diesel exhaust SRM 2975 SPE-total fractions[a] µg g^{-1}	Diesel exhaust SRM 2975 SPE-fraction[b] µg g^{-1}	Wood smoke PM SPE-total fractions[a] µg g^{-1}	Wood smoke PM SPE-fraction[b] µg g^{-1}
Nitro-PAHs			**20% DCM in hexane**		**20% DCM in hexane**
2-Methyl-1-nitronaphthalene		0.14 ± 0.01	0.16 ± 0.01	ND	ND
2-Nitronaphthalene	0.11 ± 0.02	0.35 ± 0.03	0.35 ± 0.03	ND	ND
3-Nitrobiphenyl	<0.007 ± NA	0.061 ± 0.017	0.091 ± 0.008	ND	ND
9-Nitroanthracene	2.97 ± 0.45	1.85 ± 0.09	1.84 ± 0.05	ND	ND
2-Nitro-9-fluorene		0.05 ± 0.00	0.06 ± 0.00	ND	ND
9-Nitrophenanthrene	0.444 ± 0.047	0.40 ± 0.01	0.50 ± 0.01	ND	ND
3-Nitrophenanthrene	0.185 ± 0.017	0.23 ± 0.01	0.38 ± 0.01	ND	ND
3-Nitrofluoranthene		2.39 ± 0.05	2.59 ± 0.08	ND	ND
1-Nitropyrene	34.8 ± 4.7	29.5 ± 0.6	32.5 ± 0.7	ND	ND
7-Nitrobenza[*a*]anthracene	3.46 ± 0.78	1.94 ± 0.23	2.09 ± 0.28	ND	ND
6-Nitrochrysene	2.22 ± 0.45	1.89 ± 0.20	2.14 ± 0.24	ND	ND
1,3-Dinitropyrene	1.18 ± 0.29	0.65 ± 0.08	0.74 ± 0.08	ND	ND
1,6-Dinitropyrene	2.36 ± 0.39	1.24 ± 0.04	1.41 ± 0.04	ND	ND
1,8-Dinitropyrene	3.1 ± 0.57	4.76 ± 0.30	4.43 ± 0.23	ND	ND
1-Nitrobenzo[*e*]pyrene	1.788 ± NA	0.85 ± 0.03	0.90 ± 0.02	ND	ND
6-Nitrobenzo[*a*]pyrene	1.36 ± 0.27	0.68 ± 0.04	0.76 ± 0.04	ND	ND
3-Nitrobenzo[*e*]pyrene	6.857 ± NA	3.78 ± 0.19	4.03 ± 0.14	ND	ND
Total nitro-PAHs		**50.8 ± 0.8**	**55.0 ± 0.9**		
Hydroxy-PAHs			**100% methanol**		**100% methanol**
2-Hydroxybiphenyl	NA	ND	ND	20.6 ± 3.2	20.6 ± 3.2
3-Hydroxybiphenyl	NA	ND	ND	56.3 ± 3.9	56.3 ± 3.9
4-Hydroxybiphenyl	NA	ND	ND	47.0 ± 2.9	47.0 ± 2.9
2-Hydroxy-9-fluorenone	NA	ND	ND	90.6 ± 8.6	90.6 ± 8.6
9-Phenanthrol	NA	ND	ND	143 ± 14	143 ± 14
1-Hydroxypyrene	NA	ND	ND	96.3 ± 8.1	96.3 ± 8.1
Total hydroxy-PAHs				**454 ± 19.0**	**454 ± 19.0**

[a] The amount of each analyte is calculated using total % recovery standard from all SPE fractions
[b] The amount of each analyte is calculated using recovery standard % from SPE-100% hexane for PAHs, SPE-20% DCM for oxy- and nitro-PAHs and SPE-100% MeOH for hydroxy PAHs
[c] Values reported by Bamford *et al.*[23] and NIST[57]

For the majority of PAH species, the recoveries from the single SPE (hexane) fraction were similar to those of the combined fractions. For both PM matrices, higher molecular weight PAH species (i.e., molecular structures comprised of 4–5 rings, excluding pyrene and fluoranthene) yielded relatively lower values within the single SPE fraction (45–94 %). This was due to the incomplete elution of these species in the hexane fraction, in contrast to pyrene-d_{10} (70 %), which was used as a recovery standard. The use of higher molecular weight recovery standards was designed to correct recoveries of higher molecular weight species. Many oxy-PAH species were completely isolated within the 20 % DCM fraction. Some species, such as 9-fluorenone, xanthone, and some anthrone and benzanthrone isomers, resulted in a broader distribution over SPE fractions, particularly for diesel exhaust PM. The lower concentrations of these mildly polar species in diesel exhaust PM may be more effectively retained. In addition, the less pronounced effect for wood smoke PM may be explained by the limited availability of active sites on the SPE column which may be covered by either other species or the matrix. In this work we have used both 20 and 50 % DCM in hexane both to enhance the purification and to separate the analytes from matrix. However, the isolation of most oxy-PAHs species within 20 % DCM and some species showing significant recoveries in the 50 % DCM in hexane fraction suggests that using 50 % DCM in hexane would be more appropriate. In contrast, quantification based on the isolated SPE fraction of nitro-PAHs in diesel exhaust PM produced total concentrations consistent with the values obtained in combined fractions. All hydroxy-PAHs were eluted in the last SPE fraction, resulting in similar recovery values obtained from the total and single SPE fractions.

Besides comparing the two methods of quantification, recoveries were also compared to data reported by NIST and other researchers (see Table 3).[23,24,57] For the majority of PAHs, similar abundances were obtained. However for some species, namely anthracene, pyrene, and benzo[*a*]pyrene, the observed recoveries were significantly higher than the reported values. The correct use of calibration standards for these species was verified, thus the differences may be due to greater recovery efficiencies of the new method. For nitro-PAHs, the analyte concentrations using SPE were slightly lower than the values reported by NIST using PFE with DCM and amino/cyano LC purification followed by GC-*NICI*-MS analysis, with the exception of 2-nitronaphthalene, 3-nitrobiphenyl, 3-nitrophenanthrene and 1,8-dinitropyrene which showed significantly higher recoveries in the present study. Batch variations or age of the reference material, with greater age resulting in lower recoveries, may also play a role in the differences of recoveries.

As mentioned previously, although GC-*NICI*-MS analysis of oxy-PAHs was not as sensitive as that in EI mode for the analysis of oxy-PAHs, it was useful as a tool for the identity confirmation of tentatively identified compounds. In analyzing both WS and SRM 2975 PM extracts, we identified several oxy-PAH species for which no standards were available, i.e., anthrone isomers ($C_{14}H_{10}O$), benzanthrone/benzo[*a*]fluorenone isomers ($C_{17}H_{10}O$) and benzanthracenedione isomers ($C_{18}H_{10}O_2$). These compounds were tentatively identified by comparing mass spectra to the NIST Mass Spectral Library (2005), each yielding >90 % matching quality. In order to confirm the identity of these compounds as being oxy-PAHs, the samples were re-analyzed in NICI mode using the same GC oven temperature program (see Figure 4). The resulting chromatograms

exhibited peaks with matching retention times showing that these compounds contained a sufficiently electronegative functional group (i.e., carbonyl group), thus supporting that these compounds were indeed oxy-PAHs (Figure 4).

3.3. Conclusions

An analytical method has been developed utilizing Soxhlet extraction followed by SPE fractionation for the simultaneous analysis of PAHs and their oxidation products. Using GC-MS analysis in SITI acquisition mode, several classes of PAH oxidation products were analyzed using trimethylsilylation for hydroxy species and a fairly simple ion source exchange for analysis of nitro-PAHs using NICI. The SPE protocol was applied to both diesel exhaust (SRM 2975) and WS PM, showing that a quantitative assessment of the total mass concentration within PM for each species (either PAHs or oxidation products) can be done directly through analyzing the respective SPE fractions, i.e., 50 % DCM in hexane for oxy- and nitro-PAHs and 100 % MeOH for hydroxy-PAHs using appropriate recovery standards. However due to the complexity of sample preparation, it is advisable to use recovery standards even when the quantification assessing the analyte distribution over all fractions is employed.

This SPE fractionation procedure can be a valuable asset in toxicological studies aimed at determining the mutagen capacity of polar PAHs such as oxy- and hydroxy-PAHs, which have been less studied. NICI analysis of oxy-PAHs was shown to be a useful tool for confirming the identity of species tentatively identified in EI mode through MS spectral database matching.

CHAPTER 4

4. EXTRACTION OF POLYCYCLIC AROMATIC HYDROCARBONS AND THEIR OXIDATION PRODUCTS USING PRESSURIZED FLUID EXTRACTION.

4.1. Experimental

4.1.1. Materials and Reagents

Method development was first performed using standards spiked to sand (standard Ottawa; EMD Millipore, Darmstadt, Germany) to determine the essential extraction volumes. All remaining experiments evaluating the impact of temperature on mass fractions extracted were performed using WS PM (WS PM) (~10 mg) that was generated from softwood and hardwood combustion[47], and diesel engine exhaust standard reference material (SRM 2975; NIST, Gaithersburg, MD, USA). WS PM and SRM 2975 were chosen due to their differences in their matrices, with WS PM being relatively polar and SRM 2975 being relatively non-polar,thus allowing to evaluate extraction efficiencies of target analytes in a range of different matrix interactions. More detailed information on the collection and storage methods for the WS PM can be found elsewhere. Briefly, the WS PM was collected from 22 different residential wood stoves, 14 burning hardwoods and 8 burning softwoods. The hardwood stoves were located in Grand Forks, ND and the softwood stoves in Salt Lake City, UT and Boulder, CO. During sample collection the stoves were continuously operated in similar manners. Particulate samples were collected from the inside walls of the chimney at a distance of ~ 0.5 m up the smoke plume.

All reagents were of analytical-reagent grade with a purity of ≥98 % unless stated otherwise. GC-grade DCM and LC-MS optima grade MeOH were obtained from Fisher Scientific (Chicago, IL,USA). *n*-hexane (HPLC grade, 95 %) was obtained from Sigma-Aldrich (St. Louis, MO, USA). Information on all individual standards, recovery standards (R.S.s), internal standard (I.S.), and tentatively identified species is provided in Table 4. PAH standards (15 PAHs in total) were obtained as a mixture from Sigma-Aldrich (QTM PAH Mix). For derivatization 99 % N,O-*bis*(trimethylsilyl)trifluoroacetamide (BSTFA) with 1 % of trimethylchlorosilane (TMCS) (Sigma-Aldrich) was used.

Table 4. Compound information, quantitation parameters and mass concentration in WS PM for all PAHs in this work.

Compound Name[a]	t_R (min)	Quant. Mode	Quant. Ion (*m/z*)	Calibration Based On	Recovery Standard	Manufacturer
PAHs						
naphthalene	4.570	SIM	128	Standard	naph-d8	Supelco
acenapthylene	6.657	SIM	152	Standard	phen-d10	Supelco
acenaphthene	6.943	SIM	154	Standard	phen-d10	Supelco
fluorene	7.857	SIM	166	Standard	phen-d10	Supelco
phenanthrene	9.728	SIM	178	Standard	phen-d10	Supelco
anthracene	9.835	SIM	178	Standard	phen-d10	Supelco
2-methylanthracene	11.029	SIM	192	Standard	phen-d10	Supelco
phen/anth-C1 A T	10.818	SIM	192	2-methylanthracene	phen-d10	Nac
phen/anth-C1 B T	10.868	SIM	192	2-methylanthracene	phen-d10	NA
phen/anth-C1 C T	10.969	SIM	192	2-methylanthracene	phen-d10	NA
phen/anth-C1 D T	11.033	SIM	192	2-methylanthracene	phen-d10	NA
phen/anth-C1 E T	11.085	SIM	192	2-methylanthracene	phen-d10	NA
phen/anth-C2 A T	11.923	TIC	206	phenanthrene	phen-d10	NA
phen/anth-C2 B T	12.074	TIC	206	phenanthrene	phen-d10	NA
phen/anth-C2 C T	12.136	TIC	206	phenanthrene	phen-d10	NA
phen/anth-C2 D T	12.184	TIC	206	phenanthrene	phen-d10	NA
phen/anth-C2 E T	12.251	TIC	206	phenanthrene	phen-d10	NA
fluoranthene	12.337	SIM	202	Standard	py-d10	Supelco
pyrene	12.812	SIM	202	Standard	py-d10	Supelco
1-methylpyrene	13.620	SIM	216	1-methylpyrene	py-d10	NA
flu/pyr-C1 A T	13.822	SIM	216	1-methylpyrene	py-d10	NA
flu/pyr-C1 B+C T	13.867	SIM	216	1-methylpyrene	py-d10	NA
flu/pyr-C1 D T	14.062	SIM	216	1-methylpyrene	py-d10	NA
flu/pyr-C1 E T	14.130	SIM	216	1-methylpyrene	py-d10	NA
flu/pyr-C1 F T	15.630	SIM	228	Standard	py-d10	Supelco
flu/pyr-C1 G T	15.703	SIM	228	Standard	py-d10	Supelco
benzo[e]pyrene	17.975	SIM	252	Standard	py-d10	Supelco
benz[a]anthracene	18.067	SIM	252	Standard	py-d10	Supelco
chrysene	18.234	SIM	252	Standard	py-d10	Supelco
benz[e]acephenanthrylene	18.599	SIM	252	Standard	py-d10	Supelco
benzo[k]fluoranthene	18.672	SIM	252	Standard	py-d10	Supelco
benzo[j]fluoranthene	18.841	SIM	252	Standard	py-d10	Supelco
benzo[a]fluoranthene	20.636	SIM	276	Standard	py-d10	Supelco
benzo[a]pyrene	20.707	SIM	278	Standard	py-d10	Supelco
indeno[1,2,3-cd]pyrene	21.014	SIM	276	Standard	py-d10	Supelco
benzo[ghi]perylene	9.302	SIM	180	Standard	py-d10	Sigma
benzo[ghi]perylene	11.507	SIM	208	Standard	py-d10	Sigma
dibenzo[a,h]anthracene	10.467	SIM	196	Standard	py-d10	Sigma

Table 4. cont.

Compound Name[a]	t_R (min)	Quant. Mode	Quant. Ion (*m/z*)	Calibration Based On	Recovery Standard	Manufacturer
Oxy-PAHs						
benzo[b]naphtho[2,3-d]furan T	14.124	SIM	216	9-fluorenone	2-caq	Supelco
benzo[b]naphtho[2,1-d]furan T	13.419	SIM	216	9-fluorenone	2-caq	NA
9-fluorenone	12.999	TIC	218	Standard	2-caq	NA
Xanthone	13.170	TIC	218	Standard	2-caq	NA
9,10-anthraquinone	13.342	TIC	218	Standard	2-caq	NA
benzo[b]fluoren-11-one T	14.815	SIM	230	9-fluorenone	2-caq	NA
benzo[a]fluoren-11-one T	15.072	SIM	230	9-fluorenone	2-caq	NA
benzo[c]fluoren-7-one T	15.318	SIM	230	9-fluorenone	2-caq	NA
benz[de]anthracen-7-one T	15.971	SIM	230	9-fluorenone	2-caq	NA
benz[a]anthracene-7,12-dione	16.701	SIM	258	Standard	2-caq	Sigma
Nitro-PAHs						
9-nitrophenanthrene	15.791	SIM	223	Standard	2-caq	Sigma
3-nitrofluoranthene	19.269	SIM	247	Standard	2-caq	Sigma
1-nitropyrene	19.719	SIM	247	Standard	2-caq	Sigma
6-nitrochrysene	21.822	SIM	273	Standard	2-caq	Sigma
Hydroxy- & Carboxy-PAHs[d]						
2-hydroxybiphenyl	7.843	SIM	211	Standard	2-CHM[e]	Alfa Aesar
hydroxybiphenyl T	9.171	SIM	227	4-hydroxybiphenyl	2-CHM	NA
4-hydroxybiphenyl	9.570	SIM	242	Standard	2-CHM	Alfa Aesar
7-hydroxycadalene	11.399	SIM	271	Standard	2-CHM	Sigma
9-phenanthrol	12.653	SIM	266	Standard	2-CHM	Sigma
3-phenanthrol T	12.923	SIM	266	9-phenanthrol	2-CHM	NA
2-hydroxy-9-fluorenone	12.760	SIM	253	Standard	2-CHM	Sigma
4-phenanthrenemethanol	13.231	SIM	191	Standard	1-OH-py-d9	Sigma
hydroxypyrene A T	15.496	SIM	290	Standard	1-OH-py-d9	Sigma
hydroxypyrene B T	15.733	SIM	290	1-hydroxypyrene	1-OH-py-d9	NA
hydroxypyrene C T	15.128	SIM	290	1-hydroxypyrene	1-OH-py-d9	NA
1-hydroxypyrene	15.170	SIM	290	1-hydroxypyrene	1-OH-py-d9	NA
hydroxypyrene D T	15.823	SIM	290	1-hydroxypyrene	1-OH-py-d9	NA
1,8-dihydroxyanthraquinone	16.166	SIM	369	Standard	1-OH-py-d9	Sigma
4-phenenthrene-COOH	13.824	SIM	205	Standard	1-OH-py-d9	Sigma
9-anthracene-COOH	14.201	SIM	205	Standard	1-OH-py-d9	Sigma
9-phenanthrene-COOH	14.695	SIM	205	Standard	1-OH-py-d9	Sigma
n-phen/anth-COOH	14.725	SIM	205	9-phen-COOH	1-OH-py-d9	NA
Recovery Standards						
naphthalene-d8	6.586	SIM	136			Sigma-Adrich
phenanthrene-d10	12.411	SIM	188			Supelco
anthracene-d10	12.538	SIM	188			Supleco
pyrene-d10	15.645	SIM	212			Isotec
Internal Standard						
fluoranthene-d10	15.138	SIM	212			Supelco

a Compounds that were identified without avialable standards are indicated with a "T" next to the compound name.
b Values in parenthesis are the relative reponse of the confirmation ions to that of the quantification ion listed.
c "NA" denotes that standards for that particular compound were not available during the time of the study.
d All hydroxy- and carboxy-PAHs are shown as trimethylsilyl derivatives after derivatization with BSTFA.
e 2-CHM is an acronym for 2-chloro-2-hydroxy-4-methylbenzophenone, 2-caq for 2-chloroanthraquinone and 1-OH-py-d9 for 1-hydroxypyrene-d_9.

4.1.2. Extraction

All extraction methods and parameters used in this study are listed in Table 5. The PFE extractions were performed using a home-built apparatus (previously described in detail) used for hot pressurized water extraction consisting of an HP 5890 GC oven, Waters 1100 LC pump, and the extraction vessel.[58] Needle valves (VICI, Houston, TX, USA) were placed at the inlet and outlet of the PFE extraction vessel outside the oven. The PFE extraction vessel was comprised of an empty 50 mm x 4.6 mm ID (0.83 mL internal volume) stainless steel liquid chromatography column capped with 0.5 µm pore size stainless steel frits (Chromtech, Apple Valley, MN, USA). Extractions were performed in triplicate using either DCM or MeOH, which was chosen due to their polarities being similar to the polarity range of the targeted analytes. In terms of extraction efficiency, DCM has been shown to be comparable to other relatively non-polar solvent systems in extracting lower molecular weight (2–4 ring) PAHs from SRM 2975.[59] However, it has been shown that DCM yields lower recoveries for higher molecular weight (5+ ring) PAHs than when using non-polar solvent systems (i.e., toluene).[59–61] DCM has also been previously used for the extraction of nitro-PAHs from SRM 2975.[23] For oxy-PAHs, ethyl acetate has been shown to be efficient for their extraction from urban PM and quartz fiber filters,[62] however PFE has not, to our knowledge, been investigated for other PM matrices. Currently, PFE has not been reported for extracting highly polar PAH derivatives, such as hydroxy- and carboxy-PAHs, from PM. These species may require a more polar solvent (i.e., MeOH) for efficient extraction from a polar matrix. However, such a polar solvent (when used either alone or as a modifier) has been shown to be less efficient at extracting PAHs from the PM matrix.[60]

The PFE extraction method consisted of several cycles, each including a static extraction step (5 min) followed by a dynamic extraction step at a flow rate of 0.6 mL min^{-1} for 5 min (i.e., a flushing volume of 3.0 mL, more than 3 internal cell volumes). To determine the total volume of DCM and number of extraction cycles sufficient to achieve a complete extraction of WS PM, initial experiments were performed with three cycles (each collecting 3 mL into a single vial), followed by three additional dynamic extraction steps, collecting each 3.0 mL fractions in separate vials (method 1 in Table 5).

For extractions of PM, the extraction cell was first filled to approximately half volume with sand followed by ~10 mg of the PM. R.S. mixtures were then spiked to the PM and let sit for 2 min to allow for their complete adsorption onto the PM matrix. The remaining volume of the extraction cell was then filled with sand. The amount of each R.S. spiked to PM was ~0.2 µg for the majority of analytes with the exception of hydroxy-PAHs, which was spiked at ~2.0 µg. Extraction temperatures were evaluated in a range of 130–200 °C. For these experiments three extraction cycles (giving a total of 9.0 mL) were employed. The mass fractions obtained with the final PFE method at 100 °C and 2000 psi (13.8 MPa) from WS PM and SRM 2975 were compared to those obtained using Soxhlet extraction. The extraction pressure was not evaluated since it was previously shown to have no significant role in the PAH recoveries from PM matrices.[59,63,64]

Table 5. Extraction parameters and information for the various PFE and Soxhlet methods evaluated in this work.

Method Number	Extraction Method	Extraction Parameters					
		Solvent	Temp. (°C)	Pressure (psi)	Number of Static Cycles	Total Volume of Extract (mL)	Dynamic Extraction (mL)[a]
1	PFE	DCM	100	2000	3	9	9
2	PFE	DCM	100	2000	3	9	–
3	PFE	DCM	130	2000	3	9	–
4	PFE	DCM	160	2000	3	9	–
5	PFE	DCM	200	2000	3	9	–
6	PFE	MeOH	100	2000	3	9	–
7	Soxhlet	DCM	–	–	–	90	–
8	Soxhlet	MeOH	–	–	–	90	–

a Collection of additional extract in a separate vial from the 9 mL collected during the 3 cycle extractions.

All components of the Soxhlet apparatus (i.e., the extractor, condenser, thimble and flask) were obtained from Chemglass (Vineland, NJ, USA). For all Soxhlet extractions, glass thimbles were used to avoid contamination observed for cellulose thimbles in preliminary experiments. The Soxhlet extractions were carried out with either 90 mL of DCM or 90 mL of MeOH, each for 18 h. After the extraction, the DCM and MeOH extracts were cooled to room temperature and evaporated under a stream of nitrogen while on ice to limit the loss of more volatile compounds, in addition to the losses already exhibited during Soxhlet extraction. All PM extracts were evaporated to 100 µL and then diluted to 1.0 mL with *n*-hexane and submitted to the SPE fractionation/purification (see Section 4.1.3).

4.1.3. SPE Fractionation and Preparation for GC Analysis

We have previously demonstrated an SPE fractionation protocol applied to PM extracts that is essential for the determination of trace concentrations of PAH derivatives.[65] Briefly, an aminopropyl SPE cartridge with 500 mg of sorbent, 55 – 105

μm particle size, and a 125 Å pore size was used (Sep-Pak, Waters, Milford, MA). All SPE was performed using an SPE vacuum manifold with a 10-port top (Alltech/Grace, Columbia, Maryland, USA). Prior to the fractionation, the SPE sorbent was conditioned sequentially with DCM and *n*-hexane (6 mL each). The elution solvents employed sequentially were 4.0 mL solutions of 100% *n*-hexane, 20% DCM in *n*-hexane, and 100% MeOH. All collected SPE fractions were concentrated to 200 μL under a gentle nitrogen stream, and then divided into two 100 μL aliquots. One aliquot was used to determine PAHs and oxy-PAHs whereas the other was evaporated and derivatized with 100 μL of BSTFA+TMCS at 70 °C for 6 h for the determination of hydroxy-PAHs.

4.1.4. GC-MS Analysis

Determination of PAHs, oxy-PAHs and hydroxy-PAHs was performed using an Agilent 6890N GC coupled to a 5975C MS with an electron ionization source. The analyses were accomplished on a 25 m long DB-5MS column with a 0.25 mm I.D., and 0.25 μm film thickness (J&W Scientific, Inc., Folsom, CA). Ultra-pure helium (99.999 %) was used as the carrier gas with a constant flow rate of 1.0 mL min^{-1}. Injection conditions were 1 min splitless time with a pressure pulse of 25 psi for 0.95 min and the injection volume of 1.0 μL using a splitless liner with deactivated glass wool (Restek, Bellefonte, PA). The temperatures of the injector and transfer line were 250 °C and 280 °C, respectively. The GC oven temperature program started at 40 °C for 1 min, increased at a rate of 20 °C min^{-1} to 140 °C, followed by a gradient of 10 °C min^{-1} to 290 °C, and an increase at the rate of 15 °C min^{-1} to 310 °C, and held for 12 min.

The GC-MS data were acquired using a combination of total ion current (TIC) and selected ion monitoring (SIM) modes, i.e., selected-ion-total-ion (SITI). SITI combines the advantages of improved sensitivity, resulting from the use of SIM

monitoring single ions, with simultaneous compound identification using TIC. A dwell time of 25 ms was used for all ions listed in Table 4 for the SIM mode. A range of 50–500 *m/z* was used for TIC.

4.1.5. Quantification

Quantification was based on the internal standard (IS) method, using fluoranthene-d_{10} as the IS. Calibration solutions were prepared by serial dilutions of stock mixture to obtain final analyte concentrations in the range of 9–9000 ng mL^{-1}. Volumes of each solution were the same as for the final prepared extracts, i.e., 100 µL, and spiked with the same amount of IS as the extracts.

Interday precisions of calculated slopes of multiple calibration curves for select species over different days are shown in Table 6. Prior to extraction of PM, RS compounds were spiked to the PM. The RS compounds (listed in Table 4) were used to correct for analyte loss during extraction and fractionation. For each RS compound, a recovery yield (RY) was calculated (See Eq. 1).

$$RY(\%) = \frac{m_{RS}\,extracted}{m_{RS}\,spiked} \cdot 100\% \qquad \text{Eq. 1}$$

For the extractions from both WS PM and SRM 2975, the calculated mass fractions (mass of analyte per mass of PM subjected to extraction) in each SPE fraction were summed to give a total extracted mass concentration. The summed mass concentrations were then corrected by the RY (70–110%) of the RS compounds that were added prior to extraction (See Table 4 for each analyte's assigned RS).

Prior to extractions of PM, multiple blank extractions were performed for each method until consistent background levels were observed. Species identified in the extracts were identified as background contaminants in all further experiments.

Instrumental limits of the detections for the targeted species in this study have been previously reported by Cochran et al.[65]

Table 6. Interday precisions exhibited through the slopes of calibration curves obtained during separate analyses over separate days.

Calibration Standard	Interday Precision Average Slope[a] (*n*=3)		
	Avg.	SD	RSD
PAHs			
naphthalene	1.148	± 0.112	10
phenanthrene	1.201	± 0.039	3
anthracene	1.020	± 0.140	14
fluoranthene	1.257	± 0.135	11
pyrene	1.245	± 0.150	12
chrysene	1.256	± 0.086	7
benzo[a]pyrene	0.634	± 0.066	10
indeno[1,2,3-cd]pyrene	0.490	± 0.087	18
benzo[ghi]perylene	0.724	± 0.063	9
Oxy-PAHs			
9-fluorenone	0.379	± 0.012	3
anthrone	0.100	± 0.013	13
9,10-anthraquinone	0.544	± 0.088	16
9,10-phenanthrenequinone	0.047	± 0.008	17
Hydroxy-PAHs			
2-hydroxybiphenyl-TMS	0.502	± 0.080	16
4-hydroxybiphenyl-TMS	0.557	± 0.076	14
9-phenanthrol-TMS	0.335	± 0.054	16
2-hydroxy-9-fluorenone-TMS	0.597	± 0.069	11
4-phenanthreneMeOH-TMS	1.224	± 0.181	15
1-hydroxypyrene-TMS (SIM)	0.507	± 0.067	13
1,8-dihydroxyanthraquinone-TMS	0.735	± 0.078	11
Carboxy-PAHs			
9-phenanthreneCOOH-TMS	0.311	± 0.031	10

a Slope = (Area Analyte/Area IS)/Conc Analyte

4.2. Results & Discussion

4.2.1. Optimization of PFE

PFE conditions were optimized in order to achieve an efficient extraction of both PAHs and their oxidation products observed in WS PM and diesel engine exhaust PM (SRM 2975).

Initial experiments focused on evaluating the number of extraction cycles required as well as the extraction temperature. For PAHs it was previously reported that extraction

pressures above 2000 psi (13.8 MPa) had no significant impact on the mass fractions extracted.[59] Thus a pressure of 2000 psi was selected and maintained throughout all the experiments performed. To determine the sufficient number of static/dynamic extraction cycles for WS PM, three 3 mL dynamic extraction steps were added to the previously used three extraction cycles. No PAH species were recovered in either of the additional dynamic extraction steps, showing that the use of three extraction cycles (giving a total extraction volume of 9.0 mL) was sufficient. Extraction temperatures were evaluated in the range of 100–200 °C for PM extractions. Varying the extraction temperature did not appear to have a significant impact on the extracted mass concentrations of PAHs, oxy-PAHs, or hydroxy-PAHs (shown in Figure 6 for representative species). Therefore, the extraction temperature of 100 °C was selected for all subsequent PFE experiments.

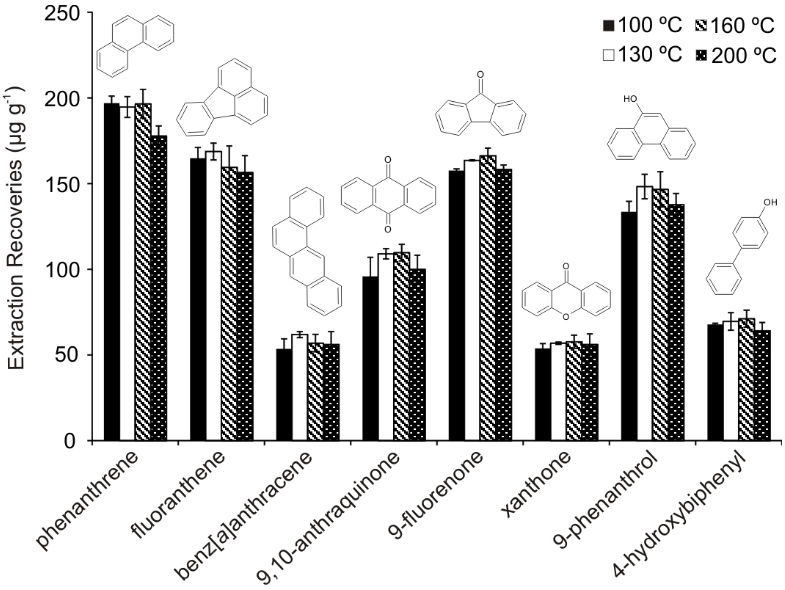

Fig. 6. PFE recoveries of representative PAHs, oxy-PAHs and hydroxy-PAHs obtained at different extraction temperatures. For all temperatures the extraction pressure was held constant at 2000 psi (13.8 MPa) and three extraction cycles were performed. All data are based on the mean value of triplicate extraction ± one standard deviation.

4.2.2. Comparison of PFE and Soxhlet

The efficiency of the optimized PFE method was determined by comparing mass concentrations extracted from WS PM and SRM 2975 to those obtained with Soxhlet extractions using DCM or MeOH for 18 h (Tables 7 & 8). The TIC chromatograms of SPE fractions for PFE extracts of WS PM are shown in Appendix III (see Appendix IV for comparison of the SPE fractions between PFE with DCM and Soxhlet with DCM and MeOH).

To evaluate the efficiency of both methods to extract the target compounds from both PM matrices, RS solutions were spiked prior to the extraction. Calculated RY values for the RS compounds spiked to WS PM and SRM 2975 are shown in Figures 7a & 7b, respectively. For WS PM, recoveries for all of the RS compounds were higher when using PFE than those obtained with Soxhlet. In comparing the extraction solvents, greater recoveries were obtained with DCM than with MeOH, with the exception of 2-chloroanthraquinone (2-caq in Figure 7). For SRM 2975, recoveries were significantly lower for the 2–3 ring PAH RS compounds for both extraction methods and solvents. This trend is likely due to the relatively non-polar matrix of the diesel exhaust PM matrix, with DCM (less polar than MeOH) providing greater recoveries for all RS compounds. For more polar RS compounds (2-CHM and 1-OH-py-d_9), both methods and extraction solvents resulted in similar recoveries (85–98%).

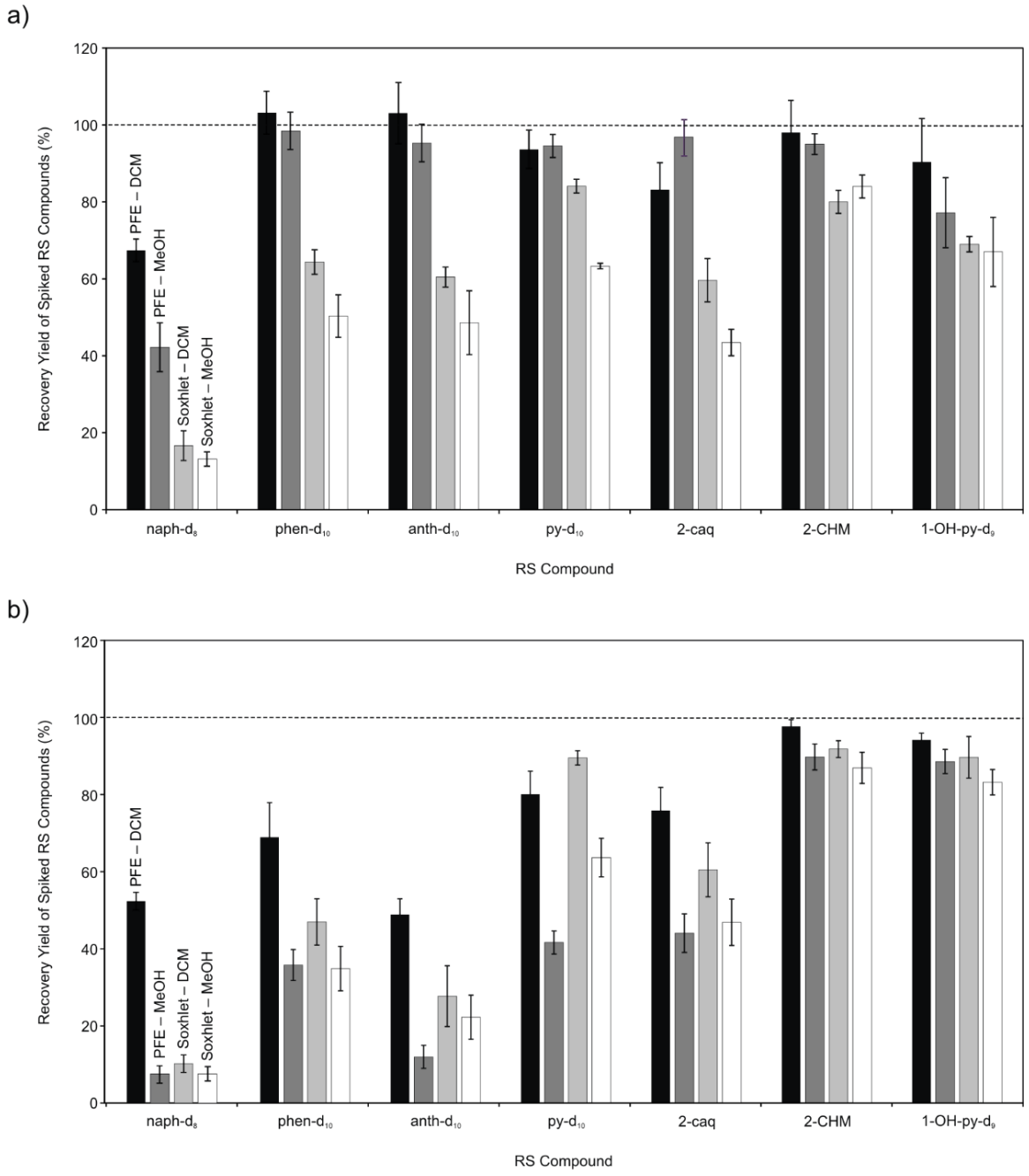

Fig. 7. Recovery yields (RY) of RS compounds observed from PFE and Soxhlet extraction of a) WS PM and b) SRM 2957. RY values are shown for extractions using both DCM and MeOH as the extraction solvents. All data are based on the mean value of multiple extractions (n=3) ± one standard deviation.

4.2.3. Comparison of PFE to Soxhlet for WS PM

The efficiency of the PFE method for extracting WS PM was determined using DCM and MeOH as the extraction solvents. Using DCM, the total mass fractions of PAHs and all polar derivatives were similar for PFE and Soxhlet (1849 and 1727 µg/g in WS PM, respectively; more detailed values are shown in Table 7). For PAHs, the total mass fractions extracted were similar between both extraction methods (1097 µg/g for PFE and 1075 µg/g for Soxhlet). All individual PFE mass fractions followed this pattern (Table 7). By contrast, PFE consistently provided higher mass fractions of most oxy-PAHs, 381±12 µg/g compared to 272±13 µg/g from Soxhlet. Specifically, 9-fluorenone had a two-fold increase in the mass fraction extracted when using PFE compared to Soxhlet (both using DCM) (Table 7). The oxy-PAH compounds studied here have similar polarities to that of DCM, possibly ruling out the solvent polarity as the limiting factor in extraction recoveries. Therefore the increased oxy-PAH mass fractions with PFE (Table 7) may be attributed to the higher temperatures used in comparison to Soxhlet, possibly due to increased disruption of the analyte–matrix interactions caused by van der Waals forces, hydrogen bonding, and/or dipole attractions of analyte molecules and active sites on the matrix. PFE also enabled the detection of benz[*a*]anthracene-7,12-dione, which was not detected in the Soxhlet extracts (using either DCM or MeOH). Perhaps the reason for the lack of response of this compound in the Soxhlet extracts could be the presence of two carbonyl groups causing stronger analyte–matrix interactions disrupted only by PFE. However a similar compound, 9,10-anthraquinone featuring two carbonyl groups, showed similar amounts extracted using both PFE and Soxhlet extraction methods (see Table 7).

For PFE using MeOH, mass fractions of PAHs extracted from WS PM were similar to those obtained with DCM (1134±13 compared 1097±16 µg g^{-1}, respectively). Overall mass fractions of oxy-PAHs were lower than with DCM (317±10 and 381±12 µg g^{-1}, respectively), however, extraction yields of 4-ring oxy-PAHs were higher with MeOH. For hydroxy- and carboxy-PAHs, the total obtained mass fractions were greater with MeOH (412±18 µg g^{-1}) than those with DCM (371±5 µg g^{-1}). This was most prevalent for carboxy-PAHs, however, the mass fractions were still lower than those determined in extracts from Soxhlet (using either DCM or MeOH).

The hydroxy-PAH mass fractions with PFE were similar to those obtained by Soxhlet DCM extraction (75–130%) (Table 7). One of the studied carboxy PAH species (4-phenanthrene-COOH) showed similar mass fractions (82% relative to those with Soxhlet) whereas the other isomers (9-anthracene-COOH and 9-phenanthrene-COOH) yielded lower recoveries (42% and 44%, respectively, relative to the amounts obtained with Soxhlet) (Table 7). In comparison to Soxhlet using DCM, a small increase in the amounts extracted (up to 15%) of these carboxy- and hydroxy-PAH species was observed when performing a Soxhlet extraction using MeOH (Table 7). Our optimization tests (Section 4.2.1) indicated that increasing the PFE temperature did not show any increase in yields for these species. When using MeOH as the extraction solvent for PFE, mass fractions extracted increased slightly for the carboxy-PAH species (23±1 compared to 19±2 µg g^{-1} for DCM), however they were still significantly lower relative to the amounts obtained with Soxhlet (with either DCM or MeOH). Nevertheless it is important to note that these carboxy species represent only ca. 1% of the total amount extracted of all species of PAHs and PAH oxidation products investigated in this study (1849±21 and

1727±33 µg/g for PFE and Soxhlet with DCM, respectively). Thus the similar mass fractions for the majority of PAHs and deratives, as well as the ease of use, support the appropriateness of PFE with DCM for the extraction of PAH derivatives from PM. However, if a highly polar species is targeted, such as a carboxy-PAH, MeOH alone or as a modifier may be essential.

Table 7. Mass fractions of PAHs and polar derivatives (oxy-, hydroxy- and carboxy-PAHs) obtained by extraction of WS PM using PFE and Soxhlet. PFE was performed at 100 °C and 2000 psi using either DCM or MeOH (Methods 2 & 6, respectively). All data are based on the mean value of multiple extractions (n=3) ± one standard deviation.

Compound	PFE						Soxhlet					
	DCM ($\mu g\ g^{-1}$)[a] mean ± st. dev (n=4)			MeOH ($\mu g\ g^{-1}$)[a] mean ± st. dev (n=4)			DCM ($\mu g\ g^{-1}$)[a] mean ± st. dev (n=4)			MeOH ($\mu g\ g^{-1}$)[a] mean ± st. dev (n=4)		
PAHs												
naphthalene	5.90	±	0.79	6.36	±	0.71	7.88	±	0.53	8.00	±	0.41
acenapthylene	2.32	±	0.27	2.75	±	0.33	2.67	±	0.25	2.70	±	0.33
acenaphthene	0.75	±	0.10	0.00	±	0.00	0.96	±	0.03	1.35	±	0.13
fluorene	9.68	±	1.18	10.46	±	0.62	9.31	±	0.81	10.25	±	0.60
phenanthrene	196.37	±	6.91	187.42	±	1.75	166.49	±	14.57	170.42	±	10.95
anthracene	23.82	±	2.40	23.57	±	0.24	31.14	±	2.98	31.82	±	3.45
2-methylanthracene	13.06	±	2.17	11.48	±	0.48	15.43	±	0.05	17.39	±	1.19
phen/anth-C1 A T	27.34	±	0.17	28.31	±	0.84	31.34	±	5.03	30.11	±	3.48
phen/anth-C1 B T	31.72	±	1.42	34.65	±	0.76	38.97	±	6.04	42.40	±	3.12
phen/anth-C1 C T	9.70	±	1.10	10.81	±	0.81	12.30	±	1.42	13.71	±	1.16
phen/anth-C1 D T	23.49	±	2.21	23.53	±	1.67	27.16	±	0.55	26.65	±	3.78
phen/anth-C1 E T	28.02	±	1.64	26.70	±	1.07	32.57	±	6.10	34.09	±	3.60
phen/anth-C2 A T	1.83	±	0.06	2.00	±	0.20	2.28	±	0.20	2.42	±	0.23
phen/anth-C2 B T	5.03	±	0.79	5.70	±	0.46	5.53	±	0.33	5.32	±	0.48
phen/anth-C2 C T	3.74	±	0.29	5.67	±	0.52	4.14	±	0.43	4.04	±	0.38
phen/anth-C2 D T	3.63	±	0.52	5.87	±	0.62	4.68	±	0.27	4.89	±	0.52
phen/anth-C2 E T	2.54	±	0.40	2.75	±	0.30	3.31	±	0.08	3.19	±	0.35
fluoranthene	165.46	±	6.49	169.29	±	4.93	134.08	±	8.22	139.03	±	4.15
pyrene	160.22	±	4.28	167.07	±	7.00	136.45	±	12.34	140.90	±	6.18
1-methylpyrene	14.00	±	2.46	14.15	±	0.44	14.35	±	2.31	14.69	±	1.04
flu/pyr-C1 A T	16.42	±	0.75	15.12	±	1.24	14.60	±	2.02	15.36	±	1.32
flu/pyr-C1 B+C T	27.97	±	1.28	29.92	±	1.13	25.09	±	4.50	23.93	±	2.93
flu/pyr-C1 D T	8.00	±	1.08	11.09	±	1.18	10.18	±	1.53	12.28	±	0.47
flu/pyr-C1 E T	13.40	±	1.78	11.52	±	0.89	13.48	±	2.38	12.58	±	1.22
flu/pyr-C1 F T	14.06	±	1.73	12.81	±	1.67	14.35	±	2.31	13.43	±	1.48
flu/pyr-C1 G T	10.99	±	1.31	11.48	±	1.45	14.37	±	0.88	14.02	±	1.54
benzo[e]pyrene	31.30	±	4.25	39.66	±	4.17	40.79	±	2.38	38.50	±	3.41
benz[a]anthracene	52.56	±	4.10	55.44	±	2.43	52.47	±	7.93	47.11	±	2.61
chrysene	53.23	±	5.36	52.89	±	2.90	55.38	±	4.86	51.15	±	4.39
benz[e]acephenanthrylene	4.57	±	0.49	5.90	±	0.56	5.17	±	0.27	5.12	±	0.27
benzo[k]fluoranthene	18.44	±	1.64	19.87	±	3.24	19.96	±	1.27	18.98	±	1.34
benzo[j]fluoranthene	9.59	±	1.01	9.60	±	0.73	9.56	±	1.18	9.84	±	0.92
benzo[a]fluoranthene	38.53	±	3.23	43.27	±	1.77	38.46	±	6.27	38.86	±	4.31
benzo[a]pyrene	31.47	±	3.08	34.77	±	1.54	37.74	±	2.36	40.70	±	1.90
indeno[1,2,3-cd]pyrene	20.40	±	3.56	24.70	±	4.27	26.19	±	1.83	26.45	±	2.50
benzo[ghi]perylene	17.72	±	1.33	16.99	±	1.71	16.38	±	2.57	16.90	±	2.00
Total PAHs	**1097**	**±**	**16**	**1134**	**±**	**13**	**1075**	**±**	**27**	**1089**	**±**	**18**
Oxy-PAHs												
benzo[b]naphtho[2,3-d]furan T	24.46	±	2.63	26.58	±	2.23	17.30	±	0.77	15.59	±	0.95
benzo[b]naphtho[2,1-d]furan T	12.25	±	0.66	13.98	±	1.22	8.51	±	1.20	7.40	±	0.47
9-fluorenone	158.47	±	8.34	68.00	±	5.79	77.58	±	7.05	74.52	±	3.53
xanthone	54.52	±	6.20	26.98	±	1.11	45.58	±	9.11	46.22	±	2.16
9,10-anthraquinone	46.69	±	4.46	31.09	±	1.73	46.83	±	3.78	53.93	±	1.80
benzo[b]fluoren-11-one T	17.63	±	0.65	37.64	±	2.63	17.62	±	1.44	17.81	±	1.47
benzo[a]fluoren-11-one T	8.78	±	0.86	19.89	±	3.42	7.90	±	0.75	6.79	±	0.56
benzo[c]fluoren-7-one T	18.95	±	2.71	33.93	±	3.05	16.91	±	1.70	17.67	±	1.57
benz[de]anthracen-7-one T	31.54	±	1.22	45.78	±	5.95	34.21	±	4.53	32.82	±	2.65
benz[a]anthracene-7,12-dione	7.47	±	0.48	13.42	±	0.97		ND			ND	
Total Oxy-PAHs	**381**	**±**	**12**	**317**	**±**	**10**	**272**	**±**	**13**	**273**	**±**	**6**

Table 7. cont.

Compound	PFE				Soxhlet			
	DCM (µg g^{-1})[a] mean ± st. dev (*n*=4)		MeOH (µg g^{-1})[a] mean ± st. dev (*n*=4)		DCM (µg g^{-1})[a] mean ± st. dev (*n*=4)		MeOH (µg g^{-1})[a] mean ± st. dev (*n*=4)	
Hydroxy- & Carboxy-PAHs[d]								
2-hydroxybiphenyl	13.35 ± 1.03		14.17 ± 0.36		12.54 ± 1.28		13.38 ± 1.45	
hydroxybiphenyl T	28.27 ± 1.12		29.43 ± 1.70		29.58 ± 3.43		30.80 ± 4.06	
4-hydroxybiphenyl	25.17 ± 0.51		27.63 ± 1.67		25.77 ± 2.87		27.98 ± 4.26	
7-hydroxycadalene	108.14 ± 2.03		101.19 ± 5.76		98.68 ± 10.36		100.77 ± 6.34	
9-phenanthrol	6.99 ± 0.48		7.53 ± 0.71		8.21 ± 0.82		8.93 ± 1.16	
3-phenanthrol T	47.91 ± 0.71		64.50 ± 7.70		45.39 ± 3.22		47.04 ± 3.98	
2-hydroxy-9-fluorenone	28.70 ± 1.39		28.55 ± 1.15		23.56 ± 2.83		23.91 ± 3.17	
4-phenanthrenemethanol	1.87 ± 0.28		1.98 ± 0.17		1.47 ± 0.18		1.75 ± 0.14	
hydroxypyrene A T	15.82 ± 1.59		17.25 ± 1.45		18.20 ± 0.67		20.15 ± 2.33	
hydroxypyrene B T	24.74 ± 1.43		30.16 ± 2.53		24.83 ± 1.15		32.82 ± 1.02	
hydroxypyrene C T	14.47 ± 1.47		19.04 ± 1.97		17.58 ± 1.46		20.69 ± 2.31	
1-hydroxypyrene-TMS	24.86 ± 1.63		33.56 ± 14.75		26.97 ± 0.55		27.60 ± 1.22	
hydroxypyrene-TMS D T	10.46 ± 1.71		14.81 ± 0.95		13.46 ± 0.85		14.74 ± 0.25	
1,8-dihydroxyanthraquinone	1.17 ± 0.52		0.00 ± 0.00		1.53 ± 0.29		0.27 ± 0.47	
4-phenenthrene-COOH	10.40 ± 1.75		11.27 ± 0.68		12.64 ± 0.59		14.27 ± 1.79	
9-anthracene-COOH	1.94 ± 0.14		3.33 ± 0.42		4.67 ± 0.52		5.59 ± 0.29	
9-phenanthrene-COOH	6.34 ± 0.72		7.93 ± 0.85		14.33 ± 0.59		16.64 ± 0.95	
Total Hydroxy- PAHs	**371**	**± 5**	**412**	**± 18**	**379**	**± 12**	**407**	**± 11**

a Recoveries are corrected by the response of recovery standards.
b "NA" denotes that standards for that particular compound were not available during the time of the study.
c "ND" denotes that response was either zero or below the limit of quantitation (determined from lowest three points of calibration curve)
d All hydroxy- and carboxy-PAHs are shown as trimethylsilyl derivatives after derivatization with BSTFA.
e 2-CHM is an acronym for 2-chloro-2-hydroxy-4-methylbenzophenone

4.2.4. Comparing PFE to Soxhlet for Diesel Exhaust PM

To investigate the efficiency of PFE for the simultaneous extraction of PAHs and their wide range of derivatives from a relatively non-polar matrix, the PFE method was applied to diesel exhaust PM (SRM 2975). Additionally the use of SRM allowed for the evaluation of the optimized PFE method's performance by comparing the mass fractions extracted to those reported in previous studies.

Similar to WS PM, the mass fractions of PAHs and oxy-PAHs extracted were similar or slightly higher for PFE than with Soxhlet. Using DCM with PFE provided increased amounts extracted for both PAHs and oxy-PAHs than when using MeOH. While MeOH provided increased mass fractions for the higher molecular weight (4–6 ring) PAHs with WS PM, extraction with DCM yielded greater amounts with SRM 2975. For 1-nitropyrene (the only nitro-PAH observed in this study when using GC-MS in EI mode), mass fractions with DCM were significantly higher than with MeOH, a trend observed for both extraction methods. The only hydroxy-PAH species observed (1-hydroxypyrene) also followed this trend. By contrast, two carboxy-PAH species were extracted from SRM 2975, which were observed in higher amounts when using MeOH as the extraction solvent, for either method.

Mass fractions obtained for PAHs in this study were compared to those reported for SRM in previous studies (also using PFE with a variety of different solvent systems) (see Table 8). For phenantherene and fluoranthene (the most abundant PAHs in SRM 2975), similar mass fractions extracted were observed in this study compared to previous work (95–110%). For the majority of the other higher molecular weight PAHs (4-6 rings) our optimized method provided slightly increased mass fractions. The most significant increases were observed for benzo[*a*]fluoranthene, benzo[*a*]pyrene and

dibenz[*a*,*h*]anthracene. For nitro-PAHs only 1-nitropyrene was observed with GC-MS analysis in EI mode. While the other nitro-PAHs found in SRM 2975 can be evaluated with the use of the more sensitivive negative-ion chemical ionization (NICI), the use of 1-nitropyrene was enough to determine the precision of the PFE method. In comparison to the amount of 1-nitropyrene extracted from SRM 2975 by Bamford et al. (using PFE with DCM) our optimized method with DCM yielded similar results (34.60±1.14 compared to 39.64±1.70 μg g^{-1}).

Table 8. Mass fractions of PAHs and polar derivatives obtained by extraction of SRM 2957 (diesel exhaust PM).

Compound	This Study												Ref 59			Ref 57		
	PFE						Soxhlet						PFE[b]			PFE[b]		
	DCM (μg g^{-1})[a] mean ± st. dev (n=4)			MeOH (μg g^{-1})[a] mean ± st. dev (n=4)			DCM (μg g^{-1})[a] mean ± st. dev (n=4)			MeOH (μg g^{-1})[a] mean ± st. dev (n=4)			DCM (μg g^{-1})			Toluene/MeOH (μg g^{-1})		
PAHs																		
phenanthrene	18.39	±	0.44	16.87	±	1.11	18.89	±	0.76	16.56	±	1.65	18.6	±	0.9	17.00	±	2.80
fluoranthene	27.59	±	0.73	22.74	±	1.60	25.55	±	1.58	23.50	±	0.87	28.9	±	1.6	26.60	±	5.10
pyrene	1.45	±	0.14	1.30	±	0.14	1.24	±	0.17	0.98	±	0.11	1.03	±	0.05	0.90	±	0.24
benz[a]anthracene	0.63	±	0.00	0.57	±	0.09	0.72	±	0.10	0.36	±	0.03	0.34	±	0.03	0.32	±	0.07
chrysene	4.46	±	0.18	4.18	±	0.22	3.70	±	0.46	3.12	±	0.21		NR		4.56	±	0.16
benzo[k]fluoranthene	1.00	±	0.10	0.78	±	0.08	0.00	±	0.00	0.59	±	0.04	0.66	±	0.08	0.68	±	0.08
benzo[e]pyrene	1.46	±	0.07	1.14	±	0.10	1.40	±	0.08	1.15	±	0.09	1.09	±	0.07	1.11	±	0.10
benzo[a]fluoranthene	2.33	±	0.14	1.88	±	0.31	1.95	±	0.21	1.37	±	0.20		NR		0.06	±	0.02
benzo[a]pyrene	1.46	±	0.05	1.22	±	0.16	1.03	±	0.05	1.06	±	0.07		<0.5		0.05	±	0.01
indeno[1,2,3-cd]pyrene	1.41	±	0.03	1.00	±	0.08	0.87	±	0.09	0.89	±	0.09	0.81	±	0.03	1.40	±	0.20
dibenzo[a,h]anthracene	1.18	±	0.00	0.85	±	0.05	0.76	±	0.04	0.77	±	0.06	1.71	±	0.12[e]	0.37	±	0.07
benzo[ghi]perylene	1.00	±	0.25	0.71	±	0.09	0.84	±	0.12	0.65	±	0.06	0.48	±	0.02	0.50	±	0.04
Total of Selected PAHs	**62**	**±**	**1**	**53**	**±**	**2**	**57**	**±**	**2**	**51**	**±**	**2**	**54**	**±**	**2**	**54**	**±**	**6**
Nitro-PAHs																		
1-nitropyrene	34.60	±	1.14	26.19	±	1.58	33.44	±	1.39	21.14	±	1.28				34.80	±	4.70
Oxy-PAHs																		
9-fluorenone	6.45	±	0.25	4.39	±	0.24	4.33	±	0.35	4.26	±	0.26			NR[c]			
9,10-anthraquinone	14.59	±	1.35	8.00	±	0.87	8.62	±	0.74	9.21	±	0.72			NR			
benzo[b]fluoren-11-one T	6.94	±	0.69	4.57	±	0.21	4.49	±	0.22	4.62	±	0.22			NR			
benzo[a]fluoren-11-one T	5.03	±	0.69	3.83	±	0.68	5.54	±	0.38	3.78	±	0.50			NR			
benzo[c]fluoren-7-one T	6.56	±	0.54	5.15	±	0.22	5.47	±	0.35	4.94	±	0.61			NR			
benz[de]anthracen-7-one T	7.20	±	0.75	7.11	±	0.56	7.40	±	0.21	7.13	±	0.42			NR			
benz[a]anthracene-7,12-dione	5.09	±	0.27	4.20	±	0.55	5.13	±	0.20	4.41	±	0.30			NR			
Total Oxy-PAHs	**52**	**±**	**2**	**37**	**±**	**1**	**41**	**±**	**1**	**38**	**±**	**1**						
Hydroxy- & Carboxy-PAHs[d]																		
9-phenanthrene-COOH-TMS	24.30	±	2.30	31.06	±	2.59	31.69	±	2.28	36.50	±	1.80			NR			
n-phen/anth-COOH-TMS A	25.04	±	1.07	32.45	±	1.70	32.51	±	2.40	41.00	±	1.94			NR			
1-hydroxypyrene-TMS	4.49	±	0.44	3.71	±	0.14	4.34	±	0.40	3.63	±	0.42			NR			
Total Hydroxy- and Carboxy-PAHs	**54**	**±**	**3**	**67**	**±**	**3**	**69**	**±**	**3**	**81**	**±**	**3**						

a Mass fractions are corrected by the response of recovery standards.
b All the reference studies shown performed PFE at 100 °C and 2000 psi.
c "NR" denotes that mass fraction were not reported in that particular study (for PAHs) or have not been previously reported in any studies (for oxy-, hydroxy- and carboxy-PAHs).
d All hydroxy- and carboxy-PAHs are shown as trimethylsilyl derivatives after derivatization with BSTFA.

4.3. Conclusions

PFE was evaluated and determined to be a suitable alternative extraction method to the commonly deployed Soxhlet extraction for the simultaneous extraction of PAHs, oxy-PAHs, hydroxy-PAHs and carboxy-PAHs from both a polar PM matrix (WS PM) and a relatively non-polar matrix (diesel exhaust PM; SRM 2975). PFE extraction with DCM resulted in similar mass fractions extracted in 15 min using only 9 mL of DCM, in contrast to a more solvent/time intensive Soxhlet DCM extraction (1080 min, 90 mL). Some oxy-PAH species exhibited greater mass fractions with PFE, most likely due to the increased temperatures employed in PFE overcoming the analyte–matrix interactions within the WS PM. By contrast, highly polar carboxy-PAHs (minor components) as well as highly polar non-aromatic species had higher extraction yields with Soxhlet using DCM or MeOH compared to PFE with DCM. Using PFE with MeOH provided slightly increase the amounts extracted for these compounds. Nevertheless, the overall extraction yields of PAHs and their derivatives obtained by both methods were similar (1849±21, 1727±33 μg/g for PFE and Soxhlet with DCM, respectively). The extraction of SRM 2975 with both PFE and Soxhlet were in agreement with previous studies. For PAHs, oxy-PAHs and nitro-PAHs DCM provided higher mass fractions while MeOH yielded greater amounts for carboxy-PAHs. Finally, it is critical to note that most environmental studies focus only on PAHs. Our data on WS PM demonstrated that PAH derivatives comprised ca. 40% of all species quantified, supporting the significance of these compounds.

CHAPTER 5

5. DETERMINATION OF NITRATED AND OXYGENATED DERIVATIVES OF POLYCYCLIC AROMATIC HYDROCARBONS USING ATMOSPHERIC PRESSURE CHEMICAL IONIZATION WITH HIGH RESOLUTION MASS SPECTROMETRY (APCI-HRMS)

5.1. Experimental

5.1.1. Reagents

The PAH derivatives including 9-nitroanthracene, 1-nitropyrene, 1,6-dinitropyrene, anthrone, 9,10-anthracenedione, 9,10-phenanthrenedione, 1,4-phenanthrenedione, pyrene-4,5-dione, 9-phenanthrenecarboxaldehyde, and 4-carboxy-5-phenanthrenecarboxaldehyde were obtained from Sigma Aldrich (Atlanta, GA, USA). 9-nitrophenanthrene, 3-nitrophenanthrene and 9,10-dinitroanthracene were obtained from Accustandard Inc. (New Haven, CT, USA). LC-MS Optima grade methanol (MeOH) and LC-MS Optima grade acetonitrile were obtained from Fisher Scientific (Chicago, IL, USA). Formic acid (LC-MS grade) was obtained from Fluka (Atlanta, GA, USA). MilliQ water (Millipore) was used during HPLC experiments.

5.1.2. HPLC-APCI-MS Analysis

HPLC-MS analyses were carried out with an Agilent 1100 HPLC system coupled to a high resolution Agilent 1969 Time-of-flight MS (ToFMS) equipped with an APCI source (Agilent Technologies, Santa Clara, CA, USA).

All HPLC separations were performed using a Restek C_{18} 200 mm × 3.2 mm reverse phase HPLC column with 5 µm particle size (Restek, Bellafonte, PA, USA). A binary solvent system consisting of A: water, B: methanol was used.

A gradient program at a flow rate of 0.2 mL min^{-1} started with 20% B for 5 min, followed with a linear increase to 90% B at 20 min, and hold at 90% until 27 min, and then was linearly decreased to 20% at 30 min and held at 20% B for 5 min to allow for equilibration. The column oven temperature was set to 30 °C and injection volume was 50 µL.

APCI was performed in both positive and negative modes with each sample containing 5 mM formic acid. Drying gas (N_2) was set to 300 °C at a flow of 3 L min^{-1}. For all experiments the capillary voltage was set to 4500 V. To minimize the contribution of post-source fragmentation, the fragmentor voltage was set to 120 V for all experiments. All HPLC-APCI-ToF-MS analyses were performed with the corona discharge current set at 10 µA. For experiments evaluating the contribution of the corona current to gas-phase ion fragmentation, the corona discharge current was varied within the range of 4–25 µA.

5.1.3. Reaction Experiments

The flow reactor used for the ozonation of pyrene consisted of three main parts: a gas injection/dilution system, mixing chamber, and reaction chamber (Appendix VI). The gas injection/dilution system delivered breathing quality air to a mixing chamber composed entirely of Teflon (31.5 cm length × 9 cm I.D.) through ¼" stainless steel tubing. Two-way stainless steel valves were used for selecting the gases used in each experiment. All gas flows through the reactor system were regulated with mass flow controllers (Alicat Scientific, Tucson, AZ, USA) to achieve the desired dilution of gases. After passing the mixing chamber, the gas flow was split into three parts using stainless steel tees, leading to the reaction chamber, an O_3 gas analyzer and an exhaust vent. During ozonation experiments, ozone levels at the outlet of the mixing chamber were

measured using a photometric O_3 gas analyzer (Model 400E, Teledyne, Thousand Oaks, CA, USA). The gas mixtures from the mixing chamber were supplied to the Teflon reaction chamber (43 cm in length x 9 cm I.D.) through an inlet located on top of the chamber. A quartz tissue filter (90 mm I.D., PALL Corporation, Port Washington, NY) was spiked with pyrene solution and placed onto a Teflon-coated aluminum mesh at the bottom of the reaction chamber. The outlet of the reactor chamber was located after the filter support. The total flow through the reaction chamber was controlled using an oil-less pump with a mass flow controller positioned between the reaction chamber and the pump. The flow drawn by the pump was always kept lower than the gas flow exiting the mixing chamber to ensure that ambient air was not drawn through the flow splitter (installed to prevent over-pressurization of the reaction chamber).

An allotted amount of a PAH stock solution (40 µL) at 100 µg mL^{-1} per compound was spiked over the quartz tissue filter and allowed to evaporate at room temperature for 60 s (resulting in a final amount of 4 µg on the filter). All quartz filters were pre-baked at 500 °C for 12 h, then placed in the flow reactor and exposed to O_3 at 1.25 ppm for 90 min.

Upon the completion of each reaction experiment, the filter was extracted using sonication with 10 mL of DCM for 30 min. After sonication, the solvent was filtered over deactivated glass wool. The vial and filter were washed twice with 10 mL of DCM each time. Ultimately all DCM solvent fractions obtained were combined and evaporated under a gentle stream of nitrogen to ~0.5 mL. The samples were then submitted to HPLC-APCI-ToFMS analysis. Identification was based on a match of retention times of

the overlayed extracted ion chromatogram (EIC) peaks, on the relative intensities as well as high resolution data of MS peaks.

5.2. Results and Discussion

5.2.1. Carboxy- & Hydroxy-PAHs

The four carboxy-PAH species investigated in this study are listed in Table 9, representing constitutional isomers in both the ring configurations and the location of the carboxy group as well as mixed functional groups.

As previously reported, the APCI in negative mode was more sensitive and resulted in more uniform ionization patterns (Table 9; spectra shown in Appendices VII & VIII).[66] The fragmentation proposed in Scheme 1 corresponds to neutral losses previously observed.[66] The tested species exhibited the deprotonated anion $[M–H]^-$ as the base peak as well as loss of $–CO_2$ and –CO from the deprotonated anion. In contrast to the previous work,[66] no ion corresponding to two subsequent losses of –CO (giving the $[M–H–CO–CO]^-$ ion) was observed. For 4-carboxy-5-phenanthrenecarboxaldehyde, the loss of –CO from the deprotonated anion was not observed, but rather the successive losses of –CO from the aldehyde group and the loss of $–CO_2$ from the carboxyl group following deprotonation.

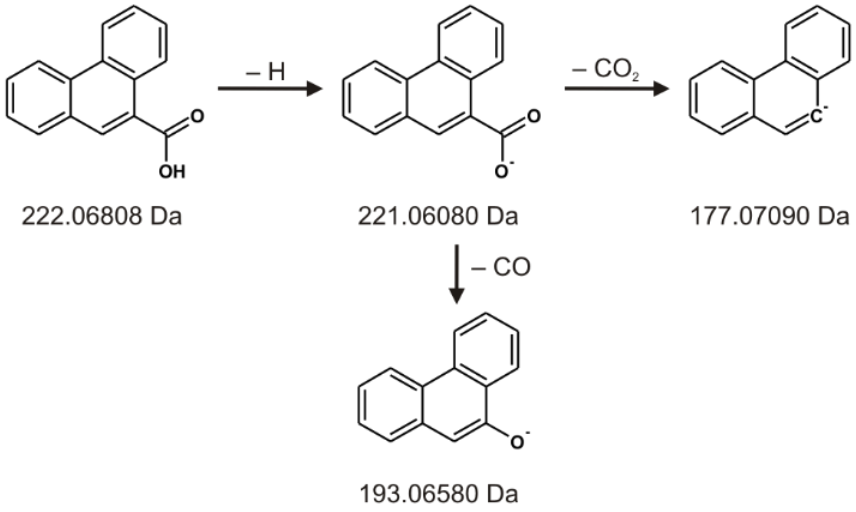

Scheme 1

Table 9. Pseudomolecular ions and fragment observed for hydroxy- and carboxy-PAHs using APCI in negative mode.

Compound	tR (min)	Measured Mass[a] (*m/z* Da)			Rel. Abund. (%)	Fragment	Formula[b]	Formula Mass (*m/z* Da)	Mass Error[c] (ppm)		
4-carboxy-phenanthrene-carboxaldehyde	18.55	**177.07074**	±	0.00014	100	$[M–H–C_2O_3]^-$	$C_{14}H_9$	177.07097	**-1.3**	±	0.8
		249.05509	±	0.00023	90	$[M–H]^-$	$C_{16}H_9O_3$	249.05572	**-2.5**	±	0.9
		205.06497	±	0.00047	40	$[M–H–CO_2]^-$	$C_{15}H_9O$	205.06589	**-5**	±	2
1-hydroxypyrene	19.21	**217.06663**	±	0.00098	100	$[M–H]^-$	$C_{16}H_9O$	217.06589	**3**	±	4
		232.05210	±	0.00103	20	$[M–2H+O]^-$	$C_{16}H_8O_2$	232.05188	**0.9**	±	4.4
9-phenanthrene-carboxylic acid	18.34	**221.06048**	±	0.00054	100	$[M–H]^-$	$C_{15}H_9O_2$	221.05971	**3**	±	2
		177.07080	±	0.00083	25	$[M–H–CO_2]^-$	$C_{14}H_9$	177.06988	**5**	±	5
		193.06566	±	0.00048	5	$[M–H–CO]^-$	$C_{14}H_9O$	193.06479	**5**	±	2
		208.05256	±	0.00044	4	$[M–CH_2]^-$	$C_{14}H_8O_2$	208.05188	**3**	±	2
4-phenanthrene-carboxylic acid	18.56	**221.06036**	±	0.00049	100	$[M–H]^-$	$C_{15}H_9O_2$	221.05971	**3**	±	2
		177.07064	±	0.00042	40	$[M–H–CO_2]^-$	$C_{14}H_9$	177.06988	**4**	±	2
		235.03951	±	0.00045	5	$[M–H+O–2H]^-$	$C_{15}H_7O_3$	235.03897	**2**	±	2
		193.06484	±	0.00088	4	$[M–H–CO]^-$	$C_{14}H_9O$	193.06479	**0.3**	±	4.6
		208.05396	±	0.00093	2	$[M–CH_2]^-$	$C_{14}H_8O_2$	208.05188	**10**	±	4
9-anthracene-carboxylic acid	18.94	**221.05990**	±	0.00042	100	$[M–H]^-$	$C_{15}H_9O_2$	221.05971	**0.9**	±	1.9
		177.07022	±	0.00009	40	$[M–H–CO_2]^-$	$C_{14}H_9$	177.06988	**2.0**	±	0.5
		208.05184	±	0.00100	10	$[M–CH_2]^-$	$C_{14}H_8O_2$	208.05188	**-0.2**	±	4.8
		193.06603	±	0.00012	5	$[M–H–CO]^-$	$C_{14}H_9O$	193.06479	**6.4**	±	0.6

[a] Measure masses are averages of the masses observed at three different points along the chromatographic peak.
[b] Empirical formulas for the observed mass were calculated with elemental ranges of C:8–18, H:6–16, O:0–4.
[c] Calculated SD from the observed masses are in ppm error to show its influence on empirical formula estimations.

While the analysis of carboxy-PAHs with APCI in positive mode resulted in lower response, the compounds studied still exhibited common ionization trends but with significantly varied ion abundances (Table 10). The differences in abundance among the isomeric compounds may be essential for accurate identification. The protonated ion $[M+H]^+$ for 4-phenanthrenecarboxylic acid and 9-anthracenecarboxylic acid featured 45% and 20% relative response of the base peak, respectively, and was not observed for 9-anthracenecarboxylic acid. For 4-carboxy-5-phenanthrenecarboxaldehyde, a higher relative response of the $[M+H]^+$ ion was observed, most likely due to protonation of the aldehyde group (see Scheme 2). The protonation followed by the loss of $–H_2O$ was observed for all carboxy-PAH species, also in varied relative intensities. For 9-phenanthrenecarboxylic acid, this was the least prevalent ion (10% relative intensity to the base peak) while for the other three species the ion was much more abundant (60–80%). Three species, 9-phenanthrenecarboxylic acid, 9-anthracenecarboxylic acid and 4-carboxy-5-phenanthrenecarboxaldehyde, exhibited a $[M+H+CH_2]^+$ ion in differing abundances of 25%, 30, and 85%, respectively. This ion is possibly a result of gas-phase esterification by methanol. For these compounds, a common ion of 205 was observed corresponding to the carbonyl phenanthrene ion ($C_{15}H_{19}O^+$).

Table 10. Pseudomolecular ions and fragments observed for hydroxy- and carboxy-PAHs using APCI in positive mode.

Compound	tR (min)	Measured Mass (*m/z* Da)			Rel. Abund. (%)	Fragment	Formula	Formula Mass (*m/z* Da)	Mass Errorb (ppm)		
4-carboxy-phenanthrene-carboxaldehyde	18.55	**235.07633**	±	0.00075	0	$[M+H-O]^+$	$C_{16}H_{11}O_2$	235.07536	**4**	±	3
		205.06540	±	0.00084	95	$[M+H-CH_2O_2]^+$	$C_{15}H_9O$	205.06479	**3**	±	4
		251.07032	±	0.00087	92	$[M+H]^+$	$C_{16}H_{11}O_3$	251.07027	**0.2**	±	3.4
		265.08714	±	0.00123	85	$[M+H+CH_2]^+$	$C_{17}H_{13}O_3$	265.08590	**5**	±	5
		191.08524	±	0.00065	75	$[M+H-CO_3]^+$	$C_{15}H_{11}$	191.08550	**-1**	±	3
		233.05973	±	0.00091	65	$[M+H-H_2O]^+$	$C_{16}H_9O_2$	233.05971	**0.1**	±	3.9
		177.06931	±	0.00067	50	$[M+H-C_2H_2O_3]^+$	$C_{14}H_9$	177.06988	**-3**	±	4
1-hydroxypyrene	19.21	**219.08350**	±	0.00158	100	$[M+H]^+$	$C_{16}H_{11}O$	219.08044	**14**	±	7
		218.07520	±	0.00122	85	$[M-e^-]^+$	$C_{16}H_{10}O$	218.07262	**12**	±	6
		233.06141	±	0.00055	75	$[M+O-H]^+$	$C_{16}H_9O_2$	233.05971	**7**	±	2
		202.07679	±	0.00046	2	$[M-e^-O]+$	$C_{16}H_{10}$	202.07770	**-5**	±	2
9-phenanthrene-carboxylic acid	18.34	**209.05907**	±	0.00182	100	$[M+H-CH_2]^+$	$C_{14}H_9O_2$	209.05971	**-3**	±	9
		237.08894	±	0.00057	25	$[M+CH_3]^+$	$C_{16}H_{13}O_2$	237.09101	**-9**	±	2
		223.07783	±	0.00054	20	$[M+H]^+$	$C_{15}H_{11}O_2$	223.07536	**11**	±	2
		205.06627	±	0.00086	10	$[M+H-H_2O]^+$	$C_{15}H_9O$	205.06479	**7**	±	4
4-phenanthrene-carboxylic acid	18.56	**221.05919**	±	0.00011	100	$[M-H-2e^-]^+$	$C_{15}H_9O_2$	221.05971	**-2.3**	±	0.5
		205.06477	±	0.00005	80	$[M+H-H_2O]^+$	$C_{15}H_9O$	205.06479	**-0.1**	±	0.3
		237.09060	±	0.00060	50	$[M+CH_3]^+$	$C_{16}H_{13}O_2$	237.09101	**-2**	±	2
		223.07500	±	0.00010	45	$[M+H]^+$	$C_{15}H_{11}O_2$	223.07536	**-1.6**	±	0.5
9-anthracene-carboxylic acid	18.94	**209.09353**	±	0.00091	100	$[M+3H-O]^+$	$C_{15}H_{13}O$	209.09609	**-12**	±	4
		195.07990	±	0.00047	85	$[M+H-CO]^+$	$C_{14}H_{11}O$	195.08044	**-2**	±	2
		205.06547	±	0.00059	60	$[M+H-H_2O]^+$	$C_{15}H_9O$	205.06479	**3**	±	2
		237.09103	±	0.00093	30	$[M+H+CH_3]^+$	$C_{16}H_{13}O_2$	237.09101	**0.1**	±	3.9

[a] Measured masses are averages of the masses observed at three different points along the chromatographic peak.
[b] Empirical formula for the observed mass were calculated with elemental ranges of C:8–18, H:6–16, O:0–4.
[c] Calculated SD from the observed masses are in ppm error to show its influence on empirical formula estimations.

In this study only one hydroxy-PAH, 1-hydroxypyrene, was considered. This compound is representative of hydroxy-PAHs in atmospheric samples, typically being the most abundant species.[65] In positive mode, ionization via protonation ($[M+H]^+$) as well as electron abstraction ($[M–e^–]^+$) was observed in 100% and 85% relative abundance, respectively. Additionally, an oxygen adduct ($[M–H+O]^+$) was observed in 75% relative abundance. In negative mode, 1-hydroxypyrene was mainly ionized via deprotonation, yielding the $[M–H]^–$ ion. As seen in positive mode, an oxygen adduct ($[M–2H+O]^–$) was again observed.

5.2.2. Oxy-PAHs

High resolution MS data of several major fragmentation pathways for 7 oxy-PAHs (Tables 11 & 12) is, to our knowledge, reported for the first time in this work.

In positive mode, several common trends were observed among the oxy-PAHs investigated. The major ionization pathway for most of the ketone and diketone compounds studied was protonation (spectra shown in Appendix IX), mirroring observations made in previous studies.[32,67–69] The most prevalent fragmentation trend was the loss of –CO from the protonated molecular ion, which showed a high degree of stereoselectivity between the studied compounds. Successive losses of –CO giving the $[M+H–C_2O_2]^+$ ion were observed for only two compounds, 9,10-phenanthrenedione and pyrene-4,5-dione (Appendix IX). This seems to be a highly stereoselective process since neither of the other two 3-ring diketone PAH species exhibit this fragment ion. This fragmentation is postulated to occur through a ring-opening mechanism (Schemes 3 & 4).

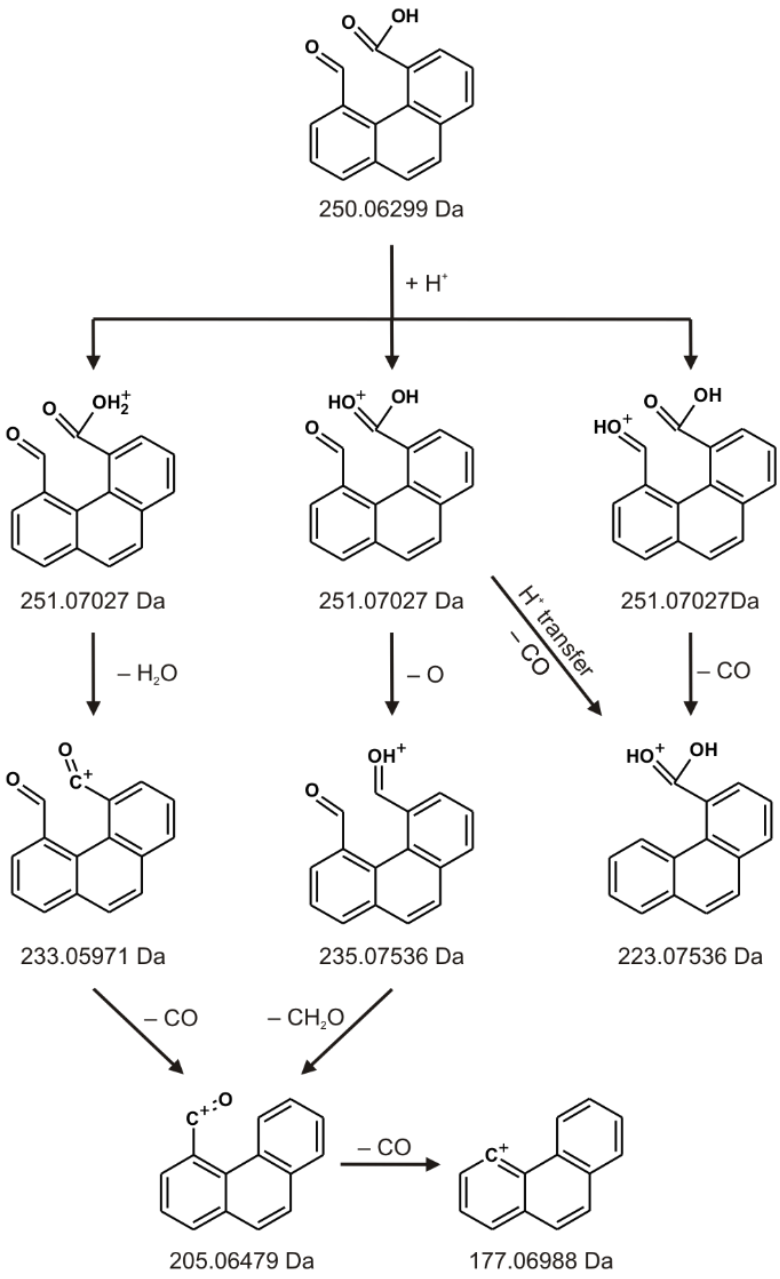

Scheme 2

For 9,10-phenanthrenedione, the $[M+H–C_2O_2]^+$ ion is similar in structure to a deprotonated biphenyl cation (Scheme 3). In contrast, for pyrene-4,5-dione, this process could result in a structure that resembles a deprotonated phenanthrene cation (Scheme 4). The ring-opening mechanism would explain the lack of formation of either the $[M+H–CO]^+$ or $[M+H–C_2O_2]^+$ ions for 9,10-anthracenedione, whose linear aromatic structure

creates a relatively high energy barrier for such a process to occur. A similar ion was not observed with 1,4-phenanthrenedione either, suggesting that the close proximity of the carbonyl groups is a requirement for the ring-opening mechanism to occur.

Dimerization was observed only for two studied species, anthrone and 9,10-anthracenedione. Anthrone exhibited a small degree of dimerization (Appendix IX), most likely into a structure similar to a protonated bianthrone ion. The anthrone dimer was observed with three ions of similar abundances: *m/z* 385, 386, and 387 (Appendix IX). A similar dimer was observed for 9,10-anthracenedione, suggesting loss of CO prior to the dimerization. For anthrone, a fragment of *m/z* 165 was attributed to $C_{13}H_9$., formed possibly by the loss of $–CH_2O$ from the $[M+H]^+$ ion; however, the exact mechanism for this process is unclear.

In positive mode, aldehyde derivatives exhibited similar ionization pathways as the ketone and diketone species. The major ionization pathway was via protonation (Appendix IX). The loss of –CO from the protonated ion was observed with both aldehyde species, showing significant differences in stereoselectivity (Table 11). In contrast to the –CO loss mechanism proposed for the diketone species, here it seems to proceed through a different pathway (Scheme 5). Rather than the loss of the protonated aldehyde group (as CH_2O), leaving a cationic phenanthrene structure at *m/z* 177, the ion at *m/z* 179 was observed, which would result from the loss of –CO. This most likely occurs through a two-step mechanism, with the two hydrogens on the protonated aldehyde group undergoing hydrogen rearrangement and transfer to the aromatic ring followed by the cleavage of the C–C bond and loss of –CO. The loss of –O was also observed for both species, not showing any degree of stereoselectivity (Appendix IX).

Table 11. Pseudomolecular ions and fragments observed for oxy-PAHs with APCI in positive mode.

Compound	Measured Mass[a] (Da)			Rel. Ab. (%)	Fragment[b]	Formula[c]	Formula Mass (Da)	Mass Error (ppm)[d]		
anthrone	**195.07934**	±	0.00043	100	$[M+H]^+$	$C_{14}H_{11}O$	195.08040	**-5**	±	2
	165.06976	±	0.00070	10	$[M+H–CH_2O]^+$	$C_{13}H_9$	165.06990	**-0.8**	±	4.3
	385.12075	±	0.00125	8	$[M+M–3H]^+$	$C_{28}H_{17}O_2$	385.12231	**-4**	±	3
	223.07483	±	0.00047	4	$[M+H+CO]^+$	$C_{15}H_{11}O_2$	223.07530	**-2**	±	2
9,10-anthracene-dione	**209.06013**	±	0.00040	100	$[M+H]^+$	$C_{14}H_9O_2$	209.05971	**2**	±	2
	193.06482	±	0.00033	30	$[M+H–O]^+$	$C_{14}H_9O$	193.06479	**0.1**	±	1.7
	385.12241	±	0.00151	10	$[M+H+M–O_2]^+$	$C_{28}H_{17}O_2$	385.12230	**0.3**	±	3.9
9,10-phenanthrene-dione	**181.06486**	±	0.00021	100	$[M+H–CO]^+$	$C_{13}H_9O$	181.06479	**0.4**	±	1.1
	209.06165	±	0.00033	90	$[M+H]^+$	$C_{14}H_9O_2$	209.05971	**9**	±	2
	153.06918	±	0.00009	60	$[M+H–C_2O_2]^+$	$C_{12}H_9$	153.06988	**-4.6**	±	0.6
	226.08584	±	0.00011	50	$[M+NH_4]^+$	$C_{14}H_{12}NO_2$	226.08620	**-1.6**	±	0.5
	223.07472	±	0.00030	50	$[M+CH_3]^+$	$C_{15}H_{11}O_2$	223.07530	**-3**	±	1
1,4-phenanthrene-dione	**209.05992**	±	0.00043	100	$[M+H]^+$	$C_{14}H_9O_2$	209.05971	**1**	±	2
	239.07032	±	0.00018	50	$[M+H+CH_2O]^+$	$C_{15}H_{11}O_3$	239.07020	**0.5**	±	0.7
	181.06548	±	0.00087	15	$[M+H–CO]^+$	$C_{13}H_9O$	181.06479	**4**	±	5
pyrene-4,5-dione	**233.05827**	±	0.00029	100	$[M+H]^+$	$C_{16}H_9O_2$	233.05970	**-6**	±	1
	205.06545	±	0.00056	85	$[M+H–CO]^+$	$C_{15}H_9O$	205.06470	**4**	±	3
	177.06969	±	0.00025	70	$[M+H–C_2O_2]^+$	$C_{14}H_9$	177.06980	**-0.6**	±	2.5
	250.08569	±	0.00036	60	$[M+NH_4]^+$	$C_{16}H_{12}NO_2$	250.08620	**-2**	±	1
phenanthrene-9-carboxaldehyde	**207.07998**	±	0.00017	100	$[M+H]^+$	$C_{15}H_{11}O$	207.08040	**-2.0**	±	0.8
	221.09549	±	0.00019	90	$[M+CH_3]^+$	$C_{16}H_{13}O$	221.09600	**-2.3**	±	0.9
	191.08501	±	0.00036	60	$[M+H–O]^+$	$C_{15}H_{11}$	191.08550	**-3**	±	2
	179.08487	±	0.00024	40	$[M+H–CO]^+$	$C_{14}H_{11}$	179.08553	**-4**	±	1
	233.06034	±	0.00051	10	$[M+CO–H]^+$	$C_{16}H_9O_2$	233.05970	**3**	±	2
	165.06739	±	0.00007	5		$C_{11}H_{10}Na$	165.06747	**-0.5**	±	0.4
anthracene-9-carboxaldehyde	**207.07961**	±	0.00042	100	$[M+H]^+$	$C_{15}H_{11}O$	207.08040	**-4**	±	2
	179.08665	±	0.00064	50	$[M+H–CO]^+$	$C_{14}H_{11}$	179.08553	**6**	±	4
	178.07803	±	0.00036	20	$[M+H–CHO]^+$	$C_{14}H_{10}$	178.07770	**2**	±	2
	191.08519	±	0.00022	8	$[M+H–O]^+$	$C_{15}H_{11}$	191.08550	**-2**	±	1

[a] Measure masses are reported as averages of the masses observed at three different points along the peak.
[b] Fragments shown to depict changes in the empirical formula and don't necessarily represent the fragmentation pathway.
[c] Possible emperical formula matches for the observed mass were calculated with elemental ranges of C:8–18, H:6–16, O:0–4, and Na:0–1 for monomers and C:16–32, H:12–32, O:0–4, and Na:0–1 for suspected dimers.
[d] Calculated SD values from the observed masses are in ppm error to show its influence on emperical formula estimations.

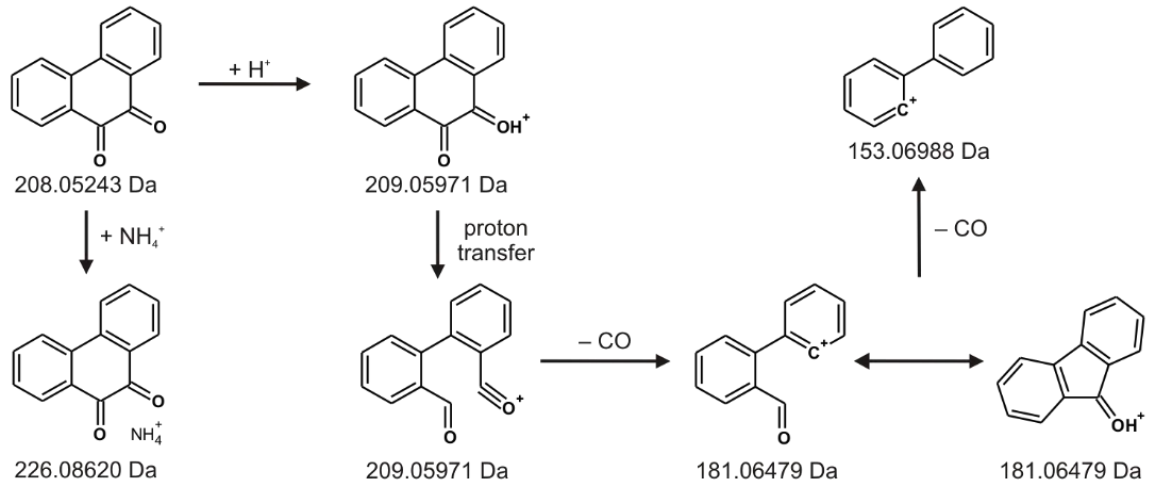

Scheme 3

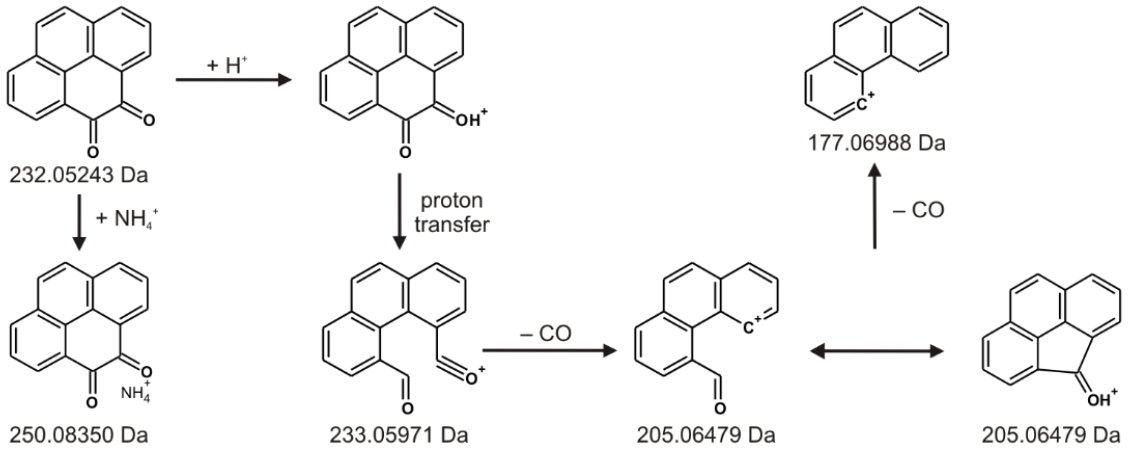

Scheme 4

For 9-phenanthrenecarboxaldehyde, an abundant ion of $[M+15]^+$, which was not observed for any other oxy-PAH besides 9,10-phenanthrenedione, was attributed to the formation of a $[M+CH_3]^+$ adduct. Scheme 4 shows the proposed pathway for the $[M+CH_3]^+$ adduct formation through the addition of methanol followed by the loss of water (Scheme 5).

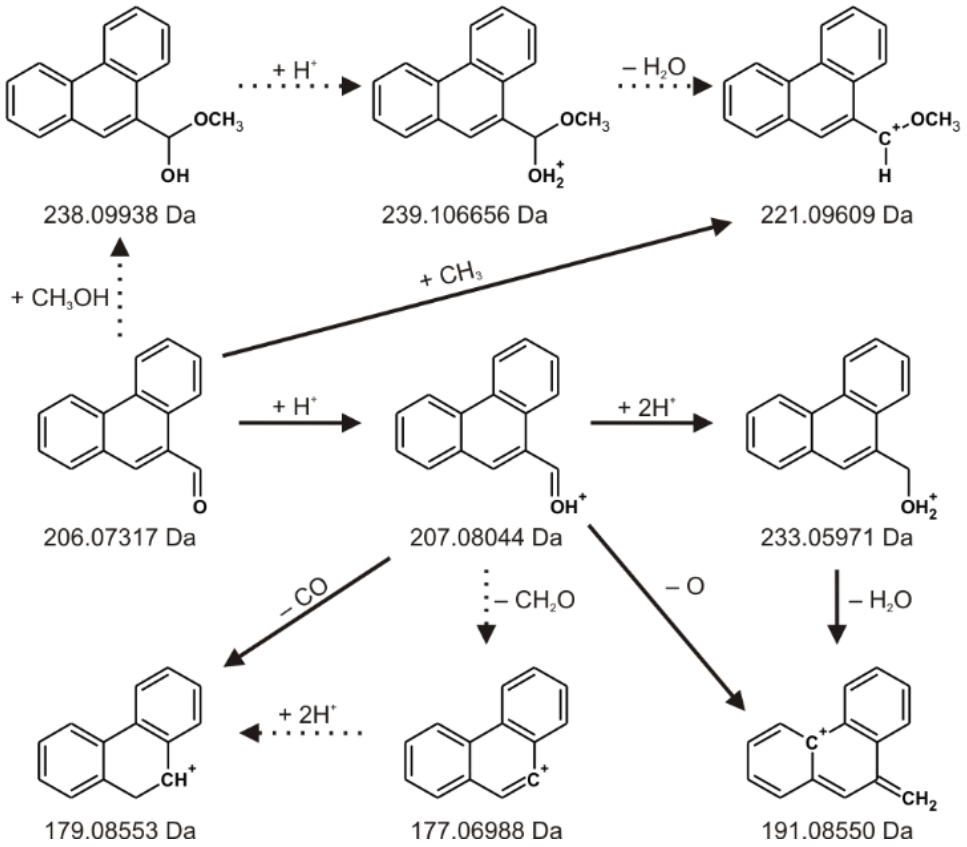

Scheme 5

The ionization of oxy-PAHs with APCI in negative mode resulted in very limited, if any, fragmentation compared to positive mode, with observed fragments having lower relative abundances (Table 12). Similar to the previous work, all oxy-PAH species with the exception of anthrone and 9-phenanthrenealdehyde featured the major ion resulting from associative electron capture giving the $[M+e^-]^-$ anion.[32,69] For anthrone, the main ionization pathway was deprotonation forming the $[M–H]^-$ anion while 9-phenanthrenealdehyde was not ionized at all.

Additional fragmentation/ionization processes in negative mode were observed for anthrone, 1,4-phenanthrenedione, and 9-anthracenecarboxaldehyde (Appendix X). We identified an oxygen adduct of the deprotonated ion (i.e., $[M–H+O]^–$) confirmed by high mass accuracy (-2 ± 5 ppm; Table 12), which was previously proposed to be a

$[M+CH_3]^-$ ion.[66] We were able to eliminate the hypothetical $[M+CH_3]^-$ adduct based on the high mass error -166 ± 5 ppm from the measured value. The process for this oxygen adduct formation is proposed for 1,4-phenanthrenedione in Scheme 6. A deprotonated methanol anion ($[CH_3O]^-$) may undergo a nucleophilic addition to the aromatic system to create a Meisenheimer complex ($[M+OCH_3]^-$) and then CH_4 is lost to leave the $[M-H+O]^-$ ion.[70]

Table 12. Pseudomolecular ions and fragments observed for oxy-PAHs with APCI in negative mode

Compound	Measured Mass[a] (Da)			Rel. Ab. (%)	Fragment[b]	Formula[c]	Formula Mass (Da)	Mass Error (ppm)[d]		
anthrone	**193.06546**	±	0.00015	100	$[M-H]^-$	$C_{14}H_9O$	193.06589	**-2.2**	±	0.8
	208.05230	±	0.00057	30	$[M-2H+O]^-$	$C_{14}H_8O_2$	208.0529	**-3**	±	3
	385.11995	±	0.00827	10	$[M+e^-M-4H]^-$	$C_{28}H_{17}O_2$	385.1234	**-9**	±	2
9,10-anthracene-dione	**208.05187**	±	0.00031	100	$[M+e^-]^-$	$C_{14}H_8O_2$	208.05298	**-5**	±	2
9,10-phenanthrene-dione	**208.05205**	±	0.00073	100	$[M+e^-]^-$	$C_{14}H_8O_2$	208.05298	**-4**	±	3
1,4-phenanthrene-dione	**208.05282**	±	0.00074	100	$[M+e^-]^-$	$C_{14}H_8O_2$	208.05298	**-0.8**	±	3.6
	195.04460	±	0.00082	45	$[M+e^--CH]^-$	$C_{13}H_7O_2$	195.0451	**-3**	±	4
	223.03901	±	0.00075	20	$[M-H+O]^-$	$C_{14}H_7O_3$	223.04007	**-5**	±	3
pyrene-4,5-dione	**232.05187**	±	0.00110	100	$[M+e^-]^-$	$C_{16}H_8O_2$	232.05298	**-5**	±	5
phenanthrene-9-carboxaldehyde										
anthracene-9-carboxaldehyde	**206.07313**	±	0.00042	100	$[M+e^-]^-$	$C_{15}H_{10}O$	206.07371	**-3**	±	2
	221.06031	±	0.00120	50	$[M-H+O]^-$	$C_{15}H_9O_2$	221.0608	**-2**	±	5

[a] Measure masses are reported as averages of the masses observed at three different points along the peak.
[b] Fragments are shown to depict changes in the empirical formula and not necessarily reflect the fragmentation pathway.
[c] Possible empirical formula matches for the observed mass were calculated with elemental ranges of C:8–18, H:6–16, O:0–4, and Na:0–1 for monomers and C:16–32, H:12–32, O:0–4, and Na:0–1 for suspected dimers.
[d] Calculated SD values from the observed masses are in ppm error to show its influence on empirical formula estimations.

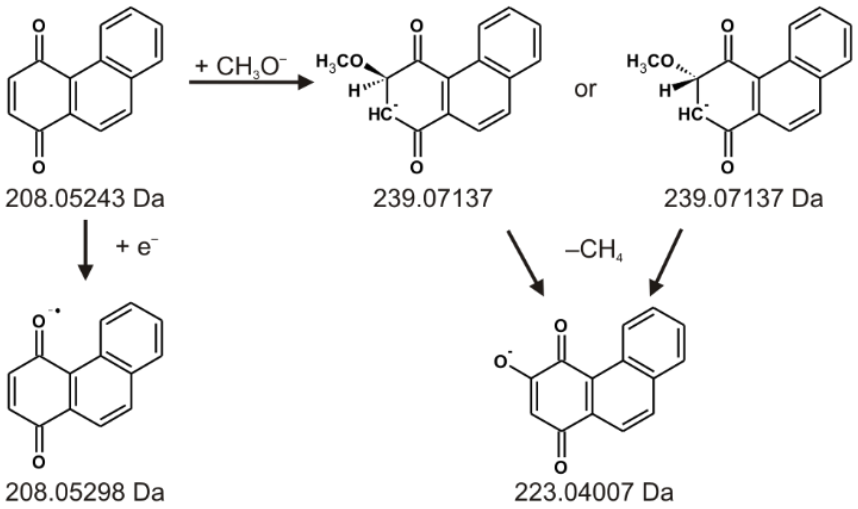

Scheme 6

5.2.3. Nitro-PAHs

The APCI ionization/fragmentation of 3–4 ring PAH derivatives containing one or two nitro groups were investigated, expanding the current understanding of these processes by evaluating the ionization processes and confirming the identities of fragments with HRMS data. The ionization/fragmentation processes of doubly-substituted nitro-PAHs in APCI have not, to our knowledge, been previously studied. The studied species were chosen to represent differences in the location of the nitro-group (constitutional isomers) and structure of the aromatic backbone, allowing any stereo- or structure-specific processes to be observed.

In positive mode each compound exhibited similar ionization/fragmentation processes with different relative abundances (see Table 13). All species consistently yielded $[M+H–16]^+$ ions, resulting from the loss of oxygen following protonation ($[M+H–O]^+$) as shown in Scheme 7. This process was highly stereoselective and was the most prevalent ionization process for 9-nitroanthracene and 9-nitrophenanthrene but was

not observed for 3-nitrophenanthrene (Appendix X). All singly substituted nitro-PAHs studied exhibited a $[M+H–30]^+$ fragment. Our high-resolution MS data support a previous experimental interpretation [71] of this ion as a result of nitro group reduction resulting in the $[M+3H-O_2]^+$ ion. Mass error calculations (data not shown) using the loss of –NO for the $[M+H–30]^+$ ion result in an error > 100 ppm, compared to < 10 ppm for the reduction of the $–NO_2$ group to $–NH_3^+$. Surprisingly, the relative abundance of $[M+H]^+$ was low for all singly substituted nitro-PAH species studied (ranging from 5–50% of the base peak response). This may be due to a competition between protonation of the neutral molecule and gas-phase reduction and oxidation.

Analysis of doubly substituted nitro-PAHs (namely 9,10-dinitroanthracene and 1,6-dinitropyrene) in positive mode resulted in more complicated spectra, arising from competing fragmentation pathways for two separate nitro groups (Table 13). As expected, the nitro group reduction to their respective protonated amines was the major ionization pathway for both compounds. However, the highest response in the MS spectra of 1,6-dinitropyrene was a result of reduction of one nitro group ($[M+H–30]^+$) while both nitro groups in 9,10-dinitroanthracene showed high reactivity towards reduction, giving $[M+H–62]^+$ as the base peak. Both species exhibited $[M+H–O]^+$ fragments with different relative abundances.

Table 13. Pseudomolecular ions and fragments observed for nitro-PAHs with APCI in positive mode.

Compound	Measured Mass[a] (Da)			Rel. Ab. (%)	Fragment[b]	Formula[c]	Formula Mass (*m/z* Da)	Mass Error (ppm)[d]		
9-nitro-anthracene	**208.07546**	±	0.00024	100	$[M+H–O]^+$	$C_{14}H_{10}NO$	208.07569	**-1.1**	±	1.2
	194.08603	±	0.00082	17	$[M+3H–O_2]^+$	$C_{14}H_{12}N$	194.09643	**-53.5**	±	4.2
	194.08603	±	0.00082	17	$[M+H–NO]^+$	$C_{14}H_{10}O$	194.07262	**69.1**	±	4.2
	224.07114	±	0.00060	10	$[M+H]^+$	$C_{14}H_{10}NO_2$	224.07060	**2.4**	±	2.7
	178.07725	±	0.00003	3	$[M+H–NO_2]^+$	$C_{14}H_{10}$	178.07770	**-2.6**	±	0.1
3-nitro-phenanthrene	**194.09626**	±	0.00031	100	$[M+3H–O_2]^+$	$C_{14}H_{12}N$	194.09643	**-0.9**	±	1.6
	194.09626	±	0.00031	100	$[M+H–NO]^+$	$C_{14}H_{10}O$	194.07262	**121.8**	±	1.6
	208.07553	±	0.00012	80	$[M+H–O]^+$	$C_{14}H_{10}NO$	208.07569	**-0.8**	±	0.6
	178.07699	±	0.00015	15	$[M+H–NO_2]^+$	$C_{14}H_{10}$	178.07770	**-4.0**	±	0.8
	224.07080	±	0.00048	6	[M+H]+	$C_{14}H_{10}NO_2$	224.07060	**0.9**	±	2.1
9-nitro-phenanthrene	**208.07512**	±	0.00031	100	$[M+H–O]^+$	$C_{14}H_{10}NO$	208.07569	**-2.7**	±	1.5
	194.09530	±	0.00012	70	$[M+3H–O_2]^+$	$C_{14}H_{12}N$	194.09643	**-5.8**	±	0.6
	194.09530	±	0.00012	70	$[M+H–NO]^+$	$C_{14}H_{10}O$	194.07262	**116.9**	±	0.6
	178.07645	±	0.00044	10	$[M+H–NO_2]^+$	$C_{14}H_{10}$	178.07770	**-7.0**	±	2.5
	224.07182	±	0.00064	5	$[M+H]^+$	$C_{14}H_{10}NO_2$	224.07060	**5.4**	±	2.8
1-nitropyrene	**218.09619**	±	0.00162	100	$[M+3H–O_2]^+$	$C_{16}H_{12}N$	218.09643	**-1.1**	±	7.5
	248.06993	±	0.00109	50	$[M+H]^+$	$C_{16}H_{10}NO_2$	248.07060	**-2.7**	±	4.4
	232.07624	±	0.00100	40	$[M+H–O]^+$	$C_{16}H_{10}NO$	232.07569	**2.4**	±	4.3
	202.07816	±	0.00035	20	$[M+H–NO_2]^+$	$C_{16}H_{10}$	202.07770	**2.3**	±	1.7
9,10-dinitro-anthracene	**207.09072**	±	0.00041	100	$[M+3H–O_4]^+$	$C_{14}H_{11}N_2$	207.09160	**-4.2**	±	2.0
	208.07501	±	0.00045	90	$[M+2H–NO_3]^+$	$C_{14}H_{10}NO$	208.07570	**-3.3**	±	2.2
	209.07809	±	0.00014	60	$[M+5H-2O_2]$	$C_{14}H_{13}N_2$	209.10732	**-139.8**	±	0.7
	194.07443	±	0.00050	60	$[M+2H–N_2O_3]^+$	$C_{14}H_{10}O$	194.07260	**9.4**	±	2.6
	224.07017	±	0.00069	25	$[M+H–NO_2]^+$	$C_{14}H_{10}NO_2$	224.07060	**-1.9**	±	3.1
	223.08860	±	0.00070	22	$[M+3H–O_3]^+$	$C_{14}H_{11}N_2O$	223.08650	**9.4**	±	3.1
	239.08356	±	0.00144	8	$[M+3H–O_2]^+$	$C_{14}H_{11}N_2O_2$	239.08150	**8.6**	±	6.0
	180.08218	±	0.00074	8	$[M+2H–CNO_4]^+$	$C_{13}H_{10}N$	180.08078	**7.8**	±	4.1
	178.07527	±	0.00096	4	$[M+2H–2NO_2]^+$	$C_{14}H_{10}$	178.07770	**-13.6**	±	5.4
	253.06031	±	0.00062	3	$[M+H–O]^+$	$C_{14}H_9N_2O_3$	253.06077	**-1.8**	±	2.4
1,6-dinitro-pyrene	**263.08100**	±	0.00014	100	$[M+3H–O_2]^+$	$C_{16}H_{11}N_2O_2$	263.08151	**-2.0**	±	0.5
	277.06074	±	0.00014	60	$[M+H–O]^+$	$C_{16}H_9N_2O_3$	277.06070	**0.1**	±	0.5
	247.08933	±	0.00050	30	$[M+3H–O_3]^+$	$C_{16}H_{11}N_2O$	247.08660	**11.0**	±	2.0
	233.08177	±	0.00329	25	$[M+5H-2O_2]^+$	$C_{16}H_{13}N_2$	233.10730	**-109.5**	±	14.1
	232.07572	±	0.00044	25	$[M+2H–NO_3]^+$	$C_{16}H_{10}NO$	232.07570	**0.1**	±	1.9
	231.07159	±	0.00177	25	$[M+H–NO_3]^+$	$C_{16}H_9NO$	231.06786	**16.1**	±	7.7
	246.07829	±	0.00021	25	$[M+2H–O_3]^+$	$C_{16}H_{10}N_2O$	246.07870	**-1.7**	±	0.8
	261.06604	±	0.00015	20	$[M+H–O_2]^+$	$C_{16}H_9N_2O_2$	261.06590	**0.5**	±	0.6
	218.09593	±	0.00020	15	$[M+4H–NO_4]^+$	$C_{16}H_{12}N$	218.09640	**-2.1**	±	0.9
	216.08061	±	0.00026	10	$[M+2H–NO_4]^+$	$C_{16}H_{10}N$	216.08080	**-0.9**	±	1.2

[a] Measure masses are reported as averages of the masses observed at three different points along the chromatographic peak.
[b] Fragments are shown to depict changes in the empirical formula and don't necessarily reflect the fragmentation pathway.
[c] Possible empirical formula matches for the observed mass were calculated with elemental ranges of C:8–18, H:6–16, O:0–4, and Na:0–1 for monomers and C:16–32, H:12–32, O:0–4, and Na:0–1 for suspected dimers.
[d] Calculated SD values from the observed masses are in ppm error to show its influence on empirical formula estimations.

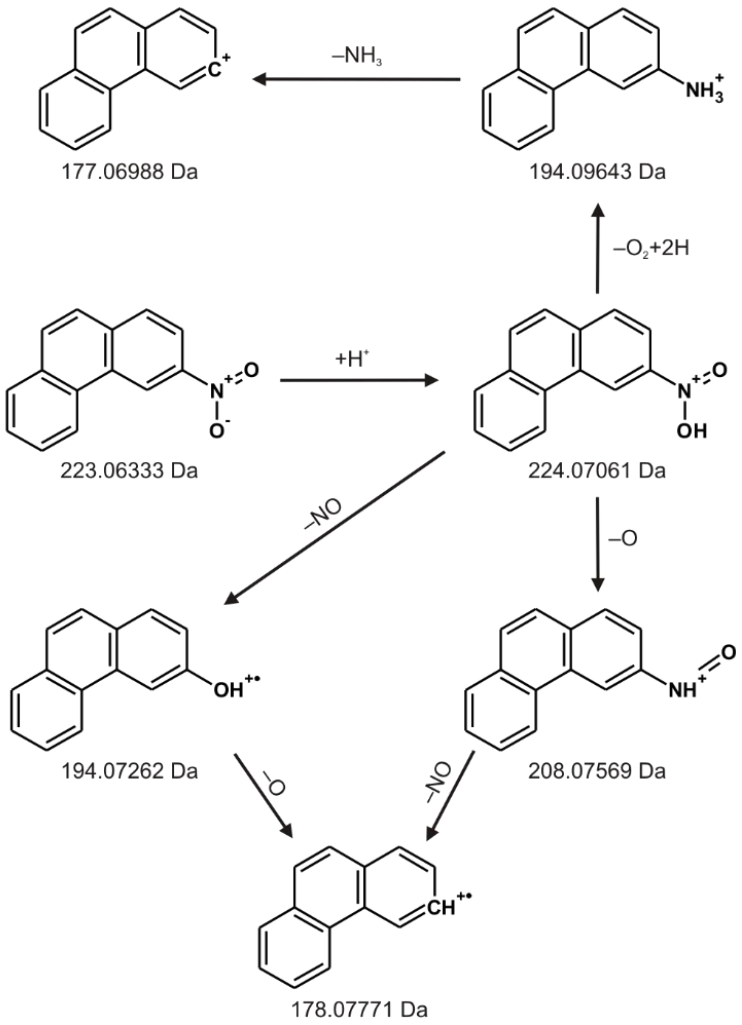

Scheme 7

APCI-MS analysis of both singly and doubly substituted nitro-PAHs in negative mode showed significantly lower fragmentation compared to the positive mode (Appendix X; see also Table 14). For all species studied, the most abundant in the MS spectra was the ion produced via associative electron capture by the neutral molecule, giving $[M+e^-]^-$. This corroborates the observation reported in previous work using low resolution MS detection.[26,29] The associative addition of oxygen following deprotonation, $[M–H+O]^-$, was common for singly substituted nitro-PAHs. The oxygen adduct has been observed in previous studies.[28,29] To evaluate the eluent solvents as possible oxygen

contributors to the $[M–H+O]^-$ ions, direct infusion of 1-nitropyrene at 1 ppm was performed in various solvents; the results are shown in Figure 8. When 1-nitropyrene was dissolved in acetonitrile (devoid of any oxygen), the response ratio of $[M–H+O]^-$:$[M+e^-]^-$ (*m/*z 262:*m/*z 247) was minimal; this was in stark contrast to oxygenated solvents. The exact mechanism for the observed oxygen mechanism is not certain. It should be noted that doubly substituted nitro-PAHs did not undergo this oxygen addition to either of the nitro groups. Thus the presence of the second nitro group might play a key role in deactivating the deprotonated ion towards oxygen addition. As with positive mode, stereoselectivity was observed, mainly between singly substituted nitro-PAHs, with 9-nitrophenanthrene exhibiting a low relative abundance (~ 8% of $[M+e^-]^-$ base peak) for the $[M–H+O]^+$ ion while 3-nitrophenanthrene and 9-nitroanthracene yielded abundances of 30% and 50% relative to the base peak.

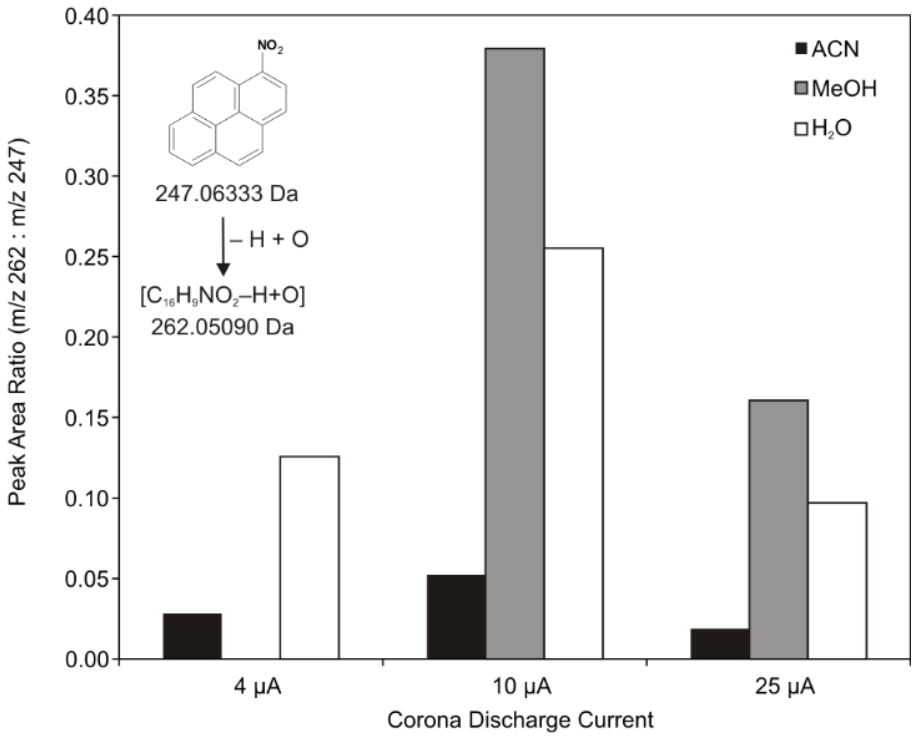

Fig. 8. The contribution of various solvents to formation of $[M–H+O]^-$ ions for 1-nitropyrene in APCI with negative polarity. Spectra were recorded and averaged during

the direct infusion of 1-nitropyrene (at 1 ppm with 5 mM formic acid) in three different solvents at a flow rate of 0.2 mL min-1. The height of each mass peak was used as the response (intensity, counts per second).

Table 14. Pseudomolecular ions and fragments observed for nitro-PAHs with APCI in negative mode.

Compound	Measured Mass[a] (*m/z* Da)			Rel. Ab. (%)	Fragmentb	Formula[c]	Formula Mass (*m/z* Da)	Mass Error (ppm)[d]		
9-nitro-anthracene	**223.06308**	±	0.00062	100	$[M+e^-]^-$	$C_{14}H_9NO_2$	223.06388	**-4**	±	3
	238.05027	±	0.00102	50	$[M-H+O]^-$	$C_{14}H_9NO_3$	238.05097	**-3**	±	4
	193.06543	±	0.00030	20	$[M+e^- – NO]^-$	$C_{14}H_9O$	193.06589	**-2**	±	2
	208.05150	±	0.00095	3	$[M-H+O–NO]^-$	$C_{14}H_8O_2$	208.05243	**-4**	±	5
	256.06066	±	0.00090	3	$[M+e^-+HO_2]^-$	$C_{14}H_{10}NO_4$	256.06153	**-3**	±	3
3-nitro-phenanthrene	**223.06250**	±	0.00049	100	$[M+e^-]^-$	$C_{14}H_9NO_2$	223.06388	**-6**	±	2
	238.04966	±	0.00107	30	$[M-H+O]^-$	$C_{14}H_8NO_3$	238.05097	**-5**	±	4
	209.05960	±	0.00109	3	$[M+e^-+O–NO]^-$	$C_{14}H_9O_2$	209.06080	**-6**	±	5
	193.06676	±	0.00043	2	$[M+e^- – NO]^-$	$C_{14}H_9O$	193.06589	**5**	±	2
9-nitro-phenanthrene	**223.06354**	±	0.00086	100	$[M+e^-]^-$	$C_{14}H_9NO_2$	223.06388	**-2**	±	4
	238.05060	±	0.00114	8	$[M–H+O]^-$	$C_{14}H_8NO_3$	238.05097	**-2**	±	5
	209.05954	±	0.00054	4	$[M+e^-+O–NO]^-$	$C_{14}H_9O_2$	209.06080	**-6**	±	3
	193.06529	±	0.00057	4	$[M+e^- – NO]^-$	$C_{14}H_9O$	193.06589	**-3**	±	3
	208.05276	±	0.00127	3	$[M–H+O–NO]^-$	$C_{14}H_8O_2$	208.05243	**2**	±	6
1-nitropyrene	**247.06206**	±	0.00079	100	$[M+e^-]^-$	$C_{16}H_9NO_2$	247.06388	**-7**	±	3
	217.06424	±	0.00096	30	$[M+e^- – NO]^-$	$C_{16}H_9O$	217.06589	**-8**	±	4
	262.05055	±	0.00105	27	$[M–H+O]^-$	$C_{16}H_8NO_3$	262.05097	**-2**	±	4
	233.05968	±	0.00149	5	$[M+e^-+O–NO]^-$	$C_{16}H_9O_2$	233.06080	**-5**	±	6
9,10-dinitro-anthracene	**268.04708**	±	0.00089	100	$[M+e^-]^-$	$C_{14}H_8N_2O_4$	268.04896	**-7**	±	3
	238.04936	±	0.00070	60	$[M+e^- – NO]^-$	$C_{14}H_8NO_3$	238.05097	**-7**	±	3
	254.04414	±	0.00035	10	$[M+e^-+O–NO]^-$	$C_{14}H_8NO_4$	254.04588	**-7**	±	1
	223.06213	±	0.00069	4	$[M+e^-+H–NO_2]^-$	$C_{14}H_9NO_2$	223.06388	**-8**	±	3
	208.05118	±	0.00074	4	$[M+e^- – N_2O_2]^-$	$C_{14}H_8O_2$	208.05298	**-9**	±	4
	193.06499	±	0.00042	2	$[M+e^-+H^-N_2O_3]^-$	$C_{14}H_9O$	193.06589	**-5**	±	2
1,6-dinitro-pyrene	**292.04801**	±	0.00131	100	$[M+e^-]^-$	$C_{16}H_8N_2O_4$	292.04896	**-3**	±	4
	262.05035	±	0.00115	20	$[M+e^- – NO]^-$	$C_{16}H_8NO_3$	262.05097	**-2**	±	4
	276.05313	±	0.00148	10	$[M+e^- – O]^-$	$C_{16}H_8N_2O_3$	276.05404	**-3**	±	5

[a] Measure masses are reported as averages of the masses observed at three different points along the peak.
b Fragments shown to depict changes in the empirical formula and don't necessarily represent the fragmentation pathway.
[c] Emperical formula matches for the observed mass were calculated with elemental ranges of C:8–18, H:6–16, O:0–4, and Na:0–1 for monomers and C:16–32, H:12–32, O:0–4, and Na:0–1 for suspected dimers.
[d] Calculated SD values from the observed masses are in ppm error to show its influence on emperical formula estimations.

5.2.4. Products from the Heterogeneous Ozonation of PAHs

In this study, the interpretation of APCI ionization/fragmentation pathways together with HRMS data demonstrated above enabled the identification of unknown products[72,73] upon exposure of pyrene adsorbed on a quartz filter to ozone (see the chromatogram in Figure 9). We were able to confirm the identity of two compounds using standards and tentatively identify five additional compounds based on the EICs

(obtained with high resolution of ±0.03 *m/z*) for the major fragment ions observed with the standards (Table 15; mass spectra shown in Appendix XII).

Hydroxy-PAHs, carboxy-PAHs and carbonyl-PAHs identified were the products formed through the ring-opening mechanism as opposed to a more energy-intensive direct oxidation.[72–74] Although most of these products have previously been observed both in aqueous media and on model particles,[72,74,75] this is the first time when the high resolution MS data were used to confirm their identification.

From the mass spectra of each chromatographic peak, specific trends in common ions were observed (Figure 11). Several compounds showed a significant fragment of *m/z* 205, possibly corresponding to an ionized phenanthrene carbonyl structure. Common ions of *m/z* 205, 235 and 191 enabled the identification of three compounds: 4-carboxy-5-phenanthrenecarboxaldehyde, phenanthrene-4,5-dicarboxaldehyde and 5-(hydroxymethyl)-4-phenanthrenecarboxylic acid. The isomers of the last two compounds were assigned based on what could be possible through the ring-opening oxidation of pyrene. The first compound confirmed by a standard seemed to coelute with 4-phenanthrenecarboxylic acid (also confirmed by the corresponding standard). 4-carboxy-5-phenanthrenecarboxaldehyde was previously observed from pyrene ozonation while adsorbed on azelaic acid particles.[74] The dicarboxaldehyde was identified based on the concurrent ions of *m/z* 205 (from the neutral loss of $–CH_2O$) and *m/z* 191 (loss of $–CO_2$),

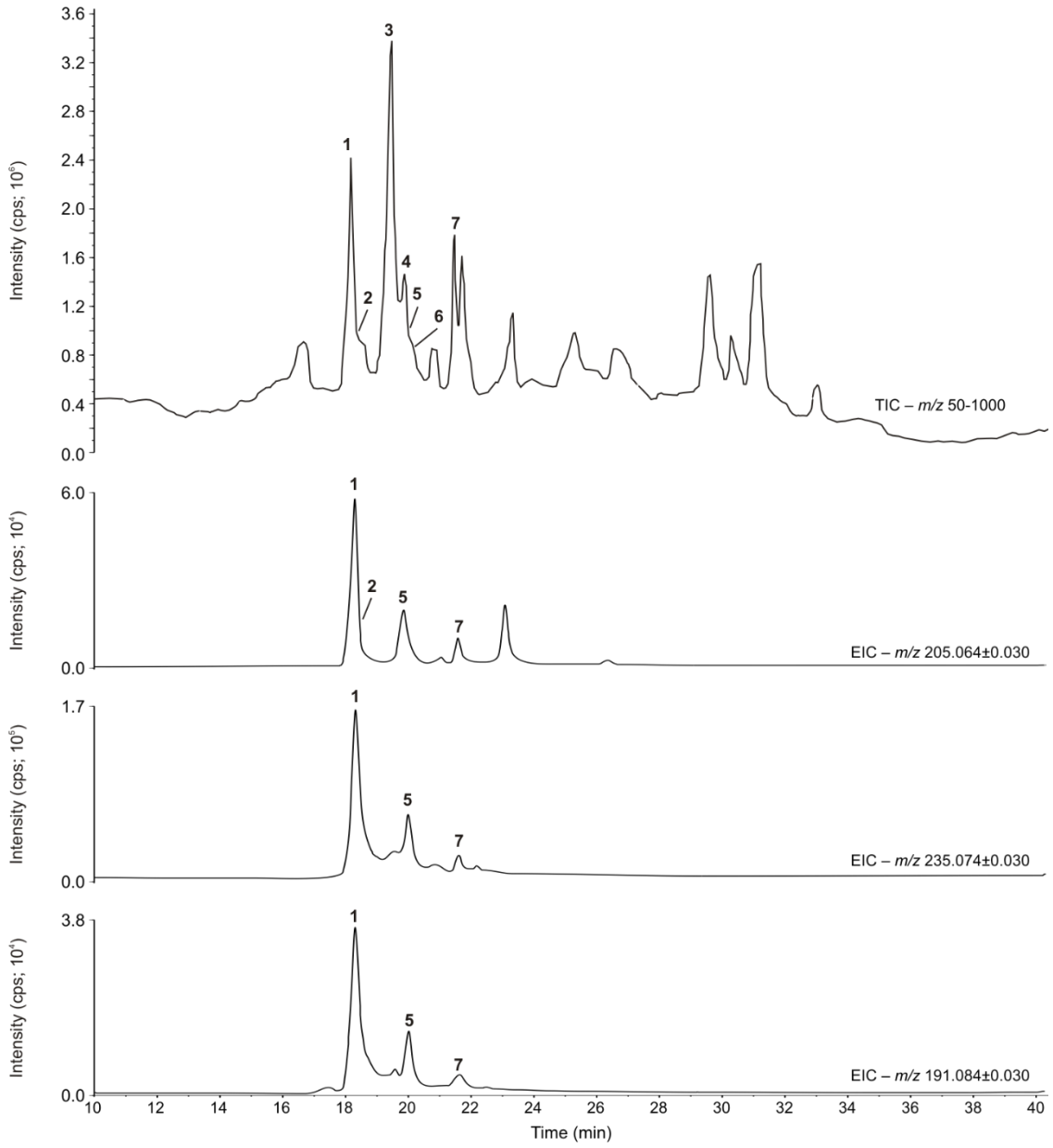

Fig. 9. HPLC-APCI-HRMS smoothed TIC and EIC chromatograms of products formed during the heterogeneous ozonation of pyrene in a small-scale flow reactor. Numbers shown correspond to those listed in Table 15 and Appendix XII.

both from the protonated ion of *m/z* 235. This product was previously observed during aqueous and heterogeneous ozonation of pyrene,[74–76] but not in atmospheric studies. The acid derivative was identified through the observed $[M+H]^+$, $[M+H–H_2O]^+$ and $[M+H–CH_2O_2]^+$ ions. While this compound was previously reported as a result of pyrene

ozonation in aqueous solution [75,76], to our knowledge it was not reported in heterogeneous ozonation reactions. We were not able to unequivocally identify the last of the *m/*z 205 peaks, however, this compound could be possibly identified as another isomer of phenanthrene carboxylic acid.

Table 15. Ion fragments observed for species tentatively identified from HPLC-APCI-HRMS analysis of extracts of filters collected during flow-reactor experiments of the ozonation of pyrene.

Peak #[a]	Proposed Compound	t_R (min)	Measured Mass[b] (*m/z* Da)			Rel. Ab. (%)	Fragment[c]	Formula	Formula Mass[d] (*m/z* Da)	Mass Error[e] (ppm)		
1	4-carboxy-5-phenanthrene- carboxaldehyde	18.18	**235.07392**	±	0.00040	100	$[M+H-O]^+$	$C_{16}H_{11}O_2$	235.07536	**-8**	±	2
		18.18	**251.06876**	±	0.00045	65	$[M+H]^+$	$C_{16}H_{11}O_3$	251.07027	**-5**	±	2
		18.18	**205.06395**	±	0.00041	40	$[M+H-CH_2O_2]^+$	$C_{15}H_9O$	205.06479	**-3**	±	2
		18.18	**191.08474**	±	0.00052	25	$[M+H-CO_3]^+$	$C_{15}H_{11}$	191.08550	**-4**	±	3
		18.18	**233.05831**	±	0.00063	20	$[M+H-H_2O]^+$	$C_{16}H_9O_2$	233.05971	**-5**	±	3
		18.18	**265.08434**	±	0.00052	20	$[M+H+CH_2]^+$	$C_{17}H_{13}O_3$	265.08590	**-5**	±	2
		18.18	**177.06856**	±	0.00039	5	$[M+H-C_2H_2O_3]^+$	$C_{14}H_9$	177.06988	**-5**	±	2
2	4-phenanthrene-carboxaldehyde	18.28	**205.06503**	±	0.00034	100	$[M+H-H_2O]^+$	$C_{15}H_9O$	205.06479	**-0.4**	±	1.7
		18.28	**221.06055**	±	0.00107	50	$[M+H-2e^-]^+$	$C_{15}H_9O_2$	221.06036	**-4**	±	5
		18.28	**223.07667**	±	0.00037	40	$[M+H]^+$	$C_{15}H_{11}O_2$	223.07536	**4**	±	2
3	4-oxapyrene-5-one	19.43	**221.06031**	±	0.00037	50	$[M+H]^+$	$C_{15}H_9O_2$	221.05971	**5**	±	2
		19.43	**193.06518**	±	0.00024	100	$[M+H-CO]^+$	$C_{14}H_9O$	193.06479	**3**	±	1
		19.43	**177.07143**	±	0.00043	25	$[M+H-CO_2]^+$	$C_{14}H_9$	177.06988	**9**	±	2
4	4-phenanthrene-carboxaldehyde	19.54	**207.08104**	±	0.00015	40	$[M+H]^+$	$C_{15}H_{11}O$	207.08044	**3.7**	±	0.7
		19.54	**191.08438**	±	0.00043	100	$[M+H-O]^+$	$C_{15}H_{11}$	191.08553	**-3**	±	2
		19.54	**179.08597**	±	0.00010	5	$[M+H-CO]^+$	$C_{14}H_{11}$	179.08553	**1.9**	±	0.5
5	phenanthrene-4,5-dicarboxaldehyde	19.84	**235.07533**	±	0.00046	100	$[M+H]^+$	$C_{16}H_{11}O_2$	235.07536	**-0.2**	±	2.0
		19.84	**205.06556**	±	0.00062	50	$[M+H-CH_2O]^+$	$C_{15}H_9O$	205.06479	**3**	±	3
		19.84	**191.08508**	±	0.00098	5	$[M+H-CO_2]^+$	$C_{15}H_{11}$	191.08553	**-7**	±	5
6	[1,1'-biphenyl]-2,2',6,6'-tetracarboxaldehyde	19.93	**239.06893**	±	0.00054	100	$[M+H-CO]^+$	$C_{15}H_{11}O_3$	239.07027	**-6**	±	2
		19.93	**251.07065**	±	0.00050	10	$[M+H-O]^+$	$C_{16}H_{11}O_3$	251.07027	**4**	±	2
		19.93	**267.06482**	±	0.00052	10	$[M+H]^+$	$C_{16}H_{11}O_4$	267.06518	**-3**	±	2
7	5-(hydroxymethyl)-4-phenanthrenecarboxylic acid	21.45	**235.07457**	±	0.00068	100	$[M+H-H_2O]^+$	$C_{16}H_{11}O_2$	235.07536	**-4**	±	3
		21.45	**205.06375**	±	0.00101	60	$[M+H-CH_4O_2]^+$	$C_{15}H_9O$	205.06479	**0.6**	±	4.9
		21.45	**191.08645**	±	0.00041	20	$[M+H-CH_2O_3]^+$	$C_{15}H_{11}$	191.08553	**7**	±	2
		21.45	**253.08556**	±	0.00041	5	$[M+H]^+$	$C_{16}H_{13}O_3$	253.08592	**-2**	±	2

[a] Peak numbers correspond to peaks labeled in Fig. 9.
[b] Measure masses are reported as averages of the masses observed at three different points along the chromatographic peak.

Two additional products proposed to result from a ring-opening attack by ozone were tentatively identified as [1,1'-biphenyl]-2,2',6,6'-tetracarboxaldehyde (peak 6 in Figure 9) and 4-oxapyrene-5-one (peak 3 in Figure 9). The former was identified based on the $[M+H–O]^+$ and $[M+H–CO]^+$ ion fragments observed with the aldehyde standards. For 4-oxapyrene-5-one, similar to the studied diketone species, a $[M+H–CO]^+$ ion was observed. In addition, a $[M+H–CO_2]^+$ ion was observed that was not with the other ketone standards.

5.3. Conclusions

Derivatives of PAHs containing a mixture of functional groups (i.e., hydroxyl, carboxylic acid, carbonyl, and nitro groups) were analyzed with APCI-HRMS. High resolution data for common fragmentation patterns between 3-4 ring PAH derivatives with similar functional groups were reported for the first time. Stereospecific pathways were found, providing useful information in identifying unknown species with no available standards. In analyzing products from the ozonation of pyrene with APCI-HRMS, many products were tentatively identified based on common ions of *m/z* 205 and 235 and 191 as well as relative intensities of common ionization/fragmentation patterns exhibited by standard compounds. For the first time high resolution MS data are reported to support the identification of these products. Some of the products identified are, for the first time, reported as occurring from the heterogeneous ozonation of pyrene.

CHAPTER 6

6. HETEROGENEOUS NITRATION AND OZONATION OF 3- AND 4-RING POLYCYCLIC AROMATICE HYDROCARBONS IN A SMALL-SCALE FLOW REACTOR.

6.1. Experimental

6.1.1. Materials and Reagents

All standards used in this study are listed in Table 16. Stock solutions were prepared in a concentration of 100 µg mL^{-1} in dichloromethane (DCM, high-resolution GC grade, Fisher Scientific, Pittsburgh, PA, USA). The internal standard method was employed for quantification using an internal standard (IS) solution consisting of deuterated fluoranthene in DCM (~100 µg mL^{-1}). Additionally, recovery standard (RS) solutions (100 µg mL^{-1}; listed in Table 16) were used to correct for any errors resulting from the extraction process. The derivatization agent, N,O-bis(trimethylsilyl)trifluoroacetamide (BSTFA) with 1% of trimethylchlorosilane (TMCS), was obtained from Sigma-Aldrich (Atlanta, GA, USA) and used to derivatize polar PAH derivatives with hydroxy groups (hydroxy-PAHs) and/or carboxylic acid groups (carboxy-PAHs) to trimethylsilyl derivatives to increase the sensitivity of their analysis.

For flow reactor experiments dry air (< 7 ppm H_2O), dry nitrogen (< 3 ppm H_2O) and nitrogen dioxide (380.1 ppm in dry air) were obtained from Airgas (Chicago, IL, USA).

Table 16. List of standards, recovery standard and internal standards used in this study with select physical and experimental information.

Compound	Empirical Formula	MW (g mol^{-1})	Quan. Ion	Confirmation Ions (Relative Abundance) 1	2	Use
PAHs						
phenanthrene	$C_{14}H_{10}$	178	178	152 (10)	89 (10)	Standard
anthracene	$C_{14}H_{10}$	178	178	152 (10)	89 (10)	Standard
fluoranthene	$C_{16}H_{10}$	202	202	101 (10)	88 (5)	Standard
pyrene	$C_{16}H_{10}$	202	202	101 (10)	88 (5)	Standard
phenanthrene-d_{10}	$C_{14}D_{10}$	188	188	184 (20)	160 (10)	RS[b]
anthracene-d_{10}	$C_{14}D_{10}$	188	188	184 (20)	160 (10)	RS
fluoranthene-d_{10}	$C_{16}D_{10}$	212	212	106 (10)	92 (5)	IS[d]
pyrene-d_{10}	$C_{16}D_{10}$	212	212	106 (10)	92 (5)	RS
nitro-PAHs						
9-nitrophenanthrene	$C_{14}H_9NO_2$	223	165	176 (90)	223 (60)	Standard
9-nitroanthracene	$C_{14}H_9NO_2$	223	176	223 (90)	165 (80)	Standard
3-nitrofluoranthene	$C_{16}H_9NO_2$	247	247	200 (75)	189 (60)	Standard
1-nitropyrene	$C_{16}H_9NO_2$	247	201	247 (85)	189 (60)	Standard
9-nitrophenanthrene-d_9	$C_{14}D_9NO_2$	232	232	184 (95)	202 (90)	RS
9-nitroanthracene-d_9	$C_{14}D_9NO_2$	232	232	184 (95)	202 (90)	RS
3-nitrofluoranthene-d_9	$C_{16}D_9NO_2$	256	256	210 (100)	208 (75)	RS
1-nitropyrene-d_9	$C_{16}D_9NO_2$	256	256	210 (100)	208 (75)	RS
oxy-PAHs						
9,10-anthracenedione	$C_{14}H_8O_2$	208	208	180 (95)	152 (75)	Standard
9,10-phenanthrenedione	$C_{14}H_8O_2$	208	180	152 (50)	208 (50)	Standard
anthrone	$C_{14}H_{10}O$	194	194	165 (65)		Standard
2-chloroanthraquinone	$C_{14}H_7ClO_2$	242	242	214 (65)	186 (55)	RS
hydroxy-PAHs						
1-hydroxypyrene	$C_{16}H_{10}O$	218	218			Standard
1-hydroxypyrene-d_9	$C_{16}D_{10}O$	227	227	197 (50)	99 (15)	RS
2'-chloro-2-hydroxy-4-methylbenzophenone	$C_{14}H_{11}ClO_2$	247	211	135 (30)	246 (25)	RS

[a] Sigma-Aldrich (Atlanta, GA, USA).
[b] Denotes "Recovery Standard" used to correct for error arising from extraction and sample preparation steps.
[c] CDN Isotopes (Pinte-Claire, Canada).
[d] "Internal Standard" used to correct for volume changes in the final sample submitted to GC-MS analysis.

6.1.2. Flow Reactor

The home-built flow reactor used in this study consisted of three main parts: a gas injection/dilution system, a mixing chamber, and a reaction chamber (Appendix VI). The gas injection/dilution system delivered breathing quality air, industrial grade nitrogen, and ultra-high purity nitrogen dioxide (at 10 ppm in balance nitrogen) to a mixing chamber composed entirely of Teflon (31.5 cm length x 9.0 cm I.D.) through ¼" stainless

steel tubing. Two-way stainless steel valves were used for selecting the gases used in each experiment. All gas flows through the reactor system were regulated with mass flow controllers (Alicat Scientific, Tucson, AZ, USA) to achieve the desired dilution of gases. After the mixing chamber stainless steel tees directed flow to the reaction chamber, gas analyzer, and exhaust vent. During ozonation experiments ozone levels at the outlet of the mixing chamber were measured using a photometric O_3 gas analyzer (Teledyne, Thousand Oaks, CA, USA). For nitration experiments NO_2 concentrations were measured using a chemiluminescence NO_x analyzer (Teledyne). The gas mixtures from the mixing chamber were supplied to the Teflon reaction chamber (43 cm in length x 9.0 cm I.D.) through an inlet located on top of the chamber. A quartz window was located directly above the reactor chamber inlet where a UV light (356 nm) was housed for photochemical experiments. At the bottom of the reaction chamber was a Teflon-coated aluminum filter support where 90 mm filters (surrogate particle phase) were placed during each reaction experiment. The outlet of the reactor chamber was located under the filter support. Following the outlet of the reaction chamber two polyurethane foam (PUF) filters were placed in series to collect residual gas phase species exiting the reaction chamber. The total flow through the reaction chamber was controlled using an oil-less pump (Model VT 4.8; Becker, Cuyahoga Falls, OH, USA) with a mass flow controller positioned between the reaction chamber and the pump. The flow drawn by the pump was always kept lower than the gas flow exiting the mixing chamber to prevent over pressurization of the reaction chamber.

6.1.3. Reaction Experiments

In this study general trends in the desorption and reactive uptake of four PAHs (phenanthrene, anthracene, fluoranthene, and pyrene) were evaluated, focusing on the

identification of the majority of the products formed. An allotted amount of a PAH stock solution was spiked over either a quartz tissue filter (90 mm I.D., PALL Corporation, Port Washington, NY) or Teflon filter (90 mm I.D., Sterlitech Corporation, Kent, WA, USA) and allowed to evaporate at room temperature for 60 s. All quartz filters were pre-baked at 500 °C for 12 h and then placed in the small scale flow reactor system (as shown in Appendix VI) and exposed to the experimental conditions specified in Table 17 with reaction times ranging between 5–300 min. Gas phase species exiting the reaction chamber were collected with two PUF filters placed in series after the quartz (is some experiments Teflon) filter. PUF filters were pre-cleaned via sonication for 30 min in DCM. For all experiments no breakthrough through the first PUF filter was observed (i.e., the amounts observed on the second PUF filter were less than 1% of those observed on the first). The conditions of the experiments that were performed in this study are summarized in Table 17. To determine PAH loss through desorption, initial experiments were performed under an atmosphere composed of only air or only nitrogen. Additional experiments were performed in the presence of UV light to determine the impact of photolysis on the loss of PAHs without the presence of oxidizing species.

Table 17. List of flow reactor experiments performed in this study (each done in triplicate). Oxidants along with their final concentrations (ppm).

Experiment	Atmosphere	Oxidant	Photolysis (356 nm)	Total Gas Flow ($L\ min^{-1}$)[a]
1	Air	-	No	2.5
2	Air	-	Yes	2.5
3	N_2	-	No	2.5
4	Air	NO_2 (7.5 ppm)	No	2.5
5	N_2	NO_2 (7.5 ppm)	No	2.5
6	Air	O_3 (1.25 ppm)	No	1.5
7	Air	O_3 (1.0 ppm)	Yes	1.5
8	Air	O_3 (1.6 ppm) NO2 (9.6 ppm)	No	1.5
9	Air	NO_2 (9.6 ppm) O_3 (1.6 ppm) NO_2 (9.6 ppm)	Yes	1.5

[a] Mass flow (corrected by temperature and pressure)

To accurately account for the analyte recoveries, a daily control sample was prepared by spiking the same amount of PAHs (4 µg) and RS compounds (1 µg) to DCM in parallel to each reaction experiment. These control solutions were prepared so that the final analyte concentrations in the controls were the same as those in the samples, assuming 100% recovery of starting reagent and products. All reaction and control experiments were performed in triplicate and evaluated based on the average ± one standard deviation.

To assess any background contamination present on the filters, in the small reaction chamber system, or in the supplied nitrogen gas, blank extractions were performed in triplicate on: 1) filters not submitted to the chamber, and 2) filters exposed to N_2 gas for 90 min. Detected species from all desorption experiments were compared to oxidation experiments with NO_2 and O_3 to avoid misidentification of oxidation products.

6.1.4. Extraction and Sample Preparation

Upon the completion of each reaction experiment, the filter was extracted using 10 mL of DCM using 30 min sonication. Prior to each extraction 40 µL of RS solution at 100 µg mL^{-1} of each compound (listed in Table 16) was added. After sonication, the extract was filtered over deactivated glass wool. The vial and filter was further washed twice with 10 mL of DCM each time. Ultimately all DCM solvent fractions obtained were combined and evaporated under a stream of nitrogen to ~0.5 mL. The concentrated extract was then divided into two parts, for 1) direct analysis and 2) analysis following the derivatization. The derivatization was performed using 100 µL of BSTFA (60 °C, 3 h). Prior to GC-MS analysis, 10 µL of IS solution (fluoranthene-d_{10} at 100 µg mL^{-1}) was added to each final sample volume.

6.1.5. GC-MS Analyses

The analyses were performed using an Agilent 6890N GC equipped with 5975C MSD (EI). All injections (1.0 µL) were into a splitless injection (1 min) port with a 30 psi pulse for 1.0 min using a splitless liner with deactivated glass wool (Restek, Bellefonte, PA). A 30 m DB-5MS column (J&W Scientific, Inc., Folsom, CA, USA) with a 0.25 mm I.D. and a 0.25 µm film thickness was used for all separations. Ultra pure helium (99.999%) was used as the carrier gas with a constant flow rate of 1.0 mL min^{-1}. The initial oven temperature was set to 40 °C held for 1.0 min, then ramped to 140 °C with a rate of 20 °C/min, then ramped to 290 °C with a rate of 10 °C, and held for 12 min. The injector temperature was set to 250 °C and the transfer line was set at 280 °C. All MS data was acquired in total ion current (TIC) mode with a mass range of *m/z* 50–550. For all analyses a 3.5 min solvent delay was used, expect for the analysis of derivatized samples which had a 5 min solvent delay.

6.1.6. HPLC-APCI-HRMS Analyses

HPLC-MS analyses were performed on an Agilent 1100 HPLC coupled to high resolution Time of Flight MS G1689A Series 6200. All HPLC separations were performed using a Restek C18 200 mm x 3.2 mm reverse phase HPLC column with 5 µm particle size. A binary solvent system consisting of A: water, B: methanol was used. A gradient program at flow rate of 0.5 mL min^{-1} started with 20% B for 5 min, followed with an increase to 90% B at 20 min, and hold at 90% until 27 min, and then was linearly decreased to 20% at 30 min and held at 20% B for 5 min to allow for equilibration. The column oven temperature was set to 30 °C and injection volume was 50 µL.

APCI was performed in both positive and negative modes. Drying gas (N_2) was set to 300 °C at a flow of 3 L min^{-1}. For all experiments the capillary voltage was set to

4500 V. In order to minimize the contribution of post-source fragmentation, the fragmentor voltage was set to 120 V for all experiments. All HPLC-HRMS analyses were performed with the corona discharge current set at 10 µA. For experiments evaluating the contribution of the corona current to gas-phase ion fragmentation the corona discharge current was varied within the range of 4–25 µA.

6.2. Results and Discussion

The aim of this project was to study the oxidation of PAHs in the presence of either nitrogen dioxide, ozone, or both, focusing on the identification of product species to enable their later identification in atmospheric studies performed either in chambers or outdoor.

6.2.1. Desorption and Background Contamination

Prior to studying oxidation processes of PAHs, small chamber experiments were performed using either N_2 gas or air without any other reactant to determine desorption rates (Figure 10). Under an N_2 atmosphere combined recoveries in the gas and particle phase for phenanthrene, fluoranthene and pyrene were near 100 % for both 90 and 300 min exposure (Figure 10). As expected, evaporation of the 3-ring PAHs (~25% at 90 min) was more pronounced than those of 4-ring PAHs (<5% at 90 min). Total recoveries for anthracene were lower, with ca. 20% lost for both exposure times. The formation of 9,10-anthracenedione and anthrone (not quantified) was observed in the particle phase, most likely attributing to the fraction of anthracene lost. This was unexpected and is possibly due to the presence of oxygen in the form of SiO_2 in the quartz filter.

When exposed to air only, the loss of phenanthrene and anthracene from the particle phase was slightly higher than with the exposure to N_2 only (Figure 10). While

the majority of this mass loss was recovered in the gas-phase, small amounts of 9,10-anthracenedione and 9,10-phenanthrenedione were observed on the quartz filter.

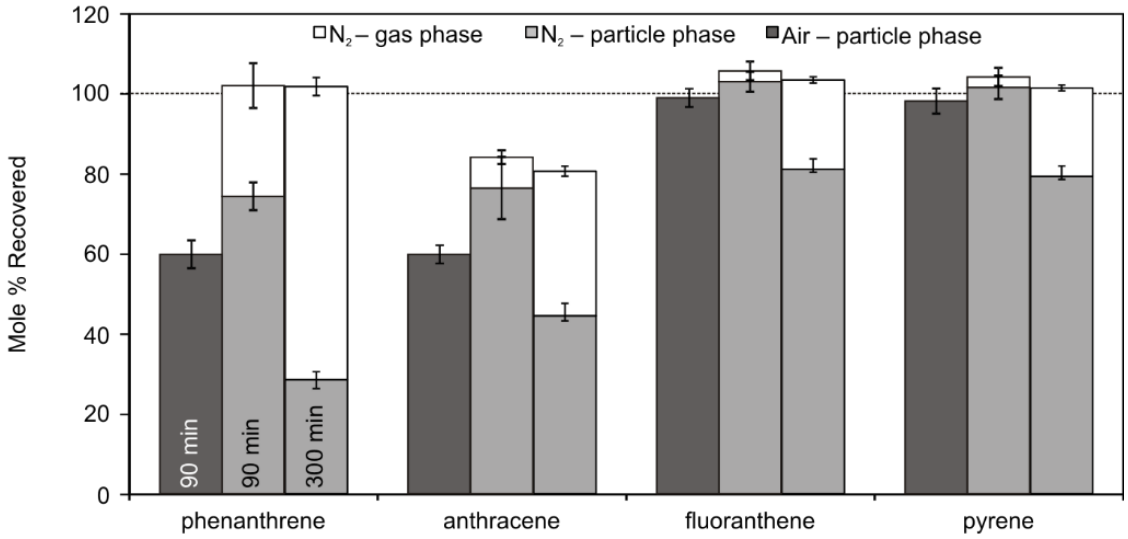

Fig. 10. Recoveries of PAHs in both the gas and particle phases during N_2 desorption experiments, from 90 and 300 min durations. Recoveries are shown as mole percent of moles originally spiked to the quartz filter. Standard deviations were calculated from recoveries determined during triplicate experiments.

6.2.2. Reaction with NO_2

As reported previously, for reaction times ranging from 5 min to 300 min, exposure of PAHs to NO_2 led to a selective loss of anthracene and pyrene (Appendix XIII).[77] The nitration reaction products reported previously as well as newly observed reaction products from phenathrene are listed in Table 18, including their characteristic EI-MS ions and retention times. As in previous work for the reaction with NO_2, the major products were 1-nitropyrene and 9-nitroanthracene (Figure 11; TIC chromatogram shown in Appendix XIV, confirmed by individual standards).[77,78] While relatively less reactive, the nitration of phenanthrene resulted in the formation of 9-nitrophenanthrene. This is, to our knowledge, the first report of the formation of this product from the heterogeneous nitration of phenanthrene.

In contrast to previous studies, mass balance on the nitration of pyrene was closed with the molar amount of 1-nitropyrene recovered (43±12 nanomoles at 90 min) being similar to the amount of pyrene lost (Figure 11). For other species yields were at least 60%, with significant amounts of parent PAHs, and for some, unexpected oxygenated products.

Table 18. Products observed from the reaction between a mixture of PAHs, pyrene only, and anthracene only with NO_2 while adsorbed to a quartz filter substrate.

Identified Oxidation Product	Parent PAH	Empirical Formula	MW	t_R (min)	EI-MS Major Ions (Relative Abundance) 1	2	3	4	MS Methods Used For Identification[a]	Standard
PAHs + NO_2										
9-nitroanthracene	anthracene	$C_{14}H_9NO_2$	223	16.73	176 (100)	223 (95)	193 (80)	165 (85)	EI-MS & APCI-HRMS	9-nitroanthracene
9-nitrophenanthrene	phenanthrene	$C_{14}H_9NO_2$	223	17.433	165 (100)	176 (80)	223 (60)	193 (25)	EI-MS	9-nitrophenanthrene
1-nitropyrene	pyrene	$C_{16}H_9NO_2$	247	20.804	201 (100)	274 (90)	217 (70)	189 (60)	EI-MS & APCI-HRMS	1-nitropyrene
Pyrene + NO_2										
1-nitropyrene	pyrene	$C_{16}H_9NO_2$	247	20.804	201 (100)	274 (90)	217 (70)	189 (60)	EI-MS & APCI-HRMS	1-nitropyrene
Anthracene + NO_2										
anthrone	anthracene	$C_{14}H_{10}O$	194	14.309	194 (100)	165 (75)			EI-MS & APCI-HRMS	anthrone
9,10-anthracenedione	anthracene	$C_{14}H_8O_2$	208	14.518	208 (100)	180 (88)	152 (67)		EI-MS & APCI-HRMS	9,10-anthracenedione
9-nitroanthracene	anthracene	$C_{14}H_9NO_2$	223	16.005	176 (100)	223 (95)	193 (80)	165 (85)	EI-MS & APCI-HRMS	9-nitroanthracene

[a] Products were identified through two different MS methods: 1) EI-MS detection following separation by GC and 2) APCI-HRMS detection following separation by HPLC.

Additional products from the oxidation of anthracene were observed, including anthrone and 9,10-anthracenedione, which are not expected oxidation products in the presence of NO_2. These products were confirmed from experiments with anthracene alone in the presence of NO_2. The relative percentage of the formed products is similar to those observed during exposure to N_2 only and thus their formation is most likely due to interaction with the SiO_2 framework of the quartz substrate. This is similar to previous studies reporting the formation of 9,10-anthracenedione when adsorbed to magnesium oxide (MgO) and SiO_2.[78] Understanding the mechanisms behind this reaction artifact is essential, thus warranting further investigation.

Nitration experiments in the presence of UV radiation yielded similar trends for anthracene and pyrene loss. However, the formation of 9-nitroanthracene and 1-nitropyrene was significantly lower, most likely due to photodegradation. Both phenanthrene and fluoranthene showed more pronounced losses compared to nitration under dark conditions, however, none of the targeted products (i.e., those with available standards in this study) were observed.

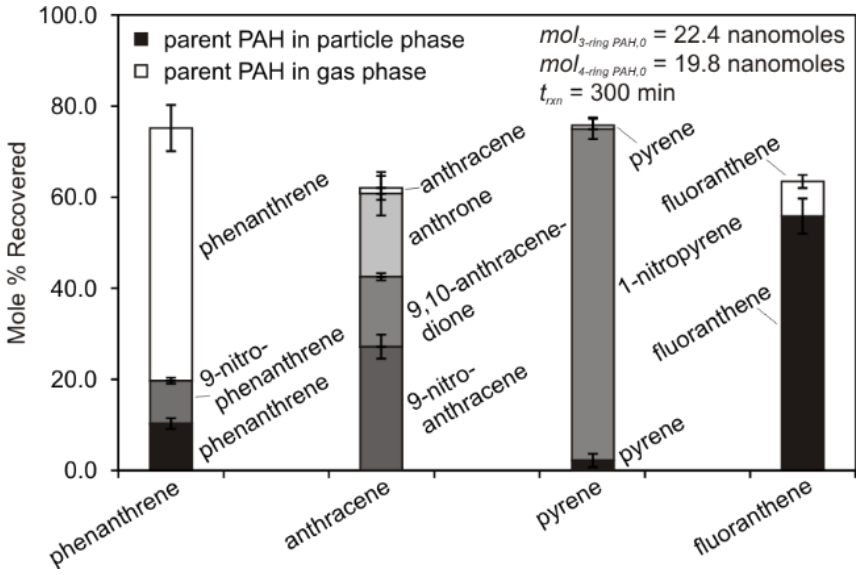

Fig. 11 Yields (mole % recovered) of PAHs and their oxidation products observed after exposing a mixture of 3- and 4-ring PAHs with NO_2 for 300 min. All products were found only in the particle phase.

6.2.3. Reaction with O_3

The losses of PAHs during heterogeneous ozonation corresponded to those previously reported and were less selective compared to nitration experiments (Appendix XIII).[72,79,80] In contrast to reactions with NO_2, ozonation yielded significantly higher number of products (20 with O_3 compared to only 3 with NO_2;Table 19; TIC chromatograms shown in Appendix XIV). The experiments were performed with a mixture of PAHs as well as pyrene and anthracene individually to confirm the relationship between parent and product species (see the chromatograms in Appendix XV). Several of these species reported previously have been identified and confirmed with standards, other compounds were confirmed based on low resolution MS. [72,80] In our work further confirmation was achieved using APCI with high resolution TOF MS with mass error < 10 ppm. Most of the products observed were those resulting from the ozonation of pyrene, which has been suggested to occur through two previously proposed

general pathways.[81] The first pathway is suggested to involve the addition of ozone to the more reactive C9═C10 double bond and subsequent ring-opening.[81] From this multiple products containing a phenanthrene backbone and a mixture of hydroxyl, aldehyde and/or carboxylic acid groups can be produced.[14] The second proposed pathway involves the addition of ozone without breaking any C═C double bonds, producing products with carbonyl and/or hydroxyl groups and is suggested to be more energy intensive and dependent on PAH-surface interactions.[81] In the present study no pyrene derivatives with hydroxyl groups that are produced through the second pathway were identified.

A number of the pyrene ozonation products observed shared a characteristics fragment ion, *m/z* 205 (Figure 12). This fragment is proposed to resemble the deprotonated radical cation of 4-phenanthrenecarboxaldehyde. From the ring-opening mechanism described above, pyrene ozonation can result in a variety of functional groups, including aldehyde, carboxylic and methylhydroxyl groups. In addition, most of the pyrene ozonation products had similar ion fragments of *m/z* 176 (Appendix XVI), resulting from the loss of all functional groups and giving a deprotonated radical ion of phenanthrene. Both the ions of *m/z* 205 and 176 may be useful in online instruments (e.g., an aerosol mass spectrometer) when monitoring the oxidation.of anthracene, phenanthrene and pyrene. In our study two major aldehyde products were observed, including 4-phenanthrenecarboxaldehyde and phenanthrene-4,5-dicarboxaldehyde.

This is the first time, to our knowledge, that the production of 4-phenanthrenecarboxaldehyde from the heterogeneous ozonation of pyrene has been reported. Yao et al. observed the formation of 4-phenanthrenecarboxaldehyde upon ozonation of pyrene while in an acetonitrile/water solution [75].

Table 19. Products observed from the ozonation reaction of a mixture of PAHs, pyrene only, and anthracene only while adsorbed to a quartz filter substrate.

						APCI-HRMS Data					
						[M+H]+ Ion (Da)			[M–H]– or [M+e–]– Ion (Da)		
	Parent		EI-MS Major Ions (Rel. Ab.)			Observed	Calculated	Error	Observed	Calculated	Error
Identified Oxidation Product	PAH	MWa	1	2	3	Mass	Mass	(ppm)	Mass	Mass	(ppm)
PAHs + O3											
1,1'-biphenyl-2,2'-dicarboxaldehyde	phenanthrene	210	181 (100)	152 (37)	210 (3)	211.07300	211.07536	-11	209.05864	209.06080	-10
anthrone	anthracene	194	194 (100)	165 (75)		195.07911	195.08044	-7	193.06543	193.06589	-2
9,10-anthracenedione	anthracene	208	208 (100)	180 (88)	152 (67)	209.05980	209.05971	0.4	208.05291	208.05298	-0.3
9,10-phenanthrenedione	phenanthrene	208	180 (100)	152 (60)	208 (40)	209.06145	209.05971	8	208.05191	208.05298	-5
4-phenanthrenecarboxaldehyde	pyrene	205	205 (100)	176 (20)	151 (15)	207.08028	207.08044	-1	206.07180	206.07371	-9
4-oxapyrene-5-one	pyrene	220	220 (100)	163 (43)	192 (21)	221.06070	221.05971	5	220.05056	220.05298	-11
phenanthrene-4,5-dicarboxaldehyde	pyrene	234	205 (100)	176 (30)	218 (10)	235.07472	235.07536	-3	233.05992	233.06080	-4
n-hydroxyanthracene	anthracene	194/266	266 (100)	251 (20)	191 (15)	195.08095	195.08044	3	193.06552	193.06589	-2
4-hydroxy-5-phenanthrenecarboxaldehyde	pyrene	222/294	205 (100)	293 (50)	176 (25)	223.07584	223.07536	2	221.05991	221.06080	-4
4-phenanthrenecarboxylic acid	pyrene	222/294	205 (100)	294 (75)	279 (65)	223.07431	223.07536	-5	221.05883	221.06080	-9
1-hydroxypyrene	flu/pyr	218/290	290 (100)	259 (55)	275 (50)	219.08129	219.08044	4	217.06608	217.06589	1
4-ring hydroxy-PAH B	flu/pyr	218/290	290 (100)	259 (55)	275 (50)	219.08141	219.08044	4	217.06535	217.06589	-2
4-ring hydroxy-PAH C	flu/pyr	218/290	290 (100)	259 (55)	275 (50)	219.08144	219.08044	5	217.06521	217.06589	-3
4-ring hydroxy-PAH D	flu/pyr	218/290	290 (100)	275 (30)	259 (20)	219.08133	219.08044	4	217.06581	217.06589	-0.4
4-ring dihydroxy-PAH A	flu/pyr	234/380	290 (40)	380 (30)	202 (30)	235.07451	235.07536	-4	233.05985	233.06080	-4
4-ring dihydroxy-PAH B	flu/pyr	234/380	290 (60)	380 (30)	202 (20)	235.07400	235.07536	-6	233.05849	233.06080	-10
4-carboxy-5-phenanthrenecarboxaldehyde	pyrene	250/322	205 (100)	293 (90)	189 (35)	251.07035	251.07027	0.3	249.05758	249.05572	7
4-hydroxyphenanthro(4,5-cde)oxepin-6-one	pyrene	250/322	189 (100)	294 (50)	205 (30)	251.07159	251.07027	5	249.05485	249.05572	-3
3-ring carboxy-PAH A	pyrene	222/294	293 (100)	189 (85)	205 (30)	223.07561	223.07536	1	221.06053	221.06080	-1
3-ring carboxy-PAH B	pyrene	222/294	293 (100)	189 (70)	279 (30)	223.07454	223.07536	-4	221.05981	221.06080	-4
Pyrene + O3											
4-phenanthrenecarboxaldehyde	pyrene	205	205 (100)	176 (20)	151 (15)	207.08028	207.08044	-1	206.07105	206.07371	-13
4-oxapyrene-5-one	pyrene	220	220 (100)	163 (43)	192 (21)	221.06070	221.05971	5	220.05219	220.05298	-4
phenanthrene-4,5-dicarboxaldehyde	pyrene	234	205 (100)	176 (30)	218 (10)	235.07472	235.07536	-3	233.06032	233.06080	-2
4-hydroxy-5-phenanthrenecarboxaldehyde	pyrene	222/294	205 (100)	293 (50)	176 (25)	223.07584	223.07536	2	221.05887	221.06080	-9
3-ring carboxy-PAH A	pyrene	222/294	293 (100)	189 (85)	205 (30)	223.07561	223.07536	1	221.06053	221.06080	-1
3-ring carboxy-PAH B	pyrene	222/294	293 (100)	189 (70)	279 (30)	223.07454	223.07536	-4	221.05981	221.06080	-4
4-carboxy-5-phenanthrenecarboxaldehyde	pyrene	250/322	205 (100)	293 (90)	189 (35)	251.07035	251.07027	0.3	249.05481	249.05572	-4
4-hydroxyphenanthro(4,5-cde)oxepin-6-one	pyrene	250/322	189 (100)	294 (50)	205 (30)	251.07159	251.07027	5	249.05369	249.05572	-8
Anthracene + O3											
anthrone	anthracene	194	194 (100)	165 (75)		195.07911	195.08044	-7	193.06543	193.06589	-2
9,10-anthracenedione	anthracene	208	208 (100)	180 (88)	152 (67)	209.05980	209.05971	0	208.05291	208.05298	0
9-methoxyanthracene	anthracene	208	193 (100)	208 (60)	165 (50)	ND			ND		
n-hydroxyanthracene	anthracene	195	266 (100)	251 (25)	165 (10)	ND			ND		
n,n-dihydroxyanthracene	anthracene	210	354 (100)	235 (10)	265 (10)	ND			ND		

a For hydroxy- and carboxy-PAHs the MW for both the non- and BSTFA-derivatized molecule are shown.
b (1) indicates observed with EI-MS and (2) indicates observed with APCI-HRMS

In this work pyrene was confirmed as the parent PAH through experiments with pyrene alone exposed to O_3 (Appendix XV). Multiple 3-ring carboxylic acid derivatives (Table 19) were also observed. This is in contrast to previous studies where only a single carboxylic acid derivative was observed from the heterogeneous and aqueous phase ozonation of pyrene.[72,75] These were confirmed to be a product of pyrene ozonation by performing experiments with pyrene only.

To our knowledge, we have for the first time identified from the heterogeneous ozonation of pyrene phenanthrene derivatives with mixed functional groups, previously only reported from the aqueous ozonation of pyrene.[75] 4-carboxy-5-phenanthrenecarboxaldehyde and 4-hydroxyphenanthro(4,5-cde)oxepin-6-one are difficult to identify due to similar molecular ions before and after derivatization (*m/z* 250 and *m/z* 322, respectively) despite having different functional groups (see EI-MS and APCI-HRMS spectra in Appendix XVII).

Fig. 12. EIC GC-MS chromatograms of the common ion *m/z* 205 showing products formed during the ozonation of 3- and 4-ring PAHs from the analysis of the filter extract without derivatization (top) and after derivatization with BSTFA (bottom). Inset of the top chromatogram shows an EIC of *m/z* 205.06±0.03 observed after the HPLC-APCI-HRMS analysis of the same extract.

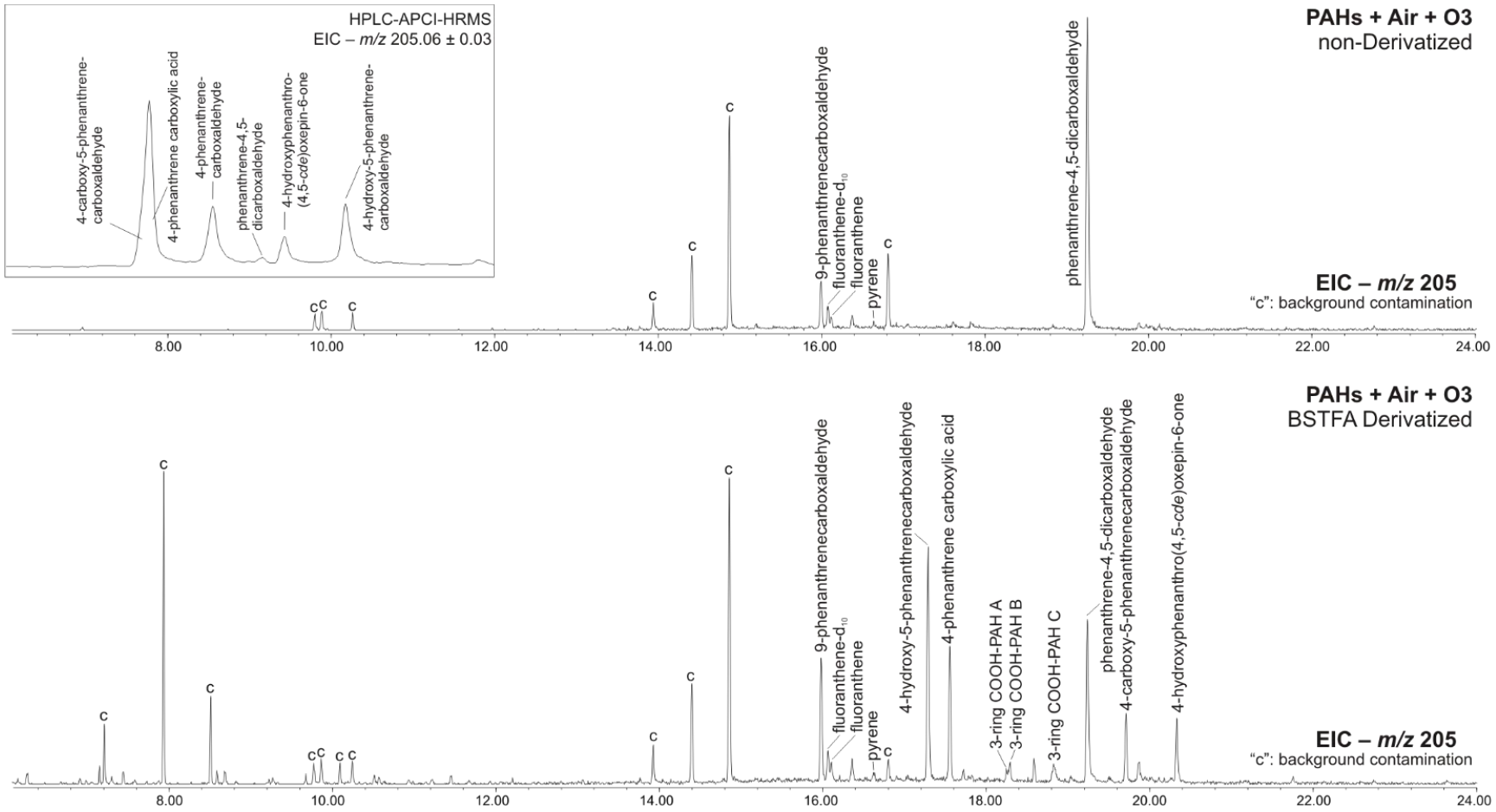

4-Hydroxy-5-phenanthrenecarboxyaldehyde was identified upon derivatization of the hydroxy group. Previously the identification of this product (with a molecular ion of *m/z* 293) was uncertain due to the MS spectra resembling that of a phenanthrenecarboxylic acid.[72] However analysis of standards of 4- and 9-phenanthrenecarboxylic acid showed a molecular ion of *m/z* 294 after derivatization. Although the molecular ion ($M^{+\bullet}$) of 4-hydroxy-5-phenanthrenecarboxaldehyde would be *m/z* 294, the aldehyde group is easily deprotonated, thus giving a $[M–H]^{+\bullet}$ molecular ion with *m/z* 293.

Similarly as for pyrene, this is the first time, to our knowledge, that hydroxy-fluoranthenes have been identified in heterogeneous ozonation reaction with fluoranthene (Table 19). Originally these hydroxy species were thought to be a product from the ozonation of pyrene, however experiments with pyrene only did not yield these products (Appendix XV). The specific isomeric identity of these hydroxyfluoranthenes could not be established due to standards not currently being available.

For anthracene the two major products observed were 9,10-anthracenedione and anthrone. The amount of 9,10-anthracenedione observed from the ozonation of anthracene was significantly higher (ca. 3-fold) than that observed during either desorption experiments or nitration. In contrast, the anthrone response was similar to that during desorption experiments, and therefore this product is not believed to be formed from the ozonation of anthracene. This finding conflicts with previous studies that report anthrone as a major product from anthracene ozonation. The ozonation of phenanthrene also produced two major products: 9,10-phenanthrenedione and 1,1'-biphenyl-2,2'-dicarboxaldehyde, the former of which has not been previously reported.

6.2.4. Reaction with NO_3/N_2O_5

Experiments were performed exposing PAHs to NO_3/N_2O_5 (formed by reacting NO_2 and O_3) under dark conditions. The loss of PAHs for the heterogeneous reaction with a mixture of NO_2 and O_3 was comparable to that with ozone alone and to previous studies (Appendix XIII).[72,77,79,82] However, the product pattern significantly differed (Table 20; GC-MS TIC chromatograms shown in Appendix XIV). For the nitration with NO_2 alone, only three major nitration products were observed. By contrast, when NO_2 was employed in combination with O_3, numerous nitro- 3-ring and 4-ring PAHs were observed. While the reaction of NO_2 with phenanthrene produced 9-nitrophenanthrene, oxidation by NO_3/N_2O_5 resulted in multiple nitrophenanthrene isomers These additional nitro-PAH products have not been reported in heterogeneous nitration or ozonation studies (Figure 13a). It was possible that these may be nitroanthracene isomers, however, experiments with anthracene alone produced only 9-nitroanthracene and no other products (Figure 13a). In addition to the nitro-phenanthrene products, phenanthrene yielded the same two oxy- products as observed from its reaction with ozone (Table 20). Anthracene, however, yielded a hydroxy-nitroanthracene isomer that has not been previously reported from heterogeneous oxidation studies (Table 20). In addition, experiments with anthracene alone yielded a hydroxyanthracene and a dihydroxyanthracene species (Table 20; mass spectra shown in Appendix XV). Similar to pyrene ozonation, the reaction of pyrene with NO_3/N_2O_5 yielded products with similar *m/z* 205 ion fragments (EIC shown in Appendix XVIII).

The difference in the reaction products between NO_2 and NO_2+O_3 can be attributed to the formation of the nitrate radical which may further react with NO_2 producing dinitrogen pentoxide, both of which have been found to be more potent

oxidizers than either NO_2 or O_3.[14,20] In our study, significantly lower concentrations (Appendix XIX) of nitration products were observed upon the addition of UV light to the experiment, likely due to reduced NO_3 lifetimes by photolysis.

Table 20. Products observed from reactions of a mixture of PAHs, pyrene only, and anthracene only with O_3+NO_2 (N_2O_5/NO_3).

						APCI-HRMS Data					
						$[M+H]^+$ Ion (Da)			$[M–H]^-$ or $[M+e^-]^-$ Ion (Da)		
Identified Oxidation Product	Parent PAH	MW[a]	EI-MS Major Ions (Rel. Ab.) 1	2	3	Observed Mass	Calculated Mass	Error (ppm)	Observed Mass	Calculated Mass	Error (ppm)
PAHs + NO_2 + O_3											
1,1'-biphenyl-2,2'-dicarboxaldehyde	phenanthrene	210	181 (100)	152 (37)	210 (3)	211.07391	211.07536	-7	209.05826	209.06080	-12
anthrone	anthracene	194	194 (100)	165 (75)		195.07838	195.08044	-11	193.06562	193.06589	-1
9,10-anthracenedione	anthracene	208	208 (100)	180 (88)	152 (67)	209.05903	209.05971	-3	208.05488	208.05298	9
9,10-phenanthrenedione	phenanthrene	208	180 (100)	152 (60)	208 (40)	209.05871	209.05971	-5	208.05250	208.05298	-2
4-oxapyrene-5-one	pyrene	220	220 (100)	163 (43)	192 (21)	221.05870	221.05971	-5	220.05320	220.05298	1
phenanthrene-4,5-dicarboxaldehyde	pyrene	234	205 (100)	176 (30)	218 (10)	235.07568	235.07536	1	233.06167	233.06080	4
4-phenanthrenecarboxaldehyde	pyrene	205	205 (100)	176 (20)	151 (15)	207.07997	207.08044	-2	206.07129	206.07371	-12
9-nitroanthracene	anthracene	223	176 (100)	223 (95)	193 (80)	224.07282	224.07060	10	223.06350	223.06388	-2
9-nitrophenanthrene	phenanthrene	223	165 (100)	176 (80)	223 (60)	224.07074	224.07060	1	223.06287	223.06388	-5
n-nitrophenanthrene A	phenanthrene	223	165 (100)	193 (60)	223 (30)	224.07154	224.07060	4	223.06333	223.06388	-2
n-nitrophenanthrene B	phenanthrene	223	165 (100)	176 (80)	223 (45)	224.07036	224.07060	-1	223.06334	223.06388	-2
n-nitrophenanthrene C	phenanthrene	223	223 (100)	176 (75)	165 (45)	224.07057	224.07060	0	223.06342	223.06388	-2
n-nitrophenanthrene D	phenanthrene	223	223 (100)	177 (60)	176 (55)	224.07044	224.07060	-1	223.06321	223.06388	-3
n-nitrofluoranthene A	fluoranthene	247	201 (100)	247 (90)	189 (45)	248.07166	248.07060	4	247.06234	247.06388	-6
n-nitrofluoranthene B	fluoranthene	247	201 (100)	247 (90)	189 (40)	248.07096	248.07060	1	247.06482	247.06388	4
n-nitrofluoranthene C	fluoranthene	247	247 (100)	201 (80)	189 (60)	248.07130	248.07060	3	247.06340	247.06388	-2
n-nitrofluoranthene D	fluoranthene	247	247 (100)	201 (90)	189 (35)	248.07156	248.07060	4	247.06293	247.06388	-4
1-nitropyrene	pyrene	247	201 (100)	247 (90)	217 (70)	248.06991	248.07060	-3	247.06529	247.06388	6
1-hydroxypyrene	pyrene	218/290	290 (100)	259 (55)	275 (50)	219.08129	219.08044	4	217.06608	217.06589	1
4-ring hydroxy-PAH B	flu/pyr	218/290	290 (100)	259 (55)	275 (50)	219.08141	219.08044	4	217.06535	217.06589	-2
4-ring hydroxy-PAH C	flu/pyr	218/290	290 (100)	259 (55)	275 (50)	219.08144	219.08044	5	217.06521	217.06589	-3
4-ring hydroxy-PAH D	flu/pyr	218/290	290 (100)	275 (30)	259 (20)	219.08133	219.08044	4	217.06581	217.06589	0
4-ring dihydroxy-PAH A	flu/pyr	234/380	290 (40)	380 (30)	202 (30)	235.07566	235.07536	1	233.06025	233.06080	-2
4-ring dihydroxy-PAH B	flu/pyr	234/380	290 (60)	380 (30)	202 (20)	235.07531	235.07536	0	233.06022	233.06080	-3
4-carboxy-5-phenanthrenecarboxaldehyde	pyrene	250/322	205 (100)	293 (90)	189 (35)	251.07089	251.07027	2	249.05715	249.05572	6
4-hydroxyphenanthro(4,5-*cde*)oxepin-6-one	pyrene	250/322	189 (100)	294 (50)	205 (30)	251.07082	251.07027	2	249.05383	249.05572	-8
n-hydroxy-*n*-nitroanthracene	anth/phen	239/311	311(100)	281 (25)	265 (20)	240.06408	240.06552	-6	239.05733	239.05879	-6
4-ring nitro-hydroxy PAH	flu/pyr	263/335	320(100)	335(30)	290(30)	264.06480	264.06552	-3	263.05719	263.05879	-6
Pyrene + NO_2 + O_3											
4-phenanthrenecarboxaldehyde	pyrene	205	205 (100)	176 (20)	151 (15)	207.07997	207.080441	-2	206.07128	206.07371	-12
4-oxapyrene-5-one	pyrene	220	220 (100)	163 (43)	192 (21)	221.05866	221.05975	-5	220.05358	220.05298	3
1-nitropyrene	pyrene	247	201 (100)	247 (90)	217 (70)	248.06989	248.07060	-3	247.06652	247.06388	11
phenanthrene-4,5-dicarboxaldehyde	pyrene	234	205 (100)	176 (30)	218 (10)	235.07481	235.07535	-2	233.05897	233.06080	-8
4-carboxy-5-phenanthrenecarboxaldehyde	pyrene	220	220 (100)	163 (43)	192 (21)	251.07121	251.07027	4	249.05917	249.05572	14
4-hydroxyphenanthro(4,5-*cde*)oxepin-6-one	pyrene	234	205 (100)	176 (30)	218 (10)	251.07220	251.07027	8	249.05544	249.05572	-1

Table 20. cont.

Identified Oxidation Product	Parent PAH	MW_a	EI-MS Major Ions (Rel. Ab.) 1	2	3	APCI-HRMS Data [M+H]+ Ion (Da) Observed Mass	Calculated Mass	Error (ppm)	[M–H]– or [M+e–]– Ion (Da) Observed Mass	Calculated Mass	Error (ppm)
Anthracene + NO_2 + O_3											
anthrone	anthracene	194	194 (100)	165 (75)		195.07838	195.08044	-11	193.06562	193.06589	-1
9,10-anthracenedione	anthracene	208	208 (100)	180 (88)	152 (67)	209.05903	209.05971	-3	208.05488	208.05298	9
9-nitroanthracene	anthracene	223	176 (100)	223 (95)	193 (80)	224.07282	224.07060	10	223.06350	223.06388	-2
n-hydroxyanthracene	anthracene	194/266	266 (100)	251 (20)	165 (18)	195.08095	195.08044	3	193.06552	193.06589	-2
n-hydroxy-*n*-nitroanthracene	anthracene	239/311	311(100)	281 (25)	265 (20)	240.06408	240.06552	-6	239.05733	239.05879	-6

a For hydroxy- and carboxy-PAHs the MW for both the non- and BSTFA-derivatized molecule are shown.

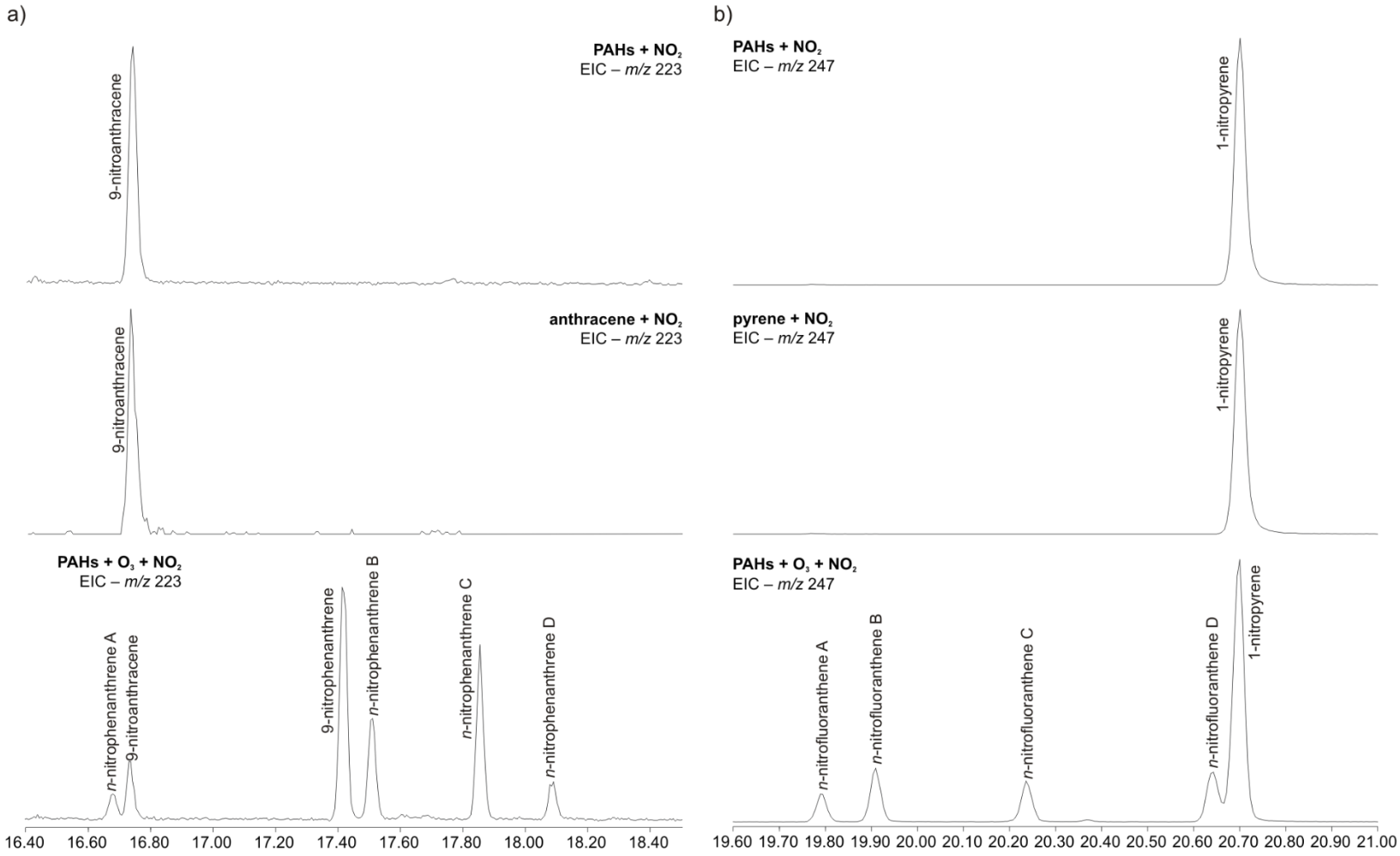

Fig. 13. Extracted Ion Chromatograms (EIC) of a) *m/z* 223 ($M^{\bullet+}$ of 3-ring nitro-PAH) and b) *m/z* 247 ($M^{\bullet+}$ of 4-ring nitro-PAH) of extracts from the reactions of a mixture of PAHs with NO_2 only (top) and PAHs with NO_2+O_3 (bottom). An EIC of an extract from the reaction anthracene with NO_2 only (middle) is also shown.

The reaction of NO_3/N_2O_5 with 4-ring PAHs yielded additional products not observed with either NO_2 or O_3 alone (Figure 13b). Fluoranthene yielded four nitro products that were not observed from its reaction with NO_2, while pyrene produced only 1-nitropyrene. This observation suggests that in the presence of a strong oxidant fluoranthene is less stereoselective than the more stereo-directing pyrene.

6.3. Conclusions

The heterogeneous oxidation of 3- and 4-ring PAHs in the presence of NO_2, O_3 or NO_2+O_3 were investigated in a small-scale flow reactor. Major products observed from each reaction were identified using a combination of available standards and the use of EI-MS spectral libraries and high resolution APCI-MS TOF data. The reaction of PAHs with NO_2 was found to be selective among the species studied, with anthracene and pyrene being more reactive than phenanthrene and fluoranthene. Ozonation of all of the PAHs was less selective, producing multiple species for each PAH reactant, some of which have not been previously identified. The reaction of NO_2+O_3 (NO_3/N_2O_5) with the studied PAHs produced additional species not observed with their reaction with either NO_2 or O_3 alone. Multiple isomers of nitrophenanthrene and nitrofluoranthene were observed, of which the former species have not been previously reported. The reaction of anthracene with NO_3/N_2O_5 also produced hydroxy-nitro derivatives, also not previously reported in literature.

6.4. Future Work

The oxidation of anthracene while adsorbed to the quartz filter and exposed to only air or N_2 was not expected. The only products observed and assumed to result from these losses of anthracene were 9,10-anthracenedione and anthrone. Preliminary experiments using Teflon filters resulted in limited losses of anthracene while both

products were not observed. Thus it is proposed that the SiO_2 framework of the filter plays a key role in this process; however, further work needs to be performed to gain a better understanding.

This work focused on identifying the products formed during the heterogeneous oxidation of PAHs while exposed to NO_2, O_3 or NO_3/N_2O_5. While a mass balance was achieved and reported here for the nitration of pyrene forming 1-nitropyrene, mass balances for other major oxidation products still needs to be performed.

CHAPTER 7

7. FORMATION AND DECAY OF AEROSOL-ASSOCIATED NITRATED PAHs IN DIESEL ENGINE EXHAUST EXPOSED TO ATMOSPHERIC OXIDANTS.

7.1. Experimental

7.1.1. Chemicals and Materials

Nitrogen monoxide (NO) and nitrogen dioxide (NO_2) were obtained from Airgas (Grand Forks, ND, USA).

7.1.2. Large-Scale Aerosol Chamber

Diesel exhaust aging experiments were performed in a 10 m^3 atmospheric simulation reactor bag (see diagram in Figure 14). The reactor was housed in an enclosure, which also included on-line instrumentation, air sampling units (for off-line analysis), a gas dilution and injection system and a transfer line system to inject diesel engine exhaust. The reactor bag was composed of transparent 2 mil (54 µm thick) fluoroethylene propylene (FEP) film (Dupont, Johnston, Iowa, USA) and was made by sealing four sheets at 2.35 m x 1.45 m each using an industrial sealer (West Coast Plastics, Inc., Culver City, CA, USA) (see Figure 15). The reactor was supported by netting stretched approximately 0.1 m off the chamber floor to reduce stress on the reactor bag walls and seals. The walls of the chamber were made with fire-proof drywall paneling supported by a steel frame. On the inside of the enclosure the walls were lined with 5 mil mirror sheeting (Nielsen Enterprises, Kent, WA, USA) to enhance light

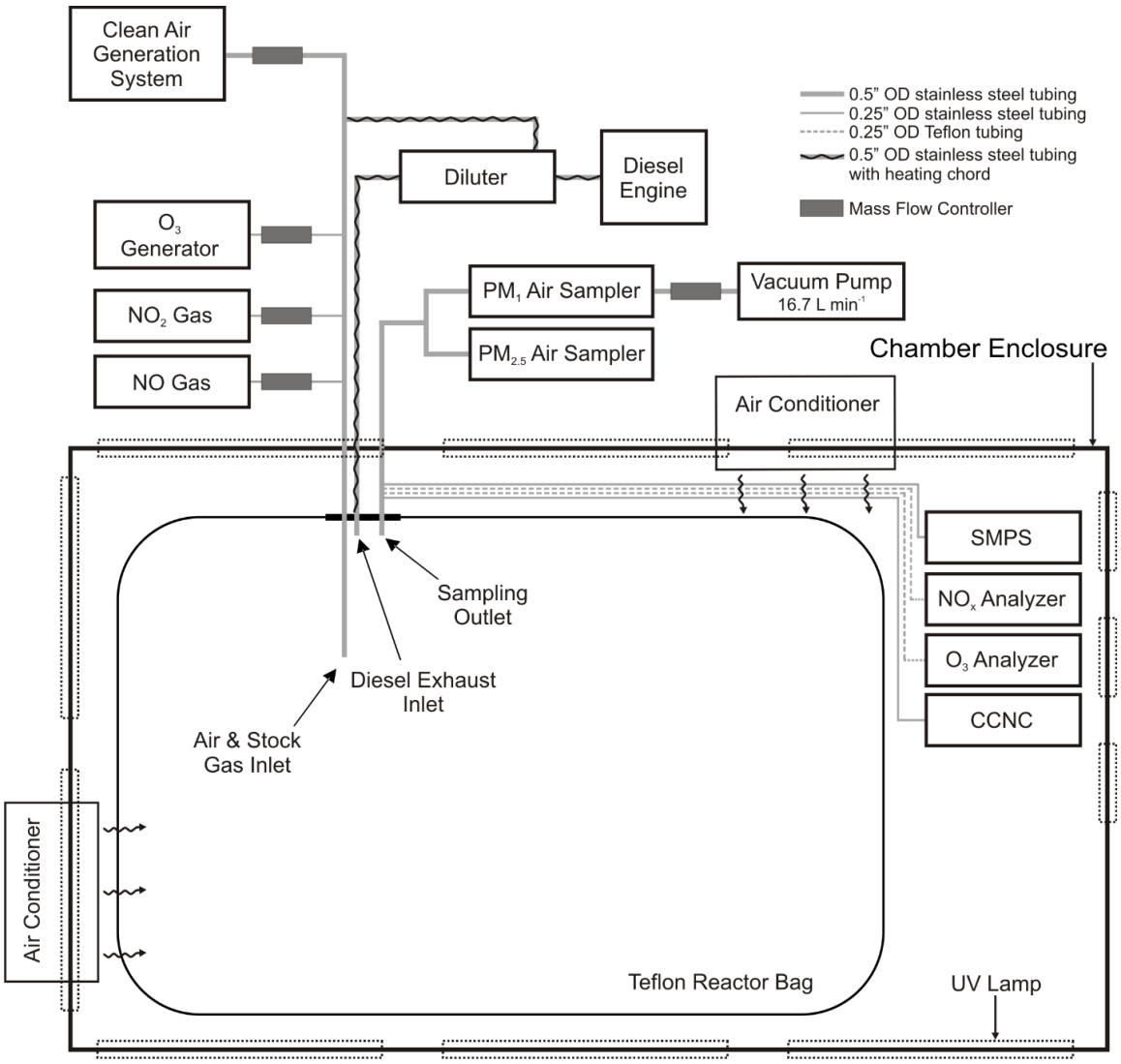

Fig. 14. Schematic representation of the large-scale aerosol chamber used for investigating the fate of PAHs and polar PAH derivatives during the aging of diesel engine exhaust.

intensity within the enclosure. The temperature inside the enclosure (and reactor bag) was controlled through two industrial air conditioners (17400 BTU/h at 1800 W; General Electric, Fairfield, CT, USA) and two electric base-board heaters. Ultraviolet irradiation was provided by eighty-one 40 in. ultraviolet black lights (40 W; Sylvannia, Danvers, MA, USA) installed along all four walls and the ceiling of the enclosure

The inlet and outlet lines for the reactor bag were located at approximately half the bag height (~ 0.8 m) and were supported by a Teflon plate. Both the inlet and outlet lines were 0.5" O.D. stainless steel (Swagelok, Solon, OH, USA). The openings of the gas inlet line was positioned to elute at the center of the bag while the particle inlet line was positioned towards the outside to avoid biased interactions prior to mixing. The outlet line was also positioned near the bag wall. Before each experiment the reactor bag was flushed with at least three whole volumes of the bag at a mass flow rate of 1.8 m^3 h^{-1} with UV irradiation for a minimum of 10 h (two entire bag volumes).

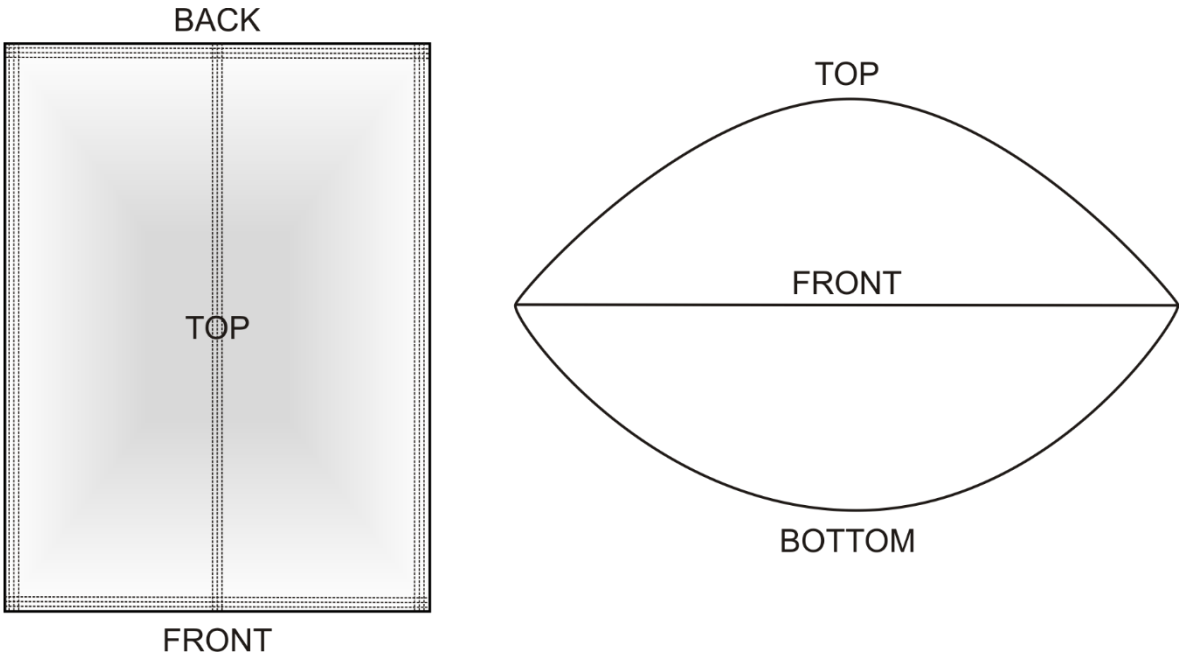

Fig. 15. Diagram of the FEP bag used to house atmospheric simulation reactions as viewed from the top (left) and the front (right). Locations of the seals are shown with dotted lines.

7.1.3. Diesel Engine

All experiments performed with injected diesel engine exhaust (DE; containing diesel exhaust particles (DEP) and gases) are listed in Table 21. All diesel exhaust aging experiments were carried out using a 2.4L displacement four-cylinder diesel engine

(Kubota, Torrance, CA, USA) with a standard power output of 49.2 kW. Prior to exhaust injection, the diesel engine was run at 1100 rpm for approximately 10 min until the engine temperature reached at least 110 °F. During injection of diesel exhaust into the reactor bag the engine was run at 1000 rpm with no added engine loads and the exhaust pipe outlet covered at ~90% to direct exhaust through the sampling line and into an exhaust dilution system. All runs were performed using standard diesel fuel (without winterizing additives) obtained from local fuel stations (Kroger, Grand Forks, ND, USA).

Diesel exhaust was sampled from the engine exhaust pipe through a 0.5 in. O.D. stainless steel tube connected to an ejector diluter (see schematic representation in Appendix XX) where the exhaust was diluted with filtered and dried air. The ejector diluter was built using 316 stainless steel, with a design based on the commercially available Dekati DI-1000 diluter. The outlet of the diluter was connected to the inlet of the reactor bag by a heated transfer line composed of 0.5" O.D. stainless steel tubing. Prior to turning on and running the diesel engine, both the dilution air line (~ 1.5 m) and diluter-reactor transfer line (~ 2 m) were heated above 150 °C to limit condensation of exhaust gases in the walls of the diluter and transfer line. Injection of diesel exhaust was controlled by a stainless steel 3-way ball valve (Swagelok) located at the end of the transfer line immediately prior to the reactor bag inlet. Initial experiments using only the dilution air as the means to draw sample from the engine exhaust resulted in PM mass concentrations (μg m^{-3}) being too low for detecting targeted PAHs and derivatives. Therefore for the final experiments the engine exhaust was partially covered to induce added flow through the exhaust sampling line (giving final a dilution ratio of ~ 1.5–2:1). During the diesel engine warmup period the valve diverted the diluted exhaust through a

stainless steel line which discarded the exhaust into the ambient air outside of the building housing the chamber system. Injection of the diesel engine exhaust into the reactor was then performed by diverting the exhaust into the chamber by a 3-way valve.

Table 21. List of experiments performed in the large-scale reaction chamber evaluating PAH oxidation during the aging of diesel engine exhaust.

			Reactor Conditions						D_p^{mean}	
Exp. #	**Gas Injected**	**Light**	**T (°C)**	**RH (%)**	**$[DEP]_{max}$ (µg/m3)[a]**	**$[O_3]_0$ (ppb)**	**$[NO]_0$ (ppb)**	**$[NO_2]_0$ (ppb)**	**t_0 (nm)**	**t_{end} (nm)**
1	Air	Dark	24.8–25.7	12.0–13.4	10	2	76	25	38	59
2[b]	Air	UV	–	–	10	–	–	–	39	54
3	Air	Dark	26.5–27.5	16.1–16.9	105	14	746	179	72	100
4	Air	Dark	25.7–26.4	19.4–22.9	802	99	3357	2	72	142
5	Air	UV	25.8–26.7	16.7–17.0	1110	102	3336	10	82	181
6	Air	Dark	25.1–26.0	15.8–16.7	744	88	3376	1	75	154
7	Air	UV	24.8–26.1	17.1–17.3	1150	102	3724	10	73	211

a For reactions under dark [DEP]max=[DEP]0; for reactions with UV [DEP]max≠[DEP]0

b Temperature, RH, and gas concentration data was not available.

7.1.4. Air Sampling Procedures

Air sampling was done using two different systems: one for collecting aerosols under 1.0 µm in diameter (PM_1) and another for aerosols under 2.5 µm ($PM_{2.5}$). PM_1 was collected using a particulate air sampling system (URG, Chapel Hill, NC, USA) consisting of a 1.0 µm cyclone, gooseneck adapter and a dual-filter cassette (for 90 mm diameter quartz filters). All components were made of aluminum and coated with Teflon to minimize interactions of both aerosols and gas-phase components. In order to collect residual gas-phase species not retained by the quartz filters, two successive polyurethane foam (PUF) filters were placed downstream of the quartz filter cassette. For $PM_{2.5}$ sampling a similar system was used but was obtained from BGI (Waltham, MA, USA) and consisted of a 2.5 µm cyclone with a dual-filter cassette (for 47 mm diameter glass-fiber filters). For both samplers quartz fiber filters were used, with each sampler having two filters in series to correct for collection of gases collected along with the aerosols. Air flow through both sampling systems was held constant at 16.7 L min^{-1}, necessary to maintain the particle diameter cut-offs (i.e., 1.0 µm for the PM_1 and 2.5 µm for the $PM_{2.5}$ sampler), using vacuum pumps The flow of the PM_1 sampler was controlled using a mass flow controller which the $PM_{2.5}$ sampler flow was controlled automatically by the sampler firmware. The air sampler inlets were installed at the very end of the outlet sampling line since the air flows of the samplers were significantly higher than all other on-line instrumentation.

Prior to use, both the quartz and glass fiber filters were prebaked at 500 °C for a minimum of 12 h. Filters were collected from the air sampling systems at the 1- and 4-hour points (from t_0) during the reaction, immediately placing the filter cassettes (with filters still inside) into Ziploc bags and placing them into a freezer at -20 °C until

extraction. PUF filters were placed into an amber-glass jar with a PTFE-lined cap, sealed and placed into a Ziploc bag and placed into a -20 °C freezer until extraction.

7.1.5. Online Analysis Instrumentation

The size distribution and mass of aerosols in the chamber were monitored by a scanning mobility particle sizer (SMPS) (TSI, Minneapolis, MN, USA), which consisted of a radioactive source (Kr-85) for producing a bipolar charge distribution on the sampled aerosols, a differential mobility analyzer (DMA) (TSI Model 3080) for classifying particles into narrow size fractions, and a condensation particle counter (CPC) (TSI Model 3775) for measuring the number concentration of the classified quasi-monodisperse aerosols. The DMA sheath air and aerosol sampling flow rates (for the CPC) were set to 1.8 and 0.3 L min^{-1}, respectively. These flow rates along with a 0.071 cm impactor (on the DMA inlet) specified an analysis range of 19.8–964.7 nm aerosol diameters. Size distribution and concentrations were measured in 3 min intervals using the Aerosol Instrument Manager (AIM) software (TSI).

Concentrations of NO_x species were measured by a chemiluminescence NO_x analyzer (Teledyne Model T200, San Diego, CA, USA). The NOx analyzer was calibrated using NO and NO_2 stock gases (stock concentration at 1 and 10 ppm, respectively) and diluting with clean, dry air in the range of 0–1000 ppb for NO and 0–2000 ppb for NO_2. Ozone levels in the reactor bag were monitored by a photometric ozone analyzer (Teledyne Model 400E). The ozone analyzer was calibrated using an 185 nm ozone generator (UVP, Upland, CA, USA) and dilution with clean, dry air in the range of 0–1500 ppb. Both the NOx and O_3 analyzers were connected to the outlet sampling train of the reactor bag with 0.25” O.D. Teflon tubing (Swagelok).

7.1.6. Filter Extraction and Sample Preparation Methods

Quartz filters collected during the aerosol simulation chamber experiments were extracted using sonication extraction. Prior to extraction, filters were spiked with recovery standard (RS) solutions composed of deuterated analogues of target PAH analytes and standards with similar structure but not naturally found in atmospheric aerosols (see Table 18 for list of RS compounds used). The filters were then extracted with 20 mL of dichloromethane three separate times (giving a final extract volume of 60 mL). The final extract volume was then reduced to ~ 0.2 mL using a gentle stream of nitrogen. The reduced extract volume was then transferred to an amino-propyl solid phase extraction (SPE) cartridge (Sep Pak, Waters, Milford, MA, USA). The extract was then fractionated into three individual volumes by elution with a series of solvent systems, starting with a non-polar solvent (*n*-hexane), then a mildly polar solvent system (20% DCM in *n*-hexane) and then a highly polar solvent (methanol) (see Section 3.1.3 for the detailed procedure). These SPE fractions were then evaporated down to 0.2 mL under nitrogen and split into two equal volumes of ~ 0.1 mL. The first volume was spiked with an internal standard (fluoranthene-d_{10}) and analyzed directly by GC-MS. The second volume was evaporated to dryness under nitrogen and then 100 µL of BSTFA was added (similar to optimized method in Section 3.1.3). The sample was then incubated at 70 °C for 6 h to allow for complete derivatization of hydroxyl and carboxylic acid groups. The derivatized samples were then spiked with internal standard (IS; fluoranthene-d_{10}) and analyzed by GC-MS.

GC-MS analysis was performed using the same system and conditions described in Section 3.1.4. The GC-MS data were acquired either in selected-ion monitoring (SIM) mode or a combination of the total ion current (TIC) and SIM modes, i.e., selected-ion-

total-ion (SITI). SITI combines the advantages of improved sensitivity, resulting from the use of SIM monitoring single ions, with simultaneous compound identification using TIC. A dwell time of 25 ms was used for all ions listed in Table 1 for both SIM and TIC mode and a range of 50–500 m/z was used for TIC. For the PM sample analysis SITI mode was employed.

7.1.7. Data Processing

For quantification of PAHs and derivatives in filter extracts an internal standard method was used employing fluoranthene-d_{10}. A single IS used was correcting for final volume changes of sample injected. To ensure and monitor for recoveries during the sample preparation RS mixture was added (Table 1) to each sample. The RS mixture consisted of representative species for each class of compounds studied and its recoveries were determined based using least square calibration curves. RSs were used to correct for analyte loss during the extraction and fractionation procedures.

GC-MS data was processed using MSD Chemstation (Agilent). SMPS data was processed using the AIM software (also used for data acquisition) and Origin 9.1. Integrations of the aerosol mass curves for the diesel exhaust aging experiments were performed using the Origin software.

7.2. Results and Discussion

7.2.1. Evaluating the Performance of the Aerosol Chamber

The overall purpose of the large-scale chamber was to simulate atmospherically relevant conditions. In comparison to the small-scale flow reactor, particle removal due to wall deposition is generally lower, however, the rates must still be determined to accurately interpret the behavior of diesel engine exhaust particles (DEP). For aerosols the three main impeding processes are wall loss, coagulation and

condensation/evaporation.[83] Typically, depending on the specific chemistry occurring on or around the aerosol, both coagulation and wall loss are the predominate processes.[83] For NO, NO_2 and O_3 gases, outside gas-phase reactions, the only major process affecting their concentration in the reactor bag is wall loss, a first-order process. To more accurately evaluate the changes in concentrations of aerosols and gases during diesel exhaust aging experiment, the loss rates for both aerosols and individual gases need to first be determined and used to correct data obtained from the aging experiments.

To evaluate the wall losses of gases, preliminary experiments were performed using NO, NO_2 and O_3 gases (those monitored during the diesel engine exhaust experiments) individually. Results from wall loss experiments for each of these gases are shown in Figure 16.

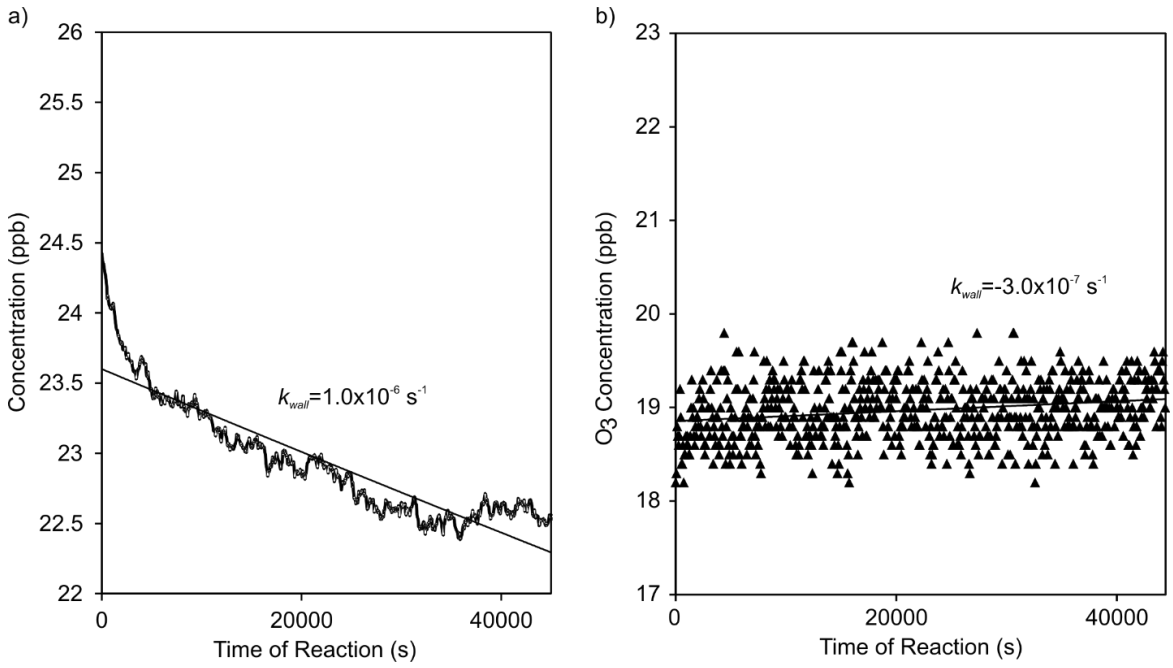

Fig. 16. Removal rates due to wall deposition of a) NO_2 and b) O_3 gases observed during experiments performed with each gas individually in clean, dry air.

During the exposure of NO_2 to air, the rate of NO_2 decline was observed to be first order, with k_{wall}=1.0x10^{-6} s^{-1}. This loss rate agrees with previous studies reporting wall deposition rates of NO_2 to FEP surfaces.[84] Exposure of O_3 to air only led to a stable concentration of O_3, observing a slight increase in levels over a ~8 h period (k_{wall}=-3.0x10^{-7} s^{-1}). This behavior also agrees well with previous studies.[83,84] To evaluate loss rate for particles in the reactor bag, experiments were performed with the injection of ammonium sulfate particles mixed with air (see Figure 17).

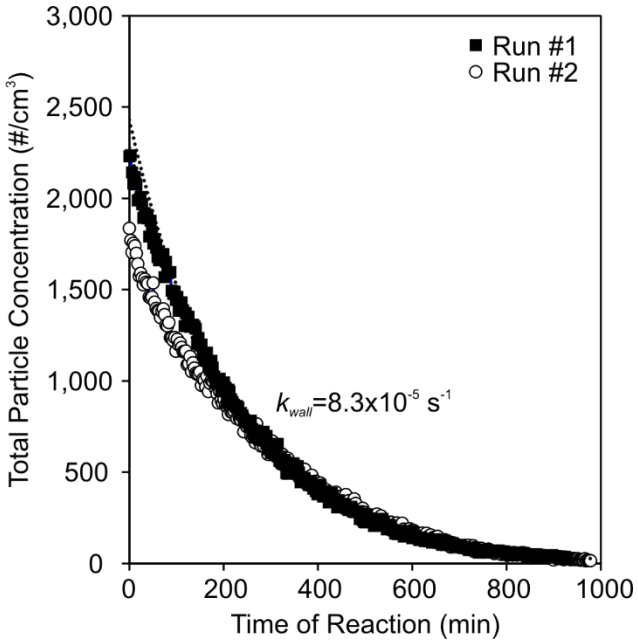

Fig. 17. Wall deposition rates of ammonium sulfate particles observed during a duplicate experiments performed in the large-scale aerosol chamber with exposure to air in dark conditions.

Dry ammonium sulfate particles were chosen as a surrogate to DEP based on their limited susceptibility to coagulation and condensation processes relative to DEP,[83] thereby allowing for a simpler estimation of particle wall loss rates. By keeping the particle number concentration small and the water levels low, contributions of both coagulation and condensation processes are minimal. From duplicate experiments with

ammonium sulfate using a starting particle concentration of around 2000 cm^{-3}, wall loss was observed to be first-order with k_{wall}=8.3x10^{-5} s^{-1}, following those previously reported for similar conditions (e.g., temperature, particle concentration, and experiment duration).[83,84]

7.2.2. Aging of Diesel Exhaust (DE)

Diesel exhaust (DE) aging experiments were performed by mixing the exhaust with air and then aging in two different environments: dark conditions and in the presence of UV irradiation. Experiments were performed with maximum DEP concentrations in the range of 10–1200 µg m^{-3}, however, to characterize the targeted organics in the aerosols (present at the ng/g level), high mass loadings of diesel exhaust particles (DEP) (700–1200 µg m^{-3}) were used. Under dark conditions, the DEP exhibited particle number loss rates were greater than those observed with ammonium sufate particles (5.2–6.5 x 10^{-4} versus 8.3 x 10^{-5} s^{-1}, respectively) as well as a slightly increased mean particle diameter (D_p) over the reaction time (Figure 18). The increase in D_p^{mean} signifies contributions of either coagulation of the DEP particles, condensation of gas-phase species onto the DEP, or both. Additionally, the increased rate of particle number loss relative to ammonium sulfate indicates a contribution from coagulation, which is expected with the very high number concentrations used. The DEP mass concentration did not show an increase during the reaction (Figure 19a & 19b). However, this may be a result of higher rates of wall losses that dominate over rates of coagulation.

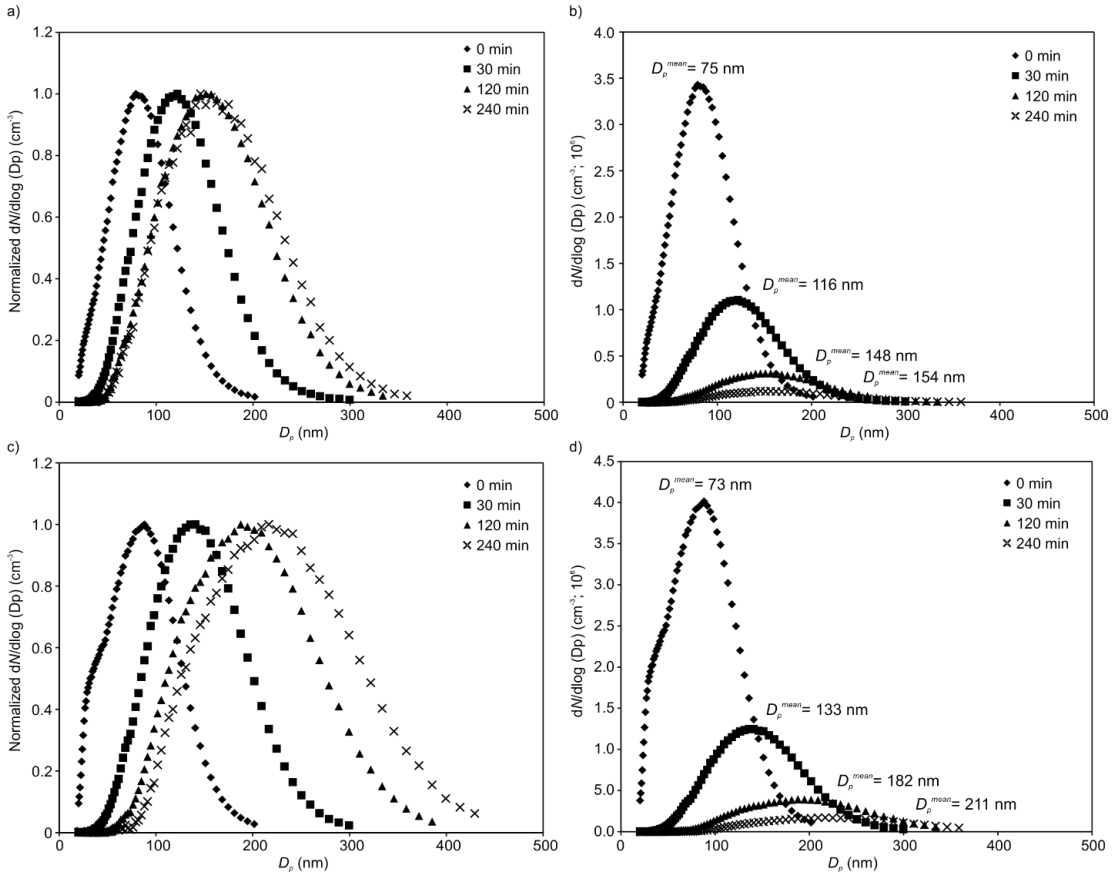

Fig. 18. Normalized (left) and raw (right) particle size distributions at 0, 30, 120 and 240 min during diesel exhaust again experiments under dark conditions (a,b) and with UV exposure (c,d).

When DEP was exposed to UV irradiation, the DEP mass concentration increased during the first 30 min of the reaction (Figure 19e), indicating the condensation of products formed during the photo-oxidation of gas-phase DE species. This is further supported by a similar rate of particle concentration decrease (Figure 19d) with a greater shift to a larger mean D_p compared to the reaction in dark conditions (Figure 19f; see Figure 19e for changes in mass concentrations).

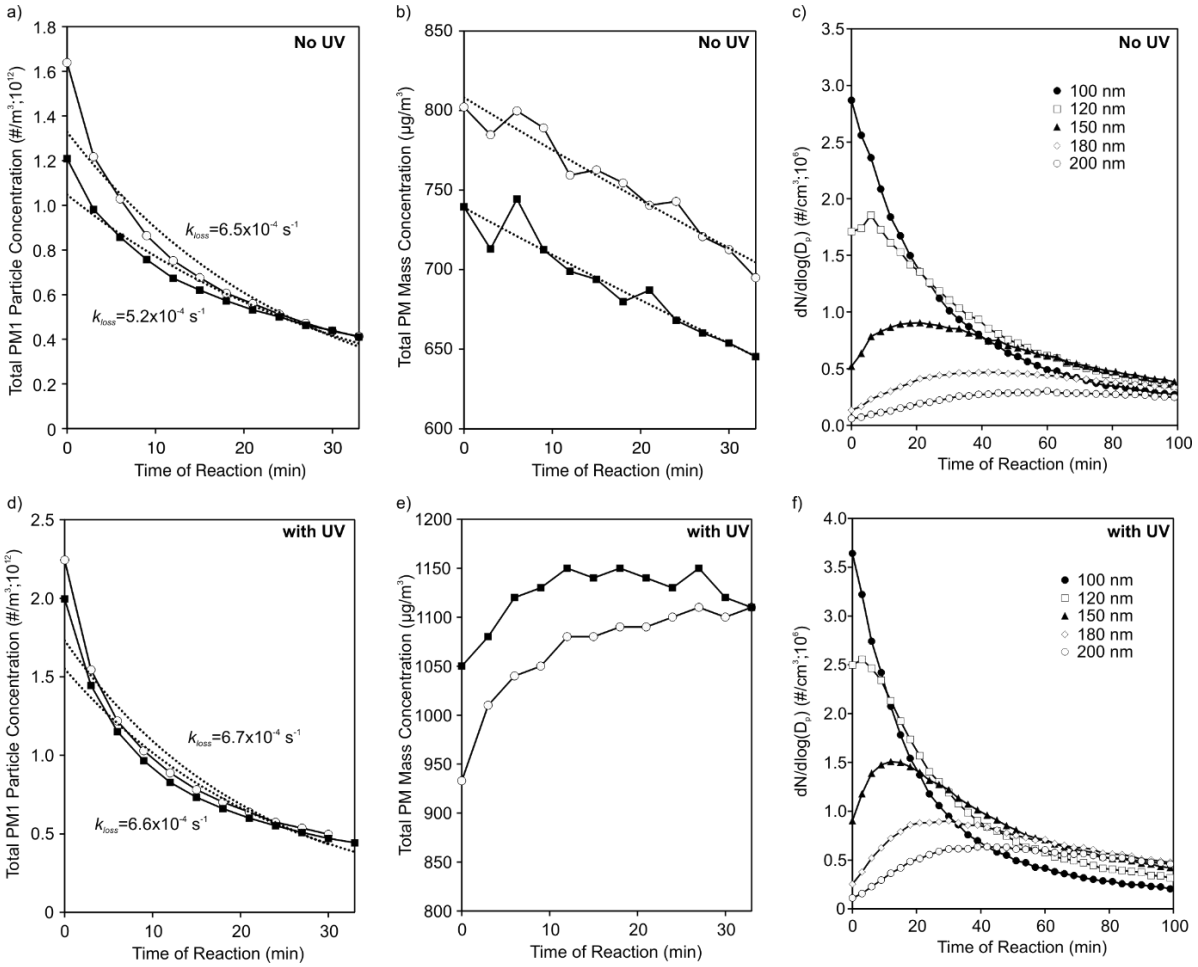

Fig. 19. SMPS measurements during DEP+Air experiment in dark conditions (top) and with UV irradiation (bottom), showing (a,d) total PM1 particle concentration, (b,e) mass concentrations, and (c,f) number concentrations for DEP at different D_p (nm). For figured a,b,d,e results from duplicate experiments are shown. Only the first 30 min of the reaction is shown to highlight the increase in mass concentration which began to decline after 30 min.

Changes in the distribution of the total mass of material in the reactor bag between the gas and particle-phases can also be viewed with the changes in masses observed for the filters collected in the air samplers during the reaction. By assigning all of the material collected by the top quartz filter as that being particle-phase only and that collected by the bottom quartz and both PUF filters as that being only gas-phase, the percentage of material in the particle phase can be estimated (Figure 20). The relationship between the DEP mass concentrations observed by the SMPS during the experiment and the mass changes of the top quartz filter (particle-phase only) was tested and found to have a direct correlation (see Figure 20c).

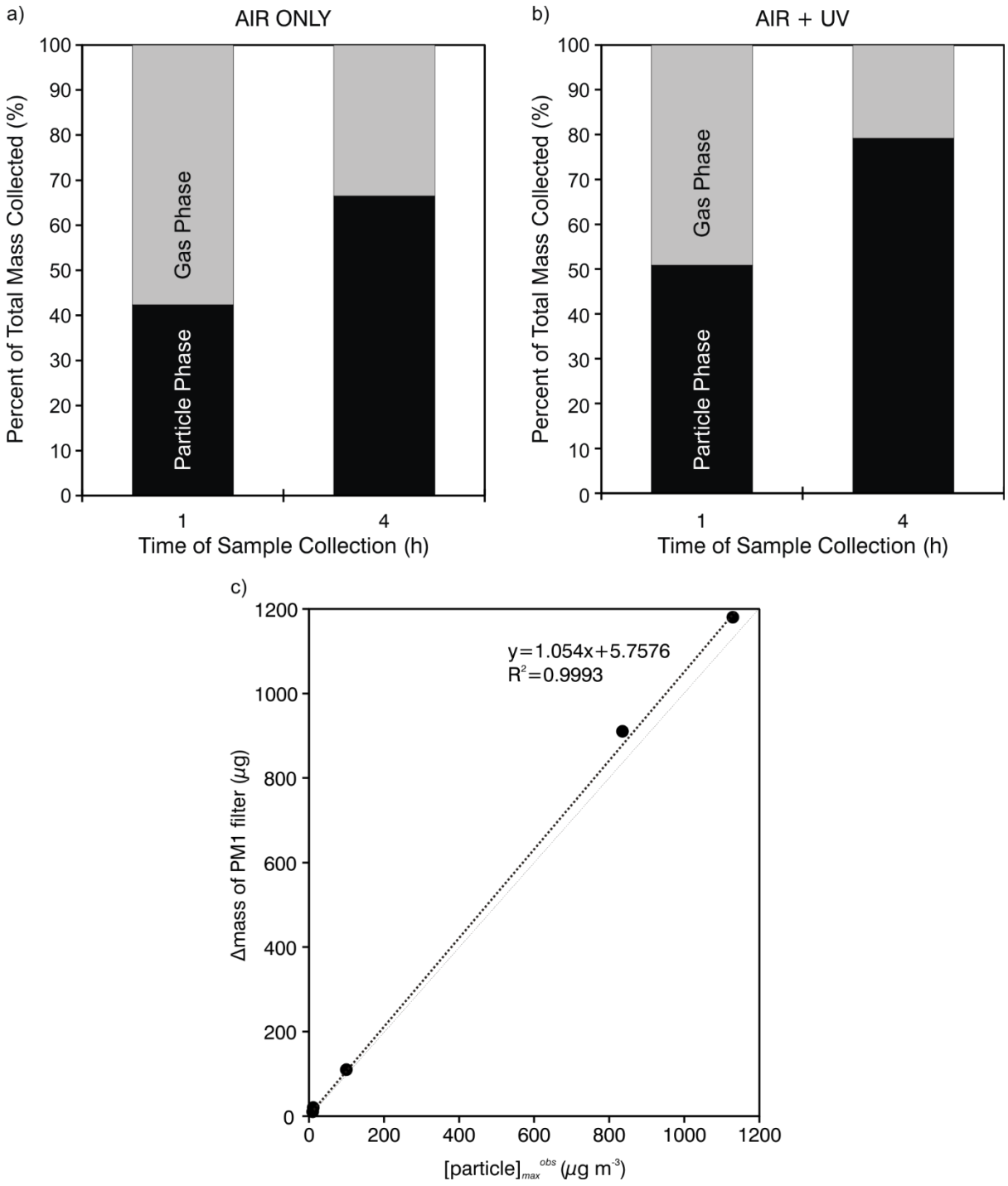

Fig. 20. Phase distributions of total mass collected on quartz and PUF filters during diesel exhaust aging experiments in the presence of a) air only and b) air with UV exposure. Mass collected on the top quartz filter was deemed to be all particle phase materials whereas the total mass collected onto the bottom quartz and two PUF filters were of gas phase. c) Comparison of observed PM_1 mass collected on the top quartz filter during the first hour of the reaction to PM_1 measured by the SMPS during diesel exhaust aging experiments at different DEP mass loadings over the same time frame.

Despite the DEP not showing an increase in mass concentration while aged under dark conditions, the higher particle-to-gas phase ratio observed at 4 h compared to 1 h (determined from the ratio of the mass on the top to bottom filters in the air sampler) still shows a degree of condensation. As expected, the distribution was more to the particle phase for DEP aging with UV exposure.

7.2.3. Kinetics of Polycyclic Aromatic Hydrocarbons During DE Aging

3–4 ring PAHs were monitored by analyzing extracts of the filters collected during each experiment of DE aging. Under dark conditions, all 3–4 ring PAHs (phenanthrene, anthracene, pyrene and fluoranthene) increased in their concentrations in the particle phase (mass of PAH per mass of PM; $\mu g\ g^{-1}$) during the reaction (Figure 21a) while their particle mass concentrations per volume of air ($\mu g\ m^{-3}$) decrease (Figure 21b), as would be expected through particle wall losses. Anthracene exhibited the largest increase in its particle-phase concentration and had the smallest change in its volumetric concentration over the same time frame. With UV exposure, PAHs were present in significantly lower concentrations in the filter extracts and all had a large decrease in their particle-phase and volumetric concentrations through the reaction (Figure 21c & 21d). This information indicates that significant photo-degradation was occurring.

In general, the transition from gas-phase to particle-phase through condensation onto DEP particles was similar for all of the 3–4 ring PAHs under dark conditions, being at 25–35% of their individual mass in the particle phase at 1 h and increasing to 68–75% at 4 h (Figure 22a). With UV exposure, they also showed similar behaviors between each other in that the percent of their individual masses in the particle phase was similar at the 1 and 4 hour points of the reactions (~50%) (Figure 22b).

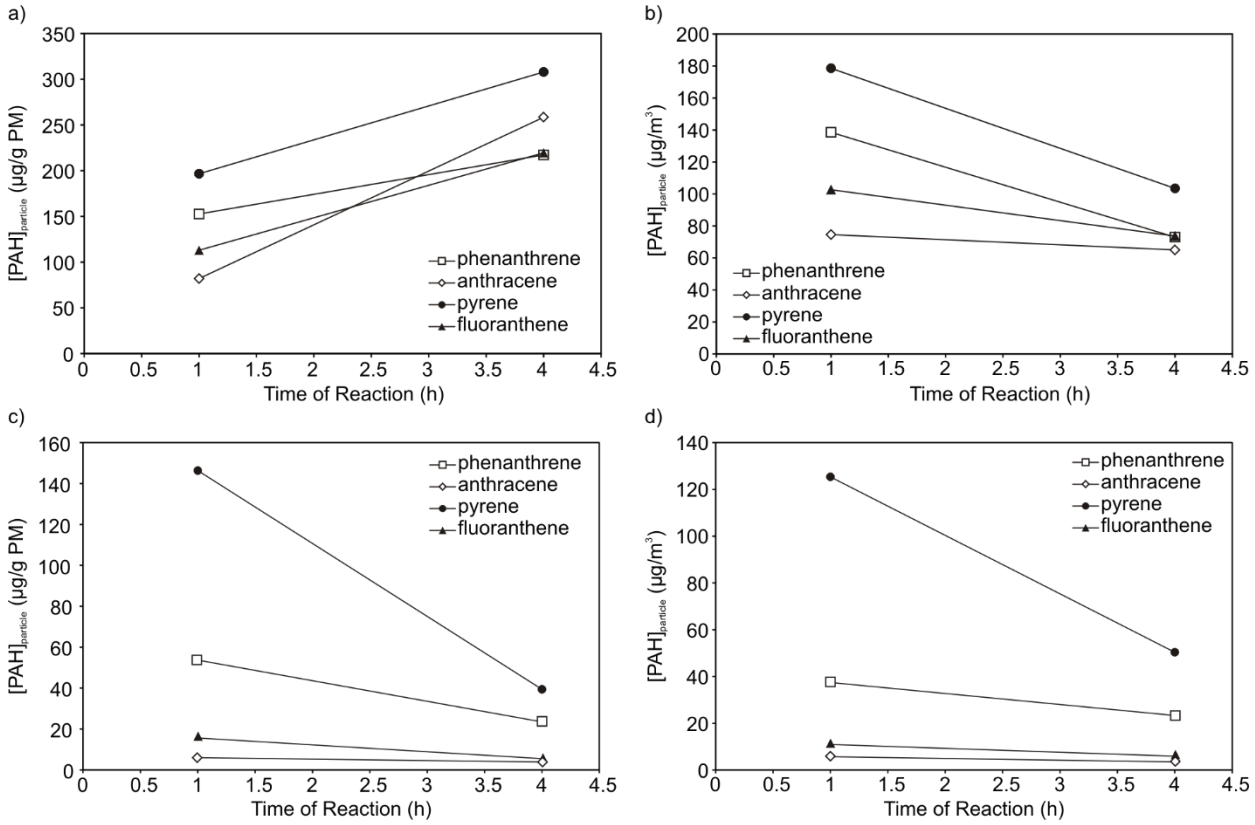

Fig. 21. Concentrations of 3–4 ring PAHs in terms of mass (left) and volume (right) concentrations obserbed during diesel exhaust aging experiments in the presence of air only (a,b) and air with UV exposure (c,d).

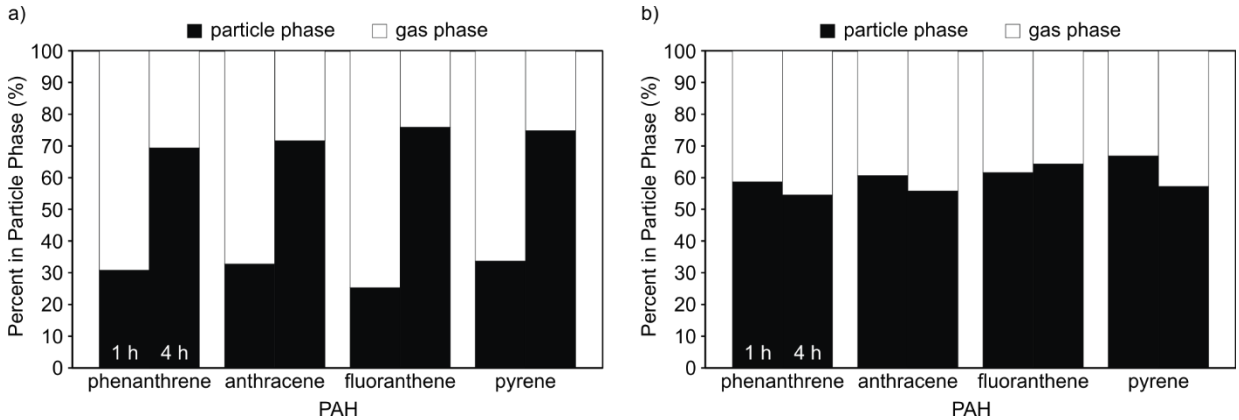

Fig. 22. Phase distributions of 3–4 ring PAHs observed during diesel exhaust aging experiments in the presence of a) air only and b) air with UV exposure.

It is unclear as to why the phase distributions of PAHs observed during both experiment (dark and with UV exposure) are significantly different. It is expected that UV irradiation

will decrease the overall mass of PAHs in the reactor volume, however, the phase distribution should remain similar.

7.2.4. Identification of Products Formed During the Aging of DE

With DE exposed to air under dark conditions, three nitro-PAH species were observed: 9-nitroanthracene, 1-nitropyrene and 3-nitrofluoranthene. These species were only observed in the extracts of the bottom quartz filters and not present in the top filter extracts (Figure 23). Both 1-nitropyrene and 3-nitrofluoranthene have been known to be emitted directly through diesel engine exhaust.[13] However, their complete partitioning into the gas-phase was not expected here. At 4 h into the reaction, only 9-nitroanthracene is observed, while both 1-nitropyrene and 3-nitrofluoranthene were not present, showing contributions of gas-phase oxidation processes.

During reactions with DE exposed to UV irradiation, the nitro-PAH species were not observed. This information shows that they are highly susceptible to photochemical processing, which corroborates previously reported studies.[85]

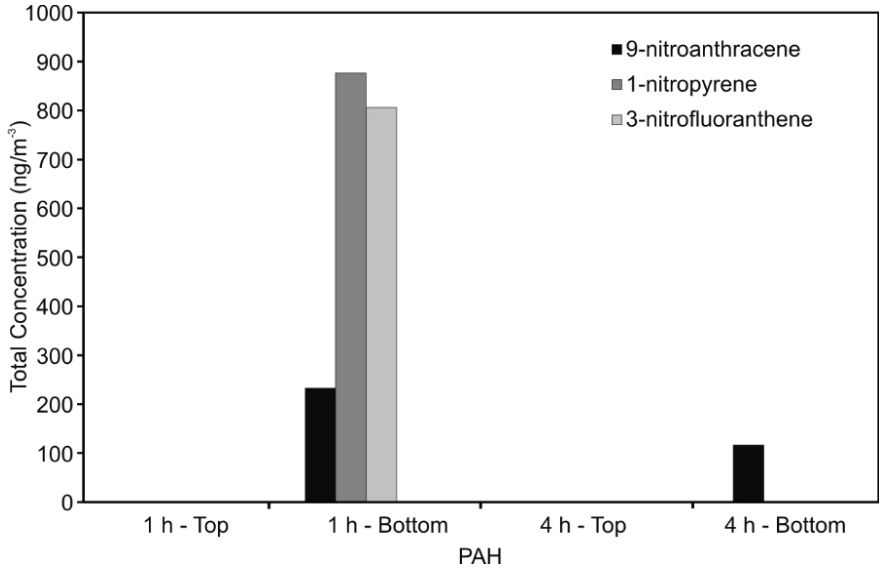

Fig. 23. Nitro-PAH species observed diesel exhaust aging experiments in the presence of a) air only and b) air with UV exposure.

7.3. Conclusions

A large-scale aerosol chamber was designed and constructed to evaluate the photo-degradation and nitration of PAHs emitted in the exhaust of a diesel engine. Initial work was performed investigating the performance of the Teflon reactor bag in terms of the loss rates of gases and particles due to various processes. From injecting individual gases and model particles (ammonium sulfate), loss rates agreed with those previously reported for similar reactor designs.

In experiments with DE in the presence of air under dark conditions, PAHs were monitored at the 1 and 4 h points of the reaction. The phase distribution of PAHs favored the gas-phase at 1 h, however, at 4 h an increased percentage was found in the particle phase, showing continual condensation of PAHs originally emitted into the gas-phase onto the particle surfaces. In the presence of UV irradiation, a significantly lower total concentration of PAHs in the reactor was observed in both phases. All of the 3–4 ring PAHs exhibited a sharp decline in their total levels from 1 to 4 h, most likely due to photo-degradation processes.

During DE aging experiments in dark conditions, three nitro-PAH species were observed. All three species were found only in the gas phase and were not present in the particle phase, and their concentrations decreased significantly from 1 to 4 h of the reaction.

7.4. Future Work

This work has focused on monitoring PAHs and their nitrated products (nitro- and amino-PAHs) during the aging of freshly emitted DE in the presence of air, air with UV irradiation and air with added NO_2 gas. Based on the work performed with the small flow reactor, the number of oxidation products in the presence of UV or NO_2 is expected to be

small compared to reactions with other gas-phase oxidants. Thus, future work using added O_3 gas as well as NO_2+O_3 (giving the NO_3 radical and N_2O_5) is planned to be performed.

So far this work has evaluated only PAHs and oxidation products observed during the aging of material emitted solely in DE. However, future work needs to be performed in evaluating the characteristics of different PAH scenarios, i.e., at various concentrations of PAHs that start in the gas-phase . This will require injection of additional PAH material (as a mixture of standards) into the reactor following the injection of DE.

CHAPTER 8

8. ESTIMATION OF THE EFFECTIVE ΔH_{vap} AND E_a^{vap} FOR PAHs DUE TO MATRIX EFFECTS ON THE SURFACE OF ATMOSPHERIC AEROSOLS.

8.1. Experimental

8.1.1. Chemicals and Materials

Standards used in this study as well as the different model particles used in this study are listed in Table 22 along with various physical parameters. All stock solutions and particle suspensions were prepared with DCM (high-resolution GC grade, Fisher Scientific, Pittsburg, PA, USA).

8.1.2. Preparation of Standards and Model Particles

All particle surfaces were cleaned prior to use by calcination in an oven at 550 °C for 12 h and then stored in a sealed glass jar until used. For adsorption of individual organic standards onto particle surfaces, particles were first weighed in 2.0 mL glass vials to ca. 50 mg. Stock solutions of an individual PAHs at high concentrations (15000–30000 ppm) were added to the particles and the suspension brought to ca. 1 mL with DCM. The amount of stock solutions spiked to the particles varied depending on the experiment. The DCM was then evaporated under a gentle stream of nitrogen with the vial on a shaker plate at 250 rpm (Labnet, Edison, NJ, USA). The DCM was evaporated until the particles moved freely at the bottom of the vial.

Table 22. List of PAH standards used in the study along with their physical parameters.

Compound Name	MW ($g\ mol^{-1}$)	T_{boil} (°C)	Ref.	ΔH_{vap}^{0} ($kJ\ mol^{-1}$)	Ref.	p_i^{o} (torr)[a]	Ref.	T_{fus} (°C)	Ref.	ΔH_{fus}^{0} ($kJ\ mol^{-1}$)	Ref.
naphthalene	128.17	217 ± 5	[14]	43.9 ± 0.80	[8]	1.59[b] x 10^{-1}	[8]	80.1 ± 0.7	[14]	19.1 ± 0.8	[14]
phenanthrene	178.22	340 ± 4	[3]	55.8 ± 0.80	[8]	2.06 x 10^{-4}	[8]	99 ± 2	[14]	16.57 ± 0.09	[15]
anthracene	178.22	340 ± 2	[3]	55.8 ± 0.80	[8]	2.06 x 10^{-4}	[8]	217 ± 3	[8]	29.84 ± 0.45	[15]
pyrene	202.25	404 ± 2	[8]	63 ± 0.80	[8]	2.28 x 10^{-6}	[8]	151 ± 3	[14]	16.68 ± 0.54	[15]
fluoranthene	202.25	375 ± 3	[8]	59.8 ± 0.8	[8]	1.73 x 10^{-5}	[8]	112 ± 2	[14]	18.73 ± 0.61	[14]

[a] Vapor pressure values at 298 K.
[b] Indicates that the solid has a significant sublimation pressure at ambient temperatures

8.1.3. Thermogravimetry-Differential Scanning Calorimetry

All thermogravimetry-differential scanning calorimetry (TGA-DSC) analyses were performed on a SDT-Q600 system (TA Instruments, New Castle, DE, USA). Analyses were performed with a dynamic oven program with linear heating rates (5–100 °C/min) and using nitrogen purge gas (20–100 mL/min). In optimizing the TGA-DSC method, two different sample cup types were used: alumina and aluminum pans, each with different sample cup configurations. Analyses with the alumina cup were performed with and without an alumina sample cup lid placed loosely over the cup opening. For the aluminum pans, samples were analyzed without a lid, with an aluminum lid placed loosely over the cup, with a lid crimped to the top of the pan, or with a pierced lid crimped to the top of the pan.

8.1.4. Calculations of Vaporization Enthalpies and Activation Energies

Vaporization enthalpies were estimated through two different techniques. The first of them utilized the heat flow signal measured during the TGA-DSC runs (Figure 24), using calculation schemes reported by Rojas & Orozco.[86] The heat flow curve was integrated within the temperature range by which vaporization occurred with respect to a baseline (determined through the analysis of blank sample cups). This area under the heat flow curve (A; W·s) was then divided by the mass lost during vaporization to give the heat capacity, Q (J g^{-1}), exhibited by the sample during the process (Eq. 1).

$$Q_i = \frac{A(W \cdot s)}{m_{initial} - m_{final}} \qquad \text{Eq. 1}$$

The calculated value of Q was then multiplied by the molecular weight of the species being vaporized to obtain the vaporization enthalpy ΔH_{vap} (J mol^{-1}) (Eq. 2).

$$\Delta H_{vap,i} = Q_i \cdot MW\left(g \cdot mol^{-1}\right) \qquad \text{Eq. 2}$$

The mass loss curve (TGA curve; example in Figure 24) was used to calculate the values for the activation energy of vaporization E_a^{vap}, using two separate calculation methods based on the linearization of the Arrhenius equation. The first, referred to as the "derivative method," uses the Friedman equation in the following form:

$$\ln\left(-\left[\frac{dm}{dT}\right]\frac{m_0}{m}\right) = \ln(A) - E_a^{vap}/RT \qquad \text{Eq. 3}$$

By plotting $\ln(m_0/m[dm/dT])$ against 1/T, the activation energy can be calculated from the slope of the resulting curve, which is close to linear during the sublimation/vaporization process.[87–90] Alternatively, another method called the "integral method," relates the activation to the mass differential functions in the following manner:

$$\ln\left(\frac{-\ln\left(m/m_0\right)}{T^2}\right) = \ln\left[\frac{AR}{CE_a^{vap}}\left(1-\frac{2RT}{E_a^{vap}}\right)\right] - \frac{E_a^{vap}}{RT} \qquad \text{Eq. 4}$$

Plotting the left-hand term against 1/T, similar to the derivative method, allows for the determination of E_a^{vap} from the slope of the near-linear curve (in the range of sublimation/vaporization).[88,89] Since the process of vaporization is highly endothermic, we can assume that $E_a^{vap} \approx \Delta H_{vap}$. Therefore, for the sake of simplification, all values will be represented in terms of ΔH_{vap} for the remainder of this paper.

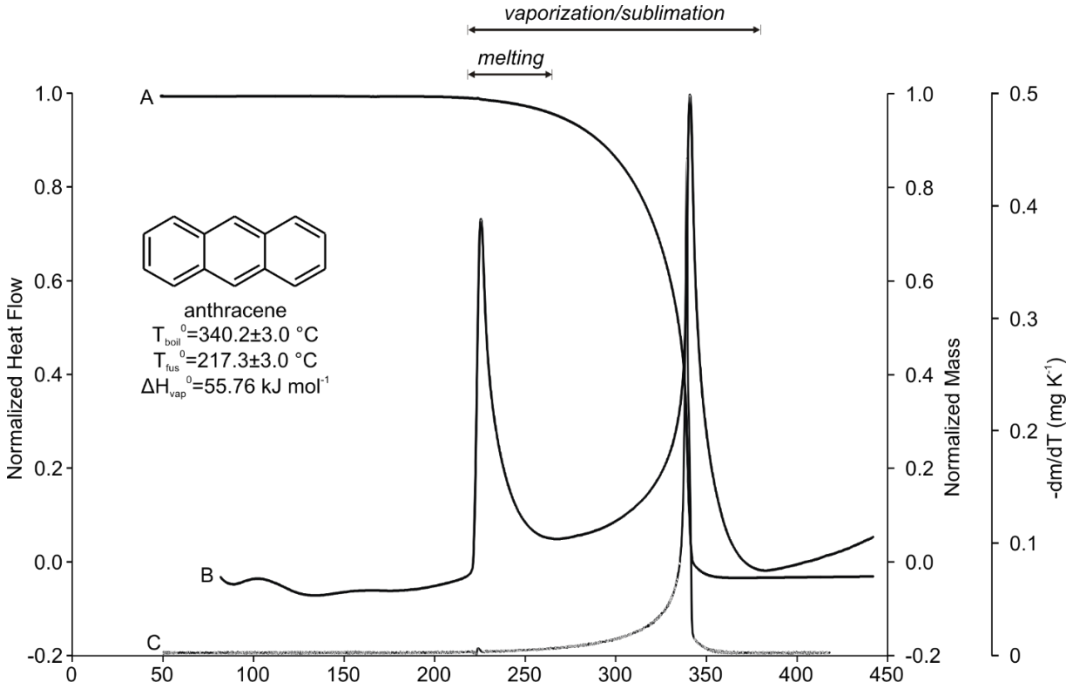

Fig. 24. An example TGA curve (A) with overlayed DSC (B) and DTG (C) curves obtained during the TGA-DSC analysis of anthracene standard (neat; solid crystal). Standard values were obtained from Reference 86.

8.1.5. Data Processing

Integration of heat flow curves was performed using Origin 9.1 software (OriginLab, Northampton, MA, USA). All other processing of TGA-DSC data was done using Microsoft Excel. In addition to determining values of ΔH_{vap} and E_a^{vap}, each TGA (mass loss) curve was evaluated by determining values of T_{low}, T_{high} and T_{avg} (an example of how they were determined is shown in Figure 25). T_{avg} is the temperature where the maximum value of dm/dT was observed. T_{low} was then the temperature at which the tangent of dm/dT at T_{avg} intersected a straight line at m/m_0=1 and T_{high} was the temperature at the point the tangent line intersected a line at m/m_0=0. These values were then used as tracers to provide extra numerical information of the TGA curve and thus vaporization behavior.

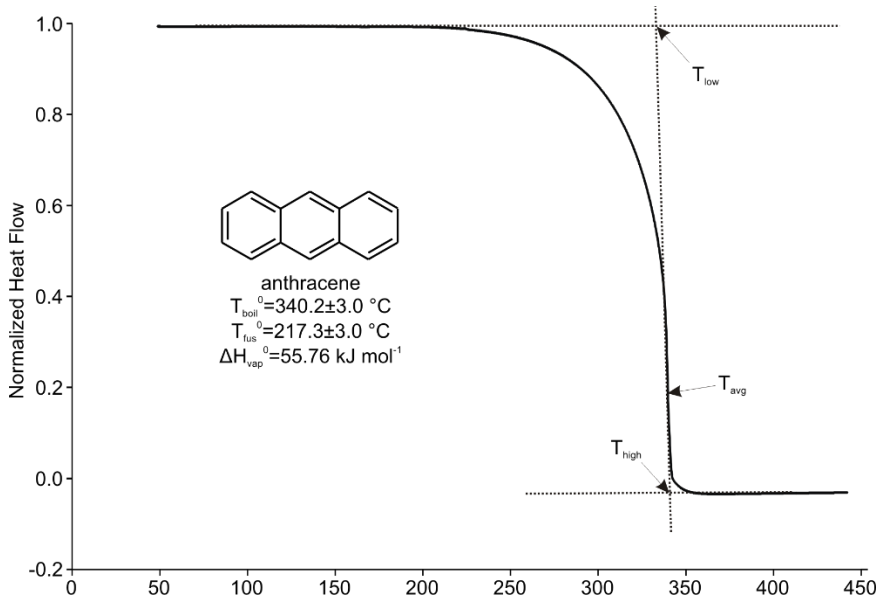

Fig. 25. Example of a TGA curve showing the determinations of T_{low}, T_{high} and T_{avg}.

8.2. Results and Discussion

8.2.1. Optimization of Thermogravimetry-Differential Scanning Calorimetry for Accurately Determining Vaporization Enthalpies and Activation Energies

Prior to defining changes in vaporization enthalpies of PAHs when adsorbed to particle surfaces, optimization of the TGA-DSC analysis method was performed to increase the accuracy and precision of calculated ΔH_{vap} and E_a^{vap} values. The instrumental parameters and conditions were first evaluated prior to evaluating the data processing methods. The main focus of the optimization was to achieve accurate and precise determinations of ΔH_{vap} and E_a^{vap} for selected compounds in the form of neat standards.

The impact of the sample mass loaded for analysis to the resulting values of ΔH_{vap} calculated from the heat flow curves is shown in Figure 26. In ranging the sample mass between 1–8 mg (of neat phenanthrene standard), the calculated values of ΔH_{vap} decreased in a linear trend. The TGA curves also exhibited major differences in the onset (T_{low}) and ending (T_{high}) temperatures of vaporization while the general shapes of each

were similar. Additionally the determined ΔH_{vap} values were lower than the standard values or those reported in previous work using DSC[86] as well as those determined when using aluminum sample pans. It is proposed that this is mainly a product of a limited heat transfer efficiency of the alumina sample cup, which is evaluated later in this work (see Table 23).

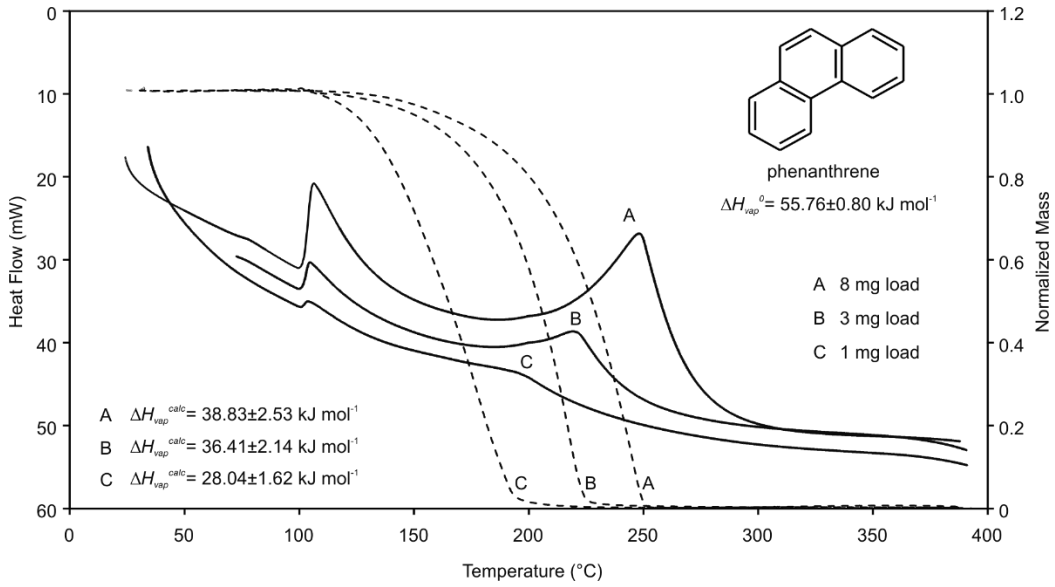

Fig. 26. Comparison of heat flow curves obtained with TGA-DSC analysis of phenanthrene with different mass loadings. Analyses were performed with alumina samples cups (no lid) with dT/dt=0.33 K s^{-1} and a N_2 purge flow rate of 20 mL min^{-1}.

The impact of the sample purge gas flow rate (gas which increases the uniformity of the temperature throughout the TGA-DSC oven) was also evaluated (Appendix XXI). Using neat phenanthrene, analyses were performed with purge gas flows in a range of 20–100 mL min^{-1}. The calculated enthalpies were the highest when using a purge gas flow of 20 mL min,$^{-1}$ and the lowest at 50 mL min^{-1}. Therefore a 20 mL min^{-1} purge flow was used for all subsequent analyses in this work.

Initial experiments using alumina sample cups consistently provided ΔH_{vap} values significantly lower than those reported in previous works.[86,91] These underestimations of

the ΔH_{vap} values could be due to the inefficient heat transfer from the samples through the alumina material and finally to the platinum head of the thermocouple sensor. To test this hypothesis, analyses were also performed with aluminum sample cups. For each sample cup material, experiments were done using three different types of lid configurations: cup with no lid, cup with a loose lid, a crimped lid, or a crimped lid with a pierced hole (hole diameter=150 µm). The latter two configurations were only available with aluminum sample pans. The results from these tests are shown in Table 23 (TGA curves are shown in Appendix XXII). Vaporization onset temperatures and calculated ΔH_{vap} values were considerably lower with the alumina pans without lids compared to analyses with either loose or crimped lids. Aluminum pans with a crimped pierced lid provided the most accurate results, yielding boiling points and ΔH_{vap} values similar to those previously reported.[86] To note, the crimped aluminum pans without a pierced hole exhibited highly inconsistent vaporization behavior due to over-pressurization in the sample cup during heating. Aluminum pans consistently yielded significantly higher calculated ΔH_{vap} values compared to those with alumina pans, again most likely due to enhanced heat transfer efficiency of the aluminum.

To conclude, aluminum pans with both a crimped and pierced lid provide the most accurate and precise determinations of ΔH_{vap} as well the shape of the TGA and DSC curves. Therefore this sample cup configurations was used in the remainder of the work

Table 23. Determinations of ΔH_{vap}, T_{low}, T_{high} and T_{avg} values for phenanthrene when analyzed with sample cup types and configurations.

Sample Cup Material[a]	Lid Type[a]	Lid Position[a]	T_{low} (°C)	T_{high} (°C)	T_{avg} (°C)	Rojas Method ΔH_{vap}^{0} (kJ mol^{-1})
alumina	open	–	215.7 ± 2.1	229.3 ± 2.4	227.9 ± 2.2	36.75 ± 2.36
alumina	full	loose	273.4 ± 3.1	305.8 ± 3.5	318.2 ± 3.1	44.63 ± 1.54
aluminum	full	loose	252.9 ± 2.8	285.6 ± 3.0	281.6 ± 3.8	78.97 ± 4.10
aluminum	full	crimped			ND	
aluminum	pierced	crimped	329.9 ± 2.6	339.0 ± 0.5	336.5 ± 0.7	95.05 ± 2.48

[a] For each analysis the reference sample cup was the same material, lid type and lid position as the sample cup.

8.2.2. Vaporization of Individual Standards of Organic Aerosol Species

To assess the applicability of the optimized TGA-DSC method, it was expanded to the analysis of multiple PAH species (those containing 2–4 aromatic rings). Each standard was analyzed three times (n=3) and ΔH_{vap} and E_a^{vap} values were determined from the DSC and TGA data, respectively. The use of the Rojas, Derivative or Integral methods have not been previously reported for PAHs with non-isothermal TGA and DSC analysis. These methods allow for the calculation of ΔH_{vap} or E_a^{vap} from a single non-isothermal run, thereby decreasing analysis time compared to traditional isothermal methods that require multiple runs at different heating rates to accurately calculate the values. Therefore, in this work, the methods are compared in terms of the accuracy and precision to previously reported ΔH_{vap} values.

Table 24 shows the experimental values as well as the calculated ΔH_{vap} and E_a^{vap} values for each PAH as a neat standard. All of the analyses were performed with the same heating rates (0.33 K s^{-1}) since it has been reported that both the derivative and integral methods are sensitive to changing temperature ramps from run to run.[89] During each run, mass losses can occur through either sublimation or vaporization, however, sublimation was not observed (i.e., $T_{low} >> T_{fus}$). Therefore, all enthalpies and activation energies resulted from vaporization alone (see Appendix XXIII for the TGA, DSC and DTG curves for each neat standard). In general, the Rojas method for calculating ΔH_{vap} from the DSC heat flow data yielded higher values than either methods for determining E_a^{vap}. The exception to this was anthracene, for which the integral method provided the highest value. For the most part, the values of ΔH_{vap} as determined using the integral method were closer to those determined with the Rojas method. Therefore the integral method was used for the remainder of the work in this study. ΔH_{vap} should be either equal

or slightly smaller than E_a^{vap} for the process of vaporization of a molecule from liquid to gas, as with any highly endothermic reaction. Thus, differences observed in this work is a function of limitations in the calculation methods in accurately defining the terms (see Figure 27 for comparisons of calculated E_a^{vap} and ΔH_{vap} values). In the linearization methods, limitations can arise from the somewhat arbitrary determination of which points to include in the linear region of the resulting curve. To avoid potential errors arising from this constraint, both methods were performed using the same points within the same temperature region. The regions used for each compound are shown in Appendix XXIV. In comparing the measured values for E_a^{vap} to ΔH_{vap} reported in previous studies, each compound exhibited slightly higher values, however, a linear trend is observed. This is likely to arise from differences in instrumentation. The determined T_{high} values for the neat standards of each PAH was found to show a linear relationship to the calculated E_a^{vap} values (see Figure 28). Therefore T_{high} of a vaporization process may serve as an observable by which to estimate values of E_a^{vap}.

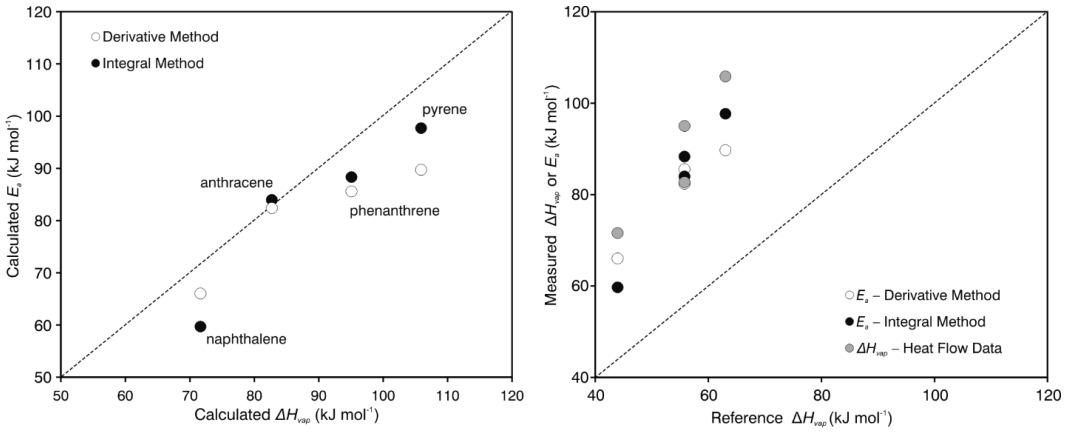

Fig. 27. Comparison of calculated E_a values to ΔH_{vap} values (left) and a comparison of the calculated ΔH_{vap} and E_a values in this work to those reported previously (right).

Table 24. Values of ΔH_{vap} and E_a as well as T_{low}, T_{high} and T_{avg} values for neat standards of 2–4 ring PAHs using the derivative and integral methods.

Compound Name	T_{low} (°C)	T_{high} (°C)	T_{avg} (°C)	Rojas Method ΔH_{vap}^{0} (kJ mol^{-1})	Friedman Method E_a (kJ mol^{-1})	Kissinger Method E_a (kJ mol^{-1})
naphthalene	221.4 ± 1.1	227.6 ± 0.6	224.7 ± 0.8	71.62 ± 3.17	66.04 ± 0.20	59.73 2.34
phenanthrene	329.9 ± 2.6	339.0 ± 0.5	336.5 ± 0.7	95.05 ± 3.17	85.59 ± 0.51	88.34 3.11
anthracene	333.1 ± 4.2	341.5 ± 0.8	339.5 ± 0.5	82.72 ± 3.17	82.41 ± 3.05	83.97 1.53
pyrene	367.8 ± 2.4	391.4 ± 0.7	386.6 ± 1.8	105.87 ± 3.17	89.74 ± 1.57	97.71 0.75

Each compound was analyzed by TGA-DSC in triplicate (n=3).

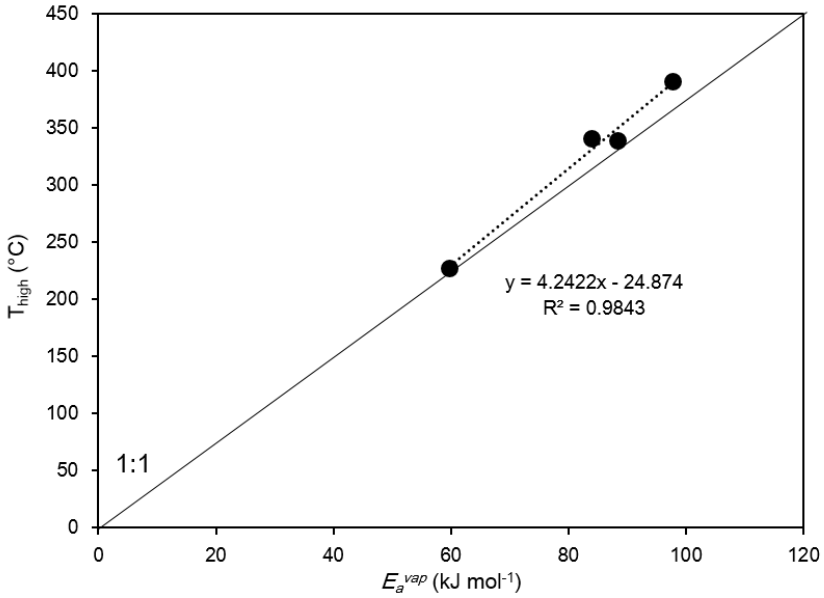

Fig. 28. Relation of calculated E_a^{vap} values to the observed T_{high} for each of the PAH neat standards investigated. E_a^{vap} values were calculated using the Integral method. For each the value shown is the mean of triplicate analyses (n=3).

8.2.3. Vaporization of Organic Aerosols Species Adsorbed to Model Particles

In addition to determining both ΔH_{vap} and E_a^{vap} values for neat PAH standards, the calculation methods were used to evaluate the contribution of surfaces of surrogate particles on the adsorption of anthracene. These effective vaporization enthalpies (ΔH_{vap}^{eff}) and activation energies ($E_a^{vap,eff}$) can help gain insight into the extent of matrix-analyte interactions that occur on the surfaces of real-world PM in the atmosphere. While theoretical models have been reported for PAH-surface interactions for carbon surfaces, experimental work showing their vaporization behavior is very limited. The surrogate particles were chosen as to represent a range of surface types (polarities) observed in various real-world PM matrices. The elemental or black carbon fraction of PM consists primarily of short stacks of graphene sheets arranged in a highly disordered fashion. Therefore graphite and other similar surfaces were investigated. The particles used in this study are listed in Table 25.

Table 25. Surrogate particles used in this study to evaluate the adsorption of anthracene on different surfaces using TGA-DSC data.

Surrogate Particle	Manufacturer	Purity	D_p^{mean} (μm)	Surface Area ($m^2\ g^{-1}$)
silica	Sigma-Aldrich	99%	75–100	480
graphite	Sigma-Aldrich	≥99.9%	≤20	50
graphene	USRN	≥99.5%	4–12	–
activated carbon	Sigma-Aldrich	≥99.5%	100–150	>500
coronene	Sigma-Aldrich	97%	–	–

Calculated values $E_a^{vap,eff}$ for anthracene adsorbed on various particle surfaces are shown in Table 26. Values for ΔH_{vap}^{eff} were not determined due to the inability to accurately integrate the heat flow curve above the baseline during vaporization of relatively small amounts of the anthracene (≤150 μg per mg of surrogate particle). Rather the Integral method was used to estimate $E_a^{vap,eff}$. All PAH species were observed to exhibited some degree of adsorption (Table 26), with naphthalene exhibiting the strongest adsorption behavior. This may be due naphthalene's smaller size enabling stronger π-π* interaction.

Table 26. Values of E_a^{eff} for anthracene adsorbed to various surrogate particle surfaces.

Adsorbed Analyte	Substrate Surface	% m_T ($T > T_{boil}^0$)	T_{low} (°C)	T_{high} (°C)	T_{avg} (°C)	$E_a^{vap,eff}$ (kJ mol^{-1})	E_a^{ad} (kJ mol^{-1})
naphthalene	neat	–	221.4 ± 1.1	227.6 ± 0.6	224.7 ± 0.8	59.73 ± 2.34	
	silica	75	214.8 ± 2.6	282.4 ± 2.9	251.7 ± 5.0	80.30 ± 0.98	20.57 ± 2.54
phenanthrene	neat	–	329.9 ± 2.6	339.0 ± 0.5	336.5 ± 0.7	88.34 ± 3.11	
	silica	60	320.4 ± 1.6	378.5 ± 2.7	356.3 ± 3.8	94.89 ± 0.66	6.55 ± 3.18
pyrene	neat	–	367.8 ± 2.4	391.4 ± 0.7	386.6 ± 1.8	97.71 ± 0.75	
	silica	15	350.5 ± 1.5	417.8 ± 2.6	390.1 ± 2.7	103.06 ± 2.25	10.81 ± 5.61
anthracene	neat	–	333.1 ± 4.2	341.5 ± 0.8	339.5 ± 0.5	83.97 ± 1.53	
	silica	25	279.0 ± 2.4	366.5 ± 3.9	336.9 ± 5.7	94.79 ± 5.40	5.35 ± 2.37
	graphite	0	248.9 ± 3.8	302.1 ± 7.8	278.3 ± 4.9	70.63 ± 3.14	
	graphene	7	230.0 ± 2.7	322.0 ± 4.0	275.3 ± 2.5	74.78 ± 3.02	
	activated carbon	0	150.1 ± 1.0	258.2 ± 2.5	208.0 ± 1.0	40.48 ± 2.67	
	coronene	0	202.2 ± 0.8	241.7 ± 1.5	228.9 ± 1.5	65.13 ± 2.55	

with the pure-carbon surfaces (e.g., graphite).[92,93] These interactions are believed to be predominated by π–π* electron donor-acceptor (π–π* EDA) interactions between a single anthracene molecule and the arene surface of graphite.[93] However, in this work, it was observed that when added to the graphite-like surfaces, anthracene evaporated at significantly lower temperatures compared to that observed with the neat standard. This in turn resulted in decreased $E_a^{vap,eff}$ values relative to E_a. In contrast, anthracene seemed to incorporate adsorption behavior to the surfaces of silica particles as seen through the increased $E_a^{vap,eff}$ values compared to E_a^{vap}. The enthalpy of adsorption (ΔH_{vap}^{ad}) can then be estimated through the following relation (assuming that $E_a^{vap}=\Delta H_{vap}$ for an adsorption process):

$$\Delta H_{vap}^{ad} = \Delta H_{vap}^{eff} - \Delta H_{vap} \qquad \text{Eq. 5}$$

Therefore for silica particles ΔH_{vap}^{ad} = 10.81 kJ mol^{-1}. For the other particle surfaces any calculation of ΔH_{vap}^{ad} would result in negative values, indicating that no adsorption process would be occurring.

The values of ΔH_{vap}^{eff} presented so far have been determined assuming only a single process for the vaporization of the bulk anthracene (i.e., ${}^{\beta}\Delta H_{vap}^{eff}$). Based on the TGA curves for the vaporization of anthracene from the particles surfaces (Figure 28), vaporization of anthracene when added to silica, graphite or activated carbon particles indeed exhibit this behavior. However, the TGA curves of anthracene on graphene and coronene show what essentially could be a "multiple site process" vaporization scheme. It is proposed that the first step of this two-process mechanisms involves the vaporization of a bulk of the anthracene on the surface (Figure 29). This leaves a small fraction of

"trace" amounts of residual anthracene (closer to concentration levels exhibited in real-world PM) which has more access to "high-energy" active

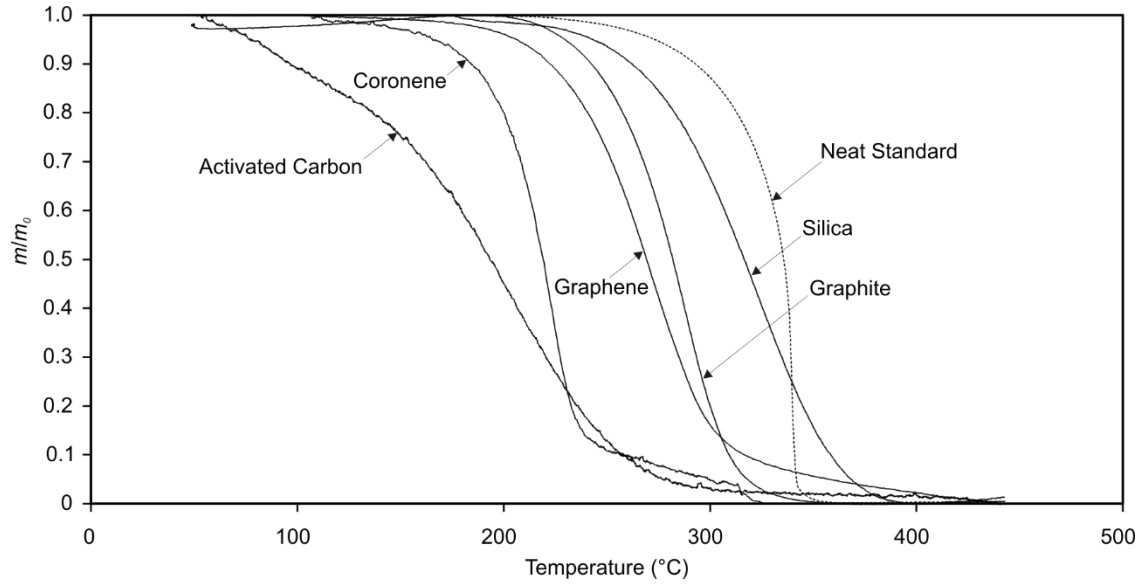

Fig. 29. TGA curves from the vaporization of anthracene from the surfaces of different surrogate particles.

sites on the particle surface. Enthalpies in this range would then refer to the trace amount only ($^{\alpha}\Delta H_{vap}^{eff}$) (see Figure 29). Recently, Lazar *et al.* showed that for graphene, only 0.24±0.03% of the total surface area includes these high-energy sites.[92] It is assumed that the interaction of anthracene with these stronger adsorption sites is a more "true" adsorption process. This is characteristic for interactions of small amounts of PAHs embedded in organic matrices of PM. Such an adsorption process would essentially require, at least within the temperature range, ΔH_{vap}^{eff} values greater than ΔH_{vap} and the mass loss to continue at temperatures beyond the T_{avg} value observed for the neat standard (i.e., 339.5±0.5 °C). The latter requirement was observed in the TGA curve for anthracene on graphene, but not on coronene. For graphene, the mass loss rate (dm/dT) observed in the temperature range above T_{avg} was linear but lower than that observed for

the bulk anthracene region, resulting in calculated ${}^{\alpha}\Delta H_{vap}{}^{eff}$ values lower than ${}^{\beta}\Delta H_{vap}{}^{eff}$. Therefore, $\Delta H_{vap}{}^{eff}$ was estimated using our proposed method based on the observed T_{high} values (described in section 8.2.1).

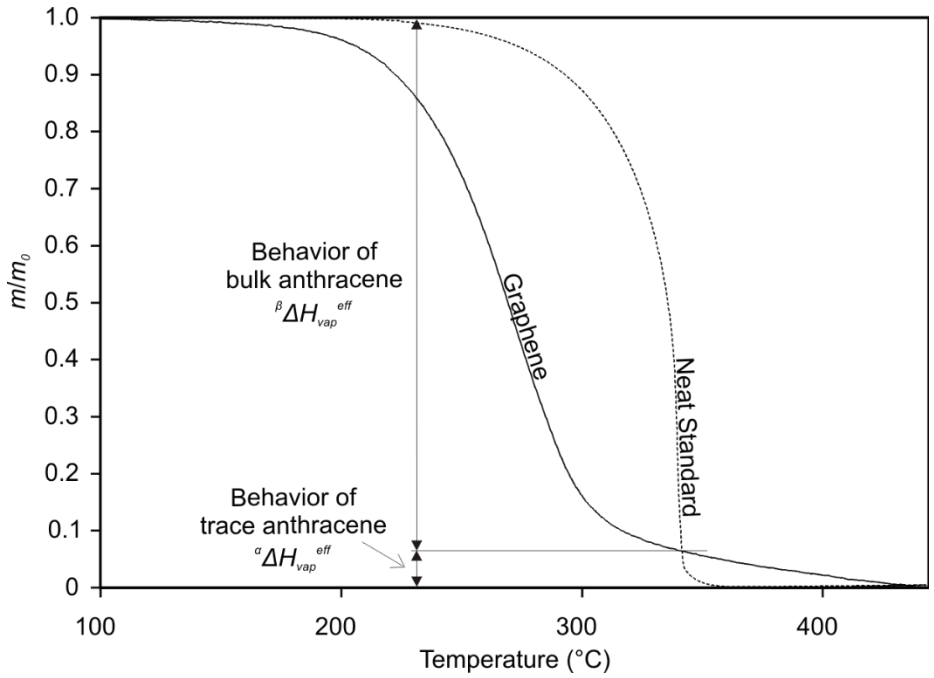

Fig. 30. TGA curves of anthracene as a neat standard and adsorbed to graphene nanoparticles. The regions of the two-process vaporization scheme ("bulk" and "trace" behavior) are shown.

8.2.4. Modeling the Influence of Particle Surface Chemistry on Organic Aerosol Partitioning

In the atmosphere, gas-phase organic species emitted by various incomplete combustion processes partition between the gas-phase and the surface of atmospheric aerosols. The fraction by which any compound is in the aerosol phase is given by the equilibrium partitioning coefficient:

$$K_A = \frac{A}{G \cdot M} \qquad \text{Eq. 6,}$$

in which *G* is the concentration of the species in the gas phase (mass per volume of air; μg m^{-3}), *A* is the concentration of it in the aerosol phase (μg m^{-3}), and *M* is the mass concentration of the total absorbing particle phase.[94] The partitioning coefficient K_A (m^{-3} μg^{-1}) is then inversely proportional to the saturation vapor pressure (c^*) of the compound. This partitioning generalization can be extended to those products formed upon oxidation of the original pollutant in the gas phase (Figure 30). These products are typically less volatile than their precursor, thus having an increased K_A value.

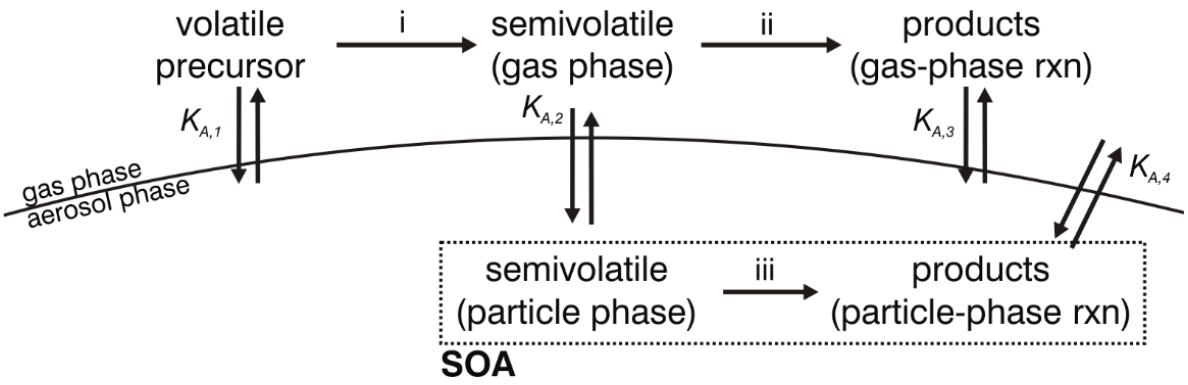

Fig. 31. Simplified representation of the partitioning of primary gas-phase organic species and their products from oxidation between the gas and aerosol phases.

KA values are dependent on the affinity of the compound for both phases, which is fundamentaly a function of partial pressure (*p*) and vaporization enthalpy (ΔH_{vap}). Currently, models focused on investigating the partitioning of organics in the atmosphere typically employ standard values for these physical parameters. This limits the accuracy of these models in that the partitioning can be grossly over- or underestimated due to uncompensated interactions of the target species with the aerosol surface, which is comprised of a dynamic mixture of a large number of other organic pollutants. These "matrix-analyte" interactions (giving rise to ΔH_{vap}^{eff}) need to be accounted for in order to

more correctly model the behavior of organic pollutants on aerosol surfaces. In this work, anthracene was observed to interact differently with various surrogate particle surfaces. This provides insight into the diversity in interactions which may exist on the surface of atmospheric aerosols. Experimentally derived values for the contribution of adsorption of single molecules to the surface of aerosols can be used to implement more accurate representation of organic pollutant portioning in the atmosphere.

8.3. Conclusions

In this work a method utilizing TGA-DSC was optimized for determining values of ΔH_{vap} and E_a^{vap} for PAH species. The method was then applied to investigating the adsorption behavior of anthracene on various surrogate particle surfaces, including different types of carbon surfaces (e.g., graphite, graphene and coronene) and silica. Unexpectedly, naphthalene showed the strongest adsorption to silica. Anthracene, while expected to show significant adsorption to carbon surfaces, exhibited vaporization at decreased temperatures compared to the neat standard. For graphene, however, two different types of vaporization were observed in the TGA curves, a "multiple site" process where ΔH_{vap}^{eff} is not a single value. The first process involved vaporization of the bulk of anthracene added to the graphene surface (~90–95% of the added mass) and the second for the residual amount of anthracene. The second vaporization step continued to display mass loss beyond the standard boiling point ($T_{avg}=[dm/dT]_{max}$) observed for the neat standard, thus showing "true" adsorption of anthracene to the surface. It is hypothesized that for graphene anthracene does not show adsorption characterics with the surface at the bulk concentrations (~150 µg mg-1 particle) but at "trace" concentrations (<20 µg) is allowed to come into better contact with the low number of "high energy" sites as described in previous computation models. This can then extend to describing the

non-adsorption of anthracene to the other carbon surfaces, which relative to graphene, do not provide high-energy sites due to disorganized layers of arene sheets.

8.4. Future Work

This work describes the interactions of anthracene with surrogate particles surfaces. Additional work should be performed extending to other PAHs species. Evaluations need to be performed looking at similarities/differences between species with the same number of aromatic rings but different in their ring configurations. The desorption of these PAHs needs to also be investigated on the surface of real-world PM. Experiments can be performed looking at the desorption behavior of PAHs already embedded into the surface of the PM as well those with deuterated PAH analogues spiked to the surface. This may allow to observe possibly differences between species embedded in the matrix versus those adsorbed to the outer layer of the matrix.

APPENDICES

Appendix I. SPE elution distribution profiles of PAHs and their oxidation products in extracts of WS PM. The elution trends were consistent with those observed using standard mixtures. Response of individual compounds was determined based on the peak area of quantitation ions (see Table 1) using SITI-SIM data. The total recovery (shown as the secondary axis) was based on the combined mass concentrations of all species evaluated within that class. Nitro-PAHs were not observed and thus are not shown.

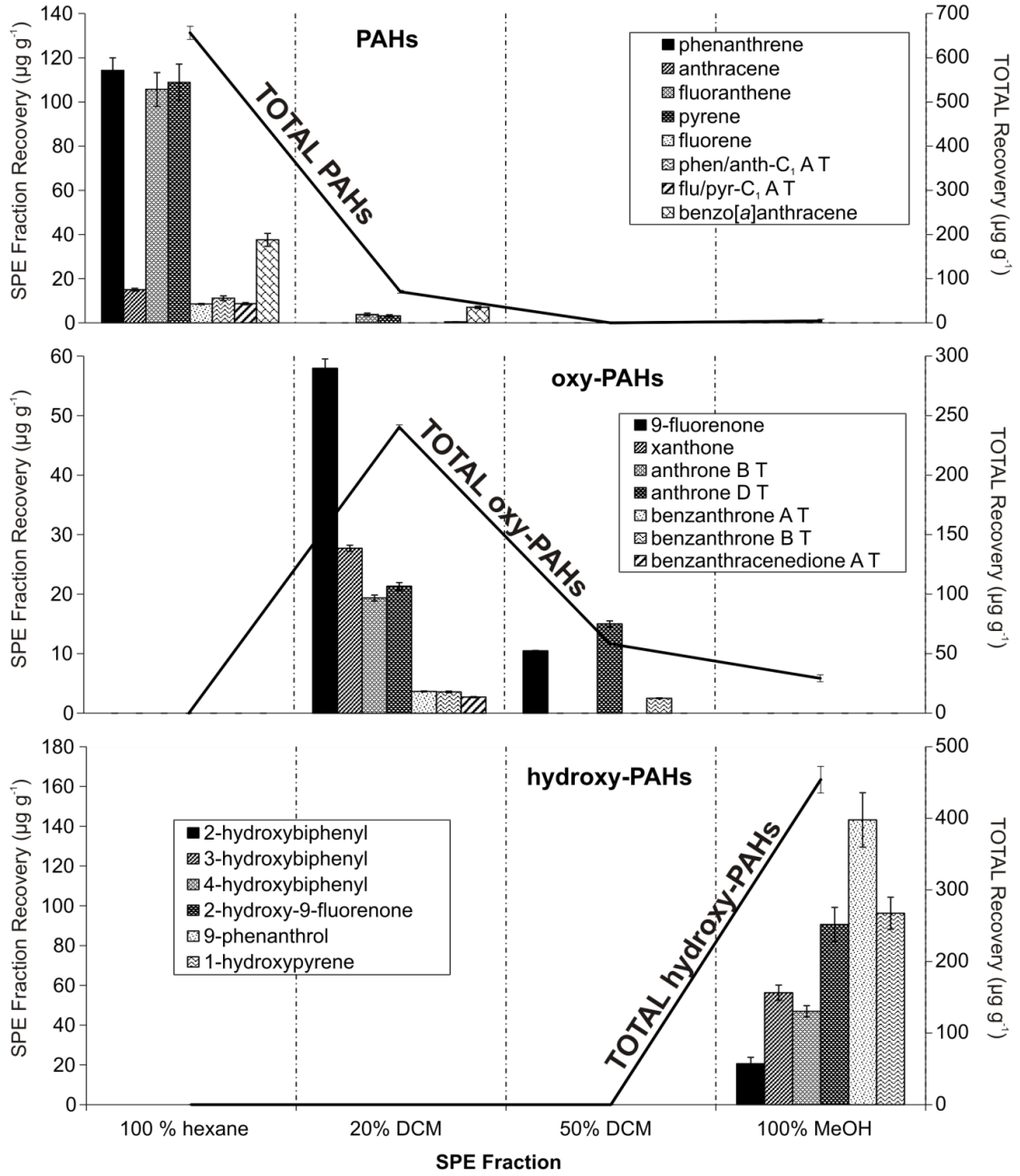

Appendix II. SPE elution distribution profiles of PAHs and their oxidation products in extracts of SRM 2975 diesel exhaust PM. The elution trends were consistent with those observed using standard mixtures. Response of individual compounds was determined based on the peak area of quantitation ions (see Table 1) using SITI-SIM data. The total recovery (shown as the secondary axis) was based on the combined mass concentrations of all species evaluated within that class. Hydroxy-PAHs were not observed and thus are not shown.

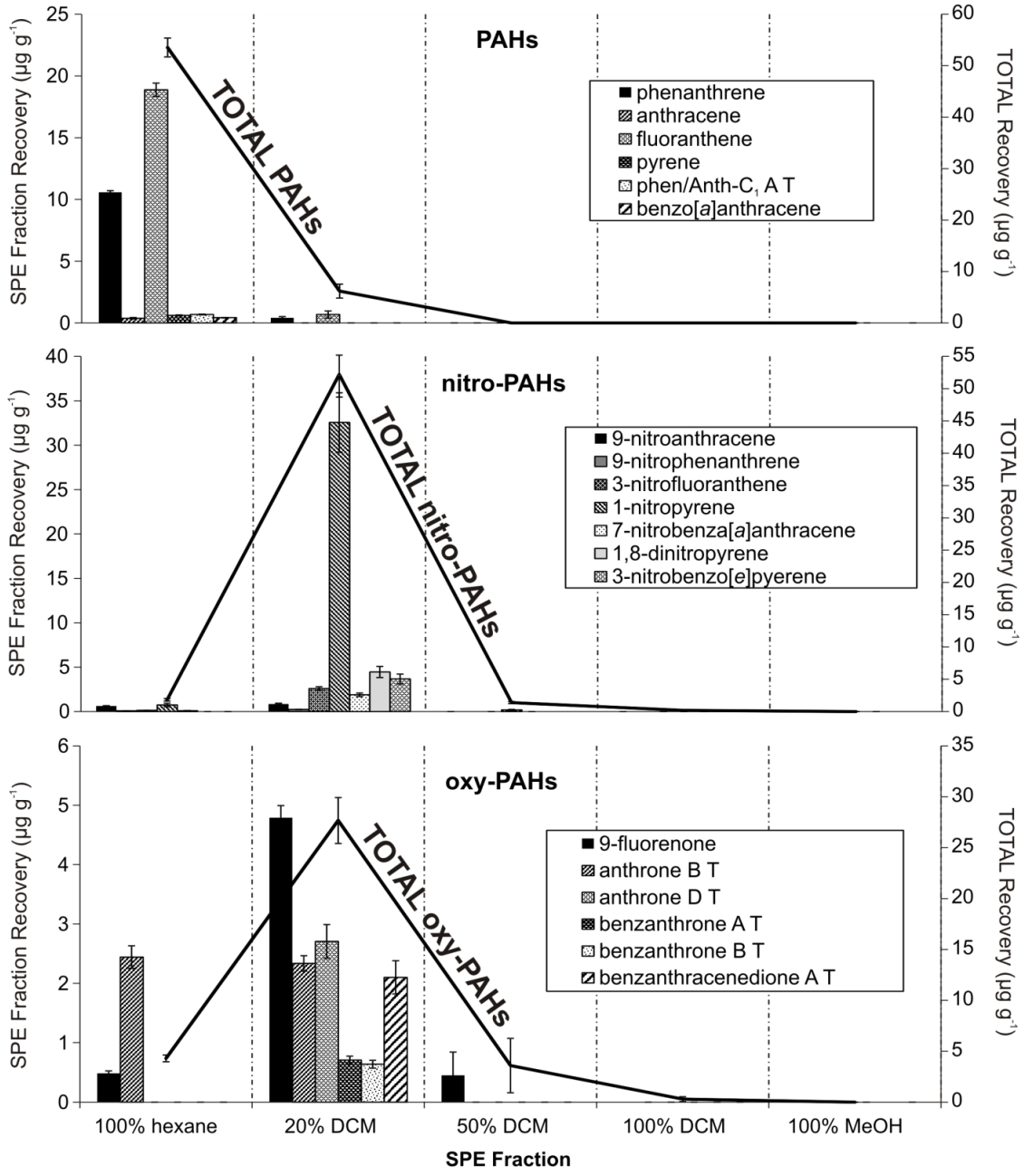

Appendix III. TIC chromatograms of SPE fractions of WS PM extract. Identified and quantified species are labeled above their corresponding chromatographic peak. Each chromatogram was obtained using MS detection with EI in SITI mode.

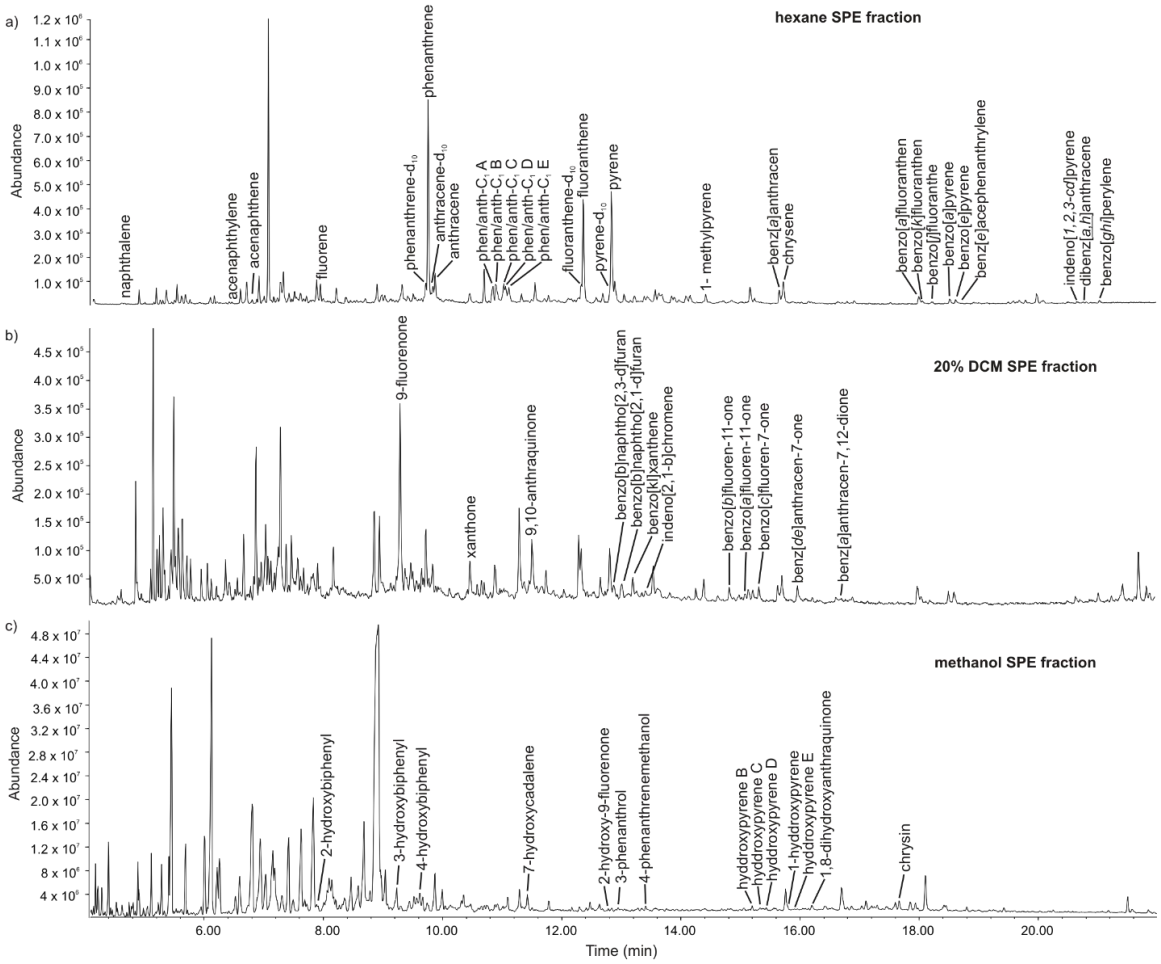

Appendix IV. TIC chromatograms of individual SPE fractions for extracts obtained using PFE with DCM (left column), Soxhlet with DCM (middle column), and Soxhlet with MeOH (right column). Each chromatogram was obtained using MS detection with EI in SITI mode.

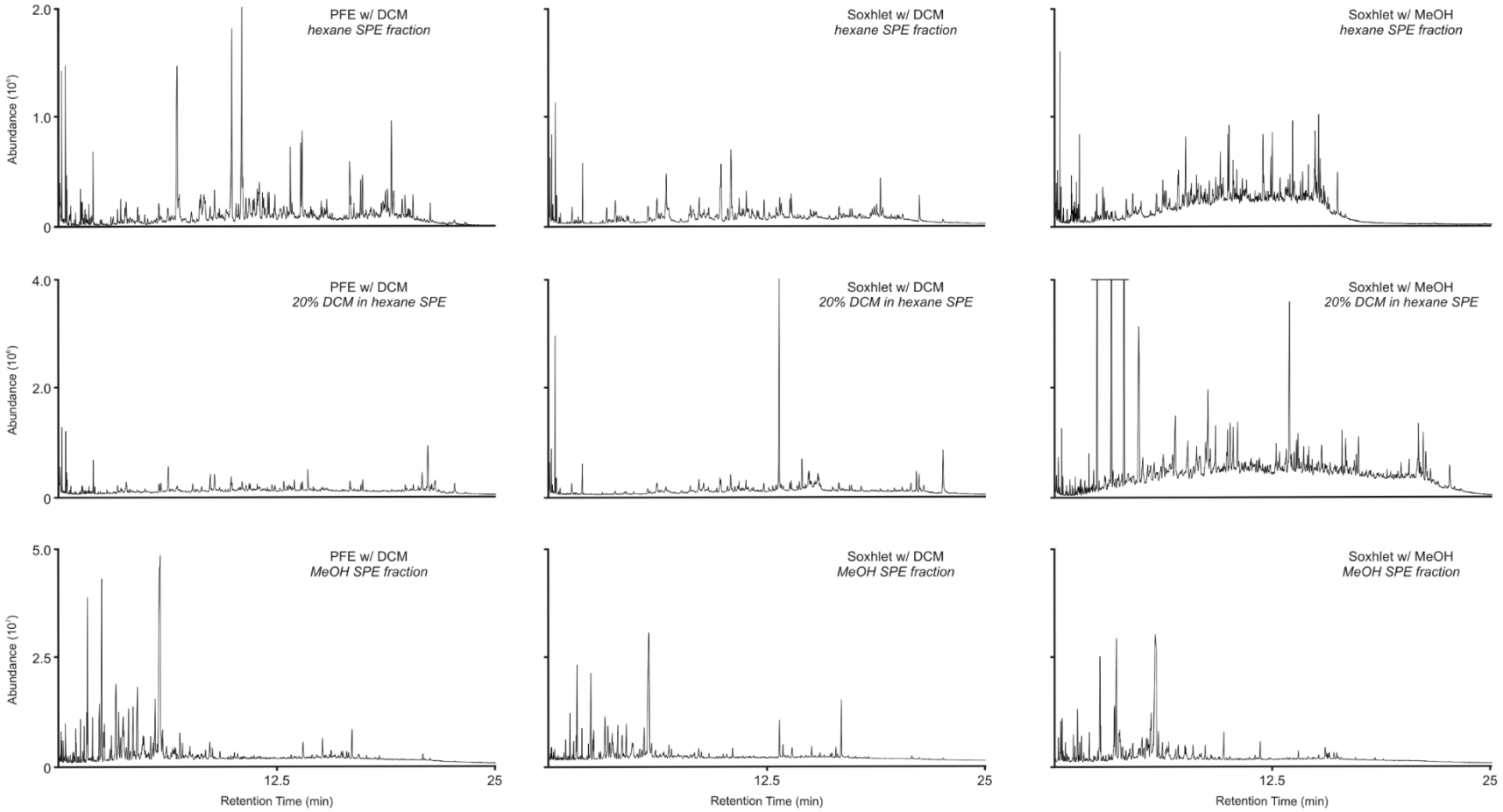

Appendix V. TIC chromatograms of extracts obtained using a) PFE with DCM, b) Soxhlet with DCM, and c) Soxhlet with MeOH. Names of non-polyaromatic polar compounds that were identified are shown above their respective chromatographic peaks. Each chromatogram was obtained using MS detection with EI in SITI mode.

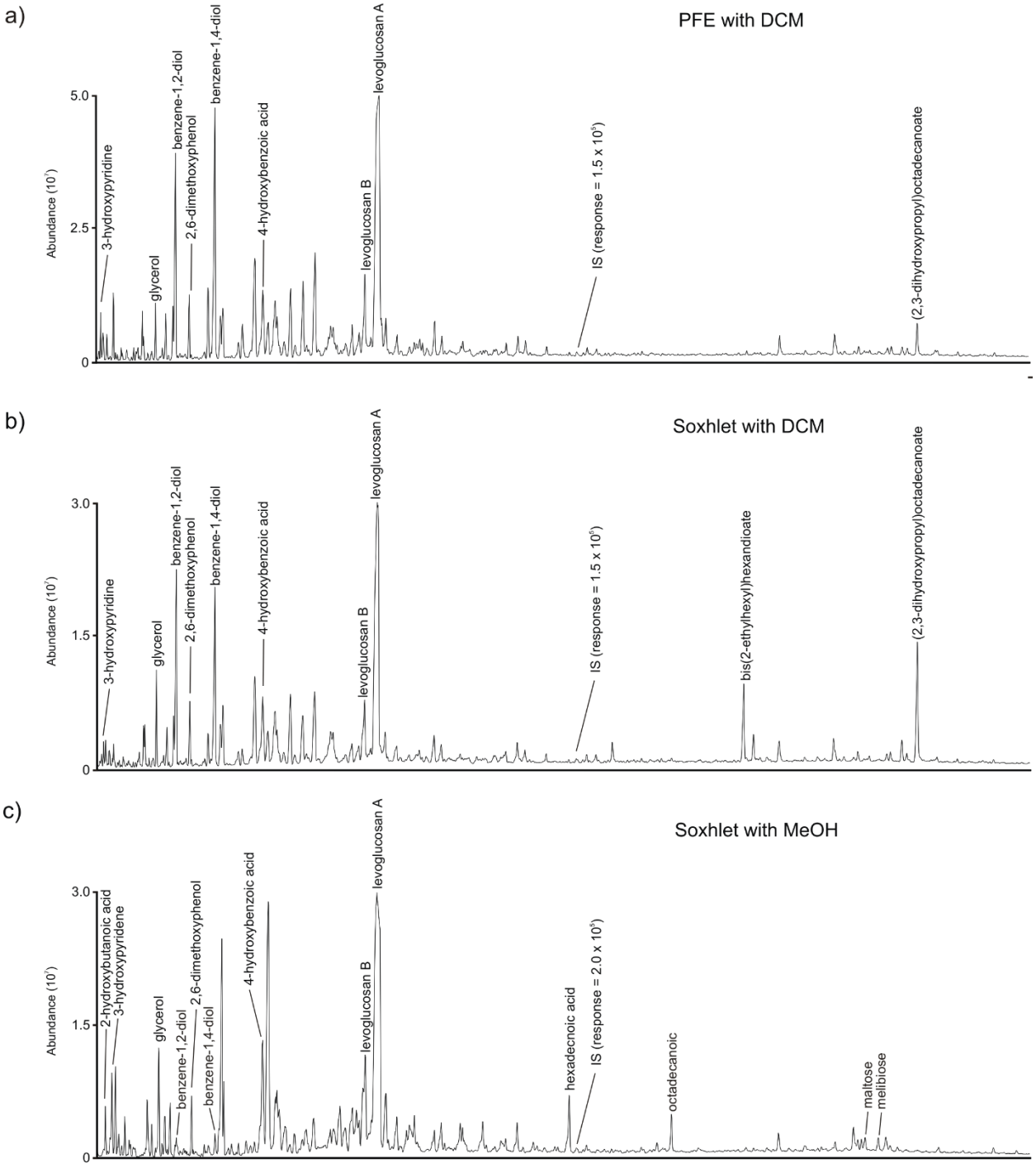

Appendix VI. Schematic representation of the small-scale flow reactor used for the ozonation of pyrene.

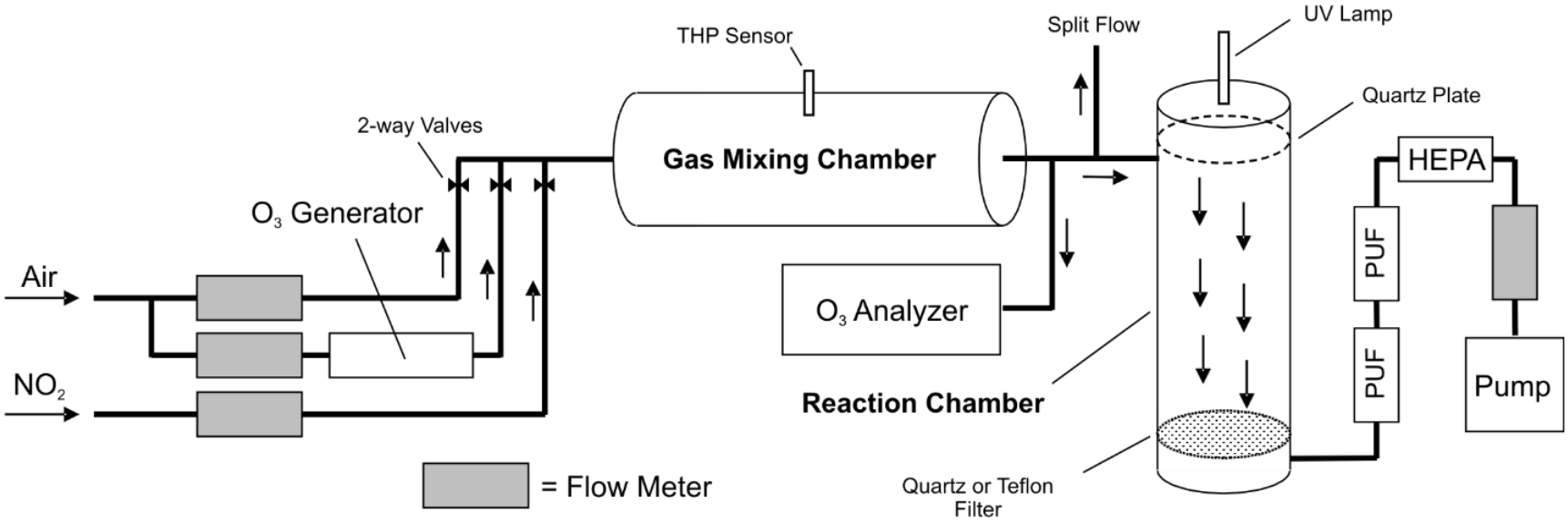

Appendix VII. APCI-HRMS spectra of carboxy-PAHs in both positive and negatives modes. Spectra shown are average spectra taken over the width of the chromatographic peak. Neutral losses or additions shown reflect only the change in the empirical formula and do not necessarily represent the specific ionization process or pathway. Each spectra was recorded during FIA with 50% methanol in water at a flow rate of 0.2 mL min-1 using a capillary voltage of 4500 V, fragmentor voltage of 120 V and corona current of 10 µA.

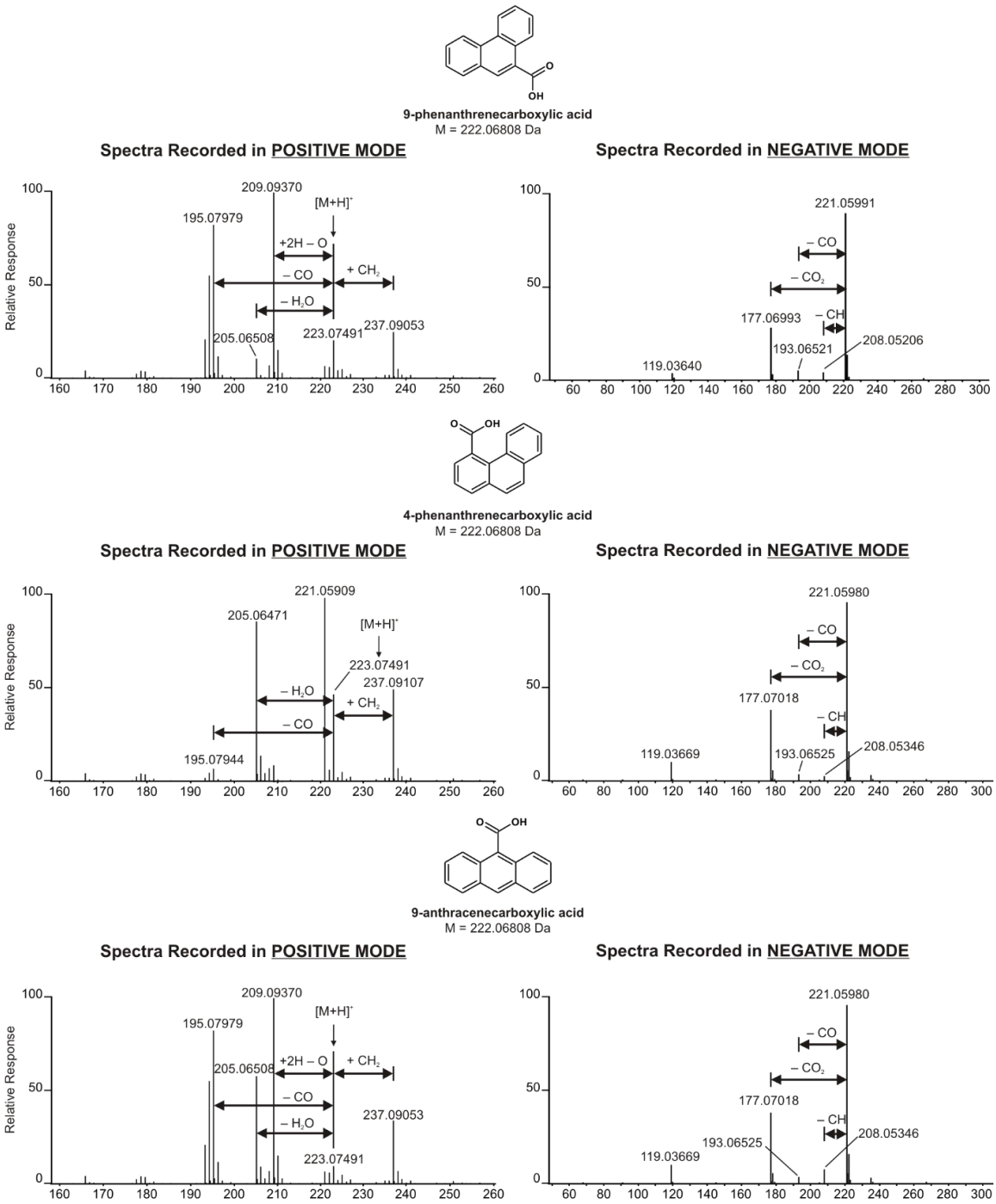

Appendix VIII. APCI-HRMS spectra of carboxy- and hydroxy-PAHs in both positive and negatives modes. Spectra shown are average spectra taken over the width of the chromatographic peak. Neutral losses or additions shown reflect only the change in the empirical formula and do not necessarily represent the specific ionization process or pathway. Each spectra was recorded during FIA with 50% methanol in water at a flow rate of 0.2 mL min-1 using a capillary voltage of 4500 V, fragmentor voltage of 120 V and corona current of 10 µA.

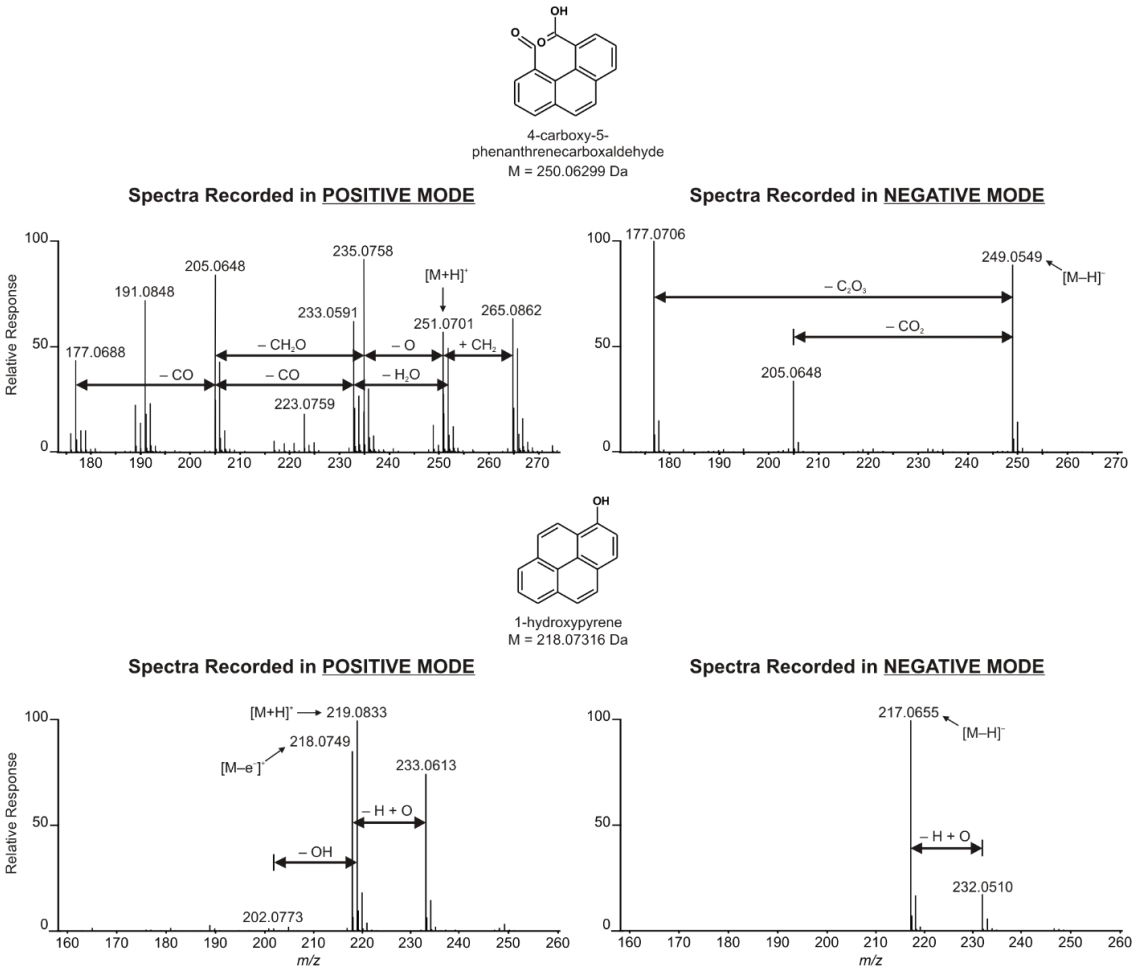

Appendix IX. APCI-HRMS spectra of oxy-PAHs in both positive and negatives modes. Spectra shown are average spectra taken over the width of the chromatographic peak. Neutral losses or additions shown reflect only the change in the empirical formula and do not necessarily represent the specific ionization process or pathway. Each spectra was recorded during FIA with 50% methanol in water at a flow rate of 0.2 mL min-1 using a capillary voltage of 4500 V, fragmentor voltage of 120 V and corona current of 10 µA.

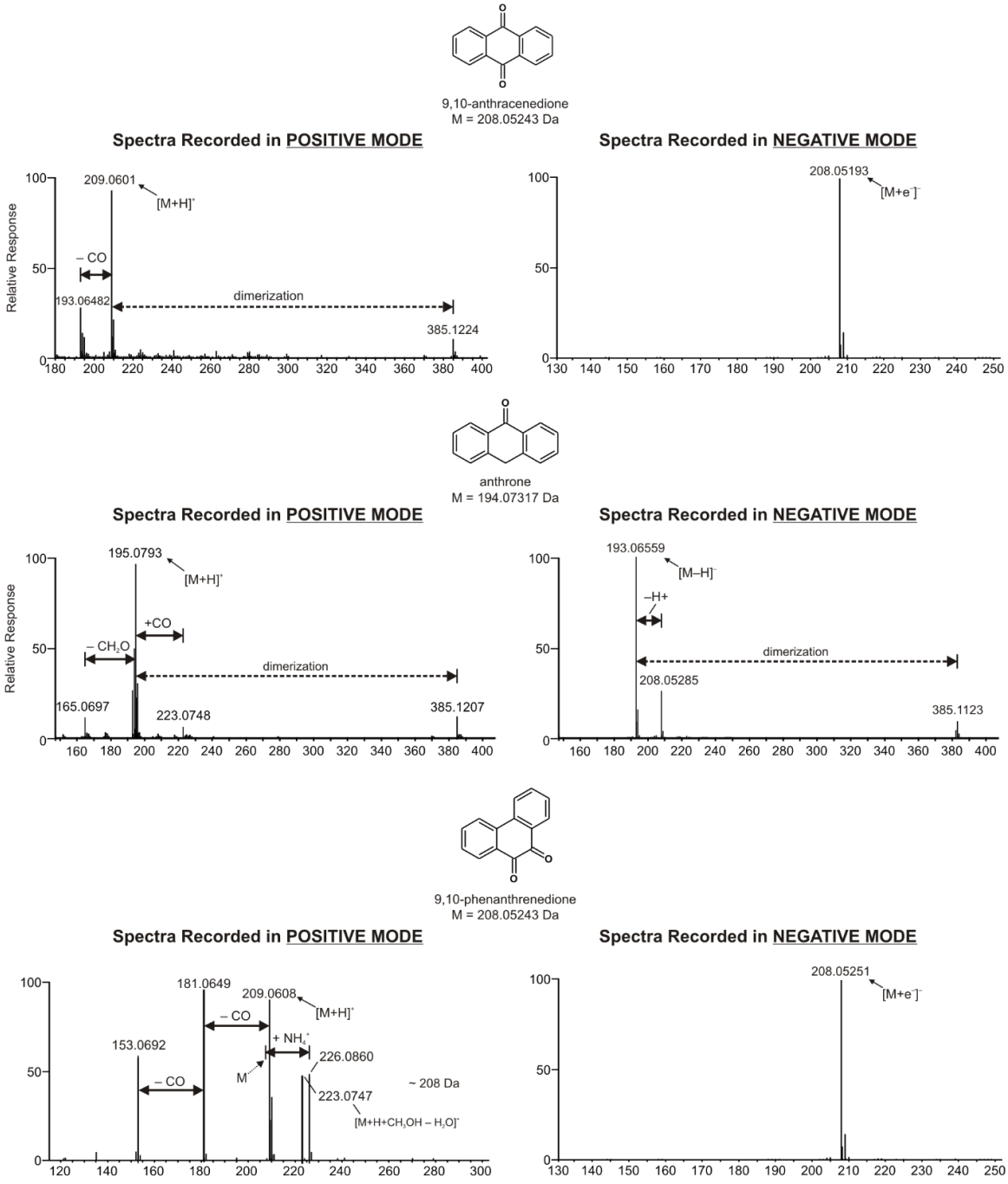

Appendix IX. cont.

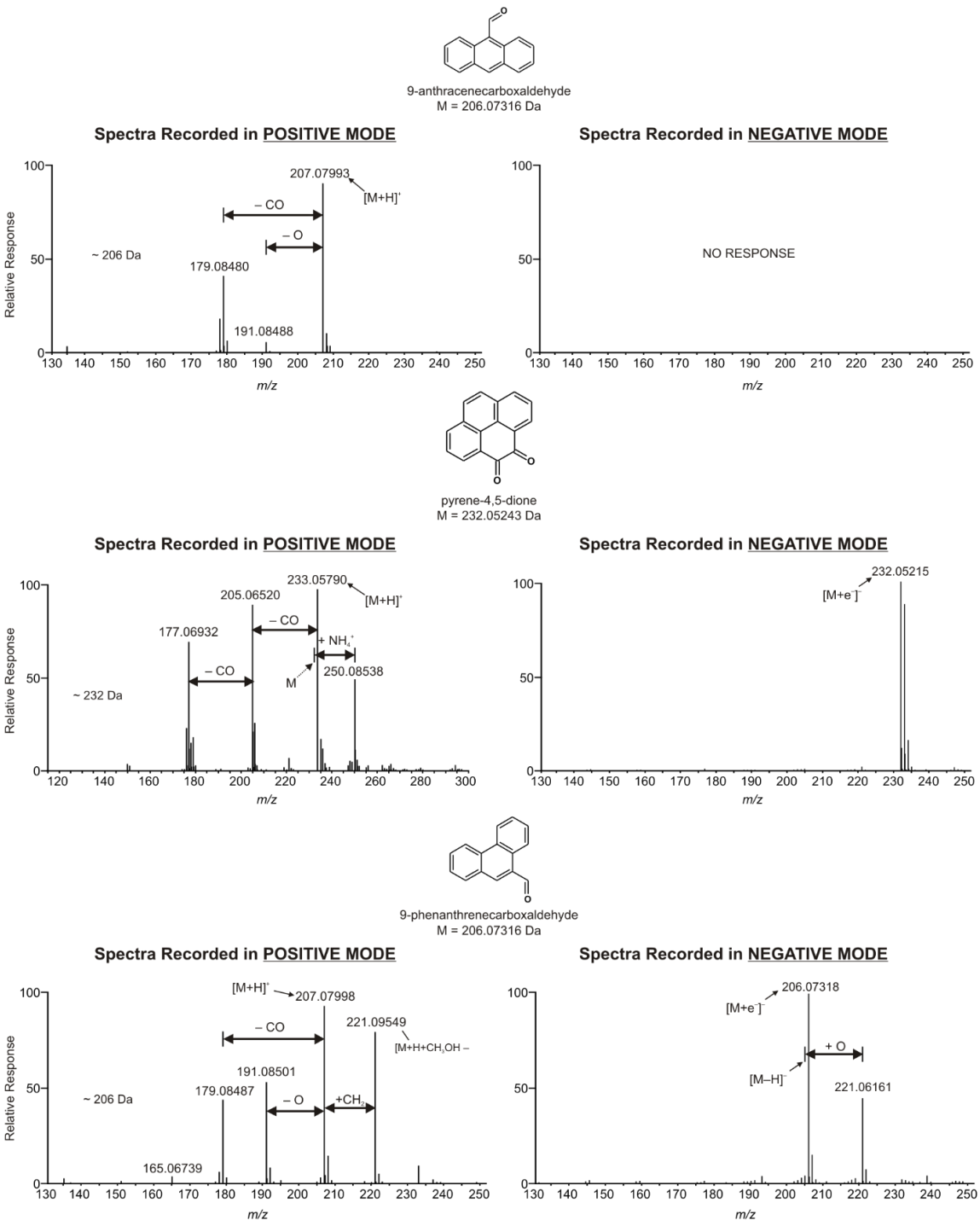

Appendix X. APCI-HRMS spectra of a) 1,4-phenanthrenedione and b) 9-anthracenecarboxaldehyde showing the formation of an oxygen adduct proposed to occur through the formation of a Meisenheimer complex intermediate. Spectra shown are average spectra taken over the width of the chromatographic peak. Neutral losses or additions shown reflect only the change in the empirical formula and do not necessarily represent the specific ionization process or pathway. Each spectra was recorded negative mode during FIA with 50% methanol in water at a flow rate of 0.2 mL min-1 using a capillary voltage of 4500 V, fragmentor voltage of 120 V and corona current of 10 µA.

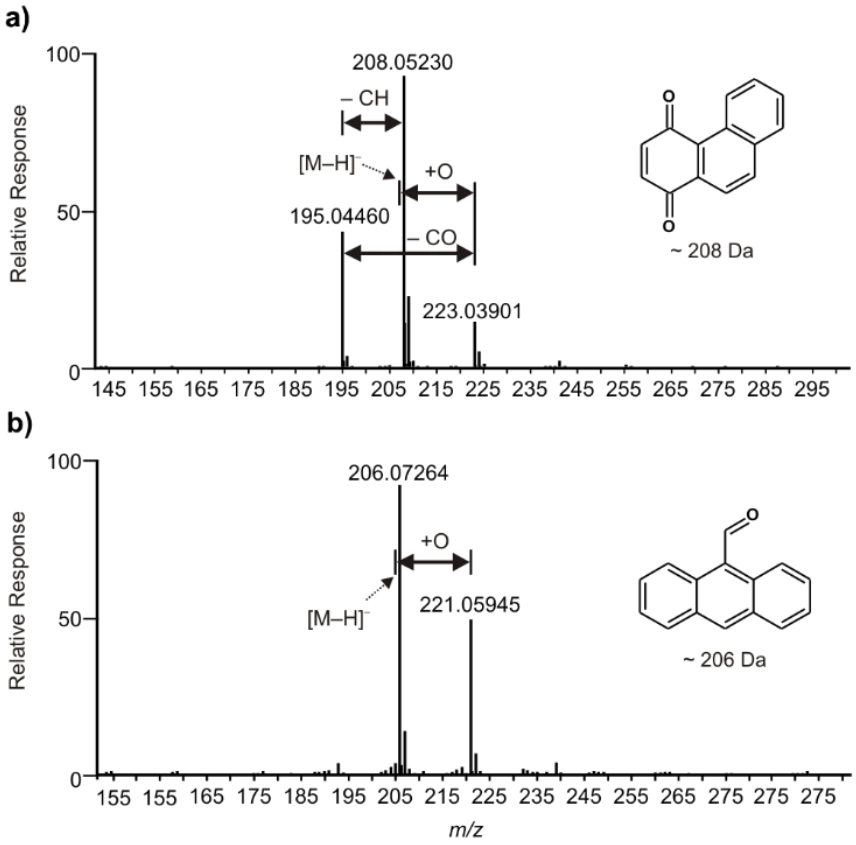

Appendix XI. APCI-HRMS spectra of nitro-PAHs in both positive and negatives modes. Spectra shown are average spectra taken over the width of the chromatographic peak. Neutral losses or additions shown reflect only the change in the empirical formula and do not necessarily represent the specific ionization process or pathway. Each spectra was recorded during FIA with 50% methanol in water at a flow rate of 0.2 mL min-1 using a capillary voltage of 4500 V, fragmentor voltage of 120 V and corona current of 10 µA.

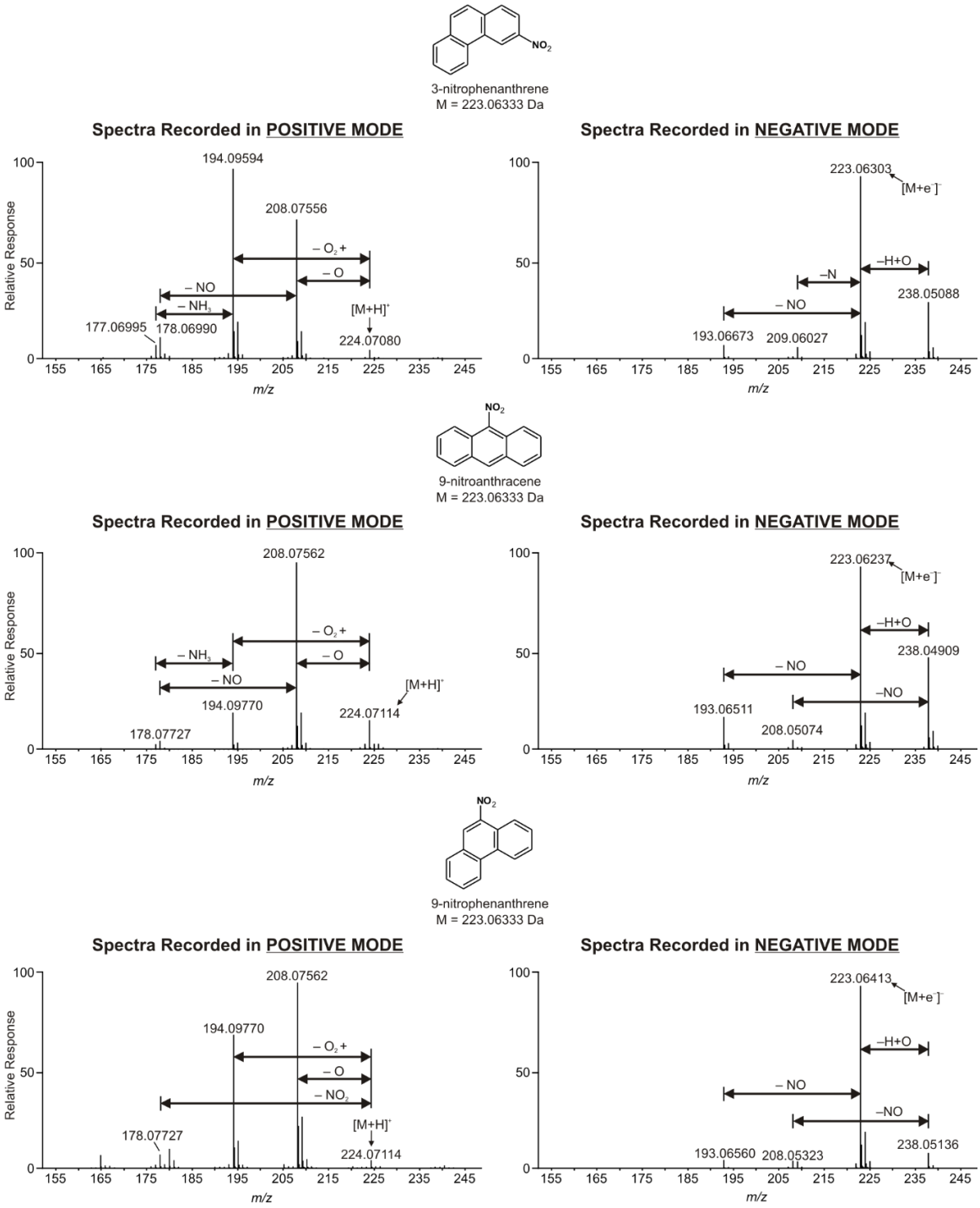

Appendix X. cont.

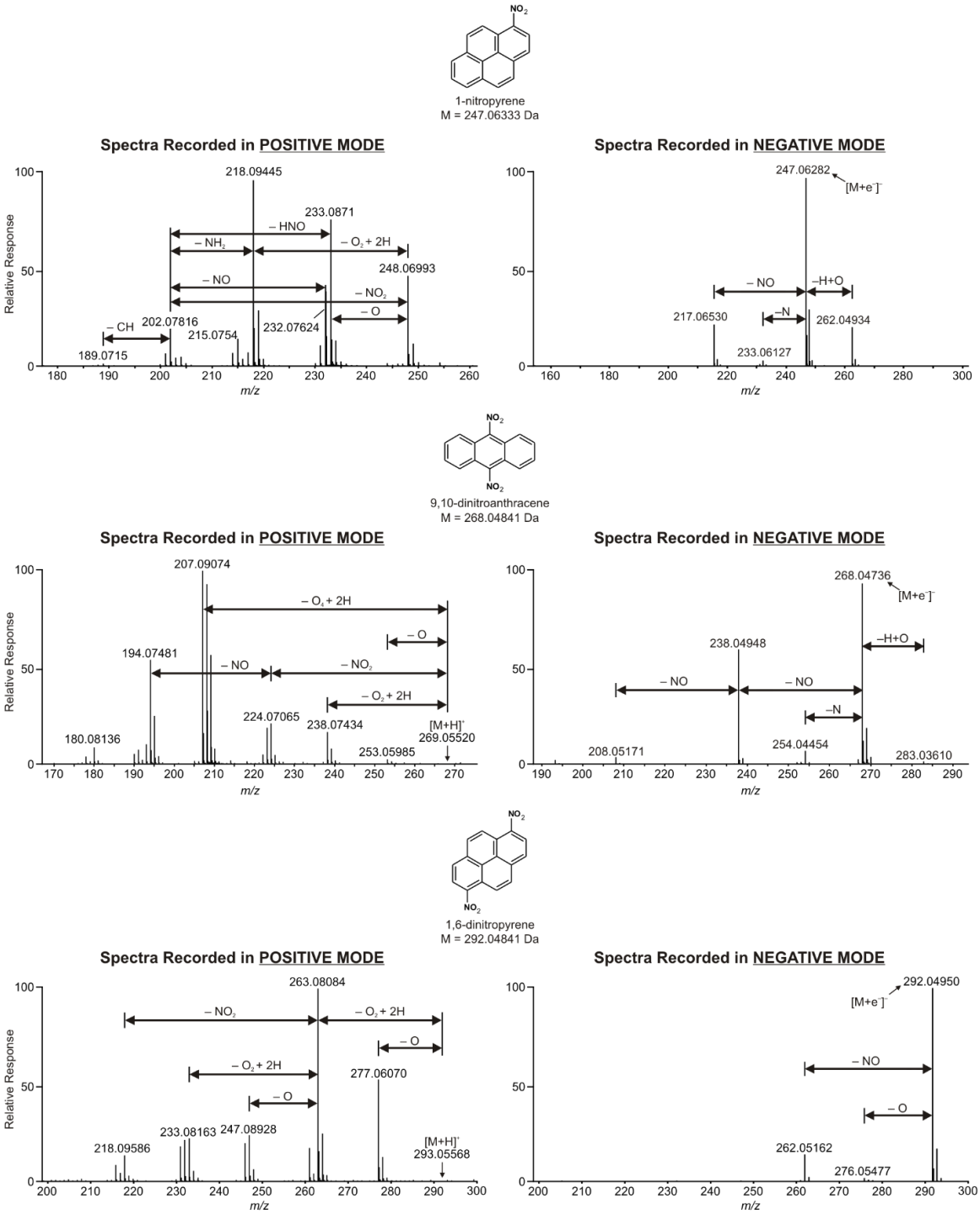

Appendix XII. APCI-HRMS spectra (left) and extracted ion chromatograms (right) of tentatively identified products formed during the ozonation of pyrene in a small-scale flow reactor. HPLC separation was performed using a C18 200 mm x 3.2 mm column (Restek) with 5 µm particle size. A gradient program of A:H2O and B:MeOH was used with a 0.2 mL min-1 flow rate: 20% B for 5 min, linear increase to 90% B at 20 min and held to 27 min, linear decrease to 20% B at 30 min and held to 35 min. Each spectra was recorded using a capillary voltage of 4500 V, fragmentor voltage of 120 V and corona current of 10 µA.

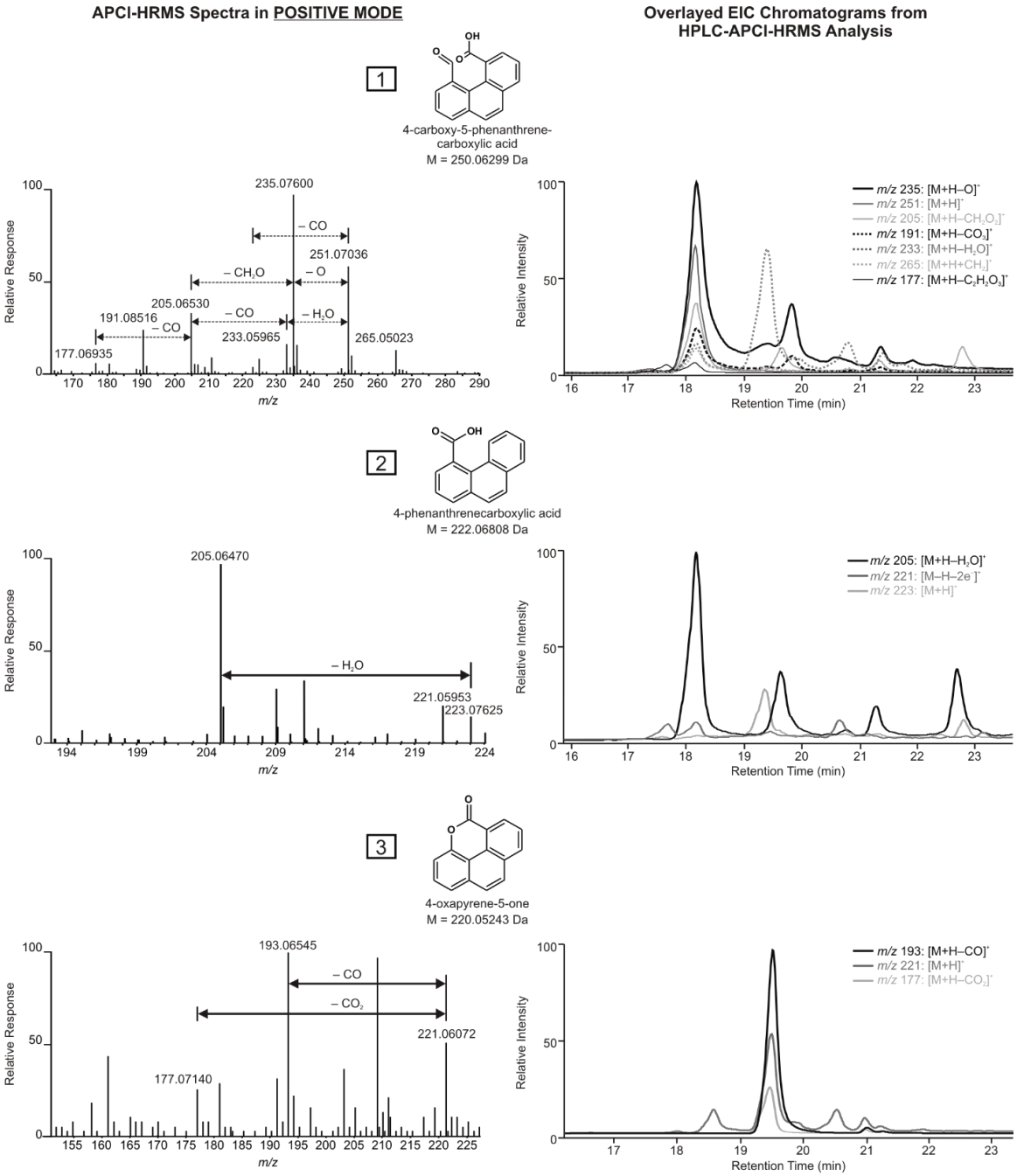

Appendix XII. cont.

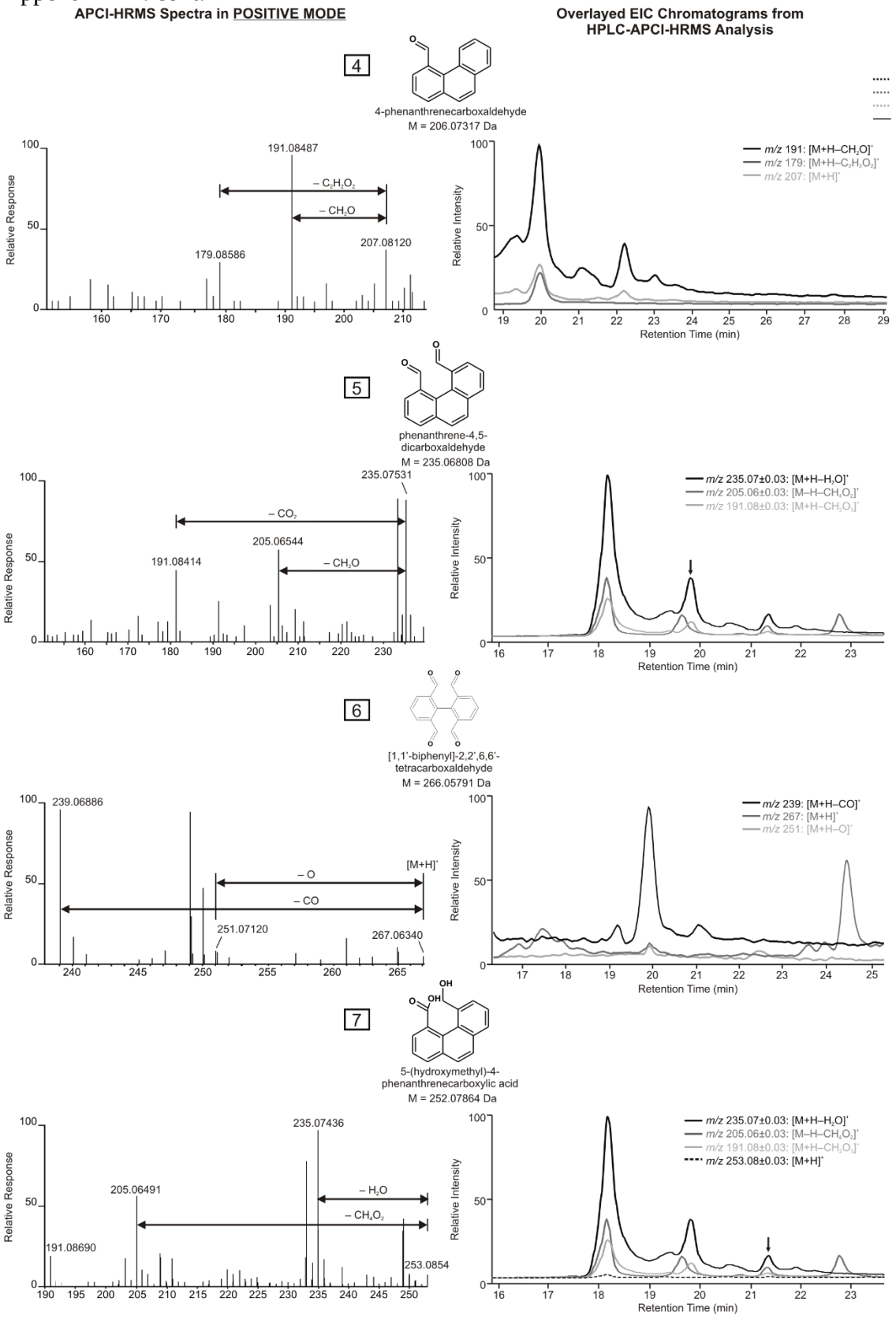

Appendix XIII. Recoveries of particle phase PAHs from a) NO2, b) O3, and c) NO2+O3 experiments. Recoveries are shown as mole percent of moles originally spiked to the quartz filter (22.4 nanomoles for 3-ring PAHs and 19.9 nanomoles for 4-ring PAHs). Standard deviations were calculated from recoveries determined during triplicate experiments.

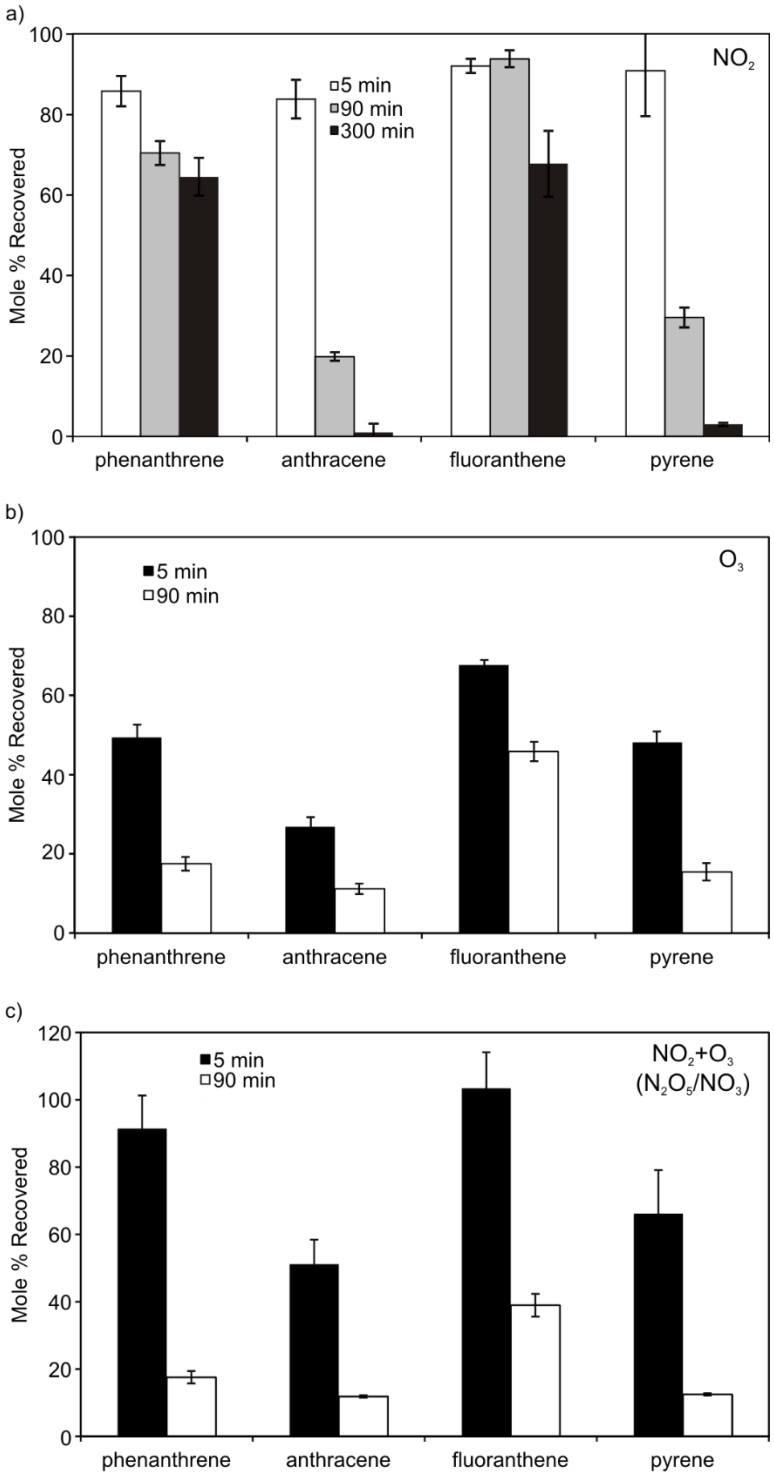

Appendix XIV. Total Ion Current (TIC) chromatograms from the analysis of extracts of quartz fiber filters collected during a PAH oxidation reaction in the small-scale flow reactor. A mixture of 3–4 ring PAHs (phenanthrene, anthracene, pyrene and fluoranthene) was exposed to a) NO_2, b) O_3, and c) NO_2+O_3. Names of the identified products are shown above their respective chromatographic peak. Species identified as background contaminants are labeled with a "c" above their respective chromatographic peak. All GC-MS analyses were performed on a 30 m DB-5ms column (0.25 mm I.D.; 0.25 µm film thickness) in splitless mode (1 min splitless time with a 30 psi pulse for 1.0 min). Species were identified by comparing the MS spectra either to standards or to MS spectral libraries (NIST 2005 & 2008). Species that were identified without any specifically assigned stereochemistry are signified with an "n" and labeled alphabetically by retention time (e.g. "n-nitrophenanthrene A").

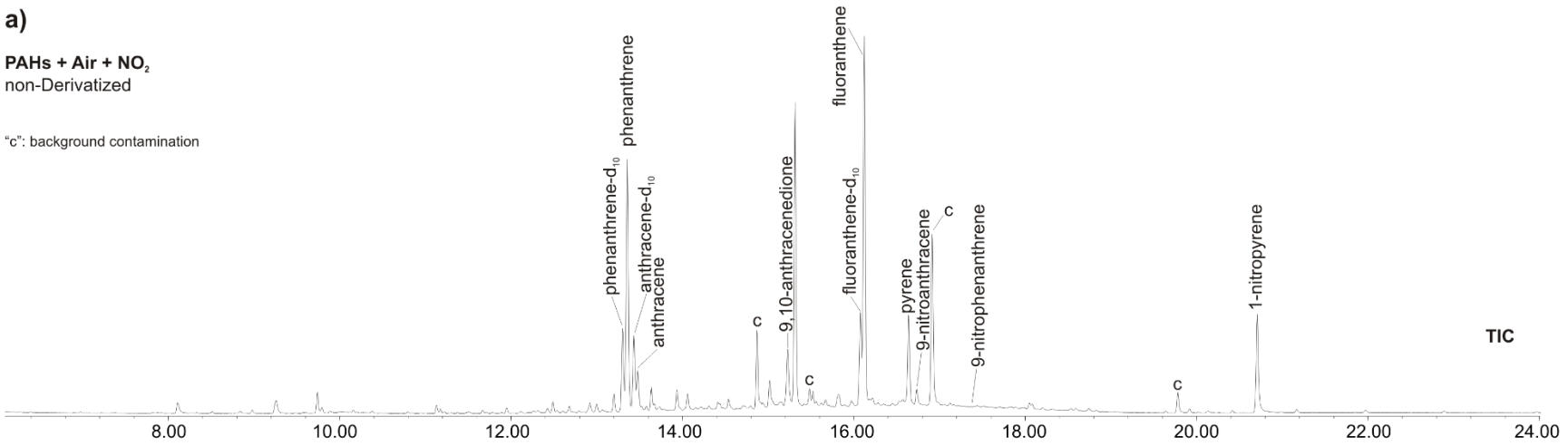

Appendix XIV. cont.

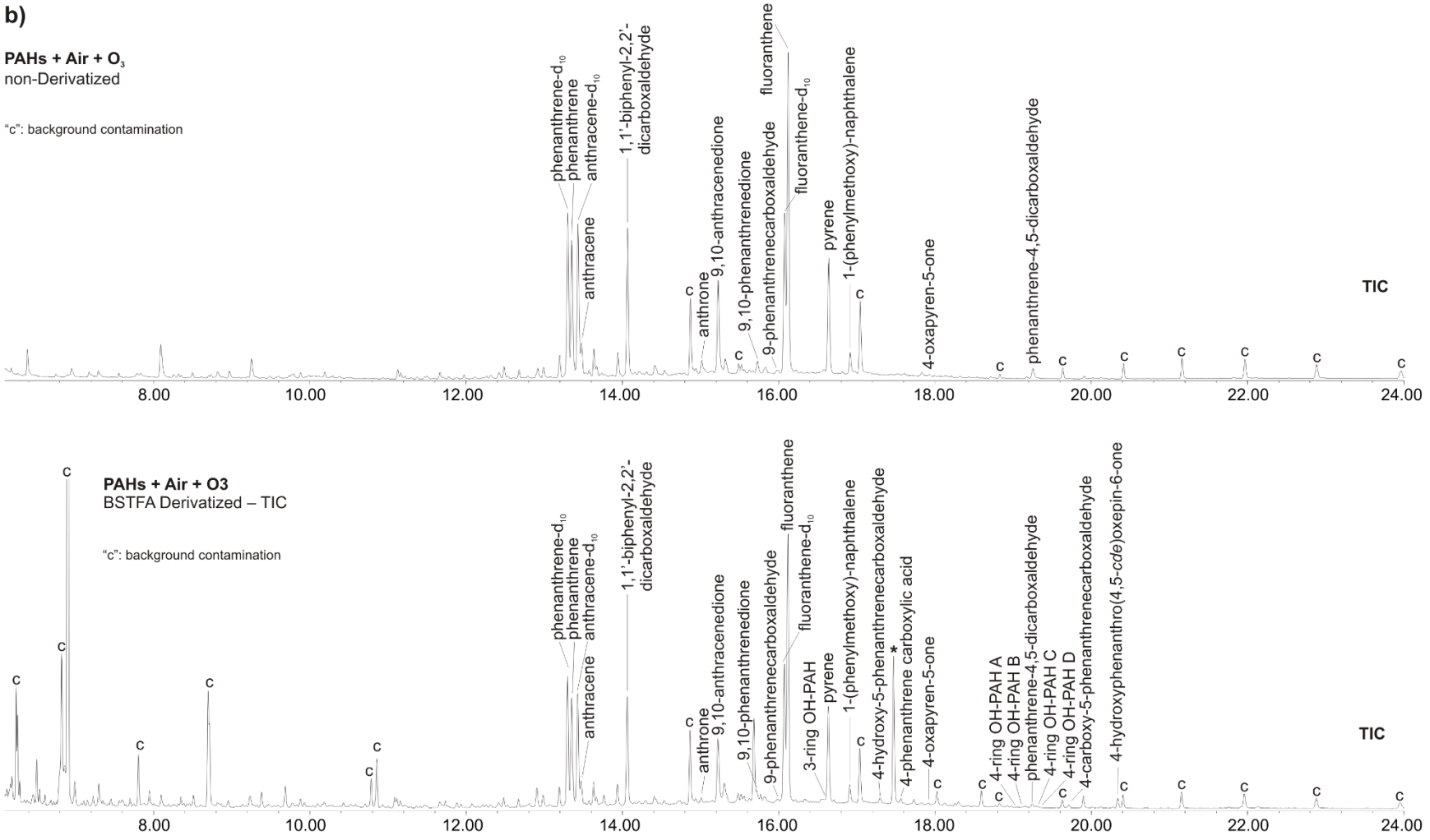

Appendix XIV. cont.

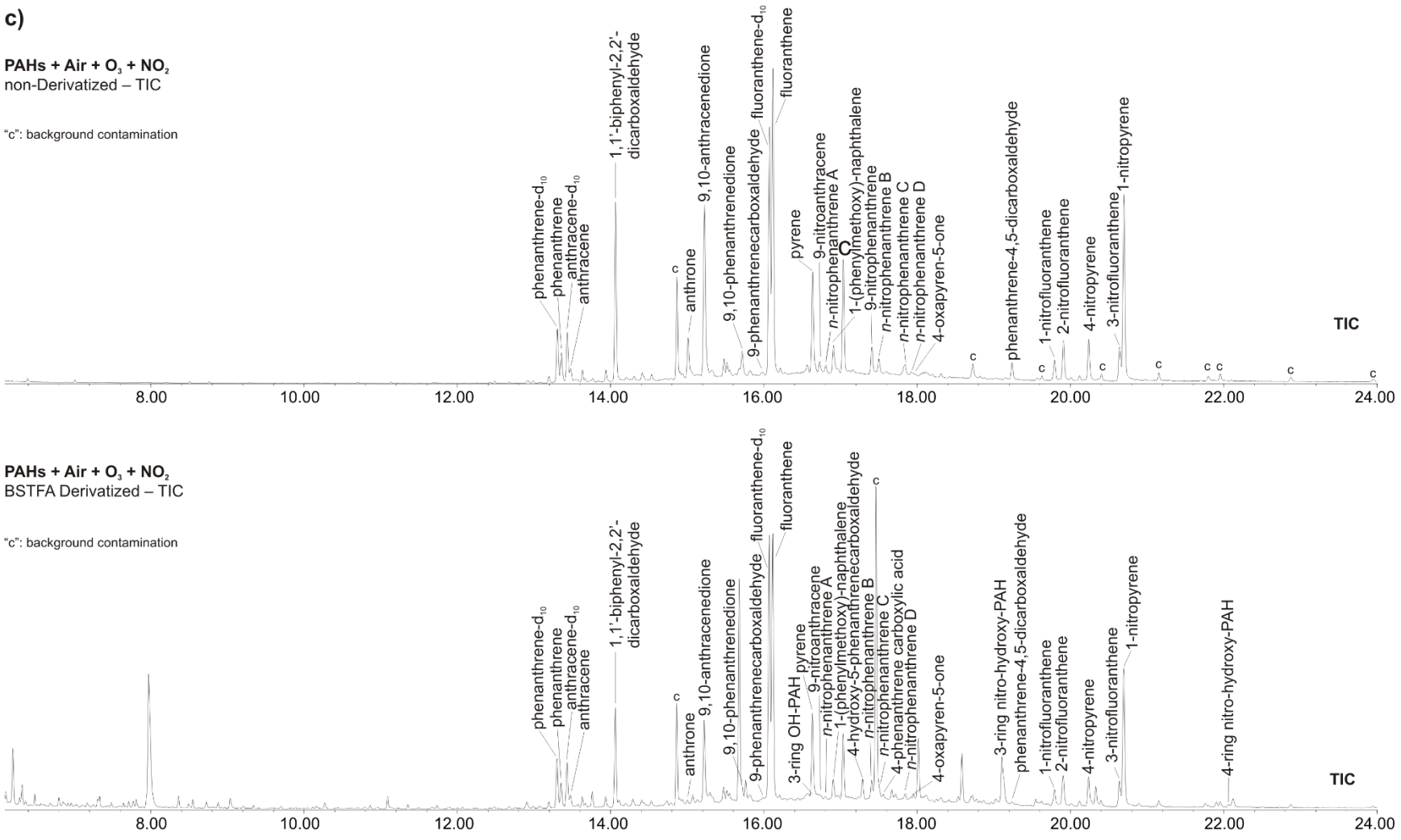

Appendix XV. Total Ion Current (TIC) chromatograms from the analysis of extracts of quartz fiber filters collected during a PAH oxidation reaction in the small-scale flow reactor. Reactions of a) a mixture of 3–4 ring PAHs (phenanthrene, anthracene, pyrene and fluoranthene), b) pyrene only, and c) anthracene only with O_3 are shown.

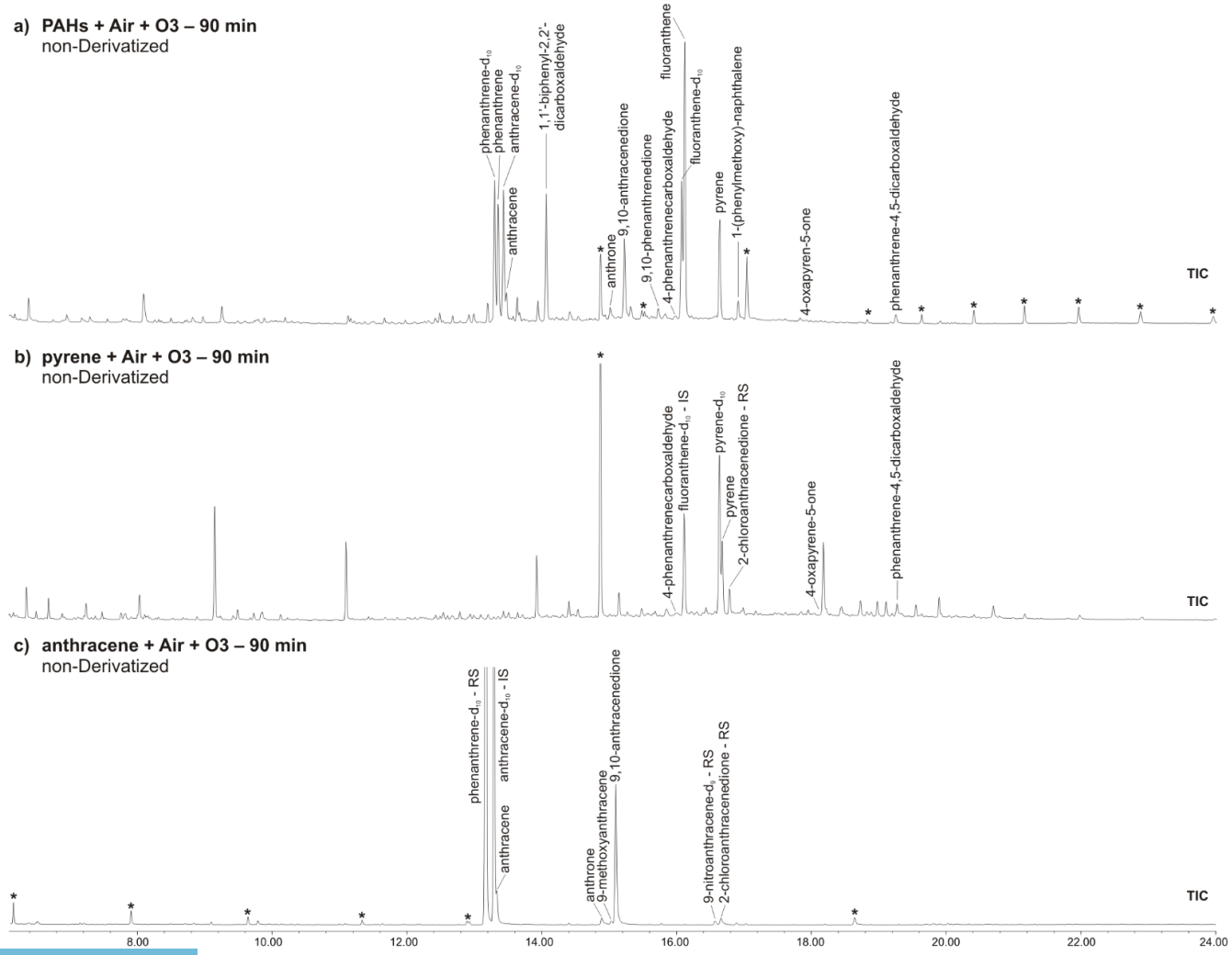

Appendix XVI. EIC chromatograms of the common ion m/z 176 showing products formed during the reaction of 3- and 4-ring PAHs with a) NO_2, b) O_3, c) O_3 with BSTFA derivatization, d) NO_2+O_3, e) NO_2+O_3 with BSTFA derivatization.

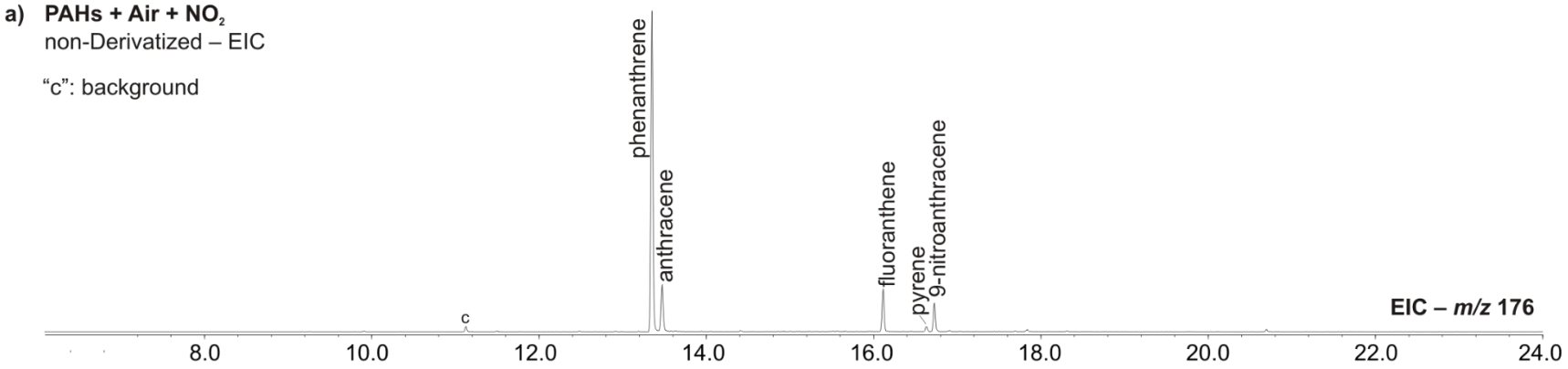

Appendix XVI. cont.

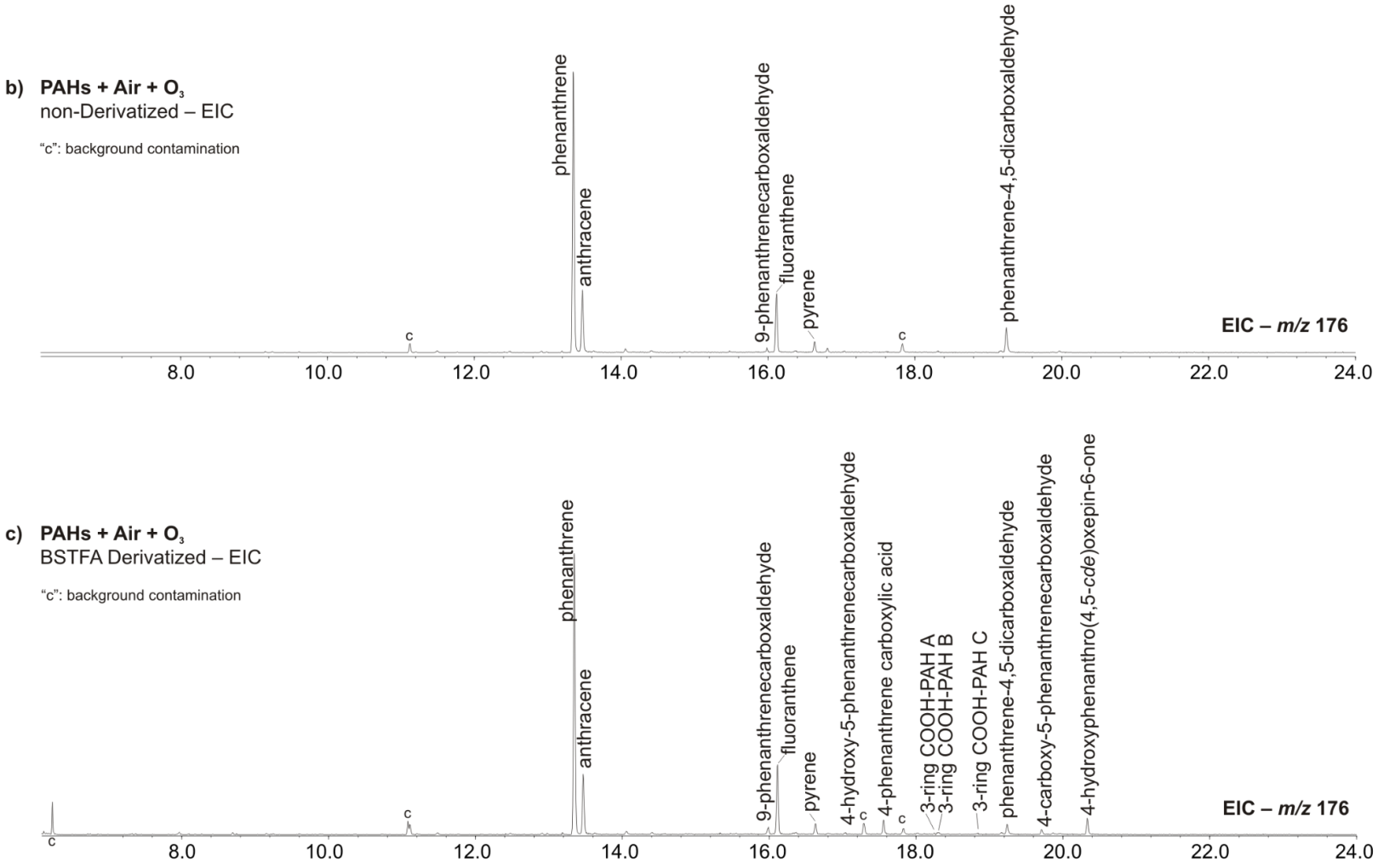

Appendix XVI. cont.

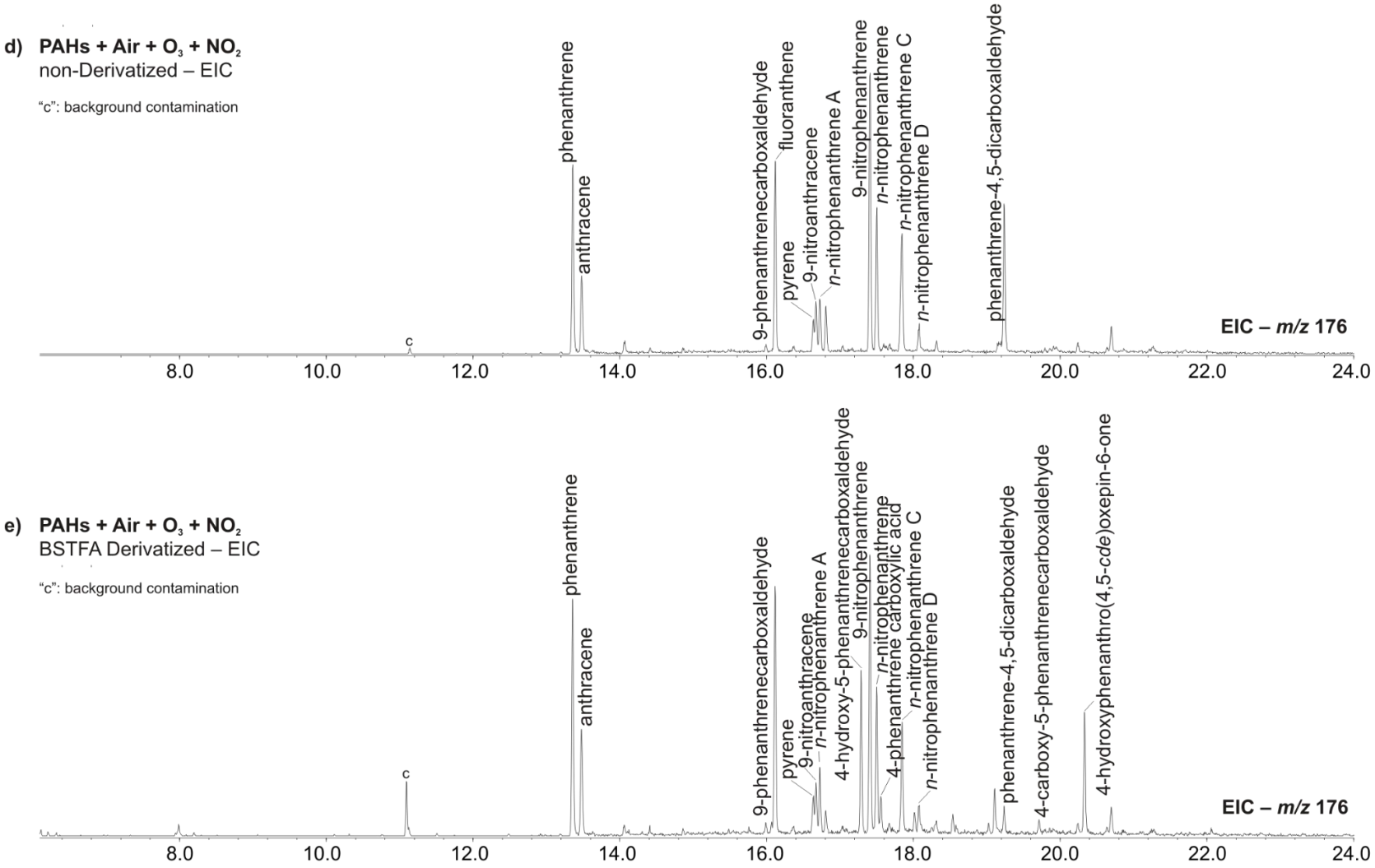

Appendix XVII. EI-MS (left) and APCI-HRMS (right) spectra of unknown compounds from the oxidation of PAHs tentatively identified in this work. EI-MS spectra was recorded following GC separation and APCI-HRMS spectra were recorded following HPLC separation. Each spectra shown is an averaged spectra over the chromatographic peak and subtracted by background spectral signals.

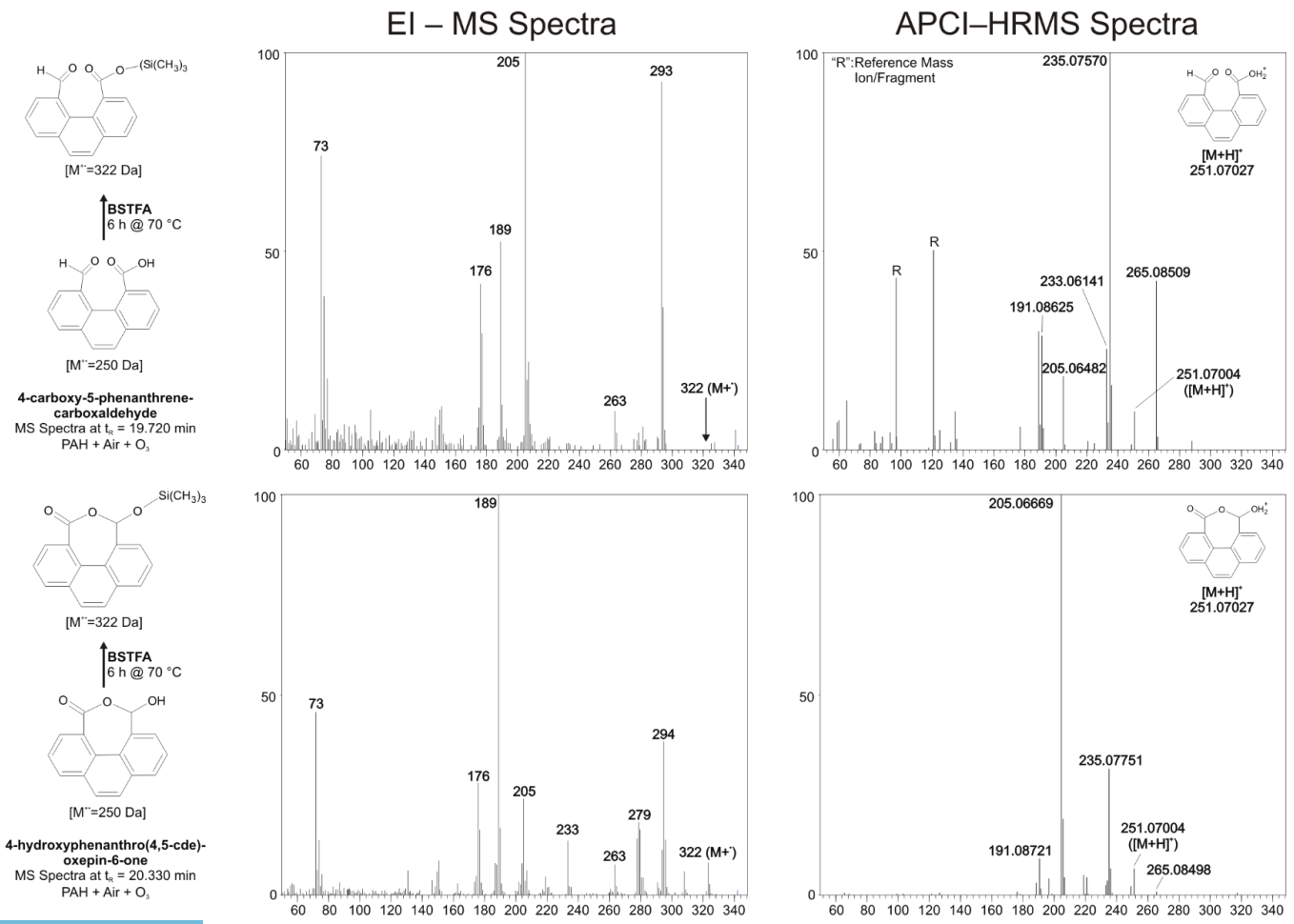

Appendix XVII. cont.

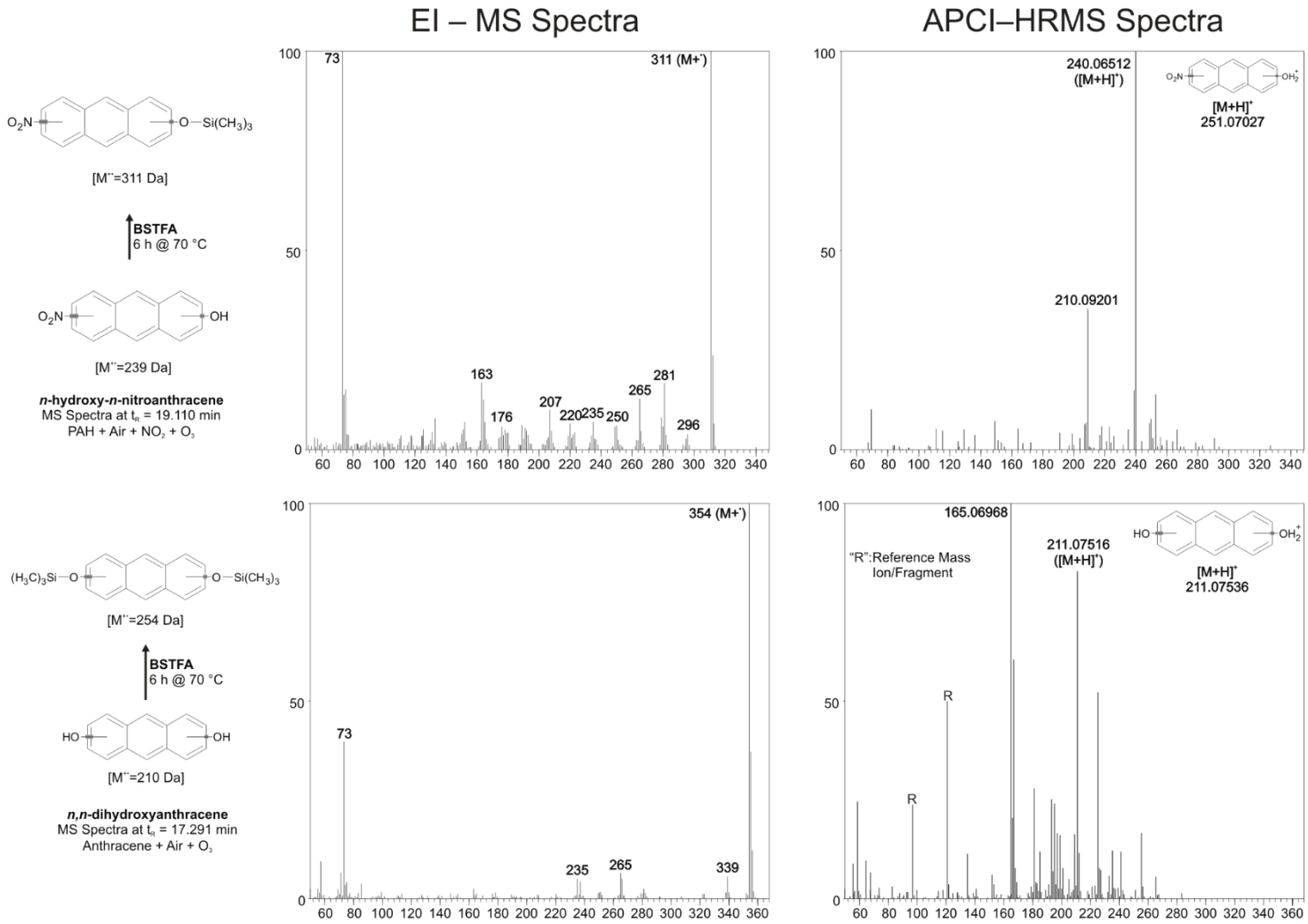

Appendix XVII. cont.

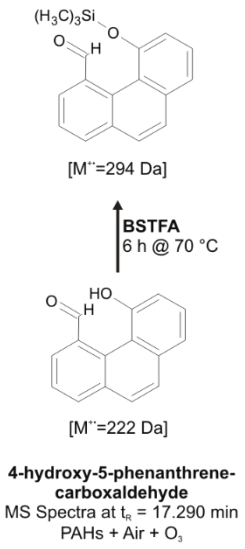

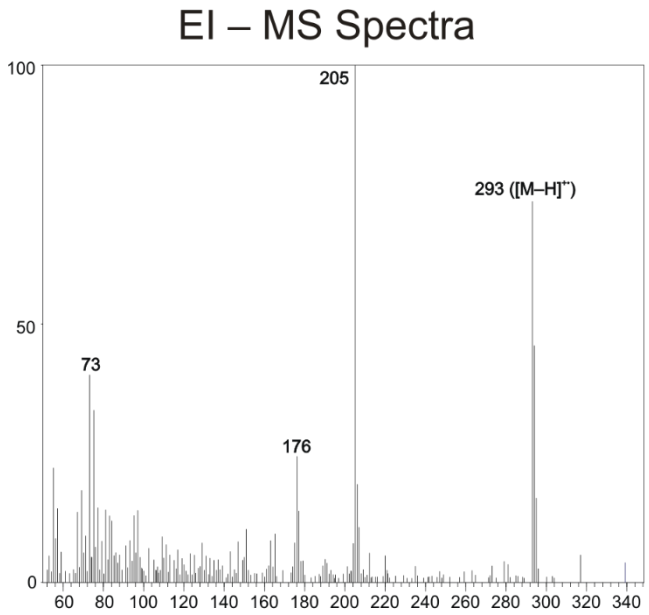

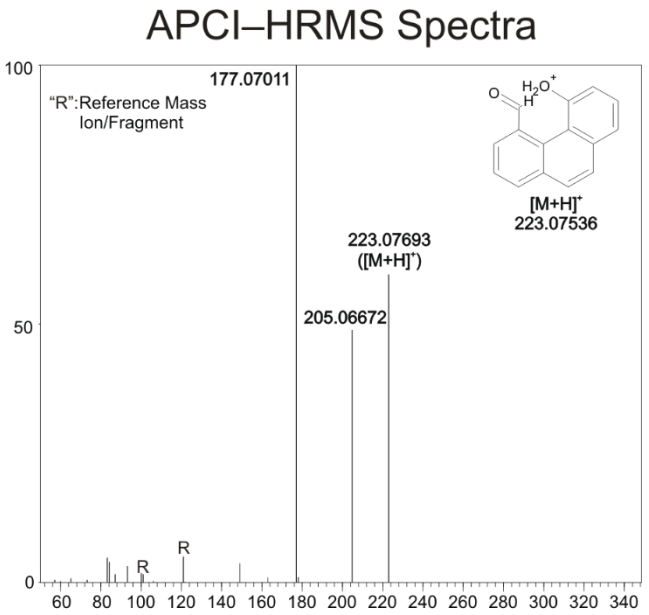

Appendix XVIII. EIC chromatograms of the common ion m/z 205 showing products formed during the reaction of 3- and 4-ring PAHs with NO_2+O_3 (N_2O_5/NO_3). Chromatograms were obtained from the analysis of the filter extract without derivatization (top) and after derivatization with BSTFA (bottom).

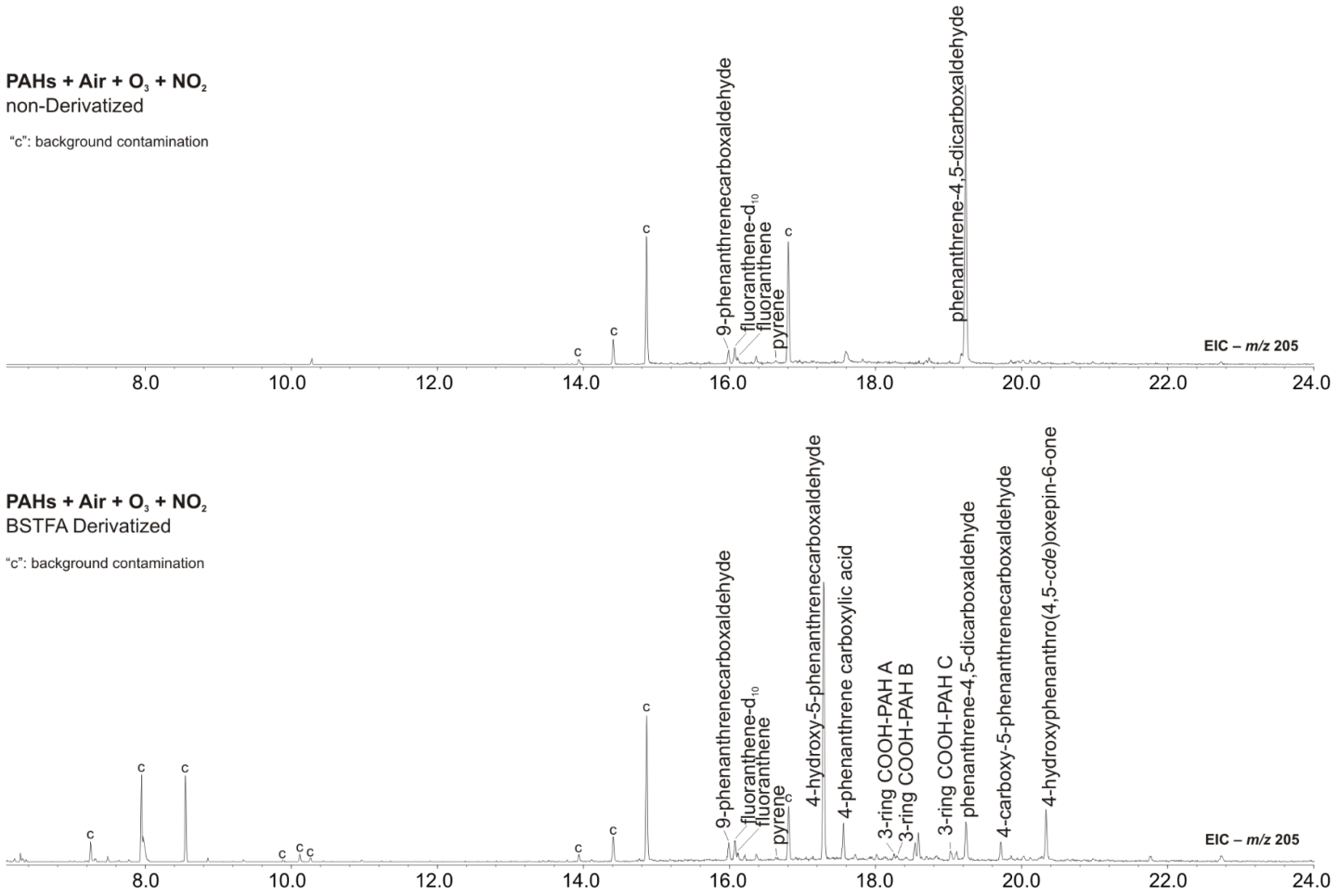

Appendix XIX. Overlayed EIC chromatograms of *m/z* 223 showing decreased amount of 3-ring nitro-PAH derivatives observed during the reaction of PAHs with NO_2+O_3 ($N_2O_5NO_3$) in the presence of UV.

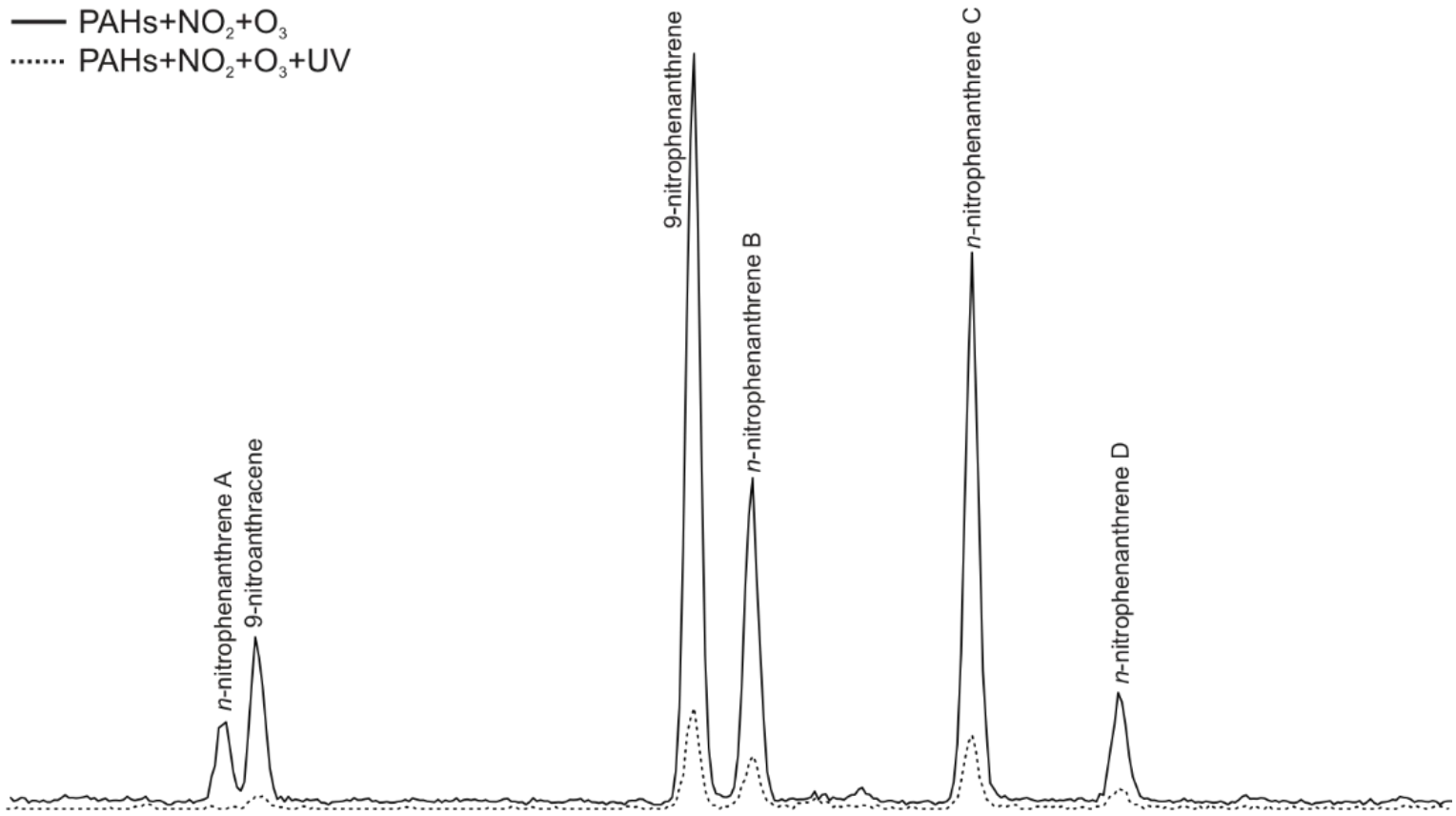

Appendix XX. Schematic representation of the diesel exhaust ejector diluter used to sample exhaust emitted from a diesel engine and transfer it to the reactor bag in the large-scale aerosol chamber.

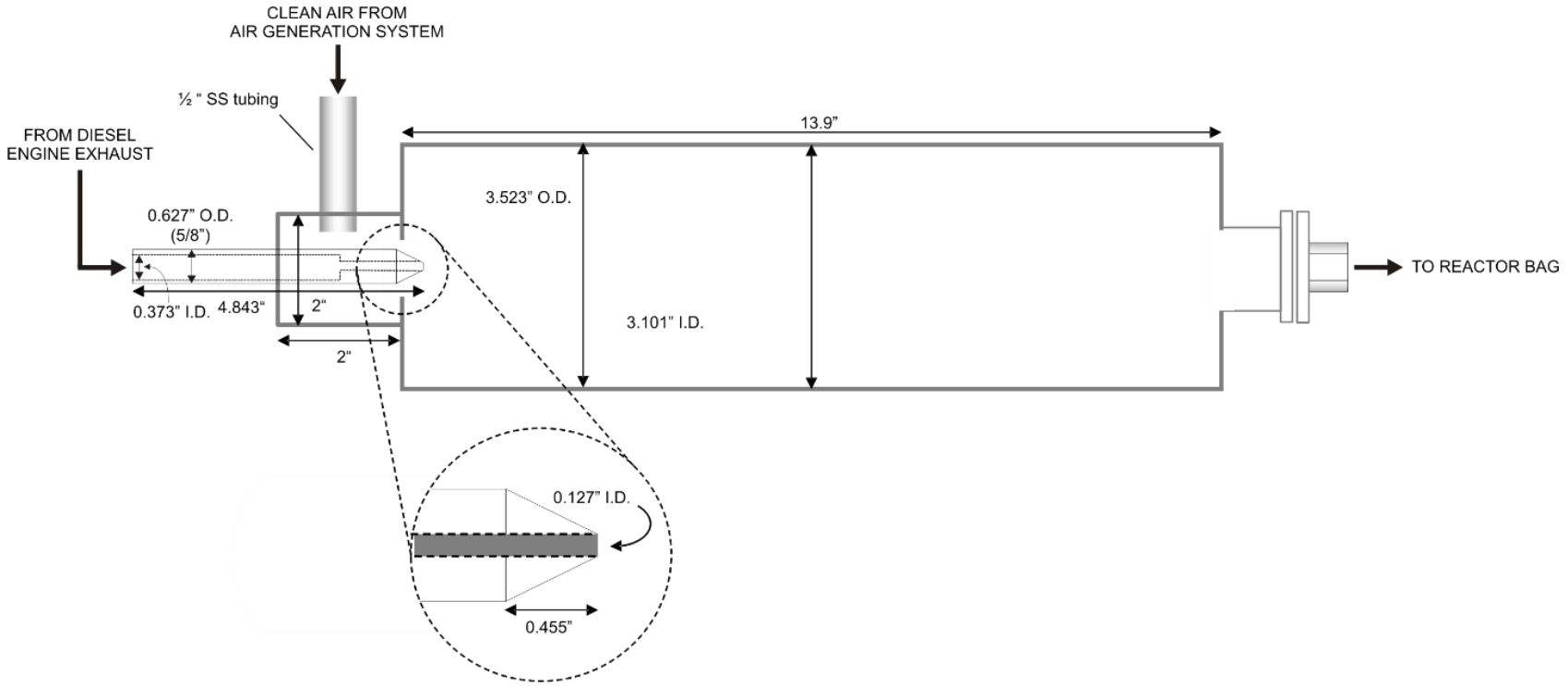

Appendix XXI. DSC heat flow curves obtained from the TGA-DSC analysis of phenanthrene standard (neat) using different N_2 purge gas flow rates. Analyzed using alumina sample cups with a linear heating ramp of dT/dt=0.33 K s^{-1}.

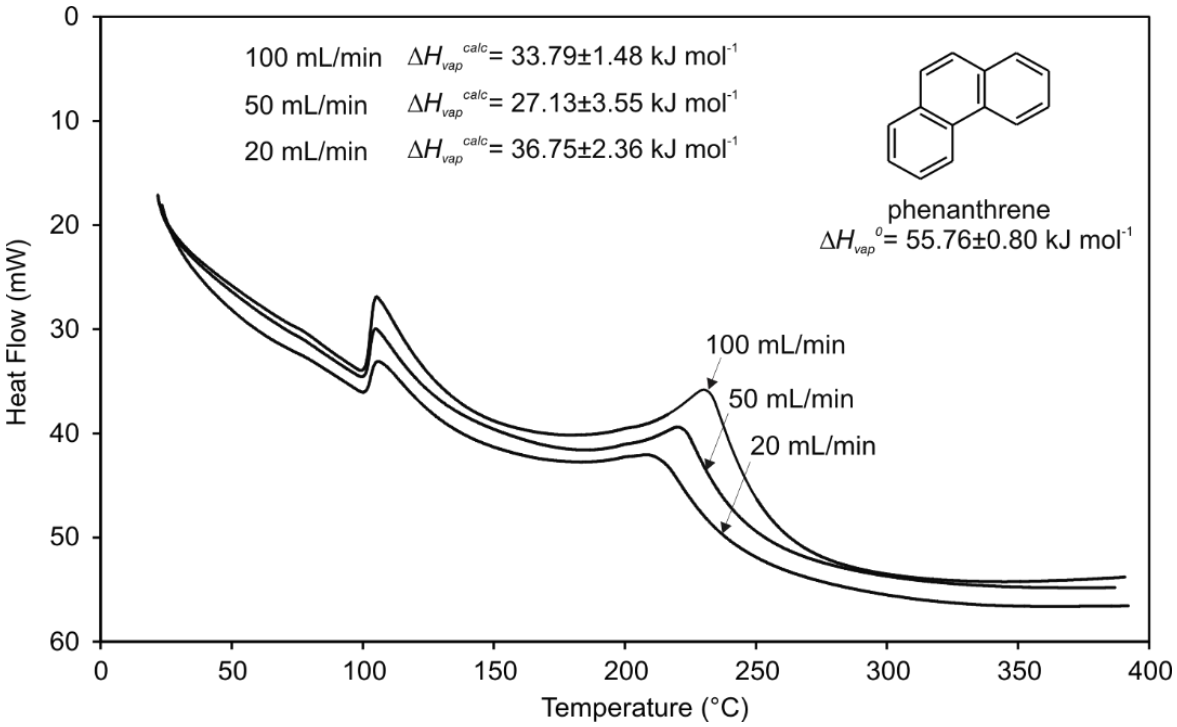

Appendix XXII. Comparison of heat flow curves obtained with TGA-DSC analysis of phenanthrene with different sample pan types and configurations. Analyzed using aluminum sample cups with a linear heating ramp of $dT/dt=0.33\ K\ s^{-1}$.

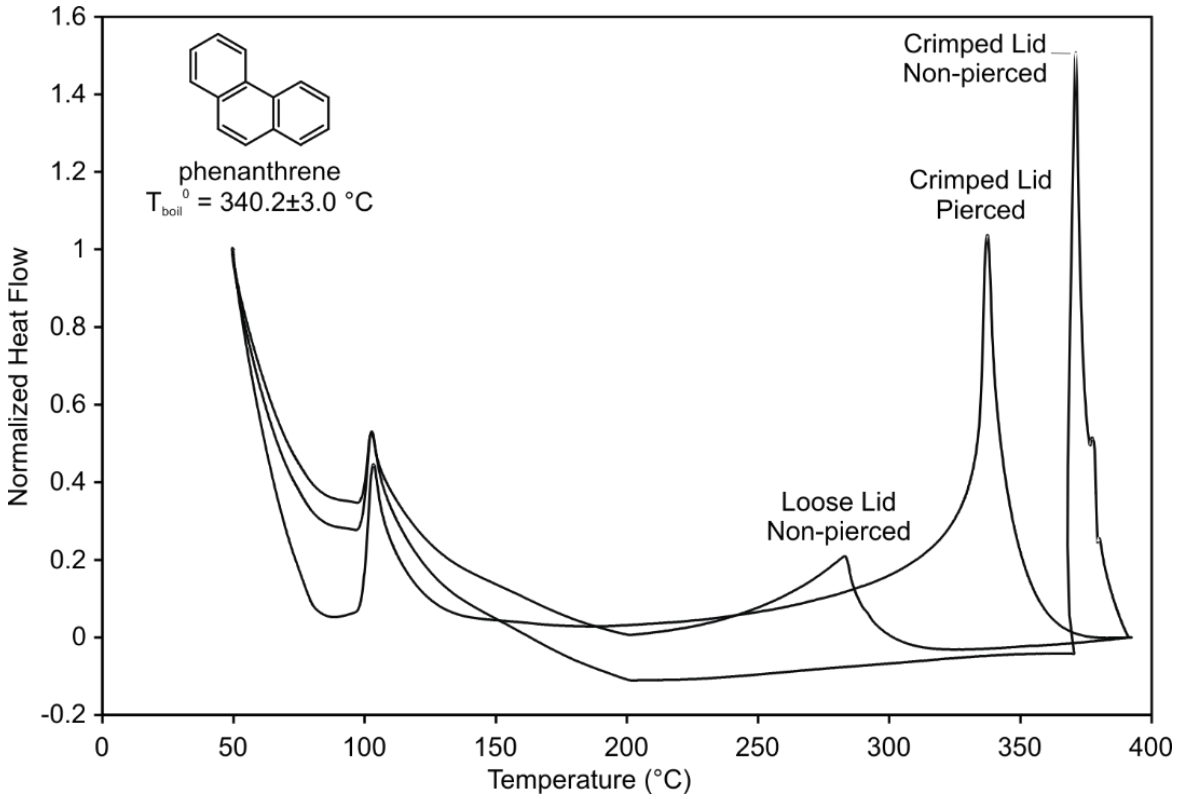

Appendix XXIII. Mass loss (TGA) curves (right) obtained for neat standards of 2–4 ring PAHs with overlayed DSC curves; their respective DTG curves are shown on the right.

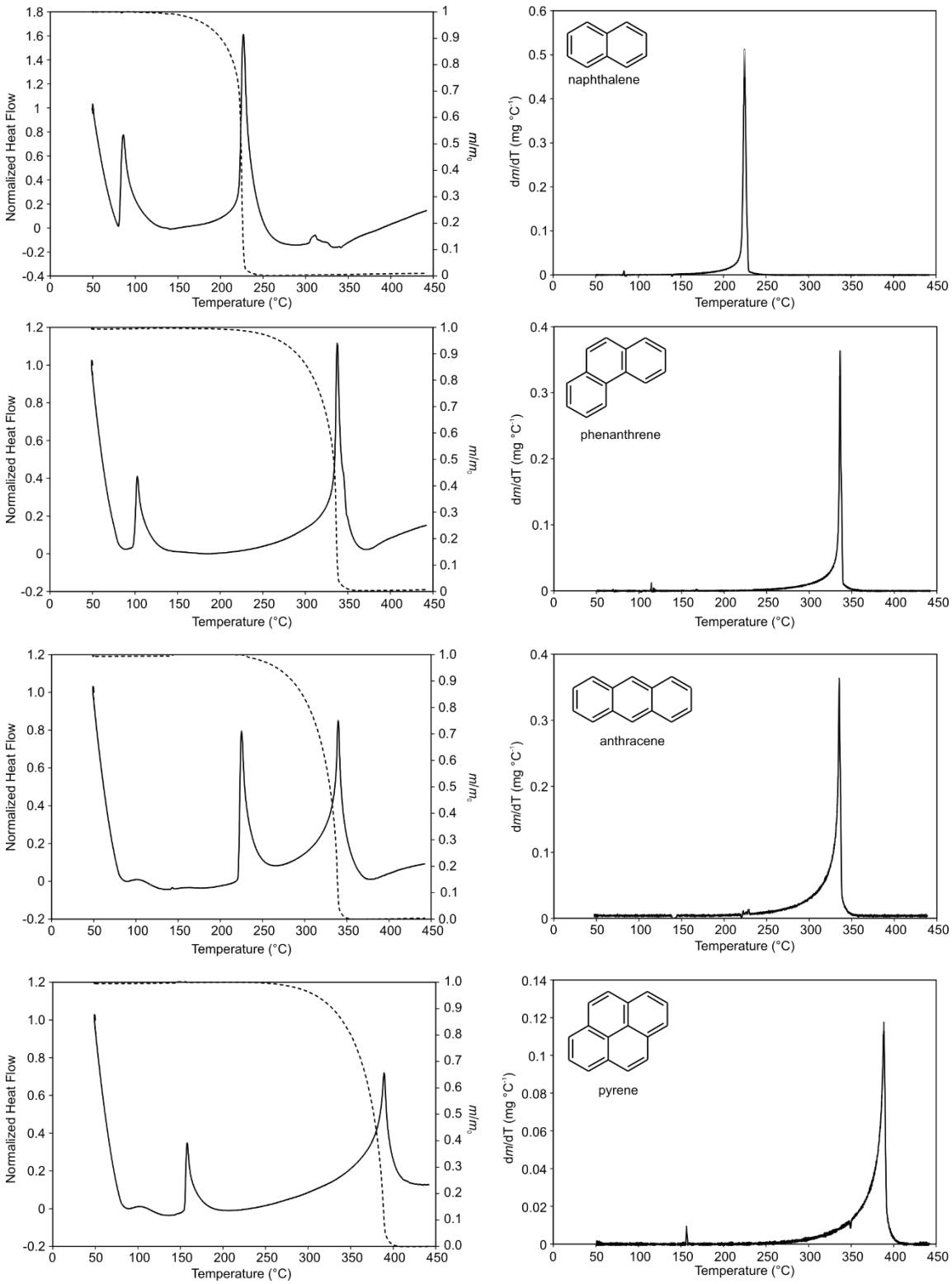

Appendix XXIV. Mass loss (TGA) curves obtained for neat standards of 2–4 ring PAHs with overlayed curves determined from the Integral (left) and Derivative (right) methods (for each the range used for determining the E_a value is shown).

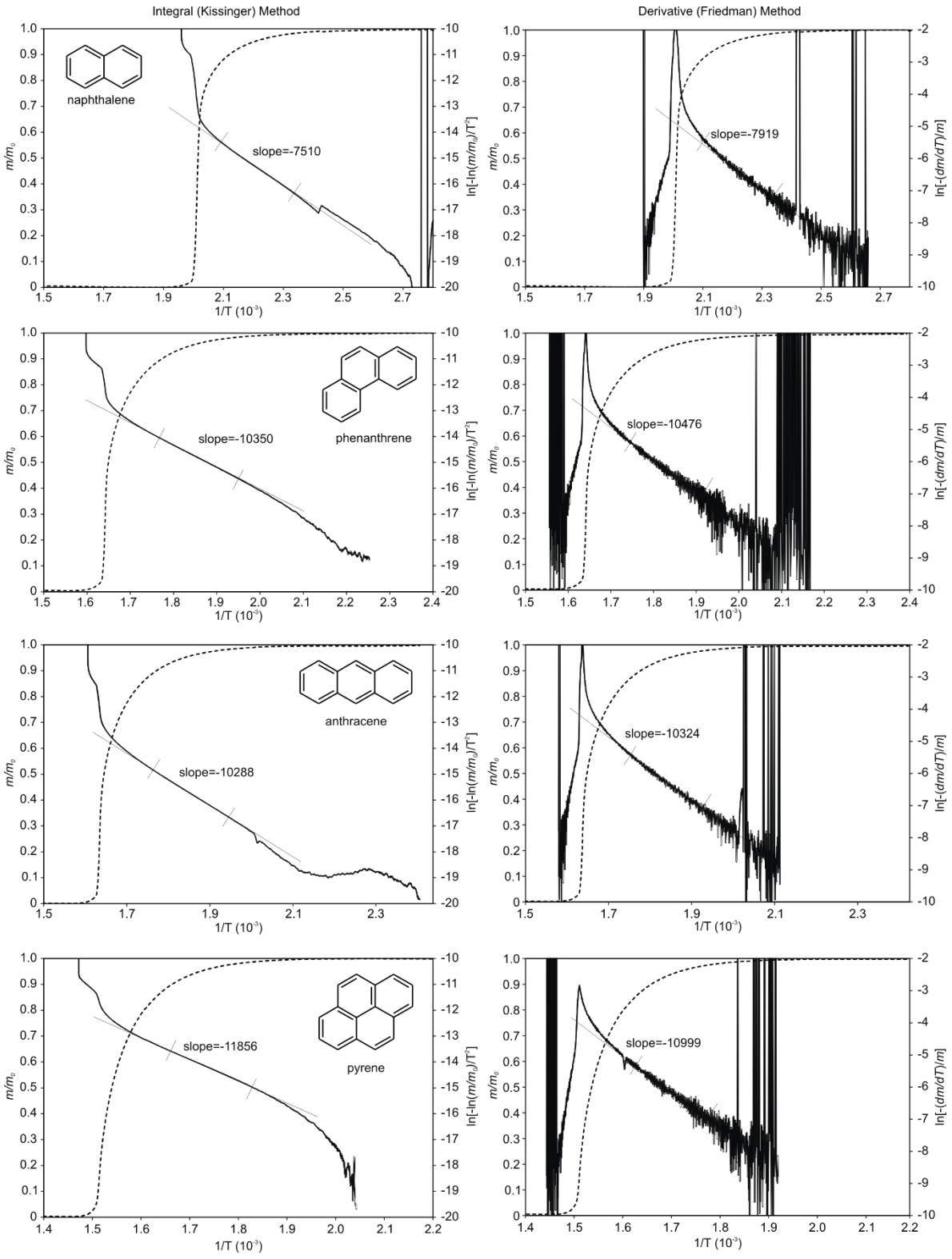

REFERENCES

(1) Pandis, S. N.; Seinfeld, J. H. *Atmospheric Chemistry and Physics*; 2nd ed.; John Wiley & Sons, Inc.: Hoboken, 2006; pp. 670–675.

(2) Pöschl, U. Atmospheric Aerosols: Composition, Transformation, Climate and Health Effects. *Angew. Chem. Int. Ed.* **2005**, *44*, 7520–7540.

(3) Finlayson-Pitts, B. J.; Pitts, Jr., J. N. *Upper and Lower Atmosphere*; 1st Editio.; Academic Press: San Diego, California, 2000.

(4) Novakov, T.; Penner, J. E. Large Contribution of Organic Aerosols to Cloud-Condensation-Nuclei Concentrations. *Nature* **1993**, *365*, 823–826.

(5) Colbeck, I. *Evironmental Chemistry of Aerosols*; Colbeck, I., Ed.; 1st ed.; Blackwell Publishing: Oxford, 2008.

(6) Ravindra, K.; Sokhi, R.; Vangrieken, R. Atmospheric Polycyclic Aromatic Hydrocarbons: Source Attribution, Emission Factors and Regulation. *Atmos. Environ.* **2008**, *42*, 2895–2921.

(7) U.S. Environmental Protection Agency. *Clean Air Act Amendment*; 1990.

(8) Reynolds, P. R.; Wasley, K. M.; Allison, C. H. Diesel Particulate Matter Induces Receptor for Advanced Glycation End-Products (RAGE) Expression in Pulmonary Epithelial Cells, and RAGE Signaling Influences NF-κB-Mediated Inflammation. *Environ. Heal. Persp.* **2011**, *119*, 332–336.

(9) Totlandsdal, A. I.; Ovrevik, J.; Cochran, R. E.; Herseth, J.-I.; Bølling, A. K.; Låg, M.; Schwarze, P.; Lilleaas, E.; Holme, J. A.; Kubátová, A. The Occurrence of Polycyclic Aromatic Hydrocarbons and Their Derivatives and the Proinflammatory Potential of Fractionated Extracts of Diesel Exhaust and Wood Smoke Particles. *J. Environ. Sci. Heal. A* **2014**, *49*, 383–396.

(10) Xia, T.; Korge, P.; Weiss, J. N.; Li, N.; Venkatesen, M. I.; Sioutas, C.; Nel, A. Quinones and Aromatic Chemical Compounds in Particulate Matter Induce Mitochondrial Dysfunction: Implications for Ultrafine Particle Toxicity. *Environ. Heal. Persp.* **2004**, *112*, 1347–1358.

(11) Pandey, S. K.; Kim, K.-H.; Brown, R. J. C. A Review of Techniques for the Determination of Polycyclic Aromatic Hydrocarbons in Air. *TrAC Trends Anal. Chem.* **2011**, *30*, 1716–1739.

(12) Poster, D. L.; Schantz, M. M.; Sander, L. C.; Wise, S. A. Analysis of Polycyclic Aromatic Hydrocarbons (PAHs) in Environmental Samples: A Critical Review of Gas Chromatographic (GC) Methods. *Anal. Bioanal. Chem.* **2006**, *386*, 859–881.

(13) Zielinska, B.; Samy, S. Analysis of Nitrated Polycyclic Aromatic Hydrocarbons. *Anal. Bioanal. Chem.* **2006**, *386*, 883–890.

(14) Calvert, J. G.; Atkinson, R.; Becker, K. H.; Kamens, R. M.; Seinfeld, J. H.; Wallington, T. J.; Yarwood, G. *The Mechanisms of Atmospheric Oxidation of Aromatic Hydrocarbons*; 1st Editio.; Oxford Press: New York, New York, 2002.

(15) Zielinska, B. Atmospheric Transformation of Diesel Emissions. *Exp. Toxicol. Pathol.* **2005**, *57*, 31–42.

(16) Lewtas, J. Air Pollution Combustion Emissions: Characterization of Causative Agents and Mechanisms Associated With Cancer, Reproductive, and Cardiovascular Effects. *Mutat. Res.* **2007**, *636*, 95–133.

(17) Walgraeve, C.; Demeestere, K.; Dewulf, J.; Zimmermann, R.; Van Langenhove, H. Oxygenated Polycyclic Aromatic Hydrocarbons in Atmospheric Particulate Matter: Molecular Characterization and Occurance. *Atmos. Environ.* **2010**, *44*, 1831–1846.

(18) Zielinska, B.; Arey, J.; Atkinson, R.; Ramdahl, T.; Winer, A. M.; Pitts, J. N. Reaction of Dinitrogen Pentoxide with Fluoranthene. *J. Am. Chem. Soc.* **1986**, *108*, 4126–4132.

(19) Sweetman, J. A.; Zielinska, B.; Atkinson, R. A Possible Formation Pathway for the 2-Nitrofluoranthene Observed in Ambient Particulate Organic Matter. *Atmos. Environ.* **1986**, *20*, 235–238.

(20) Arey, J. *Handbook of Environmental Chemistry*; 1998; p. 347.

(21) Atkinson, R. Kinetics and Mechanisms of the Gas Phase Reactions of the NO3 Radical with Organic Compounds. *J. Phys. Chem. Ref. Data* **1991**, *20*, 459–507.

(22) Zielinska, B.; Samy, S. Analysis of Nitrated Polycyclic Aromatic Hydrocarbons. *Anal. Bioanal. Chem.* **2006**, *386*, 883–890.

(23) Bamford, H. A.; Bezabeh, D. Z.; Schantz, M. M.; Wise, S. A.; Baker, J. E. Determination and Comparison of Nitrated-Polycyclic Aromatic Hydrocarbons

Measured in Air and Diesel Particulate Reference Materials. *Chemosphere* **2003**, *50*, 575–587.

(24) Bezabeh, D. Z.; Bamford, H. A.; Schantz, M. M.; Wise, S. A. Determination of Nitrated Polycyclic Aromatic Hydrocarbons in Diesel Particulate-Related Standard Reference Materials by Using Gas Chromatography/Mass Spectrometry with Negative Ion Chemical Ionization. *Anal. Bioanal. Chem.* **2003**, *375*, 381–388.

(25) Nishioka, M.; Howard, C. C.; Contos, D. A.; Bail, L. M.; Lewtas, J. Detection of Hydroxylated Nitro Aromatic and Hydroxylated Nitro Polycyclic Aromatic Compounds in an Ambient Air Particulate Extract Using. *Environ. Sci. Technol.* **1988**, *22*, 908–915.

(26) Schauer, C.; Niessner, R.; Pöschl, U. Analysis of Nitrated Polycyclic Aromatic Hydrocarbons by Liquid Chromatography with Fluorescence and Mass Spectrometry Detection: Air Particulate Matter, Soot, and Reaction Product Studies. *Anal. Bioanal. Chem.* **2004**, *378*, 725–736.

(27) Adelhelm, C.; Niessner, R.; Pöschl, U.; Letzel, T. Analysis of Large Oxygenated and Nitrated Polycyclic Aromatic Hydrocarbons Formed Under Simulated Diesel Engine Exhaust Conditions (By Compound Fingerprints with SPE/LC-API-MS). *Anal. Bioanal. Chem.* **2008**, *391*, 2599–2608.

(28) Williams, T. T.; Perreault, H. Selective Detection of Nitrated Polycyclic Aromatic Hydrocarbons by Electrospray Ionization Mass Spectrometry and Constant Neutral Loss Scanning. *Rapid Commun. Mass Spectrom.* **2000**, *14*, 1474–1481.

(29) Barreto, R. P.; Albuquerque, F. C.; Netto, A. D. P. Optimization of an Improved Analytical Method for the Determination of 1-Nitropyrene in Milligram Diesel Soot Samples by High-Performance Liquid Chromatography-Mass Spectrometry. *J. Chromatogr. A* **2007**, *1163*, 219–227.

(30) Liu, Y.; Sklorz, M.; Schnelle-Kreis, J.; Orasche, J.; Ferge, T.; Kettrup, A.; Zimmermann, R. Oxidant Denuder Sampling for Analysis of Polycyclic Aromatic Hydrocarbons and Their Oxygenated Derivates in Ambient Aerosol: Evaluation of Sampling Artefact. *Chemosphere* **2006**, *62*, 1889–1898.

(31) Albinet, A.; Leoz-Garziandia, E.; Budzinski, H.; Viilenave, E. Simultaneous Analysis of Oxygenated and Nitrated Polycyclic Aromatic Hydrocarbons on Standard Reference Material 1649a (urban Dust) and on Natural Ambient Air Samples by Gas Chromatography-Mass Spectrometry with Negative Ion Chemical Ionisation. *J. Chromatogr. A* **2006**, *1121*, 106–113.

(32) Delhomme, O.; Millet, M.; Herckes, P. Determination of Oxygenated Polycyclic Aromatic Hydrocarbons in Atmospheric Aerosol Samples by Liquid Chromatography-Tandem Mass Spectrometry. *Talanta* **2008**, *74*, 703–710.

(33) Grosse, S.; Letzel, T. Liquid Chromatography/Atmospheric Pressure Ionization Mass Spectrometry With Post-Column Liquid Mixing for the Efficient Determination of Partially Oxidized Polycyclic Aromatic Hydrocarbons. *J. Chromatogr. A* **2007**, *1139*, 75–83.

(34) Kroll, J. H.; Seinfeld, J. H. Chemistry of Secondary Organic Aerosol: Formation and Evolution of Low-Volatility Organics in the Atmosphere. *Atmos. Environ.* **2008**, *42*, 3593–3624.

(35) Kanakidou, M.; Seinfeld, J. H.; Pandis, S. N.; Barnes, I.; Dentener, F. J.; Facchini, M. C.; Van Dingenen, R.; Ervens, B.; Nenes, A.; Nielsen, C. J.; et al. Organic Aerosol and Global Climate Modelling: A Review. *Atmos. Chem. Phys.* **2005**, *5*, 1053–1123.

(36) Athanasopoulou, E.; Vogel, H.; Vogel, B.; Tsimpidi, A. P.; Pandis, S. N.; Knote, C.; Fountoukis, C. Modeling the Meteorological and Chemical Effects of Secondary Organic Aerosols During an EUCAARI Campaign. *Atmos. Chem. Phys.* **2013**, *13*, 625–645.

(37) Couvidat, F.; Kim, Y.; Sartelet, K.; Seigneur, C.; Marchand, N.; Sciare, J. Modeling Secondary Organic Aerosol in an Urban Area: Application to Paris, France. *Atmos. Chem. Phys.* **2013**, *13*, 983–996.

(38) Epstein, S. A.; Riipinen, I.; Donahue, N. M. A Semiempirical Correlation Between Enthalpy of Vaporization and Saturation Concentration for Organic Aerosol. *Environ. Sci. Technol.* **2010**, *44*, 743–748.

(39) Wei, Y.; Cao, T.; Thompson, J. E. The Chemical Evolution & Physical Properties of Organic Aerosol: A Molecular Structure Based Approach. *Atmos. Environ.* **2012**, *62*, 199–207.

(40) Beránek, J.; Kozliak, E.; Kubátová, A. Evaluation of Sequential Solvent and Thermal Extraction Followed by Analytical Pyrolysis for Chemical Characterization of Carbonaceous Particulate Matter. *J. Chromatogr. A* **2013**, *1279*, 27–35.

(41) Horan, A. J.; Gao, Y.; Hall, W. A.; Johnston, M. V. Online Characterization of Particles and Gases with an Ambient Electrospray Ionization Source. *Anal. Chem.* **2012**, *84*, 9253–9258.

(42) Gao, S.; Ng, N. L.; Keywood, M.; Varutbangkul, V.; Bahreini, R.; Nenes, A.; He, J.; Yoo, K. Y.; Beauchamp, J. L.; Hodyss, R. P.; et al. Particle Phase Acidity and Oligomer Formation in Secondary Organic Aerosol. *Environ. Sci. Technol.* **2004**, *38*, 6582–6589.

(43) Kalberer, M.; Sax, M.; Samburova, V. Molecular Size Evolution of Oligomers in Organic Aerosols Collected in Urban Atmospheres and Generated in a Smog Chamber. *Environ. Sci. Technol.* **2006**, *40*, 5917–5922.

(44) Matuschek, G.; Karg, E.; Schröppel, A.; Schulz, H.; Schmid, O. Chemical Investigation of Eight Different Types of Carbonaceous Particles Using Thermoanalytical Techniques. *Environ. Sci. Technol.* **2007**, *41*, 8406–8411.

(45) Fushimi, A.; Hashimoto, S.; Ieda, T.; Ochiai, N.; Takazawa, Y.; Fujitani, Y.; Tanabe, K. Thermal Desorption - Comprehensive Two-Dimensional Gas Chromatography Coupled with Tandem Mass Spectrometry for Determination of Trace Polycyclic Aromatic Hydrocarbons and Their Derivatives. *J. Chromatogr. A* **2012**, *1252*, 164–170.

(46) Schnelle-Kreis, J.; Welthagen, W.; Sklorz, M.; Zimmermann, R. Application of Direct Thermal Desorption Gas Chromatography and Comprehensive Two-Dimensional Gas Chromatography Coupled to Time of Flight Mass Spectrometry for Analysis of Organic Compounds in Ambient Aerosol Particles. *J. Sep. Sci.* **2005**, *28*, 1648–1657.

(47) Hawthorne, S. B.; Krieger, M. S.; Miller, D. J.; Mathiason, M. B. Collection and Quantitation of Methoxylated Phenol Tracers for Atmospheric Pollution from Residential Wood Stoves. *Environ. Sci. Technol.* **1989**, *23*, 470–475.

(48) Greenberg, A.; Lwo, J.-H.; Atherholt, T. B.; Rosen, R.; Hartman, T.; Butler, J.; Louis, J. Bioassay-Directed Fractionation of Organic Compounds Associated With Airborne Particulate Matter: An Interseasonal Study. *Atmos. Environ. - Part A Gen. Top.* **1993**, *27A*, 1609–1626.

(49) Lewis, A. C.; Robinson, R. E.; Bartle, K. D.; Pilling, M. J. On-Line Coupled LC-GC-ITD/MS for the Identification of Alkylated, Oxygentaed, and Nitrated Polycyclic Aromatic Compounds in Urban Air Particulate Extracts. *Environ. Sci. Technol.* **1995**, *29*, 1977–1981.

(50) Choudhury, D. R. Characterization of Polycyclic Ketones and Quinones in Diesel Emission Particulates by Gas Chromatography/Mass Spectrometryt. *Environ. Sci. Technol.* **1982**, *16*, 102–106.

(51) Rogge, W. F.; Hildemann, L. M.; Mazurek, M. a.; Cass, G. R. Sources of Fine Organic Aerosol . 9 . Pine , Oak , and Synthetic Log Combustion in Residential Fireplaces. *Environ. Sci. Technol.* **1998**, *32*, 13–22.

(52) Alves, C.; Pio, C.; Duarte, A. Composition of Extractable Organic Matter of Air Particles from Rural and Urban Portuguese Areas. *Atmos. Environ.* **2001**, *32*, 5485–5496.

(53) Kallio, M.; Hyötyläinen, T.; Lehtonen, M.; Jussila, M.; Hartonen, K.; Shimmo, M.; Riekkola, M.-L. Comprehensive Two-Dimensional Gas Chromatography in the Analysis of Urban Aerosols. *J. Chromatogr. A* **2003**, *1019*, 251–260.

(54) Smith, C. J.; Walcott, C. J.; Huang, W.; Maggio, V.; Grainger, J.; Patterson Jr., D. G. Determination of Selected Monohydroxy Metabolites of 2-, 3- and 4-Ring Polycyclic Aromatic Hydrocarbons in Urine by Solid-Phase Microextraction and Isotope Dilution Gas Chromatography-Mass Spectrometry. *J. Chromatogr. B* **2002**, *778*, 157–164.

(55) Harrison, A. G. *Chemical Ionization Mass Spectrometry*; 1st ed.; CRC Press: Boca Raton, 1983.

(56) Tsapakis, M.; Stephanou, E. G. Diurnal Cycle of PAHs, Nitro-PAHs, and Oxy-PAHs in a High Oxidation Capacity Marine Background Atmosphere. *Environ. Sci. Technol.* **2007**, *41*, 8011–8017.

(57) Bamford, H. M.; D. Bezabeh, M. Lopez De Alda, D.L. Poster, L.C. Sander, M.M. Schantz, P. Schubert, A. L. W. SRM 2975 Diesel Particulate Matter Certificate of Analysis. *NIST* **2004**, *64*, 321–326.

(58) Kubatova, A.; Lahren, T.; Beranek, J.; Smoliakova, I.; Braun, A.; Huggins, F. Extractable Organic Carbon and Its Differentiation by Polarity in Diesel Exhaust, Wood Smoke, and Urban Particulate Matter. *Aerosol Sci. Technol.* **2009**, *43*, 714–729.

(59) Schantz, M. M.; Nichols, J. J.; Wise, S. A. Evaluation of Pressurized Fluid Extraction for the Extraction of Environmental Matrix Reference Materials. *Anal. Chem.* **1997**, *69*, 4210–4219.

(60) Masala, S.; Ahmed, T.; Bergvall, C.; Westerholm, R. Improved Efficiency of Extraction of Polycyclic Aromatic Hydrocarbons (PAHs) From the National Institute of Standards and Technology (NIST) Standard Reference Material Diesel Particulate Matter (SRM 2975) Using Accelerated Solvent Extraction. *Anal. Bioanal. Chem.* **2011**, *401*, 3305–3315.

(61) Schantz, M. M.; McGaw, E.; Wise, S. A. Pressurized Liquid Extraction of Diesel and Air Particulate Standard Reference Materials: Effect of Extraction Temperature and Pressure. *Anal. Chem.* **2012**, *84*, 8222–8231.

(62) Walgraeve, C.; Demeestere, K.; De Wispelaere, P.; Dewulf, J.; Lintelmann, J.; Fischer, K.; Van Langenhove, H. Selective Accurate-Mass-Based Analysis of 11 Oxy-PAHs on Atmospheric Particulate Matter by Pressurized Liquid Extraction Followed by High-Performance Liquid Chromatography and Magnetic Sector Mass Spectrometry. *Anal. Bioanal. Chem.* **2012**, *402*, 1697–1711.

(63) Schantz, M. M. Pressurized Liquid Extraction in Environmental Analysis. *Anal. Bioanal. Chem.* **2006**, *386*, 1043–1047.

(64) Perraudin, E.; Budzinski, H.; Villenave, E. Analysis of Polycyclic Aromatic Hydrocarbons Adsorbed on Particles of Atmospheric Interest Using Pressurised Fluid Extraction. *Anal. Bioanal. Chem.* **2005**, *383*, 122–131.

(65) Cochran, R. E.; Dongari, N.; Jeong, H.; Beránek, J.; Haddadi, S.; Shipp, J.; Kubátová, A. Determination of Polycyclic Aromatic Hydrocarbons and Their Oxy-, Nitro-, and Hydroxy-Oxidation Products. *Anal. Chim. Acta* **2012**, *740*, 93–103.

(66) Letzel, T.; Poschl, U.; Rosenberg, E.; Grasserbauer, M.; Niessner, R. In-Source Fragmentation of Partially Oxidized Mono- and Polycyclic Aromatic Hydrocarbons in Atmospheric Pressure Chemical Ionization Mass Spectrometry Coupled to Liquid Chromatography. *Rapid Commun. Mass Spectrom.* **1999**, *13*, 2456–2468.

(67) Lintelmann, J.; Fischer, K.; Karg, E.; Schröppel, A. Determination of Selected Polycyclic Aromatic Hydrocarbons and Oxygenated Polycyclic Aromatic Hydrocarbons in Aerosol Samples by High-Performance Liquid Chromatography and Liquid Chromatography-Tandem Mass Spectrometry. *Anal. Bioanal. Chem.* **2005**, *381*, 508–519.

(68) Lintelmann, J.; Fischer, K.; Matuschek, G. Determination of Oxygenated Polycyclic Aromatic Hydrocarbons in Particulate Matter Using AHigh-Performance Liquid Chromatography-Tandem Mass Spectrometry. *J. Chromatogr. A* **2006**, *1133*, 241–247.

(69) Mirivel, G.; Riffault, V.; Galloo, J.-C. Simultaneous Determination by Ultra-Performance Liquid Chromatography-Atmospheric Pressure Chemical Ionization Time-of-Flight Mass Spectrometry of Nitrated and Oxygenated PAHs Found in Air and Soot Particles. *Anal. Bioanal. Chem.* **2010**, *397*, 243–256.

(70) Chen, H.; Cooks, R. G. Meisenheimer Complexes Bonded at Carbon and at Oxygen. *J. Am. Soc. Mass Spectrom.* **2004**, *15*, 998–1004.

(71) Karancsi, T.; Slegel, P. Reliable Molecular Mass Determination of Aromatic Nitro Compounds: Elimination of Gas-Phase Reduction Occurring During Atmospheric Pressure Chemical Ionization. *J. Mass Spectrom.* **1999**, *34*, 975–977.

(72) Miet, K.; Le Menach, K.; Flaud, P. M.; Budzinski, H.; Villenave, E. Heterogeneous Reactions of Ozone with Pyrene, 1-Hydroxypyrene and 1-Nitropyrene Adsorbed on Particles. *Atmos. Environ.* **2009**, *43*, 3699–3707.

(73) Zhang, Y.; Yang, B.; Meng, J.; Gao, S.; Dong, X.; Shu, J. Homogeneous and Heterogeneous Reactions of Phenanthrene with Ozone. *Atmos. Environ.* **2010**, *44*, 697–702.

(74) Gao, S.; Zhang, Y.; Meng, J.; Shu, J. Online Investigations on Ozonation Products of Pyrene and Benz[a]anthracene Particles with a Vacuum Ultraviolet Photoionization Aerosol Time-of-Flight Mass Spectrometer. *Atmos. Environ.* **2009**, *43*, 3319–3325.

(75) Yao, J.-J.; Huang, Z.-H.; Masten, S. J. The Ozonation of Pyrene: Pathway and Product Identification. *Water Res.* **1998**, *32*, 3001–3012.

(76) Choi, Y.-I.; Hong, A. Ozonation of Polycyclic Aromatic Hydrocarbon in Hexane and Water : Identification of Intermediates and Pathway. *Korean J. Chem. Eng.* **2008**, *24*, 1003–1008.

(77) Miet, K.; Le Menach, K.; Flaud, P.-M.; Budzinski, H.; Villenave, E. Heterogeneous Reactivity of Pyrene and 1-Nitropyrene with NO2: Kinetics, Product Yields and Mechanism. *Atmos. Environ.* **2009**, *43*, 837–843.

(78) Ma, J.; Liu, Y.; He, H. Heterogeneous Reactions between NO2 and Anthracene Adsorbed on SiO2 and MgO. *Atmos. Environ.* **2011**, *45*, 917–924.

(79) Perraudin, E.; Budzinski, H.; Villenave, E. Kinetic Study of the Reactions of Ozone with Polycyclic Aromatic Hydrocarbons Adsorbed on Atmospheric Model Particles. *J. Atmos. Chem.* **2007**, *56*, 57–82.

(80) Perraudin, E.; Budzinski, H.; Villenave, E. Identification and Quantification of Ozonation Products of Anthracene and Phenanthrene Adsorbed on Silica Particles. *Atmos. Environ.* **2007**, *41*, 6005–6017.

(81) Chu, S. N.; Sands, S.; Tomasik, M. R.; Lee, P. S.; McNeill, V. F. Ozone Oxidation of Surface-Adsorbed Polycyclic Aromatic Hydrocarbons: Role of PAH-Surface Interaction. *J. Am. Chem. Soc.* **2010**, *132*, 15968–15975.

(82) Perraudin, E.; Budzinski, H.; Villenave, E. Kinetic Study of the Reactions of NO2 with Polycyclic Aromatic Hydrocarbons Adsorbed on Silica Particles. *Atmos. Environ.* **2005**, *39*, 6557–6567.

(83) Pierce, J. R.; Engelhart, G. J.; Hildebrandt, L.; Weitkamp, E. a.; Pathak, R. K.; Donahue, N. M.; Robinson, a. L.; Adams, P. J.; Pandis, S. N. Constraining Particle Evolution from Wall Losses, Coagulation, and Condensation-Evaporation in Smog-Chamber Experiments: Optimal Estimation Based on Size Distribution Measurements. *Aerosol Sci. Technol.* **2008**, *42*, 1001–1015.

(84) McMurry, P. H.; Grosjean, D. Gas and Aerosol Wall Losses in Teflon Film Smog Chambers. *Environ. Sci. Technol.* **1985**, *19*, 1176–1182.

(85) Fan, Z.; Kamens, R. M.; Hu, J.; Zhang, J.; McDow, S. Photostability of Nitro-Polycyclic Aromatic Hydrocarbons on Combustion Soot Particles in Sunlight. *Environ. Sci. Technol.* **1996**, *30*, 1358–1364.

(86) Rojas, A.; Orozco, E. Measurement of the Enthalpies of Vaporization and Sublimation of Solids Aromatic Hydrocarbons by Differential Scanning Calorimetry. *Thermochim. Acta* **2003**, *405*, 93–107.

(87) Pena, R.; Ribet, J. P.; Maurel, J. L.; Valat, L.; Lacoulonche, F.; Chauvet, A. Sublimation and Vaporisation Processes of S(−) Efaroxan Hydrochloride. *Thermochim. Acta* **2003**, *408*, 85–96.

(88) Popescu, C.; Segal, E. Critical Considerations on the Methods for Evaluating Kinetic Parameters from Nonisothermal Experiments. *Int. J. Chem. Kinet.* **1998**, *30*, 313–327.

(89) Hillier, J.; Bezzant, T.; Fletcher, T. H. Improved Method for the Determination of Kinetic Parameters from Non-Isothermal Thermogravimetric Analysis (TGA) Data. *Energy & Fuels* **2010**, *24*, 2841–2847.

(90) Rodante, F.; Vecchio, S.; Catalani, G.; Guidotti, M.; Elena, I. R.; Elena, V. R. Thermal Analysis and Non-Isothermal Kinetic Study of Some Pesticides Part II . Chlorinate Derivatives. *J. Therm. Anal. Calorim.* **2000**, *60*, 775–781.

(91) Haynes, W. M. *Handbook of Chemistry and Physics*; 94th ed.; CRC Press: Boca Raton, 2013.

(92) Lazar, P.; Otyepková, E.; Banáš, P.; Fargašová, A.; Šafářová, K.; Lapčík, L.; Pechoušek, J.; Zbořil, R.; Otyepka, M. The Nature of High Surface Energy Sites in Graphene and Graphite. *Carbon N. Y.* **2014**, *73*, 448–453.

(93) Zhu, D.; Pignatello, J. J. Characterization of Aromatic Compound Sorptive Interactions with Black Carbon (charcoal) Assisted by Graphite as a Model. *Environ. Sci. Technol.* **2005**, *39*, 2033–2041.

(94) Barsanti, K. C.; Pankow, J. F. Thermodynamics of the Formation of Atmospheric Organic Particulate Matter by Accretion reactions—Part 1: Aldehydes and Ketones. *Atmos. Environ.* **2004**, *38*, 4371–4382.